Contribution to modeling of damage and cracking in rock-like materials by phase-field method considering friction and hydromechanical coupling

Meng Wang

École doctorale Science de l'ingénierie et des systèmes (ENGSYS-632)
Génie Civil, Énergétique, Matériaux (MGCEM)

THÈSE

présentée par

Meng WANG

Domaine

GÉNIE CIVIL

Sujet de la thèse

Contribution à la modélisation de l'endommagement et de la fissuration des matériaux rocheux par la méthode de champ de phase considérant frottement et couplage hydromécanique

Contribution to modeling of damage and cracking in rock-like materials by phase-field method considering friction and hydromechanical coupling

pour obtenir le grade de

DOCTEUR DE L'UNIVERSITÉ DE LILLE

Soutenue le **20 FÉVRIER 2023**

Thèse dirigée par :

M. **Jianfu SHAO** — Professeur, Université de Lille
M. **Wanqing SHEN** — MCF-HDR, Université de Lille

Président du jury :

M. **Albert GIRAUD** — Professeur, Université de Lorraine

Rapporteurs :

M. **Antonio GENS** — Professeur, Universitat Politècnica de Catalunya
M. **Richard GIOT** — Professeur, Université de Poitiers

Examinateur :

Mme. **Xiaoying ZHUANG** — Professeur, Leibniz University Hannover

ABSTRACT

Cracking is the main failure mechanism of most rock-like materials. The principal process contains the initiation and growth of micro-cracks and the onset of macroscopic fractures due to the coalescence of micro-cracks. In this thesis, the phase-field method has been employed to describe the transition from diffuse cracks (micro-cracks) to localized fractures.

A basic phase-field model is first applied to modeling the onset and propagation of cracks in rock-like materials with spatial variability of mechanical properties due to micro-structural heterogeneity. A series of numerical specimens with different random distributions of mineral inclusions are investigated. The numerical predicted overall stress-strain responses are compared with experimental data.

Next, we shall develop a novel phase-field model considering coupling between damage due to crack growth and frictional sliding along closed crack surfaces. It rigorously takes into account the consequences of crack opening-closure unilateral effects. The continuity conditions are verified for all energy functions, stress-strain relations and conjugated thermodynamics forces. The performance of this model is assessed through several numerical examples and by comparing the results with experimental observations.

Then, the time-dependent deformation and failure observed in most rocks are described by a viscous phase-field model which is coupled with a viscoplastic constitutive law. The crack field is driven by viscoplastic strain, while the threshold of viscoplastic deformation is weakened by the growth of cracks. The comparison between numerical predictions and experimental data in triaxial compression and creep tests verifies the efficiency of this phase-field model.

Further, two phase-field variables are introduced to capture the tensile, shear and mixed cracks in saturated and unsaturated porous rocks. To consider the influence of frictional shear stress and normal stress on the evolution of shear cracks, a new hybrid phase field model is proposed. The examples which can demonstrate the ability of this model are presented including triaxial compression for dry material and desiccation tests.

Finally, the proposed phase-field models are applied to analyze some specific engineering problems such as slope stability and landslide. The principal failure mechanisms are identified and compared with field observations.

Keywords: Cracking, Phase-field method, Frictional microcracks, Hydromechanical coupling, Viscoplastic deformation, Slope instability, Rainfall-induced landslide

RÉSUMÉ

La fissuration est le principal mécanisme de rupture de la plupart des matériaux rocheux. Le processus principal contient l'initiation et la croissance de micro-fissures et l'apparition de fractures macroscopiques dues à la coalescence de micro-fissures. Dans cette thèse, la méthode du champ de phase a été utilisée pour décrire la transition entre les fissures diffuses (micro-fissures) et les fractures localisées.

Un modèle du champ de phase simple est d'abord appliqué à la modélisation de l'apparition et de la propagation des fissures dans les matériaux rocheux avec une variabilité spatiale des propriétés mécaniques liée à l'héterogeneité micro-structurale des matériaux. Une série de spécimens numériques avec différentes distributions aléatoires d'inclusions minérales sont étudiés. Les réponses globales en contrainte-déformation prédites numériquement sont comparées aux données expérimentales.

Ensuite, nous développerons un nouveau modèle de champ de phase en considérant le couplage entre les dommages dus à la croissance des fissures et le glissement par friction le long des surfaces de fissures fermées. Il prend en compte les conséquences des effets unilatéraux d'ouverture et de fermeture des fissures. Les conditions de continuité sont vérifiées pour toutes les fonctions énergétiques, les relations contrainte-déformation et les forces thermodynamiques conjuguées. La performance de ce modèle est évaluée à travers plusieurs exemples numériques et en comparant les résultats numériques avec les observations expérimentales.

Ensuite, la déformation et la rupture en fonction du temps qui se manifestent dans la plupart des roches sont décrites par un modèle de champ de phase visqueux qui est couplé à une loi de comportement viscoplastique. Le champ de fissures est influencé par la déformation viscoplastique, tandis que le seuil de déformation viscoplastique est affaibli par la croissance des fissures. La comparaison entre les prédictions numériques et les données expérimentales dans des essais de compression triaxiale et de fluage vérifie l'efficacité de ce modèle de champ de phase.

De plus, deux variables de champ de phase sont introduites pour capturer les fissures de traction, de cisaillement et mixtes dans les roches poreuses saturées et non saturées. Afin de considérer l'influence de la contrainte de cisaillement frictionnelle et de la contrainte normale sur l'évolution des fissures de cisaillement, un nouveau modèle de champ de phase hybride est proposé. Les exemples qui peuvent démontrer la capacité de ce modèle sont présentés, y compris la compression triaxiale pour les matériaux secs et les tests de dessiccation.

Enfin, les modèles de champ de phase proposés sont appliqués pour analyser des problèmes d'ingénierie spécifiques tels que la stabilité des pentes et les glissements de terrain. Les principaux mécanismes de défaillance sont identifiés et comparés aux observations de terrain.

Mots clés: Fissuration, méthode des champs de phase, microfissures de frottement, couplage hydromécanique, déformation viscoplastique, instabilité des pentes, glissement de terrain induit par les pluies.

ACKONWLEDGEMENTS

It has been a wonderful experience pursuing my doctoral study at Laboratoire de Mécanique, Multiphydique et Multiéchelle (LaMcube). In this exciting moment, I would like to express my warmest thanks to all those who has helped me during the last three years.

I should have been impossible for my achievements without the help and support from my Ph.D. supervisor, Prof. Jian-Fu SHAO. I want to express a deep sense of thanks to him for the patient guidance, valuable suggestions, continuous support, encouragement and motivation throughout this journey, which leads me to be not only an excellent researcher but also an outstanding man.

I would like to thank M. Wan-Qing SHEN for his guidance as well as his kindness. His persistent help and support in every situation is very important for me both in scientific researched and personal struggles.

I extend my thanks to the members of jury, professor Antonio GENS, professor Albert GIRAUD, professor Richard GIOT and professor Xiaoying ZHUANG, for evaluating my works and constructive comments, helping me to improve my research.

Great thanks also give to all the members of the research group in LaMcube, including Ms. Yun JIA, Dr. Zhan YU, Dr. Yue SUN, Dr. Hai-Ling SHI, Dr. Dong-Mei ZHANG, Dr. Xi CHEN, Dr. Jian-Jian ZHAO, Dr. Jue-Liang CHEN, Dr. Si-Yu LIU, Dr. Li-Ping ZHU, Dr. Wang ZHANG, Dr. Hongzhuo FAN, Dr. Yue SHI, ... for their help and the precious memories. The experience of this journey would not be the same without these friends.

Last but not least, I would like to thank my parents, all members of my family for their moral support and their love. I consider myself very lucky for meeting my wife, Yudan JIN, without whom my life should not have been complete. Thank you for your accompany, unconditional support and for everything.

CONTENTS

LIST OF FIGURES

LIST OF TABLES

General Introduction

Damage due to initiation and propagation of cracks is commonly observed in brittle rocks. Macroscopic failure of these materials is generally driven by the transition from micro-cracks to macro-cracks or fractures (Evans et al., 1990; Wong and Baud, 2012; Cuomo et al., 2021).

Moreover, these materials usually experience complex loading paths including tensile and compressive stresses, which could induce different types of cracks and opening-closure transition of cracks. The consequences of cracks on mechanical behavior of such materials are also dependent on crack conditions. For instance, the propagation of open cracks could induces the progressive deterioration of both elastic bulk and shear modulus, while the growth of closed smooth cracks generally affects the shear modulus only. On the other hand, in rock and concrete like materials, crack surfaces are not smooth but rough and characterized by a frictional coefficient. When such cracks are closed, no elastic sliding occurs and the macroscopic elastic stiffness is then not affected by induced cracks. The growth of closed rough cracks is driven by the frictional sliding along crack surfaces, which can generate irreversible macroscopic strains, conventionally seen as plastic strains. With the increase of loading, there is transition from diffuse micro-cracks to localized macro-cracks.

Further, the so-called sub-critical slow propagation of micro-cracks and their coalescence (Atkinson, 1982; Meredith and Atkinson, 1985) can lead to time-dependent deformation and failure. Different types of experimental studies have been reported. For instance, in the framework of linear fracture mechanics, double torsion tests were performed to identify the sub-critical growth kinetics of cracks in various rocks (Henry et al., 1977; Atkinson, 1984; Nara and Kaneko, 2005, 2006). In rock-like materials, this phenomenon has been recognized as viscoelastic and viscoplastic deformation (Fabre and Pellet, 2006; Sterpi and Gioda, 2009; Yang et al., 2014; Zhou et al., 2015a; Liu and Shao, 2017). According to previous studies (Sterpi and Gioda, 2009; Zhao et al., 2017), the irrecoverable viscoplastic deformation should be the main responsible for the time-dependent delayed failure of rock engineering structures. Moreover, in many rocks, the viscoplastic deformation is intimately coupled with the growth of cracks. The macroscopic plastic and viscoplastic deformation can be partially related to the frictional sliding along micro-crack surfaces (Zhao et al., 2016; Shi et al., 2019; Hu et al., 2020). The viscoplastic deformation

can be enhanced by the induced growth of cracks while the cracking process is affected by the creep deformation of materials.

In addition, these materials usually contain the pores inside which are filled with water and air. Due to desiccation or saturation, the pressure of fluids in pores can be changed. Generally, this change of the pore pressure could induce the development of microcracks of these porous media. In literature, the hydraulic cracks have been observed in various experiment (Li et al., 2020a).

On the other hand, the damage localization makes the boundary values problems ill-posed. Therefore, several critical issues should be handled in modeling of damage and cracking of rock and concrete like materials, including the unilateral effects due to crack opening-closure, the damage-friction coupling, the time-dependent irreversible deformation, the hydro-mechanical damage coupling, the transition from diffuse damage to localized cracks and the regularization of damage localization problems.

During several decades, a large number of phenomenological damage models have been proposed for different types of engineering materials including rocks and concrete. Most of them were formulated in the framework of thermodynamics, by adopting a scalar internal variable for isotropic damage (Jefferson and Mihai, 2015; Chen et al., 2015; He et al., 2015) or tensorial variables for anisotropic damage (Voyiadjis et al., 2008; Desmorat, 2016; Zafati and Richard, 2019). Different techniques, such as the spectral decomposition of stress, strain or free energy function, have been introduced in order to consider the dissymmetric behavior between tension and compression in rock like materials. Unilateral effects have also been considered in many studies (Halm and Dragon, 1996; He et al., 2015). The emphasis was the continuity of mechanical responses at the crack opening-closure transition (Cormery and Welemane, 2002; Alliche, 2016). In some studies, the coupling between damage and frictional sliding was also taken into account (Halm and Dragon, 1998). This is particularly important for unloading-reloading paths and cyclic loading (Richard and Ragueneau, 2013; Vassaux et al., 2015; Zafati and Richard, 2019). In those phenomenological models, the links between macroscopic behavior and microscopic evolution of cracks are not explicitly established. To complete and improve the macroscopic approaches, a series of micro-mechanical models have been developed by using different homogenization schemes. With these micro-mechanical approaches, the unilateral effects can be easily taken into account, in particular for anisotropic damage (Zhu et al., 2011). The coupling between crack evolution and frictional sliding is also

more rigorously described (Gambarotta, 2004; Zhu and Shao, 2015; Zhu et al., 2016). Despite of the significant advances, the description of transition from diffuse damage to localized cracks remains an open challenge. In some micro-mechanical models, the authors have tried to include localized cracks in the representative volume element (Zhao et al., 2018a). However, the efficiency of such models for complex loading conditions remains questionable.

Moreover, different types of numerical methods have been developed. It is not the objective to give an exhaustive review of all those methods. In framework of continuum mechanics, two principal categories of approaches are available. In the first one, cracks are considered as strain or damage localization bands without explicitly considering displacement discontinuities across cracks. The bifurcation theory is widely used as the onset criterion of strain localization in plastic materials (Rudnicki and Rice, 1975). High order strain gradient models (De Borst and Mühlhaus, 1992; Chambon et al., 2001) and non-local damage models (Pijaudier-Cabot and Bažant, 1987; Jirásek and Patzák, 2002) have been proposed to regularize the ill-posed boundary values problems in the post-localization regime, respectively for plastic and brittle materials. In the second category, displacement discontinuities across cracks are explicitly taken into account. Among different types of numerical methods, we mention here two widely used ones. The enriched finite element method (EFEM) introduces specific shape functions being able to represent discontinuous displacement field at the elementary level (Oliver, 1996). On the other hand, the extended finite element method (XFEM) employs nodal enrichment techniques to incorporate displacement discontinuities (Moës et al., 1999). The extended finite element method has been extended to modeling hydraulic fracturing in saturated porous rocks (Zeng et al., 2020). It has also coupled with the meshfree method in order to easily consider fluid flow through opened cracks (Rabczuk et al., 2010). However, it is a general weak point of continuum mechanics approaches to describe fluid flow through individual cracks. In order to overcome this issue, different types of discrete approaches have been proposed. As examples, we only mention here the cracking particle method (Rabczuk and Belytschko, 2004) and the dual-horizon peridynamics model (Ren et al., 2016b; Rabczuk and Ren, 2017). In case of multiple cracks in three-dimensional problems, a very important computing effort is necessary.

In spite of these significant advances obtained, the transition from diffuse damage (micro-cracks) to localized macroscopic cracks remains an open issue. In order to com-

plete and improve the previous methods to deal with this critical issue, the so-called phase field method has been proposed and it is more and more applied to various engineering problems (Miehe et al., 2010a; Borden et al., 2012; Ambati et al., 2015). This method was initially based on the revisited brittle fracture mechanics model proposed by Francfort and Marigo (1998), which was numerically implemented by Bourdin et al. (2000). This model was also inspired by the elliptic regularization method proposed by Ambrosio and Tortorelli (1990) of the functional in image segmentation problems formulated by Mumford and Shah (1989). With the help of an auxiliary damage variable, sharp cracks surfaces are approximated by a volumetric crack surface density which is a function of damage variable and its gradient. The main advantage of the phase field method is its ability to describe the continuous transition from diffuse damage to localized cracks. There is no need to introduce a specific criterion to detect the onset of new cracks. It can also be easily applied to multiple cracks in three-dimensional problems.

Some extensions of the phase field method have been proposed to modeling mixed cracks in rock-like materials under compressive stresses (Amor et al., 2009; Zhou et al., 2019b). In some works (Zhang et al., 2017), two energy functionals were used to respectively control the evolution of tensile and shear cracks. A kinematic-consistent phase-field model has been proposed for mixed-mode cracks in anisotropic rocks (Bryant and Sun, 2018). More recently, a number of phase-field models have incorporated the coupling between plastic deformation and damage evolution (Miehe et al., 2015a; Borden et al., 2016; Choo and Sun, 2018; Samaniego et al., 2021; Khalil et al., 2022). The specific issues related to friction in geological materials have also been investigated (Fei and Choo, 2020a,b; Yu et al., 2021a). However, these models are usually devoted to a specific category of cracks or loading conditions.

In view of the dynamic cracking analysis, explicit phase field models were also reported (Ren et al., 2019). In addition, a deep neural network (DNN) based solution for solving phase-field fracture was proposed by (Goswami et al., 2020), which totally avoids a classical discretization to solve the underlying coupled partial differential equations. Despite all these advances, only few studies have been devoted to time-dependent fracturing in viscoplastic rocks (Shen et al., 2019). However, as the main limitation of phase-field method, the propagation of sharp cracks is approximated by the growth of damage field and onset of localized damage bands. Consequently, the time-dependent cracking process is described by the time-dependent evolution of damage field coupled with the

viscoplastic flow.

Another advantage of the phase field method is its flexibility to deal with multi-physical coupling problems. For example, it has been used for modeling hydraulic fracturing (Bourdin et al., 2012; Wheeler et al., 2014). Some authors (Miehe and Mauthe, 2016) have introduced a constitutive balance equation for a regularized crack surface and its modular linkage to a Darcy-Biot-type bulk response of hydro-poro-elastic media. Some recent works have been performed on hydraulic fracturing in saturated geological materials (Zhou et al., 2020; Zhuang et al., 2020). A few studies have also been devoted to modeling of cracking processes in partially saturated porous media by considering capillary forces (Cajuhi et al., 2018; Heider and Sun, 2020).

From the point of view of engineering application, the occurrence of landslides is inherently related to material failure. According to the previous survey (Haque et al., 2019), during two decades (1995-2014), 3876 landslides happened all over the world, and caused 163658 deaths and 11689 injuries in total.

One important cause of landslides is rainfall, especially in tropical areas with hot and humid climates (Tohari et al., 2007; Tsai et al., 2008; Frattini et al., 2009). Without giving an exhaustive review of the large number of previous studies devoted to landslides, the emphasis is here put on the rainfall induced catastrophe (Chen et al., 2021; Shou and Chen, 2021; Thirard et al., 2022). Based on the rainfall-induced landslides data, a variety of empirical models have been proposed to predict the occurrence of such catastrophes (McDonnell, 1990; Knighton, 1998). However, the hydromechanical coupling and the progressive cracking process are generally not properly considered in those empirical models (Zhang et al., 2005b; Kukemilks et al., 2018; Cho, 2020). Hence, in classical methods, the consequence of rainfall is considered by taking into account the variation of groundwater level. However, in most shallow failure cases, there is not much evidence of the groundwater table change (Fourie et al., 1999). The failure process is mostly linked to the propagation of a wetting front, resulting in the decrease of suction and shear strength of partially saturated soils and rocks (Fredlund and Rahardjo, 1993; Rahardjo et al., 1995; Fourie, 1996). Therefore, rainfall-induced failure processes should be studied by considering full hydro-mechanical coupling (Chang et al., 2021; Sun et al., 2021).

On the other hand, instability and failure of rock slope and natural systems can also be caused by time-dependent crack growth and viscoplastic deformation. For instance, many catastrophic landslides were induced by the accumulation of creep deformation and

slow crack propagation and localization (Dramis et al., 2002; Morelli et al., 2018). Before the final failure, a gradual increase of deformation over time was monitored in a number of typical landslides (Tavenas and Leroueil, 1981; Intrieri et al., 2019). For instance, landslide of a natural slope caused by tunnel excavation was reported in (Yashima, 2001). In that accident, the slope failure occurred a few days after an arriving entrance of the tunnel was cut through. Progressive failure was clearly observed while no evidence of rainfall or underground water movement could be monitored (Zhang et al., 2005a). In many cases, natural hazards should be analyzed as evolutionary processes by taking into account time-dependent mechanical behavior of geological formations Eker and Aydın (2021), in particular creep deformation and slow growth of cracks. The widely used limit equilibrium methods mainly focused on ultimate instability mechanisms and do not considered progressive failure processes involved.

In order to complete the limit analysis methods and provide a finer description of natural hazards, numerical modeling is now widely used for analyzing landslides and for developing suitable mitigation techniques (Rahimi et al., 2011; Ren et al., 2016a; Gao et al., 2017). Compared with theoretical solutions and experimental investigations (Ling et al., 2009; Wu, 2015; Irfan et al., 2017), numerical approaches are able incorporate complex loading and environmental conditions (Wang et al., 2019a). However, the performance of numerical modeling for landslides is dependent not only on the thorough examination of geological conditions (Li et al., 2018), but also on the correct description of physical behavior of soils and rocks (Zhang et al., 2015; Cheng et al., 2018; Lin et al., 2018).

Therefore, This thesis will be composed as following:

In Chapter 1, the state of the art in line with the purpose of this thesis is presented. Firstly, a brief introduction to the background and motivations will be given. Then, different numerical methods in literature are reviewed regarding their abilities for simulating fracture propagation and damaged materials. Finally, a review focuses on phase-field method of fracture to provide the reader with the concepts at the base of the present work.

In Chapter 2, a phase-field method is applied to modeling damage and cracking in rock-like materials by considering spatial variability of materials heterogeneities. The formulation of phase-field method is first summarized for elastic brittle materials. The effective elastic properties of rocks are determined as functions of mineral compositions by using a linear homogenization method. The randomly distribution of mineral inclusions is assumed to follow the Weibull distribution. A series of five numerical specimens

are chosen to investigate the onset and propagation of localized cracks. Comparisons between numerical results and experimental data are also presented for overall stress-strain responses.

In Chapter 3, we shall develop a novel phase-field model for modeling complex cracking processes in rock like materials under various loading paths. Both smooth frictionless and rough frictional cracks are investigated. For smooth cracks, an elastic-damage model is formulated with the unilateral effect on elastic stiffness tensor at the crack opening-closure transition. For rough cracks, an elastic-plastic damage model is developed, also incorporating the unilateral effect. In particular, for closed rough cracks, the damage evolution is explicitly coupled with the frictional sliding along cracks, which results in the macroscopic plastic deformation. The continuity conditions are verified for all energy functions, stress-strain relations and conjugated thermodynamics forces. By incorporating the friction sliding mechanism, the proposed model is able to properly take into account the dependency of mechanical behavior on confining stress of most geological materials under compressive stresses. The efficiency of the novel model is assessed through various cases, including comparisons between numerical results and experimental observations.

In Chapter 4, two main mechanisms are generally considered, the progressive growth of cracks and viscoelastic and/or viscoplastic deformation. For this purpose, cracking process is described by a viscous phase-field method which is coupled with a viscoplastic model. The evolution of crack field is controlled by both elastic and viscoplastic tensile volumetric and deviatoric strains. The threshold of viscoplastic deformation is weakened by the growth of cracks. The efficiency of the proposed model is assessed by comparing numerical predictions with experimental data in triaxial compression and creep tests.

In Chapter 5, we first present a new phase-field model for modeling the deformation and progressive failure in saturated and unsaturated porous rocks. Two independent damage variables are used to conveniently capture tensile, shear and mixed cracks. The influences of frictional shear stress and normal stress on the evolution of shear cracks are taken into account. The phase-field model is extended to variably saturated porous rocks by including the effect of pore water pressure. The proposed model is implemented in the framework of finite element method for coupled hydro-mechanical and damage problems. The phase field model is able to describe global stress-strain responses and localized cracking patterns in brittle rocks at the laboratory scale. The onset of localized cracks is directly linked to the non-uniform distribution of porosity. The proposed

phase-field model is also applied to the analysis of drying-induced cracking.

In Chapter 6, the three new phase-field models are used to analyze the slope stability and landslide under different conditions. First of all, the phase-field method considering the damage-friction coupling is employed to instability analysis of slope. Then, the proposed phase-field model for partially saturated pores media is applied to the analysis of rainfall-induced landslides. The numerical results of cracking scenarios are consistent with the real field observations in the Mayanpo slope in China. The main physical mechanisms involved in the rainfall induced instability of slopes are analyzed. Last but not least, the model coupling with viscoplastic is applied to modeling time-dependent deformation and failure process of a high slope section in the left bank of Jinping-I hydropower station in China. Numerical predictions are compared with field measurements.

Finally, some conclusion remarks are drawn and the perspectives are presented.

CHAPTER 1

State of the Art

1 Background and motivations

As the most common materials in civil engineering, rock-like materials (e.g. concrete and rocks) play an important role in stability of civil engineering structures. Furthermore, it has been observed both in laboratory tests and *in situ* monitoring of existing geotechnical and civil engineering structures that rock-like materials failure is mainly caused by onset and propagation of fracture and cracks (seeing Figure 1.1). Consequently, the fracture or cracking of rock-like materials has received lots of attention for a long time.

On the other hand, it is almost impossible to solve fracture mechanics problems using analytical tools (Mandal, 2021). Accordingly, numerical modeling of the cracking process in rock-like materials and civil engineering structure is of formidable interest, due to the important development of computer technology. Moreover, it also requires insights into understanding the underlying physical phenomena of fracture processes to enhance the accuracy and the predictiveness of computational cracking models. In addition, failure of rock-like materials in civil engineering structures may be caused not only by mechanical loading, but also by hydraulic, thermal, chemical perturbations and even time-dependent irreversible deformations. However, even though many theories and models have been developed, predictive modeling of the crack initiation and propagation in materials and structures remains one of the most significant challenges in solid mechanics.

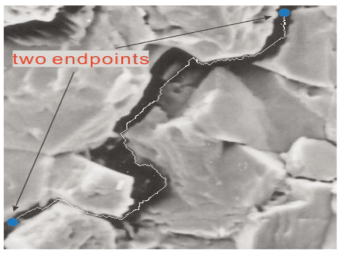

(a) Microcracks in SEM image (Luo et al., 2015)

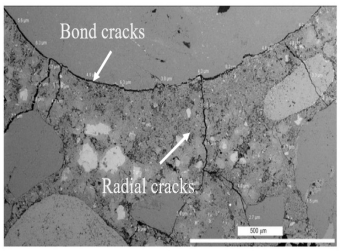

(b) Microcracks observed in dying sample (Wong et al., 2009)

(c) Cracks in rock-like disk specimens (Cao et al., 2019)

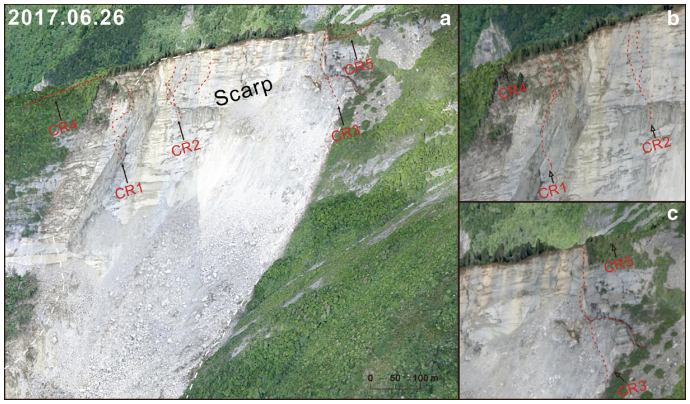

(d) Cracks reconstruction after landslides (Fan et al., 2017)

Figure 1.1: Cracks in civil engineering problems at different scales

More recently, new numerical modeling of cracking process, named as phase-field method, has attracted more and more interests (Bourdin et al., 2000; Miehe et al., 2010a; Borden et al., 2012; Ambati et al., 2015). The main advantage of the phase field method is its ability to describe the continuous transition from diffuse damage to localized cracks. There is no need to introduce a specific criterion to detect the onset of new cracks. It can also be easily applied to multiple cracks in three-dimensional problems.

In the above background, the motivations of this thesis are listed as follows:

- Introduce the basic formulation of phase-field method for simulating the onset and propagation of cracks in elastic brittle materials and apply this method in considering spatial variability of materials heterogeneities;
- Develop a novel phase-field model for modeling complex cracking processes in rock like materials for both smooth frictionless and rough frictional cracks based on micro-mechanics;

- Proposed a time-dependent phase-field model which can describe both the progressive growth of cracks and viscoelastic and/or viscoplastic deformation;
- Establish the phase-field model for modeling the deformation and progressive failure in saturated and unsaturated porous rocks;
- Present the example for applications of the proposed phase-field models into stability analysis of civil engineering structure, such as landslides.

2 Literature review on modeling of damage and cracks

One of powerful theories to model fracture is continuum damage mechanics (CDM) (Kachanov, 1958). This approach looks at the overall response at the macro or structural scale by using some internal variables to characterize damage, and thus can be termed as "macro-damage mechanics". During last decades, numerous phenomenological models have been proposed based on continuum damage mechanics to take into account of the initiate and propagation of fracture in rock-like materials. Despite the wealthy studies about phenomenological damage models, this approach exhibits some theoretical shortcomings.

Micro-mechanics based models as the alternative approach have gained a strong impetus for the capability in relating the macroscopic behaviors of the material to its microstructure characteristics and local properties (Zhu and Shao, 2017). However, further efforts for these micro-mechanics based models are still needed to describe the continuous transition from diffuse damage (micro-cracks) to macro-cracks in the form of localized damage bands.

On the other hand, many numerical simulation methods for crack propagation have been developed in the recent decades, but each faces well-known issues and drawbacks, as presented in the following.

2.1 Continuum damage models

The concept of damage mechanics was first proposed by Kachanov (1958). He introduced the concept of continuity factor which he called damage index or integrity, defined as the ratio of the differential intact area element to the original area element, and the con-

cept of effective stress to describe low stress brittle creep damage in the study of metal creep, and gave the evolution equation of integrity:

$$\dot{\psi} = B(\frac{\sigma}{\psi})^{\nu} = B\bar{\sigma}^{\nu} \tag{1.1}$$

where ψ denotes the continuity variable, B and ν are material parameters, σ represents the Cauchy stress and $\bar{\sigma}$ is the effective stress, which is the net stress acting on the undamaged area.

Rabotnov et al. (1970) then defined the concept of damage factor $D = 1 - \psi$ and coupled the damage variable with stress to form the Kachanov-Rabotnov constitutive equations:

$$\dot{\varepsilon_{cr}} = A(\frac{\sigma}{1-D})^{n} \tag{1.2}$$

$$\dot{D} = B\frac{\sigma^{\nu}}{(1-D)^{\mu}} \tag{1.3}$$

where ε_{cr} is creep strain, A and n are the Norton power law constants and μ is the tertiary creep-damage constant.

Kachanov and Rabotnov's works laid the basis of *Damage Mechanics* or *Continuum Damage Mechanics*. Since then, these concepts have been further enriched by Lemaitre (1985), Murakami (1988), Hult (1974), Hayhurst (1972) and other researchers (Chaboche, 1988; Chow and Wang, 1987; Ju, 1990; Gurson, 1977) by employing the method of continuum mechanics to further extend the *damage* as a field variable, and gradually been formed into the discipline of *Continuum Damage Mechanics (CDM)*. This theory has been extended from the initial creep damage to the analysis of elastic, plastic, brittle, fatigue and other damage phenomena, and its description of materials has been extended from metals to rocks, ceramics, composites and other non-metallic materials.

The first application of CDM to rock-like materials can be found in Burt and Dougill (1977). Then, Dragon and Mróz (1979) applied the damage concept to propose an elasto-plastic constitutive equation for rocks and concrete that reflects strain softening; Krajcinovic and Silva (1982) used thermodynamic theory to conduct a more comprehensive and in-depth study of the constitutive equation for brittle rocks, achieving remarkable results; Costin (1985) explored the damage characteristics of rocks and other materials after damage and its mechanical description; Lemaitre (1986) proposed a stress-strain relationship using the concept of equivalent strain. Many researchers have applied *Continuum Damage*

Mechanics to rock-like materials from different viewpoints and developed corresponding theories and models (Frantziskonis and Desai, 1987; Cai and Horii, 1993; Murakami, 1988; Chaboche, 1988; Ju and Chen, 1994; Homand-Etienne et al., 1998; Dragon et al., 2000; Zhang and Cai, 2010), thus enriching and improving the research on *Continuum Damage Mechanics* of rock-like materials.

The models commonly used in the brittle rock-like materials include those models proposed by Løland (1980), Mazars (1986), Krajcinovic and Fonseka (1981), Murakami and Kamiya (1997), etc. The main advantage of these models is that they provide clear and intuitive macroscopic damage equations, which are easy to implement programmatically and convenient to use in practical engineering. However, their disadvantages are also obvious, as some of the concepts and parameters in the models do not have clear physical meaning, lack of theoretical support, and cannot clarify the morphology and variation of the damage from the microstructure level. Therefore, it is difficult to study the damage at the microscopic level. At the same time, most of the macroscopic models are focused on describing the damage caused by tensile stresses, and tests have shown that these models cannot correctly describe the high pressure sensitivity of brittle materials such as rocks (Lu and Shao, 2002).

2.2 Micro-mechanical damage models

On the other hand, Gurson (1977) developed the first micro-mechanical damage model to describe the pores in materials . As the alternative approach, micro-mechanics based models have gained a strong impetus for the capability in relating the macroscopic behaviors of the material to its microstructure characteristics and local properties (Paliwal and Ramesh, 2008; Zhou et al., 2010; Xie et al., 2011; Zhu and Shao, 2017). The micro-mechanics damage is a method to understand the essence and mechanism of material damage by studying the physical process of the evolution of the microstructure and to derive the macroscopic properties of materials with the help of certain homogenization schemes. The commonly used schemes are sparse scheme (Kinoshita and Mura, 1971), Mori-Tanaka scheme (Mori and Tanaka, 1973), self-consistent scheme (Budiansky and O'connell, 1976; Horii and Nemat-Nasser, 1983) and differential scheme (Hashin, 1988; Zimmerman, 1991), etc.

Compared with other damage mechanics models, the micro-mechanical damage mod-

els have a clear physical significance of the damage variables, which can reveal the micro-damage mechanism of rock-like materials more accurately and reflect the main macro-mechanical deformation behavior of rock-like materials. As an example, Zhu et al. (2011) have derived a micromechanics thermodynamic formulation involving microcrack opening–closure transition based on Eshelby's solution. Particularly, the constitutive formulations (Zhu and Shao, 2015; Zhu et al., 2016) coupling the crack growth and frictional sliding have been proposed in micro-mechanics based approaches. By taking into account the unilateral effect due to micro-cracks opening-closure and the damage evolution driving by friction sliding, these micromechanical models established a more physically relationship between microscopic structure and macroscopic mechanical responses. Shen and Shao (2017) have developed a complete elastic-plastic model with the determination of a particular plastic hardening law and plastic potential on the basis of the analytical macroscopic yield criteria derived with a nonlinear homogenization approach (Shen et al., 2015). In the framework of irreversible thermodynamics, (Hu et al., 2020) have proposed an elastoplastic damage model based on micro-mechanics. Time-dependent deformation of rock was also taken into consideration by taking into account the subcritical development of microcracks. The developed model is then applied in the deformation analysis of the Jinping I hydropower station's left bank slope.

However, for the reason that highly concentrated strain bands or damage zones has been used to represent the localized cracks with strong discontinuities (Zhao et al., 2018a), further efforts are still needed to describe the continuous transition from diffuse damage (micro-cracks) to macro-cracks in the form of localized damage bands. At the same time, due to the complexity of micro-mechanical damage models, some of the model parameters are difficult to determine through conventional experiments, and the numerical computation is relatively cumbersome, its engineering application value still needs further research.

2.3 Numerical modeling of damage and cracks

Due to the rapid advancement of computer technology, numerical simulations are now routinely employed to solve complicated practical problems in engineering and research. In the field of materials science, numerical simulation is an effective method for validating analytical models, explaining physical phenomena, and providing significant insights

for experimental studies, where displacement discontinuities across cracks are explicitly taken into account. Many powerful computational approaches for studying brittle fracture have been developed in the last decades, each one has its advantages and drawbacks. Without giving an exhaustive list of all those methods, we mention here several methods that are widely used.

2.3.1 Extended Finite Element Method (XFEM)

The Extended Finite Element Method (XFEM) is a numerical computational method based on the idea of partition unity-based method (PUFEM), which is an important improvement of the traditional finite element method (FEM). The basic idea of this method is to represent the strong and weak discontinuities in the computational domain by the expanded form function basis with discontinuity, which has been developed rapidly since it was proposed by Professor Belytschko and his team at Northwestern University in 1999 (Belytschko and Black, 1999), and its most important feature is that the crack expansion path is not affected by the finite element meshing, which means the crack expansion process can be reproduced visually. XFEM inherits all the features and advantages of FEM, while overcoming the difficulty of high-density meshing in the high stress and deformation concentration zone at the crack tip.

The fractures in the XFEM approach are characterized separately of the mesh by inserting discontinuous enrichment functions at nodes. Two types of enrichment functions may be used in this method: one for nodes of cracked elements to create the strong discontinuity (K set in Figure 1.2), and another for nodes of elements containing a crack tip to add singular terms (J set in Figure 1.2). At the same time, on the basis of Belytschko and Black (1999), Moës et al. (1999) introduced the Heavside function to strengthen the nodes at the crack surface, which is used to solve the problem of discontinuity of the displacement field at the crack surface, the displacement function is approximated as follows

$$u^h = \sum_{i \in I} u_i N_i + \sum_{j \in J} b_j N_j H(x) + \sum_{k \in K} N_k (\sum_{l=1}^{n} c_k^l F_l(x)) \tag{1.4}$$

where u is the displacement, I is the set of all nodes, N is the enrichment function, J is the set of crack-enriched nodes, $H(x)$ is the Heaviside function and K is the set of nodes enriched by the crack tip functions $F_l(x)$; b and c are vectors of additional degrees of

freedom.

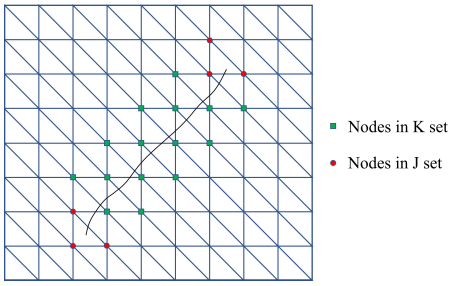

Figure 1.2: Enriched nodes in XFEM method for tracking crack

Among the numerous applications and enhancements of XFEM, expansions such as non-planar 3D crack formation (Moës et al., 2002; Gravouil et al., 2002; Sukumar et al., 2003), bi-materials (Liu et al., 2004), dynamic cracks and shear band propagation (Song et al., 2006) can be highlighted. More recent works can be found in (Wang, 2015; Agathos et al., 2019; Tan et al., 2021). XFEM is a good choice for fixed fracture and interface problems, however, the use of XFEM to model problems with multiple cracks remains limited due to its cumbersomeness to deal with high amount of discontinuity (Zi et al., 2007).

2.3.2 Embedded Finite Element Method (EFEM)

As one of the important improved methods on the basis of the traditional finite element method, same with XFEM, EFEM allows arbitrary propagation and resolution of discontinuities independently of the underlying spatial discretization. However, they have completely different theoretical foundations and are generally considered to be two unrelated approaches (Jirásek and Belytschko, 2002; Borja, 2008; Oliver et al., 2006; Dias-da-Costa et al., 2010). In EFEM, the enrichment parameters, which are normally thought of as element-wise local variables, are eliminated at the element level via static condensation, whereas in XFEM they are associated with nodes in the global sense (see Figure 1.3). The approximated displacement field for EFEM can be written as follows:

$$\boldsymbol{u}^h = \sum_{i \in I} N_i(\boldsymbol{x}) \boldsymbol{u}_i(t) + \sum_{e \in E_c} [H_S(\boldsymbol{x}) - f^h(\boldsymbol{x})]_e \boldsymbol{q}_e(t) \tag{1.5}$$

in which E_c is the set of cracked elements, $\boldsymbol{q}_e(t)$ is the displacement jump within the corresponding element, H_S is the Heaviside function with respect to the discontinuity

surface S, and the support domain for the terms in square brackets is the corresponding element.

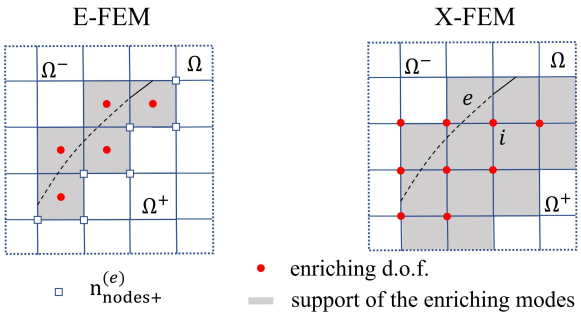

Figure 1.3: Representation of a element-based enrichment (left) and a nodal enrichment (right) (Oliver et al., 2006)

The fundamental notion was inspired initially by Ortiz (1985) and Xu and Needleman (1994), who enhanced the standard finite element by incorporating one weak discontinuity. Then, Belytschko et al. (1988) proposed a model in which two weak discontinuities form a softening band. Models with strong discontinuities were quickly proposed (Dvorkin et al., 1990; Simo et al., 1993). In the early developments (Simo and Rifai, 1990; Oliver, 1996; Armero and Garikipati, 1996; Wells and Sluys, 2000; Borja, 2000; Jirásek, 2000; Oliver et al., 2002), EFEM usually deals with with quasi-static problems. Huespe et al. (2006) expanded EFEM with a cohesive model to simulate dynamic fracture. Armero and Linder (2009) proposed a model with strong discontinuities and linear interpolations of displacement jumps. Saksala et al. (2015) employed EFEM and the rate dependency of tensile strength to characterize the rate-dependent behavior of materials.

By using the so-called static condensation procedure (Wilson, 1974), EFEM is particularly suitable for applications where multiple cracks occur. However, other drawbacks of EFEM are the strong grid dependence due to the lack of continuity of the displacement field between the two elements and the lack of convergence of the solution as the mesh size varies, which leads to unexpected approximation errors (Oliver et al., 2006; Wu et al., 2015).

2.3.3 Peridynamics (PD)

In 2000, Silling (2000) proposed a theory of Peridynamics (PD), which overcomes the dependence of Classical Continuum Mechanics on computational meshes by describing

the constitutive relations of materials through spatial integral equations. Its nonlocal core concept can be considered as a continuum version of Molecular Dynamics and relates it to Classical Continuum Mechanics (see Figure 1.4).

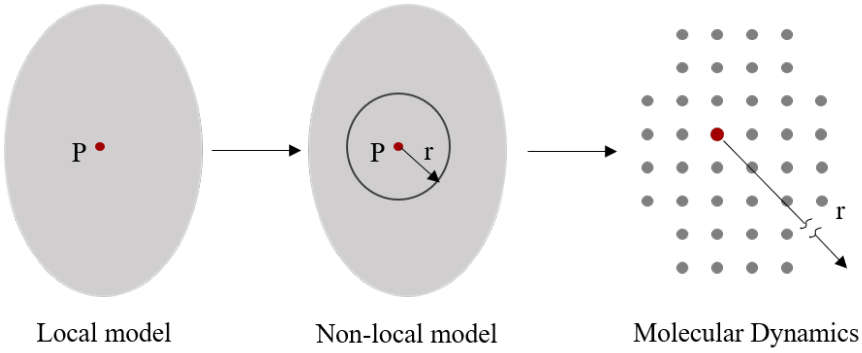

Figure 1.4: Relationship among local model, non-local model and molecular dynamics

In PD, the material model is discretized into material points, and the state of each material point $\boldsymbol{x}$ is effected jointly by all material points within a region H_x of finite radius δ, as shown in Figure 1.5(a). According to the Newton's law, the PD equation of motion at a material point $\boldsymbol{x}$ and the time t is given as (Silling and Askari, 2005):

$$\rho(\boldsymbol{x})\ddot{\boldsymbol{u}}(\boldsymbol{x},t) = \int_{H_x} \boldsymbol{f}(\boldsymbol{x},\boldsymbol{x'},\boldsymbol{u}(\boldsymbol{x},t),\boldsymbol{u}(\boldsymbol{x'},t))dV_{\boldsymbol{x'}} + \boldsymbol{b}(\boldsymbol{x},t) \tag{1.6}$$

where ρ is the density of material, $\boldsymbol{u}$ represents the displacement of material point, $\boldsymbol{f}$ is the force density between two material points, V and $\boldsymbol{b}$ is the volume and body force density of material point respectively.

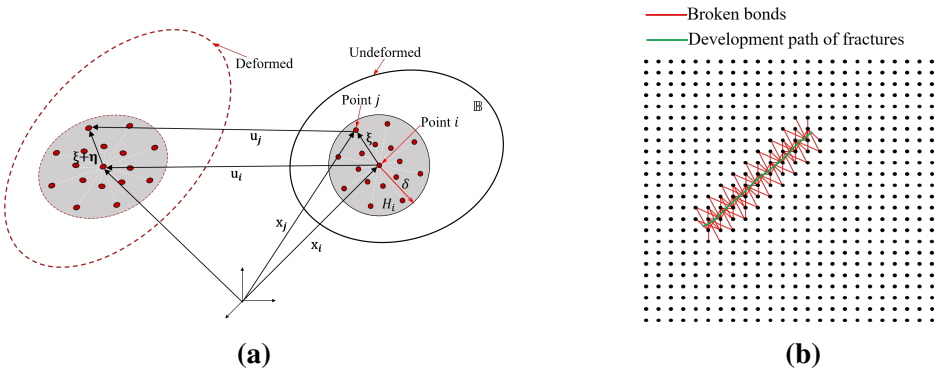

Figure 1.5: (a) Function of the force state in Peridynamics; (b) Crack initiation and propagation

PD enables the modeling of material damage through the irreversible breakage of bonds between material points, which is determined by the extension of the bonds (see Figure 1.5(b)). By treating material fracture as part of the PD constitutive equations, cracks are allowed to initiate and propagate naturally as the simulated material moves from continuity to discontinuity without the necessity of specifying crack propagation paths and introducing external criteria.

With its distinctive advantages in solving discontinuity problems such as crack extension, material damage, and structural instability, PD is widely used in many fields, including damage of macro-fine materials such as composites (Kilic et al., 2009), concrete (Gerstle et al., 2007), crystalline materials (Sun and Sundararaghavan, 2014), and ice (Wang et al., 2018), physical processes such as heat conduction (Bobaru and Duangpanya, 2012) and chemical corrosion (Rokkam et al., 2018), and multi-physical field coupled phenomena such as thermo-mechanical coupling (Wang et al., 2019b) and chemical-mechanical coupling (Rokkam et al., 2019). PD is also used extensively in rock-like materials. As an example, Zhou et al. (2015b) investigated the brittle damage of rock-like materials using the bond-based PD model, by simulating the notched semicircular bending test and the tensile-shear damage mode of rock with multiple initial fractures, respectively, demonstrated the applicability of PD in describing the failure process of rock-like materials.

Although PD theory has outstanding advantages in dealing with discontinuous problems and the simulation range from microscopic to macroscopic, its solution efficiency is low due to the computational capacity of the computer, especially when it comes to the actual engineering problem size. In dealing with continuity problems, its solution efficiency is not as good as that of Finite Elements Method.

3 Review of variational phase-field methods

In spite of significant advances obtained, the transition from diffuse damage (microcracks) to localized macroscopic cracks remains an open issue. In order to complete and improve the previous methods to deal with this critical issue, the so-called phase field method has been proposed. This method was initially based on the revisited brittle fracture mechanics model proposed by Francfort and Marigo (1998), which was numerically implemented by Bourdin et al. (2000). The name for this method, "phase-field", was first coined in Proceedings in Applied Mathematics and Mechanics by Kuhn and Müller

(2008) and their follow up journal paper (Kuhn and Müller, 2010). Over the last dozen years, researchers made a huge effort to develop novel, efficient, and accurate phase-field models and achieved enormous progress (Miehe et al., 2010a; Ambati et al., 2015; Heider, 2021; Diehl et al., 2022; Zhuang et al., 2022).

3.1 Regularization of sharp cracks

An important ingredient of phase-field method relies on a regularized description of the discontinuities related to sharp cracks. From mathematical viewpoint, it is a challenge to regularize the sharp cracks due to the lower-dimensional manifold of the cracks. In order to overcome this difficulty, the regularization method in phase-field model was initially inspired by the elliptic regularization method proposed by Ambrosio and Tortorelli (1990) of the functional in image segmentation problems formulated by Mumford and Shah (1989).

As shown in Figure 1.6, the evolution of sharp crack surface area is approximated by that of a regularized crack surface density function, which depends on an auxiliary phase-field ($d \in [0, 1]$) variable and its gradient. One of the most important features of this regularization process is the parameter l_d which defines an internal length controlling the transition zone. As the internal length parameter l_d tending to 0, the phase-field should convergence to a sharp interface of true discontinuities. Additionally, the dependence of gradient-damage can result in the phase-field method providing a non-local approach to describe the continuous transition from diffuse damage (micro-cracks) to macro-cracks in the form of localized damage bands. In other words, it dose not require any prescription about the shape geometry and allow crack nucleation and branching automatically.

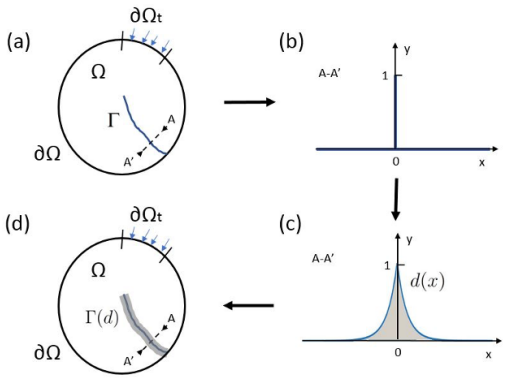

Figure 1.6: Schematic presentation of regularized crack topology

Various phase field models chose the regularized crack surface density function differently. Without loss of generality, a generic form for the crack surface density function has been proposed (Wu, 2017):

$$\Gamma_d(d, \nabla d) = \frac{1}{c_0}\left[\frac{1}{l_d}\alpha(d) + l_d|\nabla d|^2\right] \tag{1.7}$$

where $\alpha(d)$ describes the distribution of the smeared cracks, and $\alpha(d) \in [0, 1]$ for $\forall d \in [0, 1]$. While the scaling parameter $c_0 = 4\int_0^1 [\alpha(d)]^{\frac{1}{2}}\mathrm{d}d$ is introduced such that the sharp crack surface is recovered for a fully softened crack. For better understanding the phase-field regularization of the sharp crack topology, the profile of the diffused damaged normal to the crack in 1D is usually defined by (Hun, 2020):

$$d(x) = \text{Argmin}\left(\int_\Omega \Gamma_d(d, \nabla d)\mathrm{d}\Omega\right) \tag{1.8}$$

In Table 1.1, three commonly mathematical forms of geometric crack functions $\alpha(d)$ and the corresponding crack profile $d(x)$ are available. And these regularization cracks are illustrated in Figure 1.7.

As Figure 1.7(a) shows, the quadratic geometric crack function $\alpha(d) = d^2$ (Bourdin et al., 2000) and its linear counterpart $\alpha(d) = d$ (Pham et al., 2011) result in a localization bandwidth of an infinite support and of a finite one $4l_0$, respectively. While the geometric crack function $\alpha(d) = 2d - d^2$ used for PF-CZM (Wu, 2017) describes a sinusoidal distribution of the crack profile with a finite bandwidth πl_0. As a consequent, it is essential to choose an appropriate parameter l_d for a correct simulation of phase-field (Nguyen et al., 2016).

From a numerical point of view, the case of $\alpha(d) = d^2$ renders the phase-field problem satisfying the admissible range $0 \leq d \leq 1$ intrinsically. In addition, only the case of $\alpha(d) = d^2$ in Figure 1.7(b) ensure a local minimum at $d = 0$ which means that the unbroken state of the materials without mechanical strains is a minimizer of the total energy.

Table 1.1
Three commonly used geometric crack functions

$\alpha(d)$	c_0	$d(x)$	Authors
d	$8/3$	$\left(1-\frac{\lvert x\rvert}{2l_d}\right)^2$	Pham et al. (2011)
d^2	2.0	$\exp\left(-\frac{\lvert x\rvert}{l_d}\right)$	Bourdin et al. (2000)
$2d-d^2$	π	$1-\sin\left(\frac{\lvert x\rvert}{l_d}\right)$	Wu (2017)

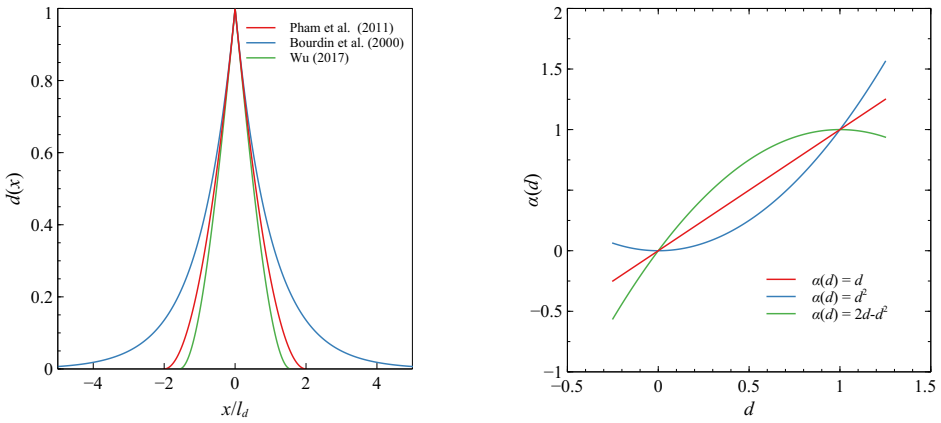

(a) 1D crack profile **(b)** crack geometric functions

Figure 1.7: Plots of different geometric functions and corresponding crack profile in 1D

3.2 Energy decomposition with unilateral effect

In standard phase-field method (Bourdin et al., 2000), the total undamaged free energy density function ψ_0 has been degraded by a degradation functional $g(d)$ which will be discussed in Section 3.3. However, this method can not distinguish the asymmetric tensile and compression behavior, which is not realistic for brittle and quasi-brittle fracture (Wu et al., 2020b). In addition, it can not account for the unilateral effect induced by microcracks opening-closure (Zhu et al., 2011; Zafati and Richard, 2019) during the cycle loading. In view of these problems, several methods for special decomposition of the bulk energy density have been proposed over last years.

3.2.1 Model of Lancioni and Royer-Carfagni (2009)

Only the "deviatoric-type fracture" is taken into account in model of Lancioni and Royer-Carfagni (2009). In view of this, the total undamaged free energy density has been split into a deviatoric part and a volumetric part:

$$\begin{cases} \psi_0(\boldsymbol{\varepsilon}, d) = g(d)w_+(\boldsymbol{\varepsilon}) + w_-(\boldsymbol{\varepsilon}) \\ w_-(\boldsymbol{\varepsilon}) = \dfrac{1}{2}\kappa_0[\mathrm{tr}(\boldsymbol{\varepsilon})]^2 \\ w_+(\boldsymbol{\varepsilon}) = \mu_0\boldsymbol{\varepsilon}_{dev} : \boldsymbol{\varepsilon}_{dev} \end{cases} \tag{1.9}$$

in which κ_0 and μ_0 represent the bulk and shear moduli of undamaged materials. Moreover, the elastic strain tensor is decomposed into a spherical part and a deviatoric part:

$$\begin{cases} \boldsymbol{\varepsilon}_{sph} = \dfrac{1}{3}\mathrm{tr}(\boldsymbol{\varepsilon})\mathbf{I} \\ \boldsymbol{\varepsilon}_{dev} = \boldsymbol{\varepsilon} - \boldsymbol{\varepsilon}_{sph} \end{cases} \tag{1.10}$$

Then, this model introduces damage for the positive part of energy density (the deviatoric part) only, while the spherical one does not induce damage.

This model has been used to reproduce fracture paths similar to that observed *in situ* of the French Panthéon (Lancioni and Royer-Carfagni, 2009), one of the most famous historical monuments in Paris. However, this model prevent the onset and propagation of tensile cracks completely, which is not realistic for rock-like materials under complex loading conditions.

3.2.2 Model of Amor et al. (2009)

In order to overcome the disadvantage of model proposed by Lancioni and Royer-Carfagni (2009), Amor et al. (2009) introduced a new decomposition based on the volumetric-deviatoric split of the strain tensor. In this model, not only the deviatoric can induce the initiate and propagation of cracks, but also the expansion part of the volumetric part. To be specifically:

$$\begin{cases} \psi(\boldsymbol{\varepsilon}, d) = w_-(\boldsymbol{\varepsilon}) + g(d) w_+(\boldsymbol{\varepsilon}) \\ w_-(\boldsymbol{\varepsilon}) = \kappa_0 \dfrac{[\langle \mathrm{tr}(\boldsymbol{\varepsilon}) \rangle_-]^2}{2} \\ w_+(\boldsymbol{\varepsilon}) = \kappa_0 \dfrac{[\langle \mathrm{tr}(\boldsymbol{\varepsilon}) \rangle_+]^2}{2} + \mu_0 \boldsymbol{\varepsilon}_{dev} : \boldsymbol{\varepsilon}_{dev} \end{cases} \tag{1.11}$$

where the bracket $\langle x \rangle_\pm$ denote $\langle x \rangle_+ = (x + |x|)/2$ and $\langle x \rangle_- = (x - |x|)/2$.

It could be noticed that this model introduces damage for the hydrostatic expansion (the positive volume strain) and the deviatoric strain, while the hydrostatic compression does not induce damage. Although it could distinguish the tensile cracks and compressive shear cracks. It could not describe the dissymmetry in mechanical behavior between tension and compression. More details about this model can be found in Chapter 2.

3.2.3 Model of Miehe et al. (2010a)

On the other hand, Miehe et al. (2010a) introduced another spectral decomposition of the strain tensor in view of the problem for the unilateral constraint in material degradation. In this model, the strain tensor has been split into positive part and negative part as following:

$$\begin{cases} \boldsymbol{\varepsilon} = \boldsymbol{\varepsilon}_+ + \boldsymbol{\varepsilon}_- \\ \boldsymbol{\varepsilon}_+ = \displaystyle\sum_{i=1}^{D} \langle \varepsilon^i \rangle_+ \boldsymbol{n}^i \otimes \boldsymbol{n}^i \\ \boldsymbol{\varepsilon}_- = \displaystyle\sum_{i=1}^{D} \langle \varepsilon^i \rangle_- \boldsymbol{n}^i \otimes \boldsymbol{n}^i \end{cases} \tag{1.12}$$

in which $D = 2$ or 3 is the dimension of the considering problem. ε^i and $\boldsymbol{n}^i$ represent the eigenvalues and the corresponding eigenvectors of the strain tensor $\boldsymbol{\varepsilon}$, respectively. Note that the positive and negative strain tensors are orthogonal in the Frobenius norm (Wu and Cervera, 2018). To be specifically, it means $\boldsymbol{\varepsilon}_+ : \boldsymbol{\varepsilon}_- = 0$.

Accordingly, the energy decomposition can be expressed as follow:

$$\begin{cases} \psi(\boldsymbol{\varepsilon}, d) = w_-(\boldsymbol{\varepsilon}) + g(d) w_+(\boldsymbol{\varepsilon}) \\ w_-(\boldsymbol{\varepsilon}) = \dfrac{1}{2}\lambda_0 [\mathrm{tr}(\boldsymbol{\varepsilon}_-)]^2 + \mu_0 \boldsymbol{\varepsilon}_- : \boldsymbol{\varepsilon}_- \\ w_+(\boldsymbol{\varepsilon}) = \dfrac{1}{2}\lambda_0 [\mathrm{tr}(\boldsymbol{\varepsilon}_+)]^2 + \mu_0 \boldsymbol{\varepsilon}_+ : \boldsymbol{\varepsilon}_+ \end{cases} \tag{1.13}$$

As a result, this model prevent the compression cracks completely.

3.2.4 Model of Zhang et al. (2020)

Similar with the model proposed by Miehe et al. (2010a) where the positive/negative projection (PNP) was employed on strain tensor, a new decomposition of strain energy based on the PNP of stress tensor was introduced by Zhang et al. (2020). In this method, the stress tensor of unbroken material is split into the positive (tensile) part and the negative (compression) part using its eigenvalues σ^i and the corresponding eigenvectors $\boldsymbol{n}^i$:

$$\begin{cases} \boldsymbol{\sigma} = \boldsymbol{\sigma}_+ + \boldsymbol{\sigma}_- \\ \boldsymbol{\sigma}_+ = \sum_{i=1}^{D} \langle \sigma^i \rangle_+ \boldsymbol{n}^i \otimes \boldsymbol{n}^i \\ \boldsymbol{\sigma}_- = \sum_{i=1}^{D} \langle \sigma^i \rangle_- \boldsymbol{n}^i \otimes \boldsymbol{n}^i \end{cases} \tag{1.14}$$

Again, the decomposition of stress tensor can meet the orthogonal condition $\boldsymbol{\sigma}_+ : \boldsymbol{\sigma}_- = 0$.

Then, the decomposition of energy ensures that only tensile stress induces the damage rather than the compression stress:

$$\begin{cases} \psi(\boldsymbol{\varepsilon}, d) = g(d) w_+(\boldsymbol{\varepsilon}) + w_-(\boldsymbol{\varepsilon}) \\ w_+(\boldsymbol{\varepsilon}) = \dfrac{1}{2} \boldsymbol{\sigma}_+ : \boldsymbol{\varepsilon} \\ w_-(\boldsymbol{\varepsilon}) = \dfrac{1}{2} \boldsymbol{\sigma}_- : \boldsymbol{\varepsilon} \end{cases} \tag{1.15}$$

Compared with the strain tensor decomposition as that used in Miehe et al. (2010a), the stress decomposition avoids the implication of elastic parameters. Thus, one of the advantages is that the stress decomposition is suitable to incorporate fluid pressure effect on crack propagation in porous media. The details of this decomposition will be presented in Chapter 5.

3.3 Degradation functionals

The energy degradation functionals in phase-field method describe the smooth transition of materials from intact state to totally broken one. For this reason, it plays an important role in governing the non-linear behavior in the post-peak stage. Therefore, the degradation function used in phase-field method should not violate the following conditions:

- $g(0) = 1$ to ensure the initial intact state of materials;
- $g(1) = 0$ to guarantee the totally damaged state of materials;
- $g'(1) = 0$ to prevent the infinite value of stress when completely broken occurs;
- $g'(d) \leq 0$ ($d \in [0, 1]$) to promise the monotonous decrease from the intact state to cracking one.

During the past decades, various energy degradation functions satisfying these conditions have been introduced in literature (Bourdin et al., 2000; Pham et al., 2011; Kuhn et al., 2015). By replacing an exhaustive list of available degradation functions, several commonly used ones are presented in Table 1.2, and the corresponding curves are presented in Figure 1.8. The effects of different choice of these degradation functions have been studied in Kuhn et al. (2015). It is found that they mainly control the localization macroscopic cracks in the material response before the onset for a phase-field model.

Table 1.2
Commonly used energy degradation functions

$g(d)$	Order	Authors
$(1-d)^2$	Quadratic	Bourdin et al. (2000)
$3(1-d)^2 - 2(1-d)^3$	Cubic	Kuhn et al. (2015)
$4(1-d)^3 - 3(1-d)^4$	Quartic	Karma et al. (2001)

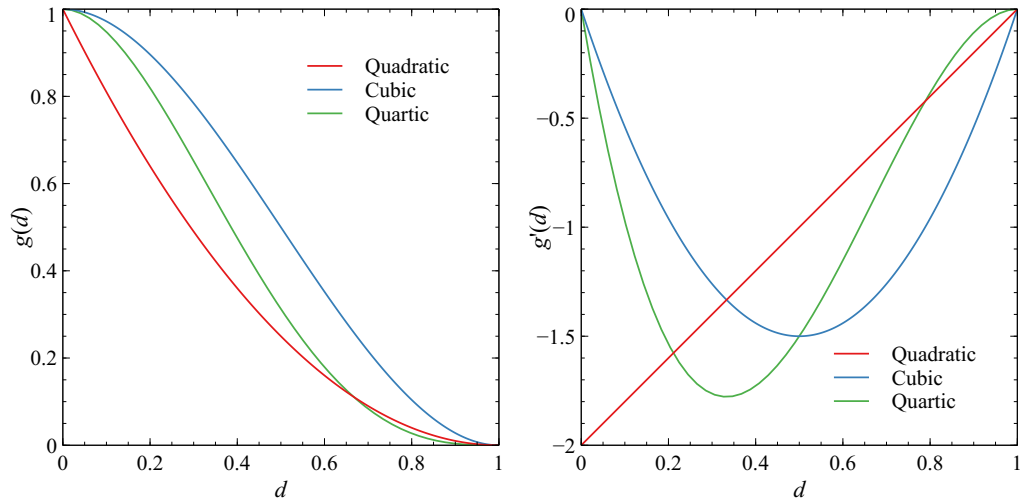

Figure 1.8: Plots of different energy degradation functions

It should be noticed that the degradation functions above usually induce the ill-posed boundary values problems in the post-localization regime during the numerical modeling. Thus, it usually introduces a small positive parameter in the degradation function. For example in Amor et al. (2009), a so-called residual stiffness $k_l \sim 10^{-4}$ has been used $g(d) = (1-d)^2 + k_l$. The similar solution can be found in many other literature (Borden et al., 2016; Lorentz, 2017; Yu et al., 2021a) for this purpose.

3.4 Advantages of phase-field method

Comparing with some other numerical methods, the phase-field method as an innovation technique to model transition of diffuse damage to localization cracks has several crucial advantages as illustrated in following. These features are also the reason why we choose the phase-field method in this thesis.

- The derivation of governing equations for phase-field method is only based on energy minimization. Therefore, the it serves as a non-local approach to model the cracks nucleation, growth and coalescence automatically without any predefined crack path;

- Due to its variational structure, the phase-field can incorporate multi-field physics problems naturally, for example, coupling with hydro-mechanics;

- The phase-field problem defined with the first-order damage gradient can be solved with classical finite elements, without modifying existing codes;
- It also has been proved that the phase-field can deal with arbitrary geometrical configurations of crack networks both in 2D (Nguyen et al., 2016) and 3D (Wu et al., 2021).

CHAPTER 2

Modeling of damage and cracking in heterogeneous rock-like materials by phase-field method

1 Introduction

In this chapter, the phase-field model based on the volumetric-deviatoric split of strain tensor (Amor et al., 2009), which could distinguish the tensile cracks and compressive shear cracks in rock-like materials very well, is first summarized. The implementation of this elastic-brittle phase-field model in finite element method framework is also presented.

Then, in order to take into account of the material heterogeneity, the effective elastic properties of the rock are first determined as functions of its mineral compositions by using a linear homogenization method. In the recent work (Hun et al., 2019), a stochastic multi-scale modeling has been proposed for crack propagation in random heterogeneous media. Inspired by that approach, the inclusion phase is assumed to be randomly distributed in the matrix phase. The onset and propagation of localized cracks are described by using the phase-field method for elastic materials. Five different types of random distributions of inclusions are considered, and their effects on localized cracking patterns are investigated and discussed.

2 Summary of the phase field method

2.1 Regularized crack surface density function

We consider a solid material occupying the volumetric domain $\Omega \subset \mathbb{R}$, containing a number of cracks. Instead of tracing those individual cracks, which is a difficult task, a density function is introduced to represent the area of crack surfaces per unit volume (Miehe et al., 2010a). For this purpose, an auxiliary variable, $d(\mathbf{x}) \in [0, 1]$, is used to define the material state, such as $d = 0$ for the sound state and $d = 1$ for the fully cracked state. The physical meaning of d is equivalent to that of the scalar damage variable of the classical continuum damage mechanics. With this approach, discontinuous cracks are approximated by highly concentrated damage zones where d is close to 1. The damage localization leads to the ill-poseness of evolution problems and induces the suspicious mesh dependency. In order to regularized the damage localization problem, a non local formulation is adopted. The cracks surface density function is expressed as a function of both the damage variable d and its gradient ∇d. Therefore, the total area of regularized cracks in Ω is given by :

$$A_{\Gamma_d} = \int_{\Omega} \Gamma_d(d, \nabla d) \mathrm{d}V \tag{2.1}$$

$\Gamma_d(d, \nabla d)$ denotes the crack surface density function. Different mathematical forms of $\Gamma_d(d, \nabla d)$ are available (Bourdin et al., 2000; Pham et al., 2011; Wu, 2017). The following widely used one in Bourdin et al. (2000) is adopted here:

$$\Gamma_d(d, \nabla d) = \frac{d^2}{2l_d} + \frac{l_d}{2}|\nabla d|^2 \tag{2.2}$$

The parameter $l_d > 0$ defines a length scale which controls the width of damage localization bands seen as regularized cracks. In addition, without incorporating reactive healing process, the damage is considered as a fully irreversible process such as $\dot{d} \geq 0$. Hence, the evolution rate of crack surface area is non-negative:

$$\dot{A}_{\Gamma_d} = \frac{\mathrm{d}}{\mathrm{d}t} \int_{\Omega} \Gamma_d(d, \nabla d) \mathrm{d}V = \int_{\Omega} \dot{\Gamma}_d \mathrm{d}V \geq 0 \tag{2.3}$$

with:

$$\dot{\Gamma}_d = (\frac{d}{l_d})\dot{d} + l_d \nabla d \cdot \nabla \dot{d} \geq 0 \tag{2.4}$$

2.2 Total energy functional

The emphasis of this chapter is put on elastic solid materials exhibiting progressive cracking process. For this purpose, based on the variational principle for fracture mechanics (Francfort and Marigo, 1998), the total energy functional is composed of two parts, the stored (or locked) energy and that used for the propagation of cracks. Namely, the following general form is adopted (Amor et al., 2009; Nguyen et al., 2015):

$$E(\boldsymbol{u}, d) = \int_{\Omega} \psi(\boldsymbol{\varepsilon}(\boldsymbol{u}), d)\mathrm{d}\Omega + \int_{\Omega} g_c \Gamma_d(d, \nabla d)\mathrm{d}\Omega \tag{2.5}$$

$\psi(\boldsymbol{\varepsilon}(\boldsymbol{u}), d)$ defines the stored energy density which is a function of the displacement field $\boldsymbol{u}(\mathbf{x})$ and the damage field $d(\mathbf{x})$. $\boldsymbol{\varepsilon}(\boldsymbol{u})$ denotes the linear strain tensor given by $\boldsymbol{\varepsilon}(\boldsymbol{u}) = \frac{1}{2}[\nabla \boldsymbol{u} + \nabla^T \boldsymbol{u}]$ under the assumption of small strains. The parameter g_c is the critical energy rate and defines the quantity of energy used for the creation of unit crack surface.

The mechanical properties of materials are generally affected by the induced cracks. We consider first the case of an elastic material containing open cracks or frictionless closed cracks in this chapter. Thus, the stored energy is fully represented by the elastic strain energy of cracked material. As the elastic stiffness can be progressively affected by the cracks, the elastic strain energy should also be a function of damage field. However, the deterioration of elastic stiffness depends on the opening state of cracks. Limiting our study to isotropic materials here, for open cracks, both the bulk and shear moduli are degraded by damage. For closed frictionless cracks, only the shear modulus is deteriorated by damage while the bulk modulus remains intact. This unilateral contact condition is taken into account in our phase field model. For this purpose, a simple crack closure criterion is introduced and it is easy for numerical implementation. We assume that cracks are open if the accumulated volumetric strain is positive (tensile); else cracks are seen as closed. Based on these conditions and assumptions, the elastic strain energy density is defined as follows:

$$\begin{cases} \psi(\boldsymbol{\varepsilon}, d) = g(d) w_+(\boldsymbol{\varepsilon}) + w_-(\boldsymbol{\varepsilon}) \\ w_-(\boldsymbol{\varepsilon}) = \kappa_0 \dfrac{[\langle \mathrm{tr}(\boldsymbol{\varepsilon}) \rangle_-]^2}{2} \\ w_+(\boldsymbol{\varepsilon}) = \kappa_0 \dfrac{[\langle \mathrm{tr}(\boldsymbol{\varepsilon}) \rangle_+]^2}{2} + \mu_0 \boldsymbol{\varepsilon}_{dev} : \boldsymbol{\varepsilon}_{dev} \end{cases} \tag{2.6}$$

where κ_0 is the bulk modulus and μ_0 the shear modulus of undamaged materials. The bracket $\langle x\rangle_{\pm}$ denote $\langle x\rangle_+ = (x+|x|)/2$ and $\langle x\rangle_- = (x-|x|)/2$. $\boldsymbol{\varepsilon}_{dev} = \boldsymbol{\varepsilon} - \frac{1}{3}\text{tr}(\boldsymbol{\varepsilon})\mathbf{I}$ is the deviatoric strain tensor, with $\mathbf{I}$ being the second rank unit tensor. The function $g(d)$ defines the degradation of elastic moduli by damage. Among different available expressions, a widely used expression is here adopted such as $g(d) = (1-k_l)(1-d)^2 + k_l$ (Amor et al., 2009; Yu et al., 2021a). The small positive value $0 < k_l \ll 1$ is added to avoid the full vanishing of elastic moduli when d tends to 1. This may cause some numerical singularity. The advantage of this expression is to keep $g'(d) = 2(1-k_l)(1-d) = 0$ for $d = 1$ and $g(d) = 1$ for $d = 0$.

The stress-strain relations of cracked material can be easily obtained by the standard differentiation of the stored energy. One gets:

$$\boldsymbol{\sigma} = \frac{\partial\psi(\boldsymbol{\varepsilon}, d)}{\partial\boldsymbol{\varepsilon}} = \kappa_0\big[\langle\text{tr}(\boldsymbol{\varepsilon})\rangle_-\big]\mathbf{I} + g(d)\Big[\kappa_0\big[\langle\text{tr}(\boldsymbol{\varepsilon})\rangle_+\big]\mathbf{I} + 2\mu_0\boldsymbol{\varepsilon}_{dev}\Big] \tag{2.7}$$

$\boldsymbol{\sigma}$ denotes the Cauchy stress tensor.

2.3 Governing equations and evolution of damage field

We consider that the solid body Ω is subjected to the body force $\boldsymbol{b}(\boldsymbol{x})$ and to the traction vector $\boldsymbol{t}(\boldsymbol{x})$ on its boundary $\partial\Omega_t$. The governing equations of the displacement (strain) and damage evolution problems can be established by the following minimization of the potential function (Francfort and Marigo, 1998; Alessi et al., 2015; Li et al., 2020b):

$$\dot{\Pi}(\dot{\boldsymbol{u}}, \dot{d}) = \dot{E}(\dot{\boldsymbol{u}}, \dot{d}) - \int_\Omega \boldsymbol{b}\cdot\dot{\boldsymbol{u}}\text{d}\Omega - \int_{\partial\Omega_t} \boldsymbol{t}\cdot\dot{\boldsymbol{u}}\text{d}A = 0 \tag{2.8}$$

By taking into account the expression of $E(\boldsymbol{u}, d)$ in Equations (2.5) and (2.6), the cracks density function in Equation (2.4), the constitutive relations $\boldsymbol{\sigma} = \frac{\partial\psi}{\partial\boldsymbol{\varepsilon}}$, and the kinematic relations $\boldsymbol{\varepsilon}(\boldsymbol{u}) = \frac{1}{2}[\nabla\boldsymbol{u} + \nabla^T\boldsymbol{u}]$, the minimization of the potential energy function can be

written the following general form respectively for frictionless cracks:

$$\begin{aligned}\dot{\Pi}(\dot{\boldsymbol{u}},\dot{d}) = &\int_{\Omega} -\big[\mathrm{div}(\boldsymbol{\sigma})+\boldsymbol{b}\big]\cdot\dot{\boldsymbol{u}}\mathrm{d}V + \int_{\partial\Omega}\big[\boldsymbol{\sigma}\cdot\boldsymbol{n}-\boldsymbol{t}\big]\cdot\dot{\boldsymbol{u}}\mathrm{d}A \\ &+\int_{\Omega}\big[-\frac{\partial\psi(\boldsymbol{\varepsilon},d)}{\partial d}+\frac{g_c}{l_d}d-g_c l_d\Delta d\big]\cdot\dot{d}\mathrm{d}V \\ &+\int_{\partial\Omega}\big[g_c l_d\nabla d\cdot\boldsymbol{n}\big]\cdot\dot{d}\mathrm{d}A = 0\,, \quad \forall\Omega\end{aligned} \tag{2.9}$$

The minimization condition should be verified for $\forall\dot{\boldsymbol{u}}$ and $\forall\dot{d}$, one gets the local balances equations of the stress tensor:

$$\begin{cases}\mathrm{div}(\boldsymbol{\sigma})+\boldsymbol{b}=0 & \text{in } \Omega \\ \boldsymbol{\sigma}\cdot\boldsymbol{n}=\boldsymbol{t} & \text{on } \partial\Omega\end{cases} \tag{2.10}$$

Similarly, the local governing equations of damage evolution are given by:

$$\begin{cases}\dfrac{\partial\psi(\boldsymbol{\varepsilon},d)}{\partial d}-\dfrac{g_c}{l_d}d+g_c l_d\mathrm{div}(\nabla d)=0 & \text{in } \Omega \\ \nabla d\cdot\boldsymbol{n}=0 & \text{on } \partial\Omega\end{cases} \tag{2.11}$$

In addition, the damage evolution is here considered as a fully irreversible process with $\dot{d}\geq 0$. In order to ensure this irreversibility condition, the concept of energy history function introduced in (Miehe et al., 2010a; Nguyen et al., 2015) is here adopted. Substituting the derivative of $\psi(\boldsymbol{\varepsilon},d)$ given in Equation (2.6) for Equation (2.10), the governing equation of d is modified to:

$$2(1-d)\mathcal{H}-g_c\big[\frac{d}{l_d}-l_d\mathrm{div}(\nabla d)\big]=0 \tag{2.12}$$

The energy function $\mathcal{H}$ satisfies the following Karush-Kuhn-Tucker conditions for a general loading path:

$$w_+-\mathcal{H}\leq 0,\quad \dot{\mathcal{H}}\geq 0,\quad \dot{\mathcal{H}}[w_+-\mathcal{H}]=0 \tag{2.13}$$

For the simplicity, the following form meet the above conditions is adopted:

$$\mathcal{H}(t)=\max_{\tau\in[0,t]}[w_+(\tau)] \tag{2.14}$$

3 Numerical implementation

The phase-field evolution is coupled with the displacement (stress) field solution. Both problems are here solved by using the classical finite element method. The main steps of numerical implementation are outlined in this section.

3.1 Weak form

By using the standard Galerkin procedure with the test functions $\delta \boldsymbol{u}$ for the displacement field and δd for the damage field, the local governing equations are transformed into the weak integral forms (Miehe et al., 2010b; Mandal et al., 2021):

$$\int_{\Omega} \boldsymbol{\sigma} : \nabla(\delta \boldsymbol{u}) \mathrm{d}\Omega = \int_{\Omega} \boldsymbol{b} \cdot \delta \boldsymbol{u} \mathrm{d}\Omega + \int_{\partial\Omega_t} \boldsymbol{t} \cdot \delta \boldsymbol{u} \mathrm{d}S \tag{2.15}$$

$$\int_{\Omega} \left[(g_c \, l_d + 2\mathcal{H}) \delta d \cdot d + g_c l_d \nabla(\delta d) : \nabla(d) \right] \mathrm{d}\Omega = \int_{\Omega} \delta d \cdot 2\mathcal{H} \mathrm{d}\Omega \tag{2.16}$$

3.2 Geometrical discretization

The computational structure domain Ω is divided into n_e elements which are defined by n_p nodes. The target here is to determine, at each loading step, the nodal values of displacement components denoted by the vector $\boldsymbol{U}$ and those of phase-field variable by $\boldsymbol{d}$. Classically, the displacement and damage fields are approximated in terms of their nodal values by using suitable shape functions. Their gradient functions are accordingly calculated:

$$\begin{aligned} \boldsymbol{u}(\boldsymbol{x}) &= \boldsymbol{N}_u(\boldsymbol{x}) \boldsymbol{U}^e & \qquad d(\boldsymbol{x}) &= \boldsymbol{N}_d(\boldsymbol{x}) \boldsymbol{d}^e \\ \boldsymbol{\varepsilon}(\boldsymbol{x}) &= \boldsymbol{B}_u(\boldsymbol{x}) \boldsymbol{U}^e & \qquad \nabla d(\boldsymbol{x}) &= \boldsymbol{B}_d(\boldsymbol{x}) \boldsymbol{d}^e \end{aligned} \tag{2.17}$$

where $\boldsymbol{N}_u(\boldsymbol{x})$, $\boldsymbol{B}_u(\boldsymbol{x})$ and $\boldsymbol{N}_d(\boldsymbol{x})$, $\boldsymbol{B}_d(\boldsymbol{x})$ are the matrices of shape functions and their derivatives for the displacement and damage fields, respectively. For the sake of simplicity, the same shape functions are usually used for both fields and their test ones. More details can be found in previous works (Miehe et al., 2010b; Nguyen et al., 2015; Mandal et al., 2021). With the geometrical discretization and elementary approximation presented above, the weak form integrals Equations (2.15) and (2.16) are transformed into two sys-

tems of discrete equations:

$$\begin{cases} \boldsymbol{K}_u \boldsymbol{U} = \boldsymbol{F}_u^{ext} \\ \boldsymbol{K}_d \boldsymbol{d} = \boldsymbol{F}_d \end{cases} \tag{2.18}$$

$\boldsymbol{K}_u$ and $\boldsymbol{K}_d$ are the global stiffness matrices, $\boldsymbol{F}_u^{ext}$, $\boldsymbol{F}_d$ the global nodal forces vectors, respectively for the displacement and damage fields:

$$\begin{cases} \boldsymbol{K}_u = \displaystyle\int_\Omega \Big[\boldsymbol{B}_u^T \mathbb{C}(d) \boldsymbol{B}_u \Big] \mathrm{d}\Omega \\ \boldsymbol{F}_u^{ext} = \displaystyle\int_\Omega \big[\boldsymbol{N}_u^T \cdot \boldsymbol{b} \big] \mathrm{d}\Omega + \int_{\partial\Omega} \big[\boldsymbol{N}_u^T \cdot \boldsymbol{t} \big] \mathrm{d}S \end{cases} \tag{2.19}$$

and

$$\begin{cases} \boldsymbol{K}_d = \displaystyle\int_\Omega \left[\left(\frac{g_c}{l_d} + 2\mathcal{H}_{n+1} \right) \boldsymbol{N}_d^T \boldsymbol{N}_d + g_c l_d \boldsymbol{B}_d^T \boldsymbol{B}_d \right] \mathrm{d}V \\ \boldsymbol{F}_d = \displaystyle\int_\Omega 2\mathcal{H}_{n+1} \boldsymbol{N}_d^T \mathrm{d}V \end{cases} \tag{2.20}$$

Here, $\mathbb{C}(d)$ denotes the elastic stiffness tensor of damaged material and it is given by:

$$\mathbb{C}(d) = r_e^- k_0 \mathbf{I} \otimes \mathbf{I} + g(d)[r_e^+ k_0 \mathbf{I} \otimes \mathbf{I} + 2\mu_0(\mathbb{I} - \frac{1}{3}\mathbf{I} \otimes \mathbf{I})] \tag{2.21}$$

$\mathbb{I}$ is the fourth-order symmetric identity tensor. The coefficients $r_e^\pm = \frac{1}{2}\{\mathrm{sign}[\pm \mathrm{tr}(\boldsymbol{\varepsilon}^e)]+1\}$ describe the fact that the bulk modulus k is affected by open cracks (r_e^+ = 1 and r_e^-=0) but not affected by closed shear cracks (r_e^+ = 0 and r_e^-=1).

3.3 Staged coupling algorithm

It is worth noticing that the displacement (and stress) and cracking evolution problems are strongly coupled. Indeed, the displacement (stress) evolution is affected by the damage process. For instance, the elastic stiffness tensor and viscoplastic threshold are functions of damage variable. Inversely, the damage evolution is driven by the mechanical field through the stored elastic and viscoplastic energy. Therefore, both problems should be solved in a coupled way. However, it is demonstrated that the energy history functional $\mathcal{H}(t)$ given in Equation (2.20) is non-convex with respect to the couple of unknowns ($\boldsymbol{u}$, d) (Bourdin et al., 2000, 2008). As a consequence, it is difficult to solve the systems of coupled equations Equation (2.18) by using the conventional Newton-Raphson procedure.

However, the functional $\mathcal{H}(t)$ is convex with respect to one of two unknowns ($\boldsymbol{u}$ or d), if the other one is fixed. In general, the so-called alternating minimization (AM) solver proposed in (Bourdin et al., 2000, 2008), which is the most robust solver among various phase-field solutions (Zhuang et al., 2022), is widely used and adopted here. In the AM solver, two solution steps are successively performed at the k^{th} iteration of a specific loading step $n+1$. This is summarized as shown in Algorithm 1. According to Ambati et al. (2015), a convergence tolerance is taken as $\epsilon = 1 \times 10^{-5}$.

Algorithm 1: An alternating minimization solution for coupled displacement damage problem

for *each successive loading step* $n+1$ **do**
  Initialzation: $\boldsymbol{u}_{n+1}^{(0)} = \boldsymbol{u}_n$, $\boldsymbol{d}_{n+1}^{(0)} = \boldsymbol{d}_n$, $iter = 0$, $err = 1$
  while $err > tol$ *and* $iter < max\_iter$ **do** // $tol = 1 \times 10^{-5}$
    $iter = iter + 1$ // iteration count

    Compute displacement field $\boldsymbol{u}_{n+1}^{(iter)}$ with fixed phase-field $\boldsymbol{d}_{n+1}^{(iter-1)}$:
    Set: $\boldsymbol{K}_u = \int_\Omega \left[\boldsymbol{B}_u^T \mathbb{C}(_{n+1}^{(iter-1)}) \boldsymbol{B}_u \right] \mathrm{d}\Omega$
    Solve: $\boldsymbol{K}_u \boldsymbol{u}_{n+1}^{(iter)} = \boldsymbol{F}_u^{ext}$

    Compute phase-field $\boldsymbol{d}_{n+1}^{(iter)}$ with fixed displacement field $\boldsymbol{u}_{n+1}^{(iter)}$:
    Set: $\mathcal{H}_{n+1} = \mathcal{H}_{n+1}(\boldsymbol{u}_{n+1}^{(iter)})$
    Solve: $\boldsymbol{K}_d \boldsymbol{d}_{n+1}^{(iter)} = \boldsymbol{F}_d$

    $err = \|\boldsymbol{d}_{n+1}^{(iter)} - \boldsymbol{d}_{n+1}^{(iter-1)}\|$
  end
  Update: $\boldsymbol{u}_{n+1} = \boldsymbol{u}_{n+1}^{(iter)}$, $\boldsymbol{d}_{n+1} = \boldsymbol{d}_{n+1}^{(iter)}$
end

4 Microstructure and properties of Beishan granite

Most rock-like materials contain different types of heterogeneities such as mineral grains and pores at different scales. The initiation and propagation of cracks in these

materials are inherently influenced by the presence of such heterogeneities. For instance, cracks may easily initiate at interfaces between mineral grains and matrix or around void surfaces. For this reason, the influence of spatial distribution of mineral grains and pores on mechanical properties of rock-like materials is considered.

4.1 Microstructure of Beishan granite

We consider here a typical brittle rock, the granite from Beishan area (Gansu Province, China) which is investigated in China as a potential host rock for geological disposal of radioactive waste. The mineralogical compositions and basic mechanical behavior of this rock have been reported in previous studies, for instance (Zhao et al., 2013, 2014; Chen et al., 2015; Zhou et al., 2019a). In particular, some quantitative mineralogical composition analyses have been conducted using the X-ray diffraction method. As an average estimation, the granite is mainly composed of 13.55 % alkali feldspar, 33.65% plagioclase, 31.10% quartz, 20.05% mica, and 1.65% clay minerals. At the microscopic level, the phases of alkali feldspar, plagioclase and mica constitute a cemented matrix phase. The quartz grains are scattered in that matrix. Therefore, as the first approximation, the representative volume element (RVE) of the granite is seen as a matrix-inclusion system. One denotes V, V_i and V_m respectively as the total volume of RVE, the volume of inclusions and that of matrix. Thus, the volume fraction of inclusions f is calculated by:

$$f = \frac{V_i}{V} = \frac{V_i}{V_i + V_m} \tag{2.22}$$

4.2 Effective elastic properties

The effective elastic properties of Beishan granite are determined by using a linear homogenization method. Due to the matrix-inclusion morphology adopted, it is convenient to apply the Mori-Tanaka scheme (Mori and Tanaka, 1973). With the assumption isotropic materials, the homogenized effective bulk and shear moduli, denoted as k^{hom} and μ^{hom}, are given by:

$$\kappa^{hom} = \frac{\sum_{r=0}^{1} f_r \frac{\kappa_r}{3\kappa_r+4\mu_0}}{\sum_{r=0}^{1} \frac{f_r}{3\kappa_r+4\mu_0}}, \quad \mu^{hom} = \frac{\sum_{r=0}^{1} f_r \frac{\mu_r}{\mu_0(9\kappa_0+8\mu_0)+6\mu_r(\kappa_0+2\mu_0)}}{\sum_{r=0}^{1} \frac{f_r}{\mu_0(9\kappa_0+8\mu_0)+6\mu_r(\kappa_0+2\mu_0)}} \tag{2.23}$$

where f_r is the volume fraction of the r^{th} phase, and k_r and μ_r being its bulk and shear moduli. k_0 and μ_0 are the bulk and shear moduli of the matrix phase. In practice, the elastic properties of different minerals involved in the granite can be found in the existing literature, see for instance (Rumble, 2017).

4.3 Description of heterogeneity of the materials

As given above, the macroscopic elastic properties of granite are explicitly expressed as functions of mineral compositions. As those mineral compositions may vary in space, the elastic properties of granite can also vary in space inside a tested sample and a structure. The spatial variability of elastic properties will affect the onset and propagation of localized cracks. In the recent work (Hun et al., 2019), random micro-structures were generated by Monte-Carlo realizations and the elastic properties fields at the mesoscopic scale were determined by using a moving-window homogenization method. A non-Gaussian distribution was proposed for the variability of elastic tensor. Inspired by that, in the present study, we assume also a random distribution of the volumetric fraction f of inclusions, for instance quartz grains, by using the standard Weibull distribution function (Tang et al., 2000):

$$\Phi(f) = \frac{m_i}{\bar{f}}\big(\frac{f}{\bar{f}}\big)^{m_i-1}\exp\big[-\big(\frac{f}{\bar{f}}\big)^{m_i}\big] \tag{2.24}$$

where f is the volume fraction of quartz grains; $\bar{f}$ is the scale parameter of the distribution which is usually estimated as the mean of the random variable; m_i is the homogeneity index of the material. According to the definition, a larger value of m_i implies a stronger material homogeneity with respect to the considered parameter, for instance the volume fraction of quartz grains. In Figure 2.1, some examples of probability density and cumulative probability for different values of m_i are illustrated. It is noticed that the critical fracture energy g_c should also depend on the randomness of micro-structural and exhibits a spatial variability. But at the stage of the present study, for the sake of simplicity, only the variability of elastic properties is considered, and that of g_c will included in future studies.

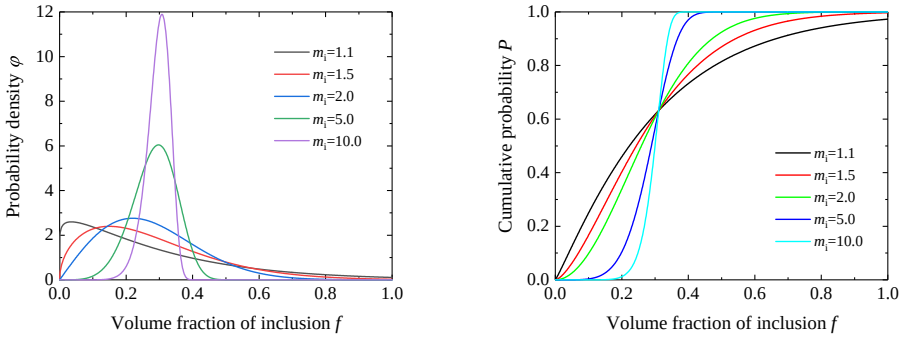

(a) Probability density **(b)** Cumulative probability

Figure 2.1: Probability density and cumulative probability for the distribution of volume fraction of quartz grains with different values of homogeneity index m_i

5 Numerical assessment

In this section, five numerical specimens with different spatial distributions of quartz grains volume fraction are considered, respectively obtained by using five values of heterogeneity indices (m_i =1.1, 1.5, 2, 5, 10). The specimen geometry is $50 \times 100mm$ and discretized into 100×200 (20 000) elements for numerical study of mechanical behavior. The input elastic parameters are as follows: Young's moduli of quartz grains and matrix $E_i = 101GPa$ and $E_m = 18.4GPa$ and Poisson's ratios $\nu_i = 0.06$ and $\nu_m = 0.122$. The average volume fraction of quartz inclusion is $\bar{f} = 31.1\%$. The length scale parameter of regularized cracks is taken as $l_d = 0.5mm$. The critical fracture energy g_c is a key parameter in the phase-field modeling. According to extensive experimental results (Evans et al., 1990; Wong and Baud, 2012), rock-like materials exhibit a transition from brittle to ductile failure with the increase of confining stress. On the other hand, by developing a micro-mechanical modeling of rocks with a homogenization technique (Hu et al., 2018; Zhao et al., 2018b), it was found that the brittle-ductile transition can be related to the increase of the local frictional coefficient of closed micro-crack surface with confining stress. Inspired by these previous studies, in this study, the brittle-ductile transition is indirectly taken into account by considering that the value of g_c increases with confining stress. However, it is not easy to determine the variation of g_c directly from experimental measurements. As an indirect method, the values of g_c are fitted from the peak differential stresses obtained in triaxial compression tests with the confining stress rang-

ing from 5 to 30 MPa. It is found that the following empirical relation can be identified: $g_c = g_{c0}e^{\varsigma(\sigma_c/\sigma_r)}$, with $g_{c0} = 2.6 \times 10^{-3}kN/mm$, $\varsigma = 0.0467$; σ_c denotes the confining stress while $\sigma_r = 1MPa$ is a fixed normalizing coefficient. To avoid the singularity of elastic stiffness tensor of damaged material when $d \to 1$, the stability parameter is taken as $k_l = 1 \times 10^{-5}$. In Figure 2.2, one shows the spatial distributions of the volume friction of quartz inclusions and the corresponding macroscopic Young's modulus obtained by using the homogenization method Equation (2.23).

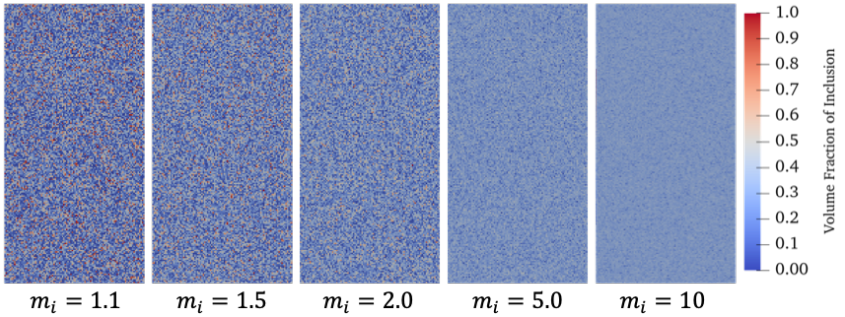

(a) distributions of the volume friction of quartz inclusions

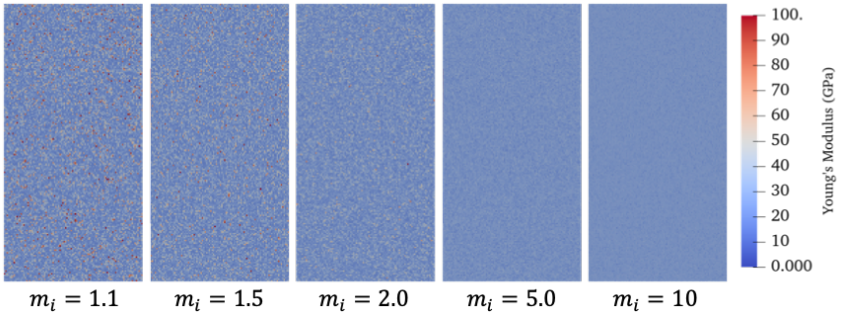

(b) corresponding macroscopic elastic modulus

Figure 2.2: Spatial distributions of quartz volume fraction obtained by five values of m_i and corresponding macroscopic elastic modulus, with an average volume fraction of quartz of $\beta = 31.1\%$

5.1 Global stress-strain curves

With the numerical specimens (or realizations of micro-structure) generated above, the mechanical behavior of Beishan granite is now investigated under conventional triaxial compression tests with different confining stresses. We shall first investigate the influence of confining stress. Therefore, we adopt a single realization of micro-structure with $m_i = 10$. This one represents a quite uniform distribution of quartz inclusions as shown on the

last column in Figure 2.2. Using this micro-structure, the global axial stress-strain curves obtained by phase-field simulations are presented in Figure 2.3 for five different tests, and compared with the experimental data reported in (Zhou et al., 2019a) (unfortunately, only axial strains are available). It seems that the elastic phase-field model well describes the basic mechanical response of granite in both the pre- and post-peak regimes. The effect of confining pressure on the peak strength is also well captured.

On the other hand, in order to evaluate the influence of micro-structure randomness on the global mechanical responses, numerical simulations are performed on five different realizations shown in Figure 2.2 for the test with a confining stress of 5MPa. The predicted axial stress-strain curves are given in Figure 2.3(b). It can be seen that the global stress-strain responses are influenced by the type of microstructure. In particular, the peak strength is lower when the material heterogeneity is stronger (low value of m_i). This seems logic because the material heterogeneity should enhance the initiation of micro-cracks.

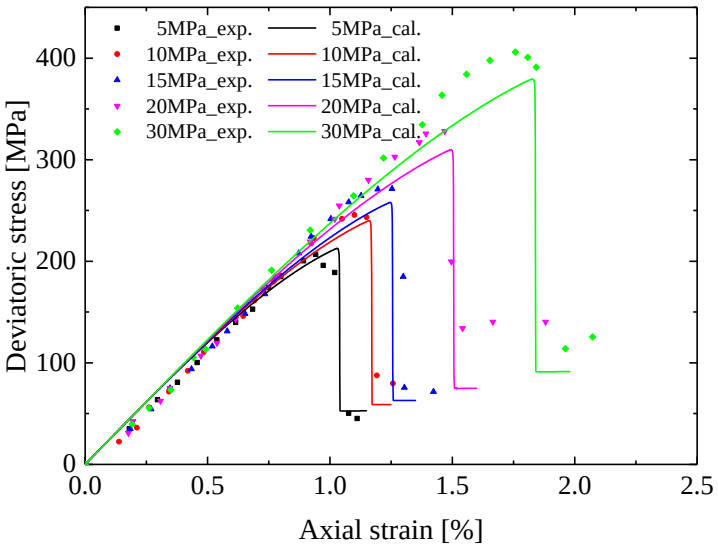

(a) Results for the specimen with $m_i = 10$

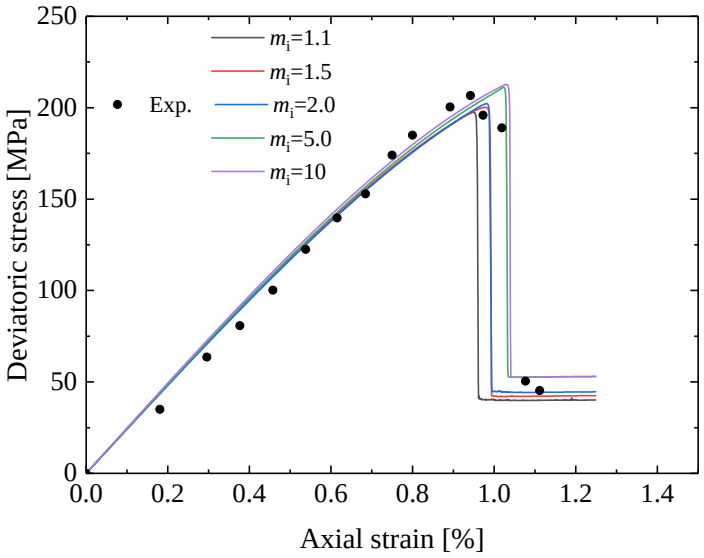

(b) Results for confining pressure of 5MPa

Figure 2.3: Axial stress-strain curves for different values of confining pressure and material heterogeneity index: comparisons between numerical results and experimental data

5.2 Effects of heterogeneity on failure pattern

In Figure 2.4, one shows the patterns of localized cracks obtained in five numerical samples with different distributions of quartz inclusions in triaxial compression test of 5MPa confining pressure. It is found that the cracking pattern is clearly influenced by the material heterogeneity. However, it is not easy to provide a clear quantitative correlation between the cracking pattern and material heterogeneity. According to the experimental study reported in (Zhou et al., 2019a), the main fracture in the tested samples was oriented at an angle of $80°$ with the horizontal axis. In the numerical results, the main crack in different samples is rather inclined with an angle of $45°$. This result seems to suggest that the failure of the numerical specimens is mainly caused by the shear strain energy as defined in Equation (2.6). The use of another form of stored energy involved in the evolution of phase-field variable should improve the orientation prediction of localized cracks. Furthermore, it is worth noticing that in most previous studies, a weak element was generally introduced in mesh in order to facilitate the onset of localized cracking. In the present study, the onset of crack localization is naturally driven by the material heterogeneity without needing to use any weak element.

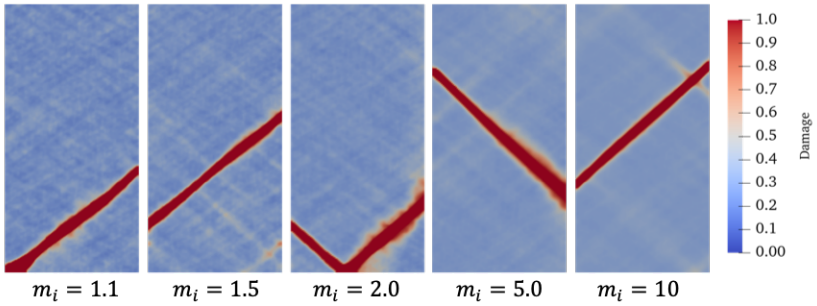

Figure 2.4: Cracking patterns obtained in five numerical specimens in triaxial compression test of 5MPa confining pressure

In order to investigate the progressive evolution of cracking process, the distributions of phase-field variable (or crack surface density) are presented in Figure 2.5 at five selected loading steps during a triaxial compression test with a confining pressure of 5MPa. When the differential stress reaches the peak value, the crack density remains relatively moderate and is clearly less than 1. The crack density increases and the cracking localization accelerates very rapidly in the post-peak regime. An inclined single localized crack is formed and crosses the whole sample in an orientation of $45°$.

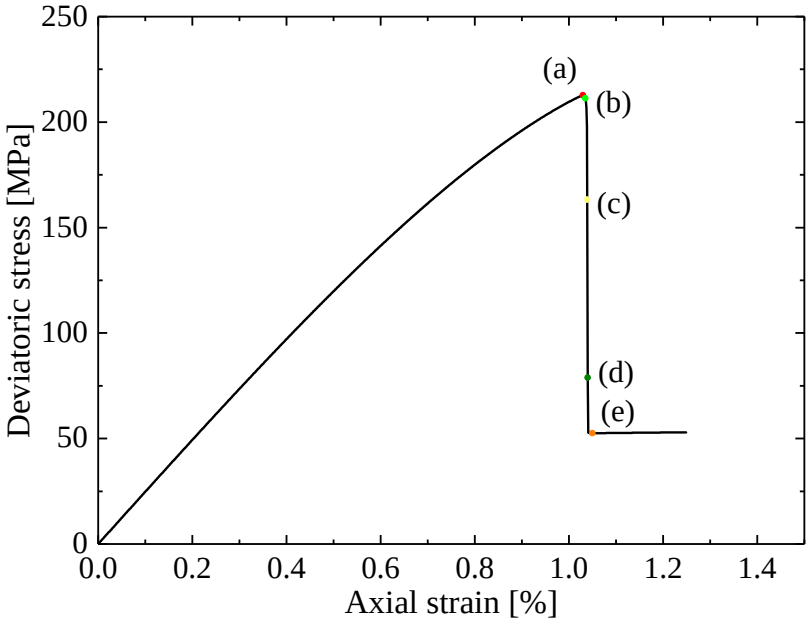

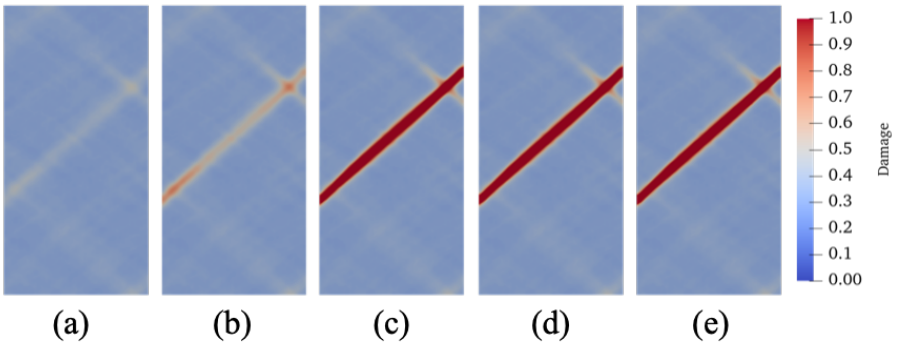

Figure 2.5: Crack density evolution and localized cracking pattern in the specimen with m_i =10 and in a triaxial compression test of 5MPa confining pressure

Furthermore, in order to better understand the energy origin of crack evolution, the respective contributions of the expansion part $\kappa_0 \frac{[\langle tr(\boldsymbol{\varepsilon})\rangle_+]^2}{2}$ and the shear part $\mu_0 \boldsymbol{\varepsilon}_{dev} : \boldsymbol{\varepsilon}_{dev}$ of the driving force given in Equation (2.6) are calculated at the loading steps (a) and (b) as indicated in Figure 2.5. Their distributions along the localized crack length are presented in Figure 2.6, together with the value of g_c. It is seen that the shear strain energy is the dominating part to drive the initiation and propagation of cracks. For instance, at the loading step (a) corresponding to the peak point, the maximum value of shear strain energy approaches to the critical fracture energy g_c while the expansion energy remains close to 0. Then at the loading (b), the shear strain energy along the whole localized crack exceeds the critical fracture energy, whereas the expansion energy does not evolve. Further, due to the material heterogeneity, the distribution of strain energy along the localized crack is not uniform. Therefore, the onset of localized cracking is a progressive process in the sample.

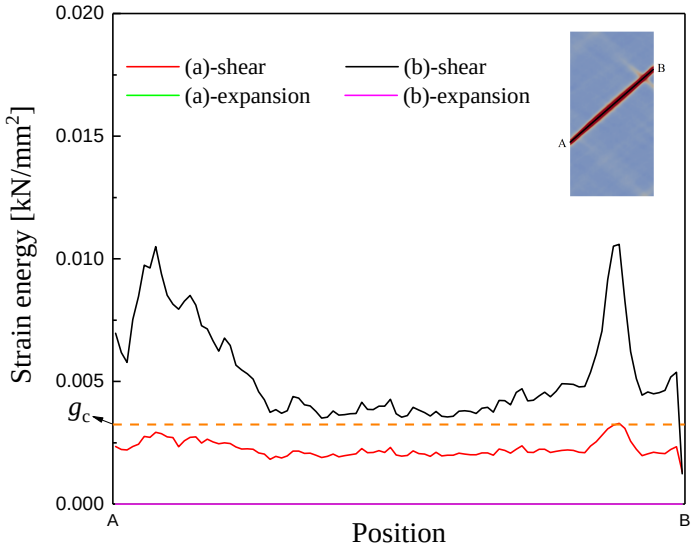

Figure 2.6: Distribution of expansion and shear strain energy parts along localized crack

6 Conclusion

In this chapter, a phase-field method considering the unilateral effect on elastic stiffness tensor at the smooth crack opening-closure transition has been summarized firstly. Next, the implementation of this phase-field model in finite element framework has been introduced. Then, it has been applied to modeling the transition from diffuse micro-cracks to localized macroscopic cracks by taking into account material heterogeneities. By using the standard Weibull distribution function, the spatial variation of mineral compositions in a typical brittle rock has been taken into account. With the help of linear homogenization method, the spatial variation of macroscopic elastic properties of the rock have been described as functions of mineral compositions. A series of triaxial compression tests have been investigated on heterogeneous numerical samples with different distributions of elastic properties. It is found that in the brittle rock studied, the localization of cracking starts around the peak strength state and accelerates in the post-peak regime. The pattern of localized cracks is directly influenced by the spatial heterogeneity of elastic properties of the rock. No artificial weak element is needed to capture the onset of crack localization. Under conventional triaxial compression tests, the shear strain energy is the dominating driving force of the evolution and propagation of cracks. The generation of a localized crack is a progressive process.

CHAPTER 3

A novel phase-field model for mixed cracks in elastic-plastic materials incorporating unilateral effect and friction sliding

1 Introduction

In this chapter, a novel phase field model is developed and it is devoted to a very wide range of cracks and loading paths. Three critical issues are consistently addressed, including smooth and rough cracks, the crack opening-closure unilateral effects, and the coupling between crack growth and frictional sliding. The new model is formulated in a rigorous thermodynamics framework and inspired by some micro-mechanical results on the frictional sliding mechanism (Peng and Johnson, 1972; Palmer et al., 1973; Gambarotta, 2004; Zhu et al., 2016). This chapter is organized as follows. The energy functionals for cracked materials are first formulated for both smooth and rough cracks under open and closed conditions. The related constitutive relations are also established. The evolutions laws of damage and frictional sliding are then deduced from the minimization of potential energy functions for the different crack situations. The proposed model is implemented in a standard finite element method framework by adopting an efficient alternating minimization algorithm. The performance of the novel model is assessed through different loading scenarios ranging from material point to structural scale.

2 Phase-field Formulation of frictional cracks with unilateral condition

2.1 Regularized crack surface description

Similar with Chapter 2, a solid material occupying the volumetric domain $\Omega \subset \mathbb{R}$, containing a number of cracks, has been considered in this chapter again. Therefore, the auxiliary variable, $d(\mathbf{x}) \in [0, 1]$, is used to regularize the damage localization problem and the estimation of total area of regularized cracks in Ω by Equation (2.1) is adopted here:

$$A_{\Gamma_d} = \int_{\Omega} \Gamma_d(d, \nabla d) \mathrm{d}V \tag{3.1}$$

2.2 Energy functionals

Geological materials are often subjected to compressive stress. Thus most cracks are closed. In addition, crack surfaces in such materials are not smooth but rough. Under compressive non-hydrostatic stresses, there is a frictional sliding along rough crack surfaces. Due to the local friction, the sliding is not elastic reversible and only activated when the applied shear stress reaches certain threshold. At the macroscopic scale, one obtains irreversible strains, conventionally called as plastic strains. Therefore, from this physical point of view, the frictional sliding along cracks is the microscopic mechanism of macroscopic plastic deformation in rock and concrete like materials. At the same time, when frictional cracks are closed, the elastic sliding is locked. As a consequence, the macroscopic elastic shear modulus is no more affected by damage.

Based on the previous analysis, the macroscopic strain tensor $\boldsymbol{\varepsilon}$ is conveniently decomposed into an elastic part $\boldsymbol{\varepsilon}^e$ and a plastic part $\boldsymbol{\varepsilon}^{pl}$. And the classical additive form is adopted, that is:

$$\boldsymbol{\varepsilon} = \boldsymbol{\varepsilon}^e + \boldsymbol{\varepsilon}^{pl} \tag{3.2}$$

Accordingly, the total stored energy ψ in Equation (2.5) should take the stored (or locked) energy due to the frictional sliding into consideration, besides of the elastic strain energy. Consequently, the following general form for the total energy functional E of

solid in Ω is adopted:

$$E(\boldsymbol{u}, d) = \int_{\Omega} \psi(\boldsymbol{\varepsilon}^e, \boldsymbol{\varepsilon}^{pl}, d)\mathrm{d}\Omega + \int_{\Omega} g_c \Gamma_d(d, \nabla d)\mathrm{d}\Omega \tag{3.3}$$

On the other hand, as the elastic moduli are not affected by damage for the closed frictional cracks, the elastic strain energy is independent of damage variable d. The stored energy is physically related to the plastic hardening process. For the sake of simplicity, we assume that the locked plastic energy is a quadratic function of deviatoric plastic strain only (Lanoye et al., 2013). Further, the kinetics of frictional sliding is coupled with the damage evolution. Thus, for closed rough cracks, the total stored energy can be written in the following form:

$$\begin{aligned} \psi(\boldsymbol{\varepsilon}^e, \boldsymbol{\varepsilon}^{pl}, d) &= \psi^e(\boldsymbol{\varepsilon}^e) + \psi^p(\boldsymbol{\varepsilon}^{pl}, d), \\ \psi^e(\boldsymbol{\varepsilon}^e) &= \frac{\kappa_0}{2}[\mathrm{tr}(\boldsymbol{\varepsilon}^e)]^2 + \mu_0 \boldsymbol{\varepsilon}^e_{dev} : \boldsymbol{\varepsilon}^e_{dev}, \\ \psi^p(\boldsymbol{\varepsilon}^{pl}, d) &= \beta(d)\mu_0 \boldsymbol{\varepsilon}^{pl}_{dev} : \boldsymbol{\varepsilon}^{pl}_{dev} \end{aligned} \tag{3.4}$$

$\boldsymbol{\varepsilon}^e_{dev}$ and $\boldsymbol{\varepsilon}^{pl}_{dev}$ are respectively the elastic and plastic deviatoric strain tensors. The scalar values function $\beta(d)$ is introduced to describe the coupling between damage evolution and frictional sliding, as suggested by micro-mechanical considerations (Gambarotta, 2004; Zhu et al., 2008).

Under general loading conditions, there is transition from open to closed cracks and inversely. It is needed to define a general expression of total stored energy function for both open and closed cracks. It is obviously that for open cracks, there is no frictional sliding induced plastic deformation. Only the elastic strain energy is stored. For closed frictional cracks, the stored energy is previously defined by the function Equation (3.4). Moreover, with the help of the pure deviatoric plastic deformation ($\mathrm{tr}(\boldsymbol{\varepsilon}^{pl}) = 0$), it is convenient to take the same opening-closure criterion as that for frictionless cracks, that is $\mathrm{tr}(\boldsymbol{\varepsilon}^{pl}) = 0$. Therefore, one obtains the following expression of total stored energy

density function for frictional rough cracks:

$$\psi(\boldsymbol{\varepsilon}^e, \boldsymbol{\varepsilon}^{pl}, d) = \begin{cases} g(d)\left[\kappa_0 \dfrac{[\mathrm{tr}(\boldsymbol{\varepsilon})]^2}{2} + \mu_0 \boldsymbol{\varepsilon}_{dev} : \boldsymbol{\varepsilon}_{dev}\right], & \text{if } \mathrm{tr}(\boldsymbol{\varepsilon}) > 0 \\ \dfrac{\kappa_0}{2}\left[\mathrm{tr}(\boldsymbol{\varepsilon}) - \mathrm{tr}(\boldsymbol{\varepsilon}^{pl})\right]^2 + \mu_0(\boldsymbol{\varepsilon}_{dev} - \boldsymbol{\varepsilon}^{pl}_{dev}) : (\boldsymbol{\varepsilon}_{dev} - \boldsymbol{\varepsilon}^{pl}_{dev}) \\ + \beta(d)\mu_0 \boldsymbol{\varepsilon}^{pl}_{dev} : \boldsymbol{\varepsilon}^{pl}_{dev}, & \text{if } \mathrm{tr}(\boldsymbol{\varepsilon}) \leq 0 \end{cases} \tag{3.5}$$

Here, the degradation function $g(d) = (1 - k_l)(1 - d)^2 + k_l$ used in Chapter 2 is adopted.

The stress-strain relations of cracked material derived from the stored energy function as follows:

$$\begin{aligned} \boldsymbol{\sigma} &= \frac{\partial \psi(\boldsymbol{\varepsilon}^e, \boldsymbol{\varepsilon}^{pl}, d)}{\partial \boldsymbol{\varepsilon}} \\ &= \begin{cases} g(d)\left[\kappa_0 \mathrm{tr}(\boldsymbol{\varepsilon})\mathbf{I} + 2\mu_0 \boldsymbol{\varepsilon}_{dev}\right] & \text{if } \mathrm{tr}(\boldsymbol{\varepsilon}) > 0 \\ \kappa_0\left[\mathrm{tr}(\boldsymbol{\varepsilon}) - \mathrm{tr}(\boldsymbol{\varepsilon}^{pl})\right]\mathbf{I} + 2\mu_0\left(\boldsymbol{\varepsilon}_{dev} - \boldsymbol{\varepsilon}^{pl}_{dev}\right) & \text{if } \mathrm{tr}(\boldsymbol{\varepsilon}) \leq 0 \end{cases} \end{aligned} \tag{3.6}$$

As for the frictionless cracks, the crucial issue here is to insure the full continuity of energy, stresses and strains at the crack opening-closure transition point. It is obviously the stress in Equation (3.6) is continuous for all set $(\boldsymbol{\varepsilon}, \boldsymbol{\varepsilon}^{pl}, d)$ with $\mathrm{tr}(\boldsymbol{\varepsilon}) \neq 0$. It is then needed to ensure the continuity of stress in Equation (3.6) for those set $(\boldsymbol{\varepsilon}, \boldsymbol{\varepsilon}^{pl}, d)$ at the crack opening-closure transition point with $\mathrm{tr}(\boldsymbol{\varepsilon}) = 0$. For this purpose, the following condition has to be met:

$$\begin{cases} \mathrm{tr}(\boldsymbol{\varepsilon}^{pl}) = 0 \\ \boldsymbol{\varepsilon}^{pl}_{dev} = \left[1 - g(d)\right]\boldsymbol{\varepsilon}_{dev} \end{cases} \tag{3.7}$$

Likewise, the continuity of the total stored energy function in Equation (3.5) has also to be verified for all cases with $d \neq 0$. This requires the following special form of the coupled coefficient $\beta(d)$:

$$\beta(d) = \frac{g(d)}{1 - g(d)} \tag{3.8}$$

It is interesting to notice that with the degradation function adopted $g(d) = (1 - k_l)(1 - d)^2 + k_l$, the coupling coefficient $\beta(d)$ is a decreasing function of the damage variable d. This means that the coupling between damage evolution and frictional sliding is very strongly at the earlier stage of damage. But closing to fully cracked state, the coupling

effect progressively vanishes. It is worth noticing that as $g(d=0)=1$, the value of $\beta(d)$ is infinite if $d=0$. This causes a numerical singularity. In general, this is avoided if the damage process is activated before the frictional sliding. If this is not the case, a small initial value of damage can be assigned.

2.3 Governing equations and evolution laws

By taking in account the body force $\boldsymbol{b}(\boldsymbol{x})$ and the traction vector $\boldsymbol{t}(\boldsymbol{x})$ on the boundary $\partial\Omega_t$ of the solid body Ω, the problems can be solved (Francfort and Marigo, 1998; Alessi et al., 2015; Li et al., 2020b) by minimizing the following potential function:

$$\dot{\Pi}(\dot{\boldsymbol{u}},\dot{d}) = \dot{E}(\dot{\boldsymbol{u}},\dot{d}) - \int_{\Omega} \boldsymbol{b}\cdot\dot{\boldsymbol{u}}\mathrm{d}\Omega - \int_{\partial\Omega_t} \boldsymbol{t}\cdot\dot{\boldsymbol{u}}\mathrm{d}A = 0 \tag{3.9}$$

By taking into account the expression of $E(\boldsymbol{u},d)$ in Equations (3.3) and (3.5), the cracks density function in Equation (2.4), the constitutive relations $\boldsymbol{\sigma} = \frac{\partial\psi}{\partial\boldsymbol{\varepsilon}}$, and the kinematic relations $\boldsymbol{\varepsilon}(\boldsymbol{u}) = \frac{1}{2}[\nabla\boldsymbol{u} + \nabla^T\boldsymbol{u}]$, the minimization of the potential energy function can be written the following general form for frictional rough cracks:

$$\begin{aligned}\dot{\Pi}(\dot{\boldsymbol{u}},\dot{d}) = &\int_{\Omega} -\big[\mathrm{div}(\boldsymbol{\sigma}) + \boldsymbol{b}\big]\cdot\dot{\boldsymbol{u}}\mathrm{d}V + \int_{\partial\Omega}\big[\boldsymbol{\sigma}\cdot\boldsymbol{n} - \boldsymbol{t}\big]\cdot\dot{\boldsymbol{u}}\mathrm{d}A + \int_{\Omega} -\mathcal{F}^{pl}\cdot\dot{\boldsymbol{\varepsilon}}^{pl}\mathrm{d}V \\ &+ \int_{\Omega}\big[-\mathcal{F}^{d} + \frac{g_c}{l_d}d - g_c l_d\Delta d\big]\cdot\dot{d}\mathrm{d}V + \int_{\partial\Omega}\big[g_c l_d\nabla d\cdot\boldsymbol{n}\big]\cdot\dot{d}\mathrm{d}A\ ,\quad\forall\Omega\end{aligned} \tag{3.10}$$

$\mathcal{F}^d$ is the thermodynamic force conjugated with the damage variable d and defined as $\mathcal{F}^d := -\frac{\partial\psi}{\partial d}$. And $\mathcal{F}^{pl}$ denotes the thermodynamics force conjugated with the plastic deformation due to frictional sliding. It is defined as $\mathcal{F}^{pl} := -\frac{\partial\psi}{\partial\boldsymbol{\varepsilon}^{pl}}$.

The minimization condition should be verified for $\forall\dot{d}$, one gets the local balances equations of the stress tensor:

$$\begin{cases}\mathrm{div}(\boldsymbol{\sigma}) + \boldsymbol{b} = 0 & \text{in } \Omega \\ \boldsymbol{\sigma}\cdot\boldsymbol{n} = \boldsymbol{t} & \text{on } \partial\Omega\end{cases} \tag{3.11}$$

Similarly, the local governing equations of damage evolution are given by:

$$\begin{cases} \mathcal{F}^d - \dfrac{g_c}{l_d} d + g_c l_d \mathrm{div}(\nabla d) = 0 & \text{in } \Omega \\ \nabla d \cdot \boldsymbol{n} = 0 & \text{on } \partial\Omega \end{cases} \tag{3.12}$$

2.3.1 Damage evolution laws for rough cracks

By considering the stored energy density given in Equation (3.5), one obtains the driving force for damage evolution of frictional rough cracks:

$$\mathcal{F}^d = -\frac{\partial \psi(\boldsymbol{\varepsilon}, \boldsymbol{\varepsilon}^{pl}, d)}{\partial d} = \begin{cases} -\, g'(d) w_+^t(\boldsymbol{\varepsilon}) & \text{if } \mathrm{tr}(\boldsymbol{\varepsilon}) > 0 \\ -\, \beta'(d) w_+^s(\boldsymbol{\varepsilon}^{pl}) & \text{if } \mathrm{tr}(\boldsymbol{\varepsilon}) \leq 0 \end{cases} \tag{3.13}$$

The driving energy per unit volume of sound material is given by:

$$\begin{cases} w_+^t(\boldsymbol{\varepsilon}) = \kappa_0 \dfrac{[\mathrm{tr}(\boldsymbol{\varepsilon})]^2}{2} + \mu_0 \boldsymbol{\varepsilon}_{dev} : \boldsymbol{\varepsilon}_{dev} & \text{if } \mathrm{tr}(\boldsymbol{\varepsilon}) > 0 \\ w_+^s(\boldsymbol{\varepsilon}^{pl}) = \mu_0 \boldsymbol{\varepsilon}_{dev}^{pl} : \boldsymbol{\varepsilon}_{dev}^{pl} & \text{if } \mathrm{tr}(\boldsymbol{\varepsilon}) \leq 0 \end{cases} \tag{3.14}$$

It is important to point out that due to continuity condition involved in the stored energy ψ in Equation (3.5), the thermodynamics force $\mathcal{F}^d$ in Equation (3.13) is also fully continuous at the crack opening-closure transition $\mathrm{tr}(\boldsymbol{\varepsilon}) = 0$.

Differently to frictionless cracks, two energy history functionals (Miehe et al., 2010a; Nguyen et al., 2015) are here defined respectively for open and closed cracks:

$$\mathcal{H}^t(t) = \max_{\tau \in [0,t]} [w_+^t(\tau)] \qquad \text{and} \qquad \mathcal{H}^s(t) = \max_{\tau \in [0,t]} [w_+^s(\tau)] \tag{3.15}$$

Accordingly, the governing equation for damage evolution of frictional rough cracks with unilateral effect can be written as:

$$\mathcal{F}_{\mathcal{H}}^d - g_c \Big[\frac{d}{l_d} - l_d \Delta d \Big] = 0 \tag{3.16}$$

$\mathcal{F}_{\mathcal{H}}^d$ represents the damage driving force by considering the history functionals in Equa-

tion (3.15):

$$\mathcal{F}_{\mathcal{H}}^{d} = \begin{cases} 2(1-d)\mathcal{H}^{t} & \text{if } \mathrm{tr}(\boldsymbol{\varepsilon}) > 0 \\ \dfrac{2(1-d)}{\left[1-g(d)\right]^{2}}\mathcal{H}^{s} & \text{if } \mathrm{tr}(\boldsymbol{\varepsilon}) \leq 0 \end{cases} \tag{3.17}$$

2.3.2 Frictional sliding evolution laws for rough cracks

On the other hand, the thermodynamic force conjugated with the frictional sliding is expressed as:

$$\begin{aligned} \mathcal{F}^{pl} &= -\frac{\partial \psi(\boldsymbol{\varepsilon}^{e}, \boldsymbol{\varepsilon}^{pl}, d)}{\partial \boldsymbol{\varepsilon}^{pl}} \\ &= \begin{cases} 0 & \text{if } \mathrm{tr}(\boldsymbol{\varepsilon}) > 0 \\ \kappa_0 \Big[\mathrm{tr}(\boldsymbol{\varepsilon}) - \mathrm{tr}(\boldsymbol{\varepsilon}^{pl})\Big]\mathbf{I} + 2\mu_0\Big(\boldsymbol{\varepsilon}_{dev} - \boldsymbol{\varepsilon}_{dev}^{pl}\Big) - 2\beta(d)\mu_0\boldsymbol{\varepsilon}_{dev}^{pl} & \text{if } \mathrm{tr}(\boldsymbol{\varepsilon}) \leq 0 \end{cases} \end{aligned} \tag{3.18}$$

Again, due to the continuity conditions Equations (3.7) and (3.8), the driving force of frictional sliding $\mathcal{F}^{pl}$ is also fully continuous at the crack opening-closure transition state $\mathrm{tr}(\boldsymbol{\varepsilon}) = 0$.

The frictional sliding occurs when the driving force $\mathcal{F}^{pl}$ reaches certain threshold. It is needed to define a suitable friction criterion as a function of $\mathcal{F}^{pl}$ to describe the evolution of plastic strain $\boldsymbol{\varepsilon}^{pl}$. Inspired by the classical Drucker-Prager criterion for pressure sensitive materials, the following linear function is adopted:

$$F_p(\mathcal{F}^{pl}) = \| \mathcal{F}_{dev}^{pl} \| + \eta^{pl}\mathrm{tr}(\mathcal{F}^{pl}) \leq 0 \tag{3.19}$$

The variable $\| \mathcal{F}_{dev}^{pl} \| = \sqrt{\mathcal{F}_{dev}^{pl} : \mathcal{F}_{dev}^{pl}}$ denotes the generalized deviatoric sliding force, with $\mathcal{F}_{dev}^{pl} = \mathcal{F}^{pl} - \frac{1}{3}\mathrm{tr}(\mathcal{F}^{pl})\mathbf{I}$. The parameter η^{pl} is the frictional coefficient of rough cracks.

Substituting Equation (3.6) for Equation (3.18), the frictional sliding criterion can be conveniently rewritten in terms of stress tensor:

$$F_p(\boldsymbol{\sigma}, \boldsymbol{\varepsilon}^{pl}, d) = \| \boldsymbol{\sigma}_{dev} - 2\beta(d)\mu_0\boldsymbol{\varepsilon}_{dev}^{pl} \| + \eta^{pl}\mathrm{tr}(\boldsymbol{\sigma}) \leq 0 \tag{3.20}$$

The other term $2\beta(d)\mu_0\boldsymbol{\varepsilon}_{dev}^{pl}$ describes the influence of damage on the frictional sliding.

It plays the role of a kinematic hardening. The last term allows considering the effect of mean stress on frictional sliding, widely observed in rock and concrete like materials.

The evolution rate of the plastic strain $\boldsymbol{\varepsilon}^{pl}$ is determined by introducing a plastic flow rule. It is reminded that the continuity conditions between open and closed cracks given in Equation (3.7) requires $\mathrm{tr}(\boldsymbol{\varepsilon}^{pl}) = 0$. Consequently, a non-associated pure deviatoric plastic flow rule is adopted:

$$\dot{\boldsymbol{\varepsilon}}^{pl} = \dot{\lambda}^{pl}\mathcal{G}^{p} = \dot{\lambda}^{pl}\frac{\boldsymbol{\varepsilon}^{pl}_{dev}}{\|\boldsymbol{\varepsilon}^{pl}_{dev}\|} = \dot{\lambda}^{pl}\frac{\boldsymbol{\varepsilon}^{pl}_{dev}}{\sqrt{\boldsymbol{\varepsilon}^{pl}_{dev} : \boldsymbol{\varepsilon}^{pl}_{dev}}} \tag{3.21}$$

The plastic multiplier $\dot{\lambda}^{pl}$ is determined by the following consistency condition:

$$\dot{\lambda}^{pl} \geq 0 \quad , \quad F_p(\boldsymbol{\sigma}, \boldsymbol{\varepsilon}^{pl}, d) \leq 0 \quad , \quad \dot{\lambda}^{pl} F_p(\boldsymbol{\sigma}, \boldsymbol{\varepsilon}^{pl}, d) = 0 \tag{3.22}$$

3 Numerical implementation

The new phase field model is also implemented in the framework of finite element method (FEM). In order to avoid redundancy, the following discrete nodal residuals can be derived by using the standard Galerkin procedure and geometrical discretization used in Chapter 2:

$$\mathbf{R}_u = \int_{\Omega} \boldsymbol{N}_u^T \boldsymbol{b} \mathrm{d}\Omega + \int_{\partial\Omega_t} \boldsymbol{N}_u^T \boldsymbol{t} \mathrm{d}S - \int_{\Omega} \boldsymbol{B}_u^T \boldsymbol{\sigma} \mathrm{d}\Omega = \mathbf{0} \tag{3.23}$$

$$\mathbf{R}_d = \int_{\Omega} \boldsymbol{N}_d^T \left[\mathcal{F}_{\mathcal{H}}^d - \frac{g_c}{l_d} d\right] \mathrm{d}\Omega - \int_{\Omega} \boldsymbol{B}_d^T \left[g_c l_d \nabla d\right] \mathrm{d}\Omega = \mathbf{0} \tag{3.24}$$

3.1 Return-mapping algorithm for plastic deformation

In order to determine the displacement field at each loading step, it is necessary to calculate the stress tensor $\boldsymbol{\sigma}$ at every quadrature point for evaluating the nodal force residual $\mathbf{R}_u$ in Equation (3.23) with a fixed value of d. According to the constitutive relations Equation (3.6), there is a linear relation between the strain and stress tensors for the case of open cracks ($\mathrm{tr}(\boldsymbol{\varepsilon}) > 0$). However, for closed cracks, the problem becomes strongly nonlinear due to the existence of plastic strain $\boldsymbol{\varepsilon}^{pl}$.

As for classical plastic problems with a pressure sensitive yield criterion (Sysala et al., 2016), an implicit return-mapping algorithm is employed and briefly presented here. The first step is to make an elastic prediction. A trial stress state is determined by assuming a full elastic behavior of material. The trial stress is then checked to see whether it is admissible or not for the plastic yield condition. If the yield function $F_p(\boldsymbol{\sigma}^{tr}, \boldsymbol{\varepsilon}^{pl}, d)$ is found to be non-positive, the trial stress becomes the true one. Otherwise, the plastic correction of the trial stress is operated with the return mapping algorithm. The main steps can be found in Algorithm 2. $\mathbb{C}^0$ denotes the fourth order elastic stiffness tensor of sound material.

Algorithm 2: An implicit return-mapping algorithm for plastic correction

Input: $\boldsymbol{\varepsilon}_{n+1}$, d_{n+1}, $\boldsymbol{\varepsilon}_n^{pl}$

Output: $\boldsymbol{\sigma}_{n+1}$, $\boldsymbol{\varepsilon}_{n+1}^{pl}$

Elastic prediction: $\boldsymbol{\sigma}^{tr} = \mathbb{C}^0 : \left(\boldsymbol{\varepsilon}_{n+1} - \boldsymbol{\varepsilon}_n^{pl}\right)$

Check yield criterion: $F_p^{tr} = F_p(\boldsymbol{\sigma}^{tr}, \boldsymbol{\varepsilon}_n^{pl}, d_{n+1})$

if $F_p^{tr} \leq 0$ **then** `// Elastic loading`

  $\boldsymbol{\sigma}_{n+1} = \boldsymbol{\sigma}^{tr}$

  $\boldsymbol{\varepsilon}_{n+1}^{pl} = \boldsymbol{\varepsilon}_n^{pl}$

else `// plastic loading`

  Find $\Delta\lambda^{pl} \geq 0$:

    $\| \boldsymbol{\sigma}_{dev}^{tr} - 2\beta(d)\mu_0\boldsymbol{\varepsilon}_{n,dev}^{pl} - 2[\beta(d)+1]\mu_0\Delta\lambda^{pl}\mathcal{G}^p \| + \eta^{pl}\mathrm{tr}(\boldsymbol{\sigma}^{tr}) = 0$

  Set: `// plastic correction`

    $\boldsymbol{\sigma}_{n+1} = \boldsymbol{\sigma}^{tr} - \mathbb{C}^0 : \Delta\lambda^{pl}\mathcal{G}^p$

    $\boldsymbol{\varepsilon}_{n+1}^{pl} = \boldsymbol{\varepsilon}_n^{pl} + \Delta\lambda^{pl}\mathcal{G}^p$

end

3.2 Staggered algorithm for coupled damage-sliding problem

It is clear that both displacement and damage evolution problems are strongly coupled and highly non-linear, especially for the energy history functionals which are non-convex with respect to the couple of unknowns $(\boldsymbol{u}, d)$ (Bourdin et al., 2000, 2008). It is difficult to solve the coupled systems given in Equations (3.23) and (3.24) by using the conventional Newton-Raphson procedure. For this reason, we adopt here the so-called alternating minimization (AM) solution strategy (Bourdin et al., 2008; Miehe et al., 2010a; Mandal et al.,

2021). It consists of alternatively solving the displacement problem for a fixed damage state and inversely. The main lines are presented in Algorithm 3.

At the same time, due to the plastic frictional sliding and the nonlinear damage-friction coupling function $\beta(d)$, it is no more possible to transform Equations (3.23) and (3.24) into linear systems as in many previous studies (Nguyen et al., 2015; Yu et al., 2021b). However, the standard Newton-Raphson iteration method can be used to solve each of two unknown fields. Accordingly, a linearized system of equations for the i^{th} iteration at the loading step $n+1$ is obtained by differentiating the residual of each problem Equations (3.23) and (3.24):

$$\begin{cases} \mathbf{K}_u^i \delta \boldsymbol{u} = \mathbf{R}_u^i & \Longrightarrow \quad \boldsymbol{u}^{i+1} = \boldsymbol{u}^i + \delta \boldsymbol{u} \\ \mathbf{K}_d^i \delta \boldsymbol{d} = \mathbf{R}_d^i & \Longrightarrow \quad \boldsymbol{d}^{i+1} = \boldsymbol{d}^i + \delta \boldsymbol{d} \end{cases} \tag{3.25}$$

The Jacobian matrices $\mathbf{K}_u$ and $\mathbf{K}_d$ are calculated by:

$$\mathbf{K}_u = -\frac{\partial \mathbf{R}_u}{\partial \boldsymbol{u}} = \begin{cases} \displaystyle\int_\Omega \boldsymbol{B}_u^T \left[g(d) \mathbb{C}^0 \right] \boldsymbol{B}_u \mathrm{d}\Omega & \text{if } \mathrm{tr}(\boldsymbol{\varepsilon}) > 0 \\ \displaystyle\int_\Omega \boldsymbol{B}_u^T \left[\mathbb{C}^{ep} \right] \boldsymbol{B}_u \mathrm{d}\Omega & \text{if } \mathrm{tr}(\boldsymbol{\varepsilon}) \leq 0 \end{cases} \tag{3.26}$$

and

$$\mathbf{K}_d = -\frac{\partial \mathbf{R}_d}{\partial \boldsymbol{d}} = \begin{cases} \displaystyle\int_\Omega \boldsymbol{N}_u^T \left[2 + \frac{g_c}{l_d} \right] \boldsymbol{N}_u \mathrm{d}\Omega + \int_\Omega \boldsymbol{B}_u^T \left[g_c l_d \right] \boldsymbol{B}_u \mathrm{d}\Omega & \text{if } \mathrm{tr}(\boldsymbol{\varepsilon}) > 0 \\ \displaystyle\int_\Omega \boldsymbol{N}_d^T \left[\beta''(d) + \frac{g_c}{l_d} \right] \boldsymbol{N}_d \mathrm{d}\Omega + \int_\Omega \boldsymbol{B}_d^T \left[g_c l_d \right] \boldsymbol{B}_d \mathrm{d}\Omega & \text{if } \mathrm{tr}(\boldsymbol{\varepsilon}) \leq 0 \end{cases} \tag{3.27}$$

with

$$\beta''(d) = \frac{2[1-g(d)] + 8(1-d)^2}{[1-g(d)]^3}$$

It is useful to mention that in practice, numerical integration calculations are conducted over all elements by using Gauss method. The crack opening-closure criterion is checked at each Gauss point.

Algorithm 3: An alternating minimization solution for coupled displacement friction-damage problem

for *each successive loading step* $n+1$ **do**
  Initialzation: $\boldsymbol{u}_{n+1}^{(0)} = \boldsymbol{u}_n$, $\boldsymbol{d}_{n+1}^{(0)} = \boldsymbol{d}_n$, $iter = 0$, $err = 1$
  while $err > tol$ *and* $iter < max\_iter$ **do** // $tol = 1 \times 10^{-4}$
    $iter = iter + 1$ // iteration count
    Compute displacement field $\boldsymbol{u}_{n+1}^{(iter)}$ with fixed phase-field $\boldsymbol{d}_{n+1}^{(iter-1)}$:
    Set: $\boldsymbol{u}_{n+1}^{(iter),0} = \boldsymbol{u}_{n+1}^{(iter-1)}$, $i = 0$
    repeat // Newton iteration
      stress update: $\boldsymbol{\sigma}^i = \boldsymbol{\sigma}(\boldsymbol{\varepsilon}(\boldsymbol{u}_{n+1}^{(iter),i}), d_{n+1}^{(iter-1)})$ // Algorithm 2
      $\mathbf{R}_u^i = \int_\Omega \boldsymbol{N}_u^T \boldsymbol{b} \mathrm{d}\Omega + \int_{\partial\Omega_t} \boldsymbol{N}_u^T \boldsymbol{t} \mathrm{d}S - \int_\Omega \boldsymbol{B}_u^T \boldsymbol{\sigma}^i \mathrm{d}\Omega$
      $\delta\boldsymbol{u} = [\mathbf{K}_u^i]^{-1} \mathbf{R}_u^i$
      $\boldsymbol{u}_{n+1}^{(iter),i+1} = \boldsymbol{u}_{n+1}^{(iter),i} + \delta\boldsymbol{u}$
      $i = i + 1$
    until $\|\delta\boldsymbol{u}\| \leq 1 \times 10^{-8}$
    Compute phase-field $\boldsymbol{d}_{n+1}^{(iter)}$ with fixed displacement field $\boldsymbol{u}_{n+1}^{(iter)}$:
    Set: $\boldsymbol{d}_{n+1}^{(iter),0} = \boldsymbol{d}_{n+1}^{(iter-1)}$, $i = 0$
    repeat // Newton iteration
      $\mathbf{R}_d^i = \int_\Omega \boldsymbol{N}_d^T \left[\mathcal{F}_{\mathcal{H}}^d - \frac{g_c}{l_d} d\right] \mathrm{d}\Omega - \int_\Omega \boldsymbol{B}_d^T \left[g_c l_d \nabla d\right] \mathrm{d}\Omega$
      $\delta\boldsymbol{d} = [\mathbf{K}_d^i]^{-1} \mathbf{R}_d^i$
      $\boldsymbol{d}_{n+1}^{(iter),i+1} = \boldsymbol{d}_{n+1}^{(iter),i} + \delta\boldsymbol{u}$
      $i = i + 1$
    until $\|\delta\boldsymbol{d}\| \leq 1 \times 10^{-8}$
    $err = \|\boldsymbol{d}_{n+1}^{(iter)} - \boldsymbol{d}_{n+1}^{(iter-1)}\|$
  end
  Update: $\boldsymbol{u}_{n+1} = \boldsymbol{u}_{n+1}^{(iter)}$, $\boldsymbol{d}_{n+1} = \boldsymbol{d}_{n+1}^{(iter)}$
end

4 Application examples

In this section, various examples of particular interest are presented to showcase the capabilities of the new phase-field model. In particular, we shall investigate the unilat-

eral effect due to crack opening-closure transition and the coupling mechanism between damage evolution and frictional sliding.

4.1 Uniaxial test with tension-compression loading

The purpose of this example is to show the efficiency of the model in predicting the unilateral behavior of cracked materials. A single cubic element of the unity (mm) size is considered. The material element is subjected to uniaxial tension and compression loading and unloading paths. Two-dimensional plane strain calculation is performed. The geometry and prescribed axial displacement path are presented in Figure 3.1. The mechanical properties of material are taken from the previous study (Lanoye et al., 2013): Young's modulus $E_0 = 32000$MPa, Poisson's ratio $\mu_0 = 0.2$, and internal friction coefficient $\eta^{pl} = 0.6$. As the objective here is not to capture damage localization, the length scale parameter is set to the size of element $l_d = 1$mm. The related critical energy is then determined from the uniaxial tensile strength and one gets $g_c = 2.7 \times 10^{-3}$ N/mm. The equivalent deviatoric plastic strain $\varepsilon_{eq}^{pl} = \sqrt{\boldsymbol{\varepsilon}_{dev}^{pl} : \boldsymbol{\varepsilon}_{dev}^{pl}}$ is used to represent the evolution of plastic deformation.

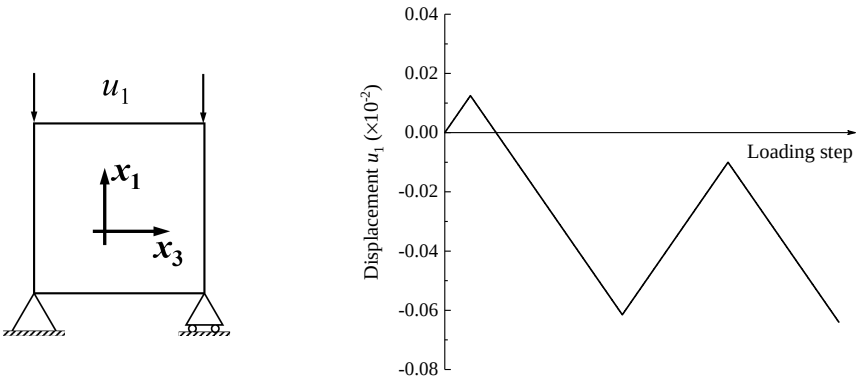

Figure 3.1: Single element geometry and prescribed axial displacement paths

The axial stress-strain curves during the whole loading history are presented in Figure 3.2. We compare the results respectively obtained by using the coupled damage-friction model (left sub-figure) and the frictionless damage model in Chapter 2 (right sub-figure). The mechanical responses are identical for both models during the tensile loading and unloading steps. A clearly non-linear response is obtained at the tensile loading step (O→A→B) due to the evolution of tensile damage (see Figure 3.3). Then the

mechanical behavior is fully linear elastic during the unloading step (B→O). There is no evolution of damage during this step. After the complete unloading of tensile stress, there is no residual strain observed. However, the elastic modulus of material is clearly deteriorated by the induced damage. During the tensile stage, only open cracks are created. The frictional sliding does not occur. Therefore, it is logic that the two models provide the identical results.

The loading is continued by applying a compressive axial strain. The material responses are significantly different between the two models. For the frictionless crack model, one obtains a linear elastic phase with any evolution of damage (O→C). The point C represents the elastic limit in uniaxial compression from which the damage evolves again to reach the peak uniaxial compression strength (point D). During the unloading-reloading step (D→E→D), one gets a pure linear elastic behavior, with a clear degradation of elastic modulus. With this model, one indeed observes a dissymmetric behavior between the tension and compression phases. The damage evolution under compressive loading ($\mathrm{tr}(\boldsymbol{\varepsilon}) \leq 0$) is slower than that in tension ($\mathrm{tr}(\boldsymbol{\varepsilon}) > 0$), due to the consideration of unilateral condition in the damage driving force defined in Equation (2.6). But the dissymmetry remains relatively small and does not reflect the experimental data observed in rock and concrete like materials.

Comparing with the frictionless model in Chapter 2, with the coupled damage-friction model, several significant improvements are obtained. The compressive damage threshold (point C in the left sub-figure) is much higher than the tensile one. Indeed, according to the damage criterion proposed in Equation (3.14), the damage evolution of closed frictional cracks is fully driven by the plastic strains. For this purpose, the evolution of equivalent plastic strain is presented in Figure 3.4. As no cohesion is considered in this model, the frictional sliding starts at the beginning of uniaxial compression (point O). But the damage threshold is not reached until the point C. Thus there is no damage evolution during the step O→C. During the step C→D, the evolution of damage is activated. At the same time, the plastic deformation is also accelerated. It is obvious that the frictional sliding is strongly coupled with the damage evolution. At the point D, a unloading-reloading cycle is performed and the stress-strain path is presented by the loop D→E→F→G→D in Figure 3.2(a). Several interesting features are observed in Figure 3.3(a) and Figure 3.4. During the step D→E, there is no evolution of damage and plastic strain; it is a pure elastic unloading phase. For the step E→F, due to the action of kinematic hardening involved in

Equation (3.20), the frictional sliding is again activated but along the opposite direction. As the accumulated equivalent plastic strain (algebraic value) is decreased, there is no damage evolution. This step is followed by an elastic reloading phase (F→G). Finally, with the help of kinematic hardening term, we obtain a new plastic sliding phase G→D. But the damage evolution is still locked as the value of accumulated plastic strain is lower than its initial value at the point D before the unloading. After the point D, both the plastic strain and damage evolve quickly, inducing a rapid material softening during the post-peak region. It is clear that the proposed friction-damage model is able to predict complex features of mechanical behavior of rock-like material under compressive stress.

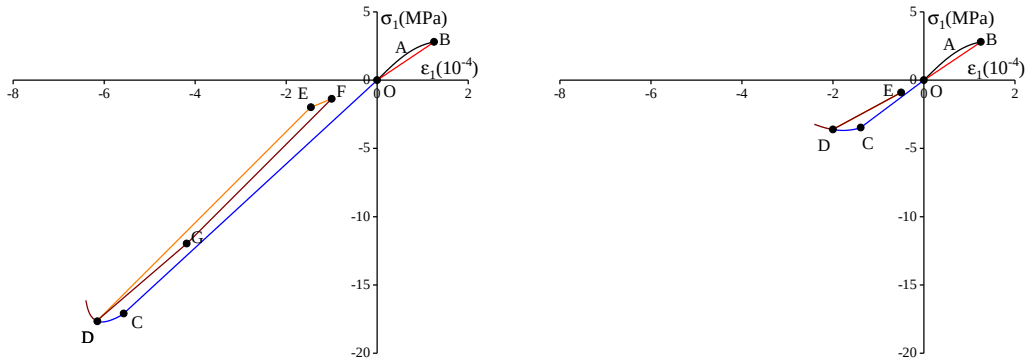

(a) Coupled friction-damage unilateral model **(b)** Frictionless damage unilateral model

Figure 3.2: Stress–strain curves for a single element under uniaxial tension and compression: comparison between the coupled friction-damage unilateral model and frictionless unilateral model

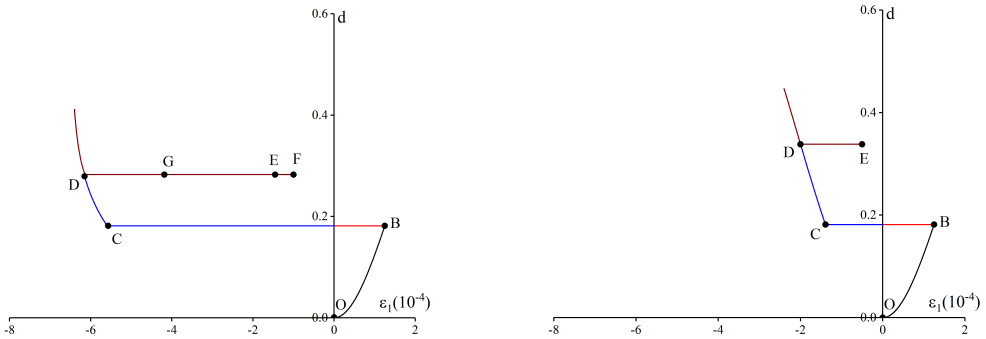

(a) Coupled friction-damage unilateral model **(b)** Frictionless damage unilateral model

Figure 3.3: Evolution of damage during different loading steps of uniaxial tension and compression: comparison between the coupled friction-damage unilateral model and frictionless unilateral mode

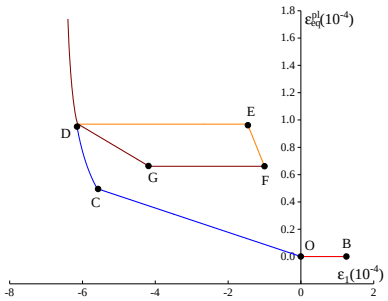

Figure 3.4: Evolution of equivalent plastic strain during the different loading steps of uniaxial tension and compression on a single material element

4.2 Propagation of an inclined frictional crack

Due to the obvious advantages of the coupled friction-damage model demonstrated above, this one is now applied to investigating the propagation of cracks in different cases. In this example, we consider the propagation of an inclined initial crack in a rectangular plate, as shown in Figure 3.5(a). The size of plate is $2m \times 4m$, the initial crack is inclined at $45°$ to the horizontal orientation. The bottom boundary is blocked for vertical displacement but free for horizontal one. A constant vertical displacement rate of 1×10^{-4} m per step is prescribed on the top boundary without any horizontal restrain. Two dimensional plane strain calculations are performed.

The elastic parameters taken from the previous study (Fei and Choo, 2020a), such as: Young's modulus $E = 10000$MPa and Poisson's ratio $\mu = 0.3$. The length scale l_d is a key parameter in the phase-field modeling which defines the width of localized cracks. Its value should be chosen in relation with the element size h. To get a good balance between the accuracy and calculation efficiency, we take here $l_d = 0.02$ m and $l_d/h = 4$. The critical energy release rate g_c is chosen as 35×10^{-6} N/mm for this case. To investigate the influence of friction on crack propagation, three different values of the friction coefficient are used such as $\eta^{pl} = 0.01, 0.10, 0.20$. Further, comparisons between the coupled friction-damage model and frictionless damage model are again presented.

Moreover, the initial crack is considered as an initially fully damaged zone. In general, the value of $d = 1$ is assigned to the cracked zone. However, such a trivial solution can lead to numerical instability. We adopt here an alternative solution by assigning an initial

value H_0 to two energy history functionals such that:

$$\begin{cases} H_0^t(\boldsymbol{x}) = \dfrac{g_c}{2l_d}\dfrac{d_0}{1-d_0}\left(1-\dfrac{2L(\boldsymbol{x})}{l_d}\right) & \text{if } L(\boldsymbol{x}) \le \dfrac{l_d}{2}\ ,\ H_0^t(\boldsymbol{x}) = 0 \quad \text{otherwise} \\ H_0^s(\boldsymbol{x}) = \dfrac{g_c}{2l_d}\dfrac{d_0[1-g(d_0)]^2}{1-d_0}\left(1-\dfrac{2L(\boldsymbol{x})}{l_d}\right) & \text{if } L(\boldsymbol{x}) \le \dfrac{l_d}{2}\ ,\ H_0^s(\boldsymbol{x}) = 0 \quad \text{otherwise} \end{cases} \tag{3.28}$$

$L(\boldsymbol{x})$ represents the shortest distance from an arbitrary point $\boldsymbol{x}$ to the initial crack (Borden et al., 2012). With the above distribution of energy history functionals, the corresponding initial damage distribution can be calculated and it is shown in Figure 3.5(b).

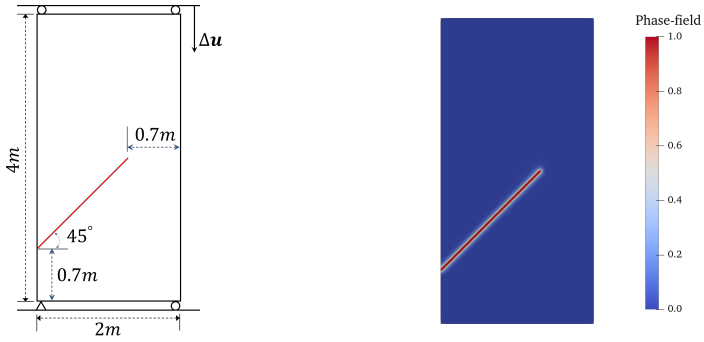

(a) Geometry and initial crack configuration

(b) Initial distribution of damage

Figure 3.5: Setup for the problem of an inclined crack in a rectangular plate

In Figure 3.6, the overall load-displacement curves for the three different values of friction coefficient of rough crack are presented and compared with that of smooth cracks. It is seen that both the peak load and displacement increase with the friction coefficient. This seems to be logic as a larger shear force is needed to create plastic sliding when the crack surface friction is higher. For the same reason, the residual strength also increases with the rise of frictional coefficient. For the case of smooth cracks, the small residual strength obtained in the numerical results is due to the small residual elastic stiffness used to ensure the stability of calculation.

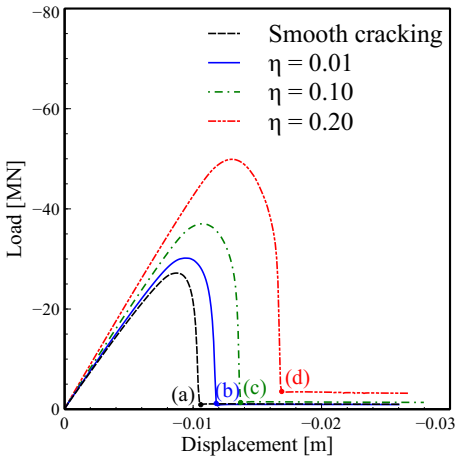

Figure 3.6: Overall load–displacement curves for different values of frictional coefficient ($\eta^{pl} = 0$ for smooth crack)

In Figure 3.7, the distributions of damage at the fully cracked states, as indicated in Figure 3.6, are presented for four different cases. It is obvious that the crack propagation pattern is significantly affected by the friction coefficient. In the case of frictionless cracks, there is no plastic deformation. The crack propagation is driven by the strain energy $w_+(\boldsymbol{\varepsilon})$ defined in Equation (2.6). As most cracks are closed, the crack propagation is mainly controlled by the deviatoric strain tensor. Therefore, one gets a quasi pure shearing mechanism. As a consequence, the initial crack propagates nearly along its initial direction.

For the frictional cracks, the crack propagation is affected by the plastic sliding induced deformation, as defined in Equation (3.14). Differently with smooth cracks, the propagation of closed cracks is fully driven by the plastic deviatoric strain tensor as the elastic deformation is locked by the friction. Therefore, the crack propagation pattern is influenced by the frictional coefficient. More precisely, the crack propagation orientation progressively deviates from its initial direction. The deviation angle is more and more large when the frictional coefficient is higher.

In Figure 3.8, the distribution of the accumulated equivalent plastic strain has been investigated when those initially cracked plate with different frictional coefficient were fully broken. An obviously accumulation of the inelastic deformation can be seen along the pre-existing crack for all three cases with different frictional coefficient of cracks. However, differently with the continuous distribution of accumulated equivalent plastic strain along the crack propagation path in case with $\eta^{pl} = 0.01$, a discontinuous segment

can be found in the crack propagation path for higher frictional coefficients such as $\eta^{pl} = 0.1$ and 0.2.

In order to further explain how the frictional slide of initial crack affects on the crack propagation, the distribution of driving history energy (H^t and H^s) around the initial crack tip has been investigated. Meanwhile, a simplified opening-closure criterion ($\langle \mathrm{tr}(\boldsymbol{\varepsilon})\rangle_+$ and $\langle \mathrm{tr}(\boldsymbol{\varepsilon})\rangle_-$) is here adopted. For a consequence, one can distinguish the opening-closure state and propagation path of cracks based on the distribution of $H^t\langle \mathrm{tr}(\boldsymbol{\varepsilon})\rangle_+$ and $H^s\langle \mathrm{tr}(\boldsymbol{\varepsilon})\rangle_-$. Firstly, the crack opening-closure state and propagation direction have been compared for cases with $\eta = 0.01$ and $\eta^{pl} = 0.2$ at the beginning of crack propagation. For $\eta^{pl} = 0.01$ in Figure 3.9(a), the deformation mainly induces the increasment of $H^s\langle \mathrm{tr}(\boldsymbol{\varepsilon})\rangle_-$ around the crack tip while the $H^t\langle \mathrm{tr}(\boldsymbol{\varepsilon})\rangle_+$ remains 0. It means that the closed crack could appear firstly along the distribution of $H^s\langle \mathrm{tr}(\boldsymbol{\varepsilon})\rangle_-$. While, the case $\eta = 0.2$ shows a different behavior. As illustrated in Figure 3.9(b), the deformation induced cracking driving energy are $H^t\langle \mathrm{tr}(\boldsymbol{\varepsilon})\rangle_+$, which means the propagation crack is open crack due to tensile deformation. It also can be found that the deviation angle of opening propagation crack is larger than the closed propagation crack. Then, the propagation crack opening-closure state for $\eta^{pl} = 0.01$ and $\eta^{pl} = 0.2$ when they are fully broken are presented in Figures 3.9(c) and 3.9(d). In case of $\eta^{pl} = 0.01$, the propagation crack is all consisted of closed crack. However, a segment of open propagation crack can be seen from the initial crack tip and a segment of closed crack at the end of propagation in case of $\eta^{pl} = 0.2$.

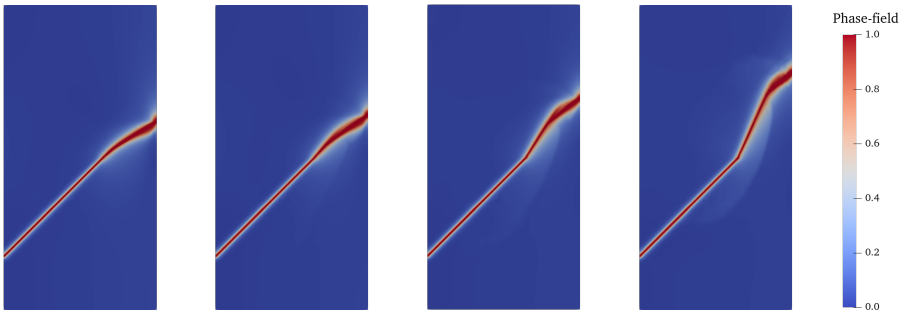

(a) Frictionless **(b)** $\eta^{pl} = 0.01$ **(c)** $\eta^{pl} = 0.1$ **(d)** $\eta^{pl} = 0.2$

Figure 3.7: Cracking patterns of initially cracked plate at fully broken state with different values of frictional coefficient

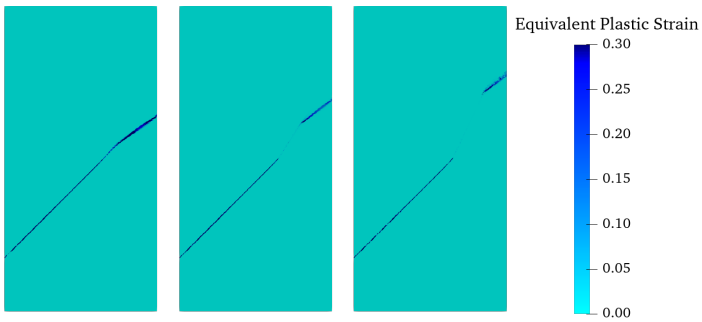

(a) $\eta = 0.01$ **(b)** $\eta = 0.1$ **(c)** $\eta = 0.2$

Figure 3.8: Equivalent plastic strain distribution of initially cracked plate at fully broken state with different values of frictional coefficient

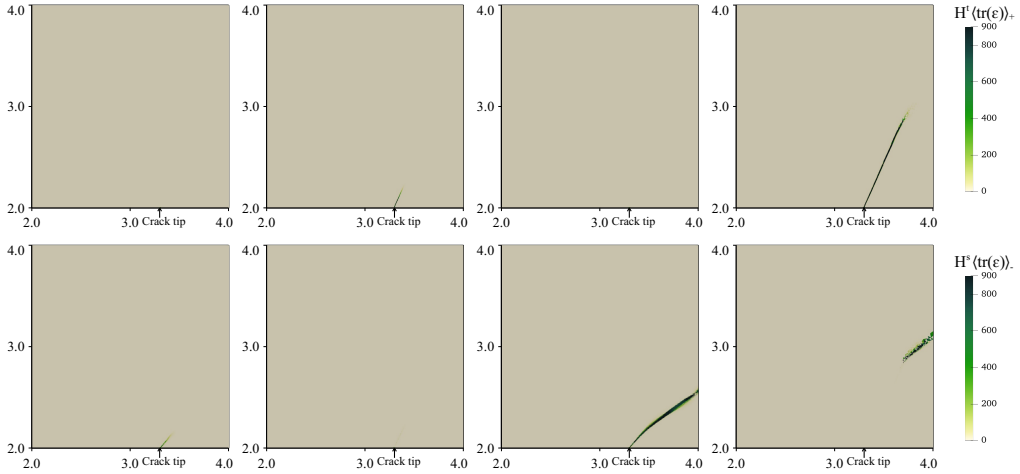

(a) $\eta = 0.01$ $u = 0.0099$m **(b)** $\eta = 0.2$ $u = 0.0135$m **(c)** $\eta = 0.01$ $u = 0.0119$m **(d)** $\eta = 0.2$ $u = 0.0170$m

Figure 3.9: Comparing of driving history energy considering with the cracks opening-closure state for different values of frictional coefficient at different loading steps

4.3 Crack bridging of two pre-existing flaws

In this example, the coupled damage-friction phase-field model is used to investigate crack bridging between two pre-existing flaws in a plate under uniaxial compressive. This case is based on the experimental tests conducted by Yang et al. (2008). The geometry of plate and the configuration initial flaws are presented in Figure 3.10(a). The size of rectangular plate is $50mm \times 100mm$. Two different types of configurations of pre-existing flaws are considered, type B and type C. The geometrical parameters for pre-existing flaws

are given in Table 3.1. According to the experimental observations, a tensile failure mode was observed in specimens with the type-B initial flaws while a shear failure mode in specimens with the type-C initial flaws.

Similarly to the previous example, an initial distribution of energy history functionals are affected to the pre-existing flaws by using Equation (3.28). The corresponding initial distributions of damage are presented in Figure 3.10(b) and Figure 3.10(c) for the two types of configurations. The plate is subjected to a prescribed axial displacement increment of 0.002 mm per loading step on the top surface of the plate. The elastic parameters are determined from the experimental data reported in (Yang et al., 2008): Young's modulus $E = 18.54$GPa and Poisson's ratio $\mu = 0.25$. For localized cracking modeling, the length scale is $l_d = 0.4$mm and the ratio between length scale and element is $l_d/h = 4$. Finally, the critical energy release rate and frictional coefficient are calibrated from the peak strength of triaxial compression tests reported in (Yang et al., 2008), and one gets $g_c = 0.010$N/mm and $\eta^{pl} = 0.36$.

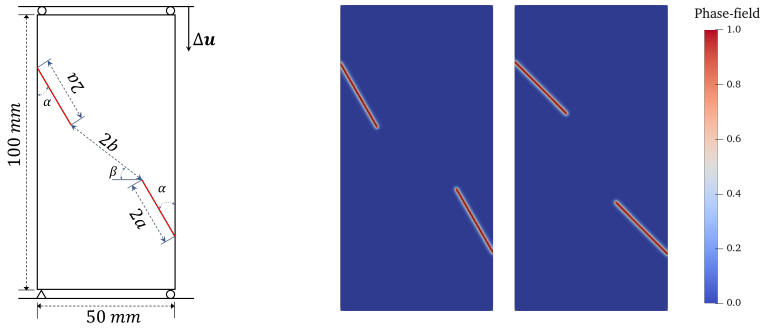

(a) Geometry parameters **(b)** Type-B **(c)** Type-C

Figure 3.10: Geometrical parameters of plate with two pre-cracking flaws and initial distributions of damage

Table 3.1
Geometrical parameters for two pre-flaws

Flaw geometry	Flaw angle $[\alpha/^\circ]$	Ligament angle $[\beta/^\circ]$	Flaw length $[2a/\text{mm}]$	Ligament length $[2b/\text{mm}]$
Type-B	30	38	24	33
Type-C	45	61	24	33

The average axial stress-strain curves predicted by the friction-damage model are presented and compared with the experimental data (Yang et al., 2008) in Figure 3.11 for the two types of pre-existing flaws. It can be seen that in both the pre- and post-peak regimes, the proposed phase-field model describes well the mechanical responses of the two cracked plates. Moreover, the overall mechanical behavior of plate is affected by the configuration of two pre-existing flaws.

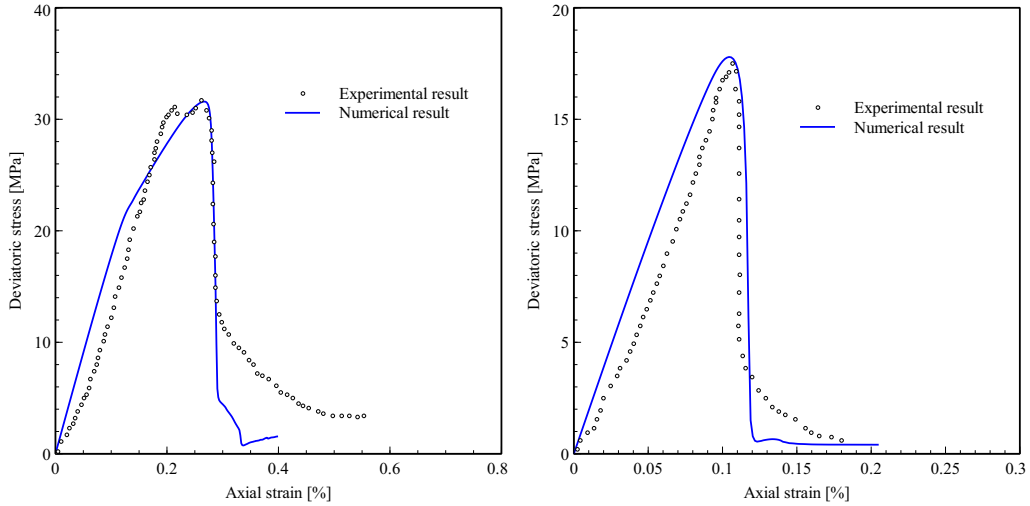

(a) Type-B **(b)** Type-C

Figure 3.11: Average axial stress–strain curves of plates with two different types of pre-existing flaws: comparison between numerical results and experimental data

The failure patterns of two pre-existing flaws configurations are also investigated. For the type B configuration, a typical tensile failure mode was observed in the laboratory test (Yang et al., 2008), as shown in Figure 3.12. Starting from the inner ends of existing

flaws, two main wing cracks propagate in the quasi vertical direction, respectively towards the top and bottom surfaces of the sample. Due to the boundary condition effects, secondly cracks are also created in the top and bottom regions. These ones are finally coalesced with the main wing cracks, leading to a dramatic stress drop. It is found that the proposed friction-damage phase field model is able to correctly describe the experimental observations.

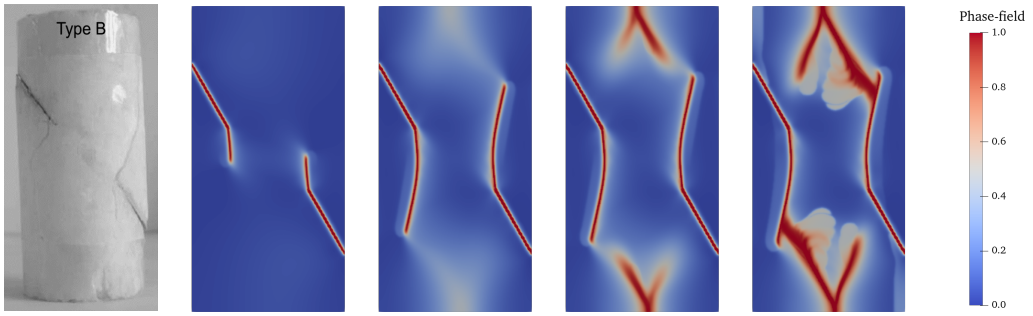

(a) Experiment **(b)** $\Delta u =$ 0.162mm **(c)** $\Delta u =$ 0.266mm **(d)** $\Delta u =$ 0.276mm **(e)** $\Delta u =$ 0.292mm

Figure 3.12: Crack initiation and propagation patterns in the specimen with type B pre-existing flaws

Differently with the type B configuration, the failure pattern is significantly different for the type C pre-existing flaws. As shown in Figure 3.13, a shear-dominating failure mode is obtained. After the new cracks occur at the inner ends of pre-existing flaws, they propagate toward each to other along the initial orientation of pre-existing flaws, to progressively form a connected crack bridge. Again, this complex failure pattern is well captured by the proposed phase-field model.

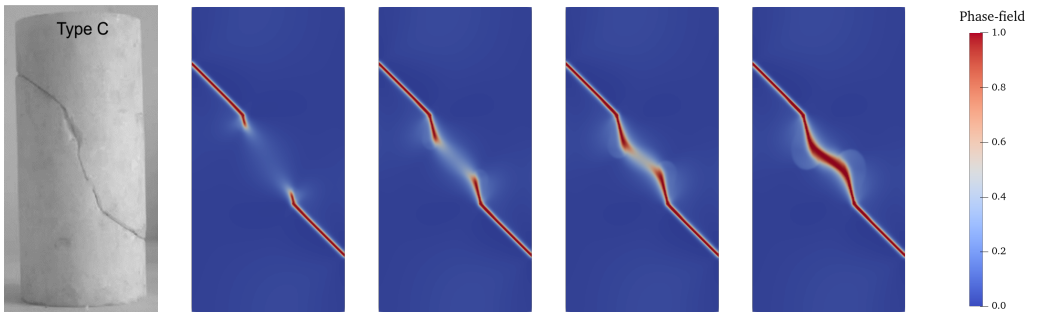

(a) Experiment **(b)** $\Delta u =$ 0.102mm **(c)** $\Delta u =$ 0.114mm **(d)** $\Delta u =$ 0.116mm **(e)** $\Delta u =$ 0.122mm

Figure 3.13: Crack initiation and propagation pattern in specimen with type C pre-existing flaws

4.4 Influence of confining stress

It is known that the mechanical behavior of rock and concrete like materials is strongly dependent on the confining stress. The underlying physics is related to the internal friction of this type of materials. In order to consider this effect by using phase field method, some empirical relations have been proposed in previous studies to describe the variation of critical energy release rate g_c as a function of confining stress (Wang et al., 2021; Yu et al., 2021b). But the physical background of such empirical relations is not clearly explained. In our new coupled friction-damage model, the frictional sliding in closed cracks is explicitly taken into account. In order to assess its efficiency, based on the experimental data reported in Yang et al. (2012), triaxial compression tests on sandstone with different confining stresses are considered.

On the other hand, the transition from diffuse damage to localized cracks is another key issue. In many previous studies, a weak element was artificially introduced to enhance the apparition of localized cracks. But in real materials, the strain and damage localization is inherently related to the material heterogeneity. Consider the case of sandstone, according to X-ray diffraction analysis presented in (Yang et al., 2012), the sandstone is mainly composed of feldspar (45%), quartz (13.5%), debris (31.5%), agglutinate (10%) and inter-particular pores. The solid particles are cemented to constitute an equivalent matrix phase. The pores are randomly embedded inside the solid matrix. The macroscopic elastic properties can be estimated by using a suitable homogenization method.

In the case of sandstone, it seems that the widely used Mori-Tanaka scheme (Mori and Tanaka, 1973) is a good choice. Thus, the macroscopic elastic bulk modulus κ^{hom} and shear modulus μ^{hom} are given by:

$$\kappa^{hom} = \frac{4(1-\phi)\kappa_s\mu_s}{4\mu_s + 3\phi\kappa_s}; \qquad \mu^{hom} = \frac{(1-\phi)\mu_s}{1 + 6\phi\frac{\kappa_s+2\mu_s}{9\kappa_s+8\mu_s}} \tag{3.29}$$

where κ_s and μ_s are the bulk and shear moduli of the equivalent solid matrix, and ϕ is the porosity. Knowing the average of porosity $\phi = 8.8\%$ and the macroscopic Young's modulus and Poisson's ratio presented (Yang et al., 2012), it is possible to calculate the values of κ_s and μ_s by inverting the relations Equation (3.29). One gets $\kappa_s = 51.2$GPa and $\mu_s = 17.8$GPa.

In order to represent the material heterogeneity, it is assumed that the porosity is not uniform inside the sample but exhibits a spatial variation (Wang et al., 2022). The widely used Weibull distribution Equation (2.24) is adopted to generate a random distribution of the porosity ϕ:

$$\Phi(\phi) = \frac{m_i}{\bar{\phi}}\left(\frac{\phi}{\bar{\phi}}\right)^{m_i-1}\exp\left[-\left(\frac{\phi}{\bar{\phi}}\right)^{m_i}\right] \tag{3.30}$$

where $\bar{\phi}$ denotes the average value of porosity and m_i is the homogeneity index.

Based on the distribution of porosity and by using the values of κ_s and μ_s, one can calculate the macroscopic elastic properties κ^{hom} and μ^{hom} by using Equation (3.29), and then the macroscopic Young's modulus and Poisson's ratio. As an example, the spatial distributions of macroscopic Young's modulus with the homogeneity index $n = 10$ is presented in Figure 3.14(a). For a quantitative illustration, the variations of Young's modulus along two selected sections are presented in Figure 3.14(b).

The size of sample is 50×100mm. A uniform mesh is adopted. The length scale for phase field modeling is $l_d = 0.4$mm with a ratio between length scale and element size of $l_d/h = 4$. The critical energy release rate and internal friction coefficient are determined from the peak strength and the following values are obtained: $g_c = 0.208$N/mm and $\eta^{pl} = 0.29$.

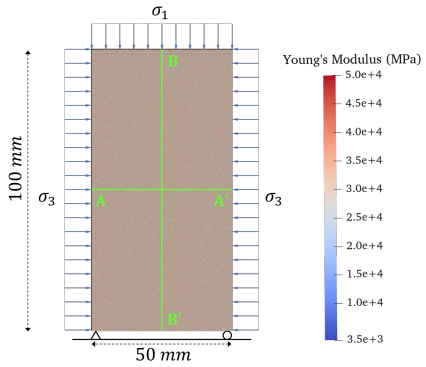

(a) Geometry of samples in triaxial compression tests

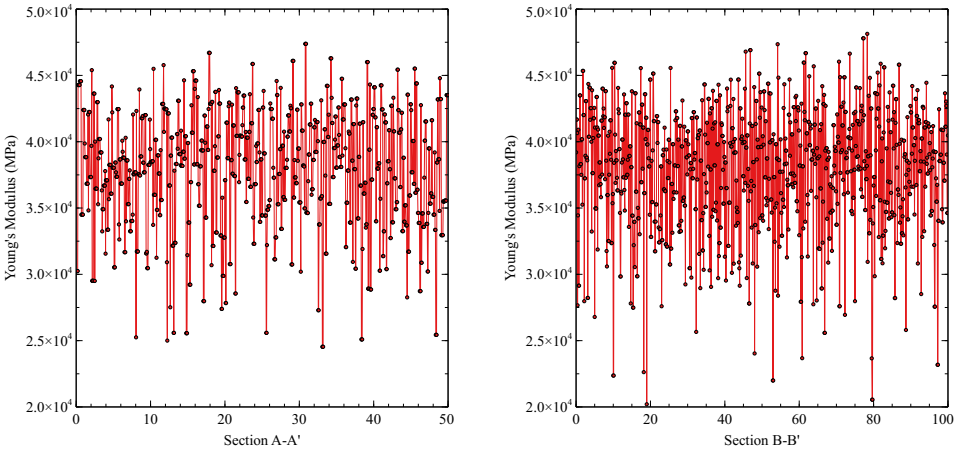

(b) Spatial distributions of Young's modulus

Figure 3.14: Illustration of specimen geometry, boundary conditions and spatial distribution of macroscopic Young's modulus

Three conventional triaxial compressive tests with different confining stresses ($\sigma_c = 20, 35, 50$MPa) are here considered. In Figure 3.15, the axial stress-strain curves predicted by the coupled friction-damage model are presented and compared with the experimental data (Yang et al., 2012). There is a good agreement in both pre- and post regions. In particular, the influence of confining stress on the peak and residual strength is well captured by the proposed model. Due to technical issues, some oscillations are observed in the post-peak region of experimental data.

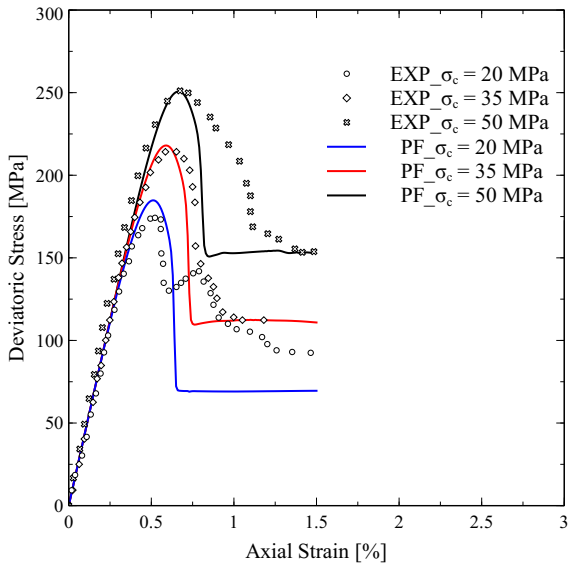

Figure 3.15: Axial stress-strain curves in three triaxial compression tests on sandstone: comparison between numerical results and experimental data

Moreover, the distributions of damage and equivalent plastic strain at four different loading steps are presented in Figure 3.16 for the test with a confining stress of 20 MPa. These results illustrate the gradual evolution of strain localization and localized cracking process during the loading history. One can see that at $\varepsilon_a = 0.516\%$, both the distributions of damage and plastic strain are almost uniform in the sample. Starting from $\varepsilon_a = 0.572\%$, the plastic strain and damage are progressively localized into a number of narrow bands to form major cracks. It is needed to point out that the localization pattern is inherently related to the heterogeneous distribution of porosity. At $\varepsilon_a = 0.604\%$, which is close to the peak strength, one inclined major crack is obtained and accompanied by several secondary cracks. It seems that two quasi orthogonal crack networks are observed. This type of failure pattern is very consistent with the experimental observations (Yang et al., 2012).

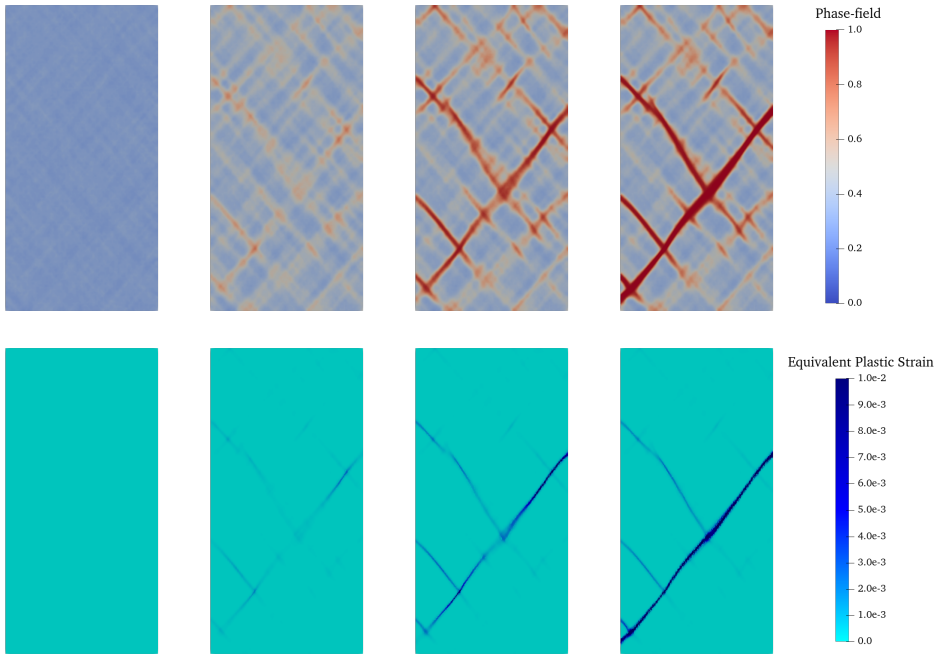

(a) $\varepsilon_a = 0.516\%$ **(b)** $\varepsilon_a = 0.572\%$ **(c)** $\varepsilon_a = 0.584\%$ **(d)** $\varepsilon_a = 0.604\%$

Figure 3.16: Evolution of damage and equivalent plastic strain at four different loading levels for the triaxial compression tests with a confining stress of 20 MPa

5 Conclusions

In this chapter, we have proposed a novel phase field model for modeling mixed cracking process in rock and concrete like materials under complex loading paths. Several new features are incorporated, in particular the unilateral contact condition and the coupling between damage and frictional sliding. The proposed model is able to describe open and closed cracks, smooth and frictional crack surfaces. The general continuity conditions at the crack opening- closure transition point are fully verified for the energy functions, the stress-strain relations, and the driving forces for crack propagation. The evolution criteria are formulated in a rigorous thermodynamics framework.

The proposed model is applied to investigate cracking processes in different loading scenarios, on both single material element and structural scales. A number of interesting results are obtained. It is found that under compressive stresses, the frictional sliding plays a crucial role on the deformation and cracking of rock and concrete like materials.

The evolution of closed rough cracks is driven by the frictional sliding induced plastic deformation; and the evolution of plastic sliding is affected by the damage state. With the help of the friction effect, the proposed model is able to physically take into account the influence of confining stress on the mechanical behavior of materials. Moreover, a kinematic hardening rule is incorporated in the frictional sliding law. This allows us to correctly describe the unloading-reloading hysteresis loop.

The proposed model is able to describe tensile, shear and mixed modes of cracking. The numerical predictions of failure patterns are very consistent with most experimental observations such as crack propagation deviation and crack bridging.

CHAPTER 4

Numerical study of time-dependent deformation and cracking in brittle rocks with a novel phase-field model

1 Introduction

In this chapter, we shall develop an efficient numerical modeling method of progressive cracking process in rocks exhibiting an elastic-viscoplastic behavior. The initiation and propagation of cracks is described by a time-dependent phase field method while the creep deformation of rocks by a viscoplastic model. The growth of phase field is affected by the viscoplastic deformation and inversely the threshold of viscoplastic flow is degraded by the induced cracks. The proposed numerical method is implemented in a standard finite element framework. Its efficiency is assessed through comparisons with both laboratory tests and field observations.

2 Time-dependent phase-field model for viscoplastic rocks

In this work, we consider $\Omega \subset \mathbb{R}$ to be a volumetric domain of solid material with an external boundary $\partial\Omega$, which contains a number of cracks $\Gamma_i, i = 1, ..N$. The approxima-

tion of the total area of sharp crack surfaces A_Γ in Chapter 2 is adopted here again:

$$A_\Gamma = \sum_{i=1}^{N} A_{\Gamma_i} \cong A_{\Gamma_d} = \int_\Omega \Gamma_d(d, \nabla d) \mathrm{d}V \tag{4.1}$$

Similarly, the crack density functions in Equations (2.2) and (2.4) are used in this chapter.

2.1 Energy functional

In this study, we consider an isotropic rock material exhibiting an elastic-viscoplastic behavior and the transition from diffuse damage to localized cracking which is described by the phase-field method. With the assumption of small strains, the total strain tensor $\boldsymbol{\varepsilon}$ is conventionally divided into an elastic part $\boldsymbol{\varepsilon}^e$ and a viscoplastic part $\boldsymbol{\varepsilon}^{vp}$ such as $\boldsymbol{\varepsilon} = \boldsymbol{\varepsilon}^e + \boldsymbol{\varepsilon}^{vp}$. The total energy functional can be expressed in the following general form:

$$E(\boldsymbol{\varepsilon}^e, \boldsymbol{\varepsilon}^{vp}, d) = \int_\Omega \left[w^e(\boldsymbol{\varepsilon}^e, d) + w^{vp}(\boldsymbol{\varepsilon}^{vp}, d) \right] \mathrm{d}v + E^{crack} \tag{4.2}$$

w^e is the elastic strain energy density per initial unit volume of damaged material. w^{vp} denotes the viscoplastic strain energy density (dissipated and stored). The third term E^{crack} represents the energy needed to create cracks in Ω.

2.1.1 Elastic strain energy

The elastic strain energy of material is affected by cracking process and it is a function of the damage variable d. Inversely, the damage evolution is driven by the growth of elastic strain energy. In this work, it is assumed that the damage evolution is motivated only the tensile (positive) volumetric strain and deviatoric (or shear) strains. For this purpose, the elastic strain energy of undamaged material is conveniently decomposed as the one in Chapter 2:

$$\begin{cases} w_0^e(\boldsymbol{\varepsilon}^e) = w_{0-}^e(\boldsymbol{\varepsilon}^e) + w_{0+}^e(\boldsymbol{\varepsilon}^e) \\ w_{0-}^e = \dfrac{k_0}{2}[\langle \mathrm{tr}(\boldsymbol{\varepsilon}^e)\rangle_-]^2 \qquad\qquad , \boldsymbol{\varepsilon}_{dev}^e = \boldsymbol{\varepsilon}^e - \dfrac{\mathrm{tr}(\boldsymbol{\varepsilon}^e)}{3}\boldsymbol{I} \\ w_{0+}^e = \dfrac{k_0}{2}[\langle \mathrm{tr}(\boldsymbol{\varepsilon}^e)\rangle_+]^2 + \mu_0 \boldsymbol{\varepsilon}_{dev}^e : \boldsymbol{\varepsilon}_{dev}^e \end{cases} \tag{4.3}$$

Accordingly, the elastic strain density function of damaged material is written as:

$$w^e(\boldsymbol{\varepsilon}^e, d) = w^e_{0-}(\boldsymbol{\varepsilon}^e) + g(d)w^e_{0+}(\boldsymbol{\varepsilon}^e, d) \tag{4.4}$$

The elastic stress-strain relations of damaged material are obtained from the standard derivation of w^e:

$$\boldsymbol{\sigma} = \frac{\partial w^e}{\partial \boldsymbol{\varepsilon}^e} = \mathbb{C}(d) : \boldsymbol{\varepsilon}^e \tag{4.5}$$

$\boldsymbol{\sigma}$ is Cauchy stress tensor. $\mathbb{C}(d)$ denotes the elastic stiffness tensor of damaged material and it is here given by:

$$\mathbb{C}(d) = r_e^- k_0 \boldsymbol{I} \otimes \boldsymbol{I} + g(d)[r_e^+ k_0 \boldsymbol{I} \otimes \boldsymbol{I} + 2\mu_0(\mathbb{I} - \frac{1}{3}\boldsymbol{I} \otimes \boldsymbol{I})] \tag{4.6}$$

$\mathbb{I}$ is the fourth-order symmetric identity tensor. The coefficients $r_e^{\pm} = \frac{1}{2}\{\text{sign}[\pm\text{tr}(\boldsymbol{\varepsilon}^e)]+1\}$ describe the fact that the bulk modulus k is affected by open cracks (r_e^+ = 1 and r_e^-=0) but not affected by closed shear cracks (r_e^+ = 0 and r_e^-=1).

It is noticed that the choice of $g(d)$ leads to different types of elastic properties degradation. Among various forms of $g(d)$ proposed in previous studies (Miehe et al., 2010a; Choo and Sun, 2018; Zhou et al., 2020), the form in Chapter 2 which is the most widely used one is $g(d) = (1 - k_l)(1 - d)^2 + k_l$ by satisfying the condition $g'(d = 1) = 0$. It is adopted in this chapter.

2.1.2 Viscoplastic strain energy

Furthermore, since the concept of elasto-viscoplasticity was firstly introduced by Perzyna (1966), the elasto-viscoplastic behavior of rocks has been widely discussed and some significant progresses have been reported in Debernardi and Barla (2009) and Yang et al. (2014). Moreover, An elasto-viscoplastic model based on Perzyna's general theory was proved to be in good agreement with both laboratory and in situ data by Bonini et al. (2007). Consequently, the classical Perzyna's formulation (Perzyna, 1966; Cristescu et al., 1994) will be coupled with the phase-field method to describe the time-dependent behavior of brittle rocks in this paper.

Time-dependent deformation of rocks can be related to various mechanisms such as viscoplastic flow, sub-critical growth of micro-cracks etc. In this work, for the sake of simplicity, it is assumed that the time-dependent deformation and cracking is mainly

driven by the viscoplastic flow. Further, by putting the emphasis on cracking modeling by the phase-field method, the viscoplastic deformation is described by using the classical Perzyna's formulation (Perzyna, 1966; Cristescu et al., 1994) and a simple constitutive model.

The accumulated viscoplastic strain ε^{vp} is calculated by time integration of its flow rate $\dot{\varepsilon}^{vp}$:

$$\varepsilon^{vp}(t) = \int_0^t \dot{\varepsilon}^{vp}(\tau)\mathrm{d}\tau \tag{4.7}$$

The viscoplastic strain rate is defined by the following widely used exponential form:

$$\dot{\boldsymbol{\varepsilon}}^{vp} = \eta^{vp}\langle f^{vp}(\boldsymbol{\sigma})\rangle_+^n \dot{\lambda}^{vp}\frac{\partial G^{vp}}{\partial \boldsymbol{\sigma}} \tag{4.8}$$

η^{vp} is a viscosity parameter controlling the initial rate of viscoplastic flow. $\langle\rangle_+$ are the Macaulay brackets. f^{vp} represents the viscoplastic loading function. Similarly to some previous studies (Borden et al., 2016), it is assumed that the viscoplastic flow of rocks can be enhanced by the induced damage. Therefore, the following damage-coupled form is adopted (Mánica et al., 2017):

$$f^{vp}(\boldsymbol{\sigma}) = \frac{q - g_{vp}(d)\sigma_s}{p_r} \tag{4.9}$$

$q = \sqrt{3\boldsymbol{s} : \boldsymbol{s}/2}$ is the conventional generalized deviatoric stress, with $\boldsymbol{s} = \boldsymbol{\sigma} - \frac{\mathrm{tr}(\boldsymbol{\sigma})}{3}\boldsymbol{I}$ being the deviatoric stress tensor. The parameter σ_s denotes the initial threshold for viscoplastic flow and p_r =1 MPa is a fixed normalizing stress. $g_{vp}(d)$ is the degradation function for viscoplastic flow. The use of product form in $g_{vp}(d)\sigma_s$ means that the viscoplastic threshold is progressively reduced by the growth of damage. For the sake of simplicity, the same form as the elastic degradation function is here used: $g_{vp}(d) = g(d)$.

The coefficient $\dot{\lambda}^{vp}$ defines the current amplitude of the viscoplastic strain rate, which is a function of the accumulated viscoplastic strain:

$$\dot{\lambda}^{vp} = (1 - \varepsilon_{vp}^{eq})^m \text{ , with } \varepsilon_{vp}^{eq} = \int_0^t \sqrt{\frac{2}{3}\dot{\boldsymbol{\varepsilon}}_{dev}^{vp}(\tau) : \dot{\boldsymbol{\varepsilon}}_{dev}^{vp}(\tau)}\mathrm{d}\tau \tag{4.10}$$

in which $\dot{\boldsymbol{\varepsilon}}_{dev}^{vp} = \dot{\boldsymbol{\varepsilon}}^{vp} - \frac{\mathrm{tr}(\dot{\boldsymbol{\varepsilon}}^{vp})}{3}\boldsymbol{I}$ is the viscoplastic deviatoric strain tensor. n and m are two material parameters.

In the viscoplastic flow rule Equation (4.8), the scalar-valued function G^{vp} is a potential which defines the components of viscoplastic strain rate. Different forms are available in literature. For hard rocks, it was widely assumed that the viscoplastic flow produced the time-dependent deviatoric strains only. Therefore, a very simply viscoplastic flow potential $G^{vp} = q$ was used in some previous studies (Su, 2003; Mánica et al., 2017). However, according to laboratory creep tests on Jinping marble diabase (Liu and Shao, 2017), large volumetric creep strain was also obtained. For this reason, the following viscoplastic flow potential is proposed in this work:

$$G^{vp} = q + c_v p \tag{4.11}$$

where $p = \mathrm{tr}(\boldsymbol{\sigma})/3$ is the mean stress. The parameter c_v defines the volumetric viscoplastic strain rate.

In consistency with the elastic strain energy decomposition Equation (4.3), the viscoplastic strain energy of undamaged material is also decomposed into two parts: respectively coupled and not with the induced damage d. Therefore, the viscoplastic strain energy of damaged materials is given by:

$$\begin{cases} w^{vp}(\boldsymbol{\varepsilon}^{vp}, d) = w^{vp}_{0-}(\boldsymbol{\varepsilon}^{vp}) + g(d) w^{vp}_{0+}(\boldsymbol{\varepsilon}^{vp}) \\ w^{vp}_{0-} = \displaystyle\int_0^t \boldsymbol{\sigma}(\tau) : \dot{\boldsymbol{\varepsilon}}^{vp}_{sph-}(\tau) \mathrm{d}\tau \\ w^{vp}_{0+} = \displaystyle\int_0^t \boldsymbol{\sigma}(\tau) : [\dot{\boldsymbol{\varepsilon}}^{vp}_{sph+}(\tau) + \dot{\boldsymbol{\varepsilon}}^{vp}_{dev}(\tau)] \mathrm{d}\tau \end{cases}, \quad \begin{cases} \dot{\boldsymbol{\varepsilon}}^{vp}_{sph-} = \dfrac{\langle \mathrm{tr}(\dot{\boldsymbol{\varepsilon}}^{vp}) \rangle_-}{3} \boldsymbol{I} \\ \dot{\boldsymbol{\varepsilon}}^{vp}_{sph+} = \dfrac{\langle \mathrm{tr}(\dot{\boldsymbol{\varepsilon}}^{vp}) \rangle_+}{3} \boldsymbol{I} \\ \dot{\boldsymbol{\varepsilon}}^{vp}_{dev} = \dot{\boldsymbol{\varepsilon}}^{vp} - \dfrac{\mathrm{tr}(\dot{\boldsymbol{\varepsilon}}^{vp})}{3} \boldsymbol{I} \end{cases} \tag{4.12}$$

2.1.3 Crack growth related energy

In the variational framework for fracture mechanics, the crack growth or the evolution of damage variable is seen as an energy minimization problem (Francfort and Marigo, 1998; Bourdin et al., 2008). As in previous studies (Miehe et al., 2010b; Choo and Sun, 2018), the energy related to fracture growth is here assumed to be fully dissipated. Moreover, the classical Griffith-type critical energy release rate is here adopted to quantify the work needed for an instantaneous crack surface creation (Griffith, 1921). Therefore, using the crack surface density defined in Equation (2.4), the total energy dissipated in

instantaneous crack creation can be expressed as follows:

$$E^{crack-ins} = \int_{\Omega} g_c \Gamma_d \mathrm{d}V \tag{4.13}$$

The parameter g_c denotes the energy needed for the creation of unit crack surface in unit initial volume (N/m). By assuming that the value of g_c is time-independent, the crack energy dissipation rate can be calculated as:

$$\dot{E}^{crack-ins} = \int_{\Omega} g_c \dot{\Gamma}_d \mathrm{d}V = \int_{\Omega} g_c \big[(\frac{d}{l_d}) \dot{d} + l_d \nabla d \cdot \nabla \dot{d} \big] \mathrm{d}V \tag{4.14}$$

In some situations, it is important to take into account a time-dependent or rate-dependent growth of cracks. Therefore, we shall also quantify the energy needed for such a crack growth process. Based on previous studies (Hofacker and Miehe, 2013; Loew et al., 2019), the following specific form is adopted:

$$\dot{E}^{crack-vis} = \int_{\Omega} \eta_d \dot{d}^2 \mathrm{d}V \tag{4.15}$$

in which $\eta_d \geq 0$ ($N.s/m^2$) is a viscosity parameter. Accordingly, the total dissipation rate crack growth is given by:

$$\dot{E} = \dot{E}^{crack-ins} + \dot{E}^{crack-vis} \tag{4.16}$$

2.2 Governing equations

The mechanical boundary values problem with crack growth (or phase-field evolution) can be solved by the minimization of the following potential function:

$$\dot{\Pi}(\dot{\boldsymbol{u}}, \dot{d}) = \dot{E}(\dot{\boldsymbol{u}}, \dot{d}) - \dot{P}(\dot{\boldsymbol{u}}) = 0 \tag{4.17}$$

By using the elastic strain energy, viscoplastic strain energy and crack growth energy defined above, the rate of the total energy functional $\dot{E}$ is given by:

$$\begin{aligned} \dot{E}(\dot{\boldsymbol{\varepsilon}}^e, \dot{\boldsymbol{\varepsilon}}^{vp}, \dot{d}) = \int_{\Omega} \dot{w}^e + \dot{w}^{vp} \, \mathrm{d}V = \int_{\Omega} \big[\frac{\partial (w^e + w^{vp})}{\partial d} \dot{d} + \boldsymbol{\sigma} : (\dot{\boldsymbol{\varepsilon}}^e + \dot{\boldsymbol{\varepsilon}}^{vp}) \big] \mathrm{d}V \\ + \int_{\Omega} \{ g_c \big[(\frac{d}{l_d}) \dot{d} + l_d \nabla d \cdot \nabla \dot{d} \big] + \eta_d \dot{d}^2 \} \mathrm{d}V \end{aligned} \tag{4.18}$$

As the evolution of phase-field variable d is driven by elastic and viscoplastic strains (or equivalently by dis displacement field $\boldsymbol{u}$) (Miehe et al., 2010a; Nguyen et al., 2015), the external applied work rate is simply expressed as:

$$\dot{P} = \int_{\Omega} \boldsymbol{b} \cdot \dot{\boldsymbol{u}} \mathrm{d}V + \int_{\partial\Omega_t} \boldsymbol{t} \cdot \dot{\boldsymbol{u}} \mathrm{d}A \tag{4.19}$$

where $\boldsymbol{b}$ is a given body force field per unit volume (N/m^3) and $\boldsymbol{t}$ a prescribed surface traction (N/m^2) on the external boundary $\partial\Omega_t$.

The energy balance condition $\dot{\Pi} = 0$ leads to the following integral equation:

$$\begin{aligned} &\int_{\Omega} -\big[\mathrm{div}(\boldsymbol{\sigma}) + \boldsymbol{b}\big] \cdot \dot{\boldsymbol{u}} \mathrm{d}V + \int_{\partial\Omega} \big[\boldsymbol{\sigma} \cdot \boldsymbol{n} - \boldsymbol{t}\big] \cdot \dot{\boldsymbol{u}} \mathrm{d}A \\ &+ \int_{\Omega} \big[\frac{\partial(w^e + w^{vp})}{\partial d} + \frac{g_c}{l_d} d - g_c l_d \Delta d + \eta_d \dot{d}\big] \cdot \dot{d} \mathrm{d}V + \int_{\partial\Omega} \big[g_c l_d \nabla d \cdot \boldsymbol{n}\big] \cdot \dot{d} \mathrm{d}A = 0, \quad \forall\Omega \end{aligned} \tag{4.20}$$

in which $\Delta d = \mathrm{div}(\nabla d)$. Accordingly, one gets easily the following local governing equations for the mechanical (or displacement) problem:

$$\mathrm{div}(\boldsymbol{\sigma}(t)) + \boldsymbol{b} = 0 \text{ , with } \boldsymbol{\sigma}(t) = \mathbb{C}(d) : \big[\boldsymbol{\varepsilon} - \boldsymbol{\varepsilon}^{vp}(t)\big] \tag{4.21}$$

It is worth noticing that as the viscoplastic strains evolve with time, the current stress tensor is also a function of time. However, for the sake of simplicity, it is assumed that the time-dependent progressive deformation and cracking in rock structures can be seen as a quasi-static process. Therefore, the inertia terms are not taken into account in the balance equations. The governing equation for the phase-field evolution is given by:

$$\eta_d \dot{d} = 2(1-d)(w^e_{0+} + w^{vp}_{0+}) - g_c\big[\frac{d}{l_d} - l_d \Delta d\big] \tag{4.22}$$

In order to verify the irreversible condition of crack growth $\dot{\Gamma}_d \geq 0$ and $\dot{d} \geq 0$, the concept of energy history functional introduced in Miehe et al. (2010a) is here adopted and expressed by:

$$\mathcal{H}(t) = \max_{\tau \in [0,t]} \big[w^e_{0+}(\tau) + w^{vp}_{0+}(\tau)\big] \tag{4.23}$$

Consequently, the governing equation of phase-field evolution problem is rewritten as

follows:

$$\eta_d \dot{d} = 2(1-d)\mathcal{H} - g_c\big[\frac{d}{l_d} - l_d \Delta d\big] \tag{4.24}$$

3 Numerical implementation

The time-dependent phase-field evolution is coupled with the displacement (stress) field solution. Both problems are here solved by using the classical finite element method.

Like the previous chapters, the weak forms can be derived by using using the standard Galerkin procedure with the test functions $\delta \boldsymbol{u}$ and δd respectively:

$$\int_\Omega \boldsymbol{\sigma} : \nabla(\delta \boldsymbol{u}) \mathrm{d}V = \int_\Omega \boldsymbol{b} \cdot \delta \boldsymbol{u} \mathrm{d}V + \int_{\partial\Omega} \boldsymbol{t} \cdot \delta \boldsymbol{u} \mathrm{d}S \tag{4.25}$$

$$\int_\Omega \big[(2\mathcal{H} + \frac{g_c}{l_d})d + \eta_d \dot{d}\big]\delta d \mathrm{d}V + \int_\Omega g_c l_d \nabla d \cdot \nabla(\delta d) \mathrm{d}V = \int_\Omega 2\mathcal{H}\delta d \mathrm{d}V \tag{4.26}$$

3.1 Time and geometrical discretization

The total loading history (designed by the time T) is divided into a number of incremental steps such as $t = 0, t_1, t_2, ..., t_n, t_{n+1}, ..., T$. For the current loading step $n+1$, the time increment is denoted as $\Delta t = t_{n+1} - t_n$. For the sake of simplicity, the evolution rate of d is assumed to be constant in the time increment under consideration, and it is calculated by:

$$\dot{d} = \frac{d_{n+1} - d_n}{\Delta t} \tag{4.27}$$

where d_n and d_{n+1} represent the damage values at the loading steps t_n and t_{n+1}, respectively.

Further, starting from the initial state, the value at the end of previous step t_n is known, the current viscoplastic strain is calculated by:

$$\boldsymbol{\varepsilon}^{vp}_{n+1} = \boldsymbol{\varepsilon}^{vp}_n + \int_{t_n}^{t_{n+1}} \dot{\boldsymbol{\varepsilon}}^{vp}(\tau) \mathrm{d}\tau \tag{4.28}$$

where $\boldsymbol{\varepsilon}^{vp}_n$ and $\boldsymbol{\varepsilon}^{vp}_{n+1}$ are the accumulated viscoplastic strains at the time steps t_n and t_{n+1} respectively. Again for the simplicity, the viscoplastic strain rate is considered to be constant and determined by the state at the loading step t_n with Equation Equation (4.8).

Thus, the accumulated viscoplastic strain for the current step is given by:

$$\boldsymbol{\varepsilon}_{n+1}^{vp} = \boldsymbol{\varepsilon}_{n}^{vp} + \Delta t \dot{\varepsilon}^{vp}(t_n) \tag{4.29}$$

It iw worth noticing that due to the simplified explicit time integration scheme adopted here, a small time increment should be chosen for a stable numerical solution. In general, preliminary calculations are performed in order to choose a suitable time increment.

With the time discretization scheme presented above, the weak form integrals for the current loading step t_{n+1} are rewritten as:

$$\int_{\Omega} \left\{ \mathbb{C}(d_{n+1}) : \left[\boldsymbol{\varepsilon}_{n+1} - \boldsymbol{\varepsilon}_{n+1}^{vp} \right] \right\} : \nabla(\delta \boldsymbol{u}) \mathrm{d}V = \int_{\Omega} \boldsymbol{b} \cdot \delta \boldsymbol{u} \mathrm{d}V + \int_{\partial\Omega} \boldsymbol{t} \cdot \delta \boldsymbol{u} \mathrm{d}S \tag{4.30}$$

and

$$\int_{\Omega} \left[(2\mathcal{H}_{n+1} + \frac{g_c}{l_d}) d_{n+1} + \eta_d \frac{d_{n+1} - d_n}{\Delta t} \right] \delta d \mathrm{d}V + \int_{\Omega} g_c l_d \nabla d_{n+1} \cdot \nabla(\delta d) \mathrm{d}V = \int_{\Omega} 2\mathcal{H}_{n+1} \delta d \mathrm{d}V \tag{4.31}$$

It is noticed that H_{n+1} is calculated from the values of $\boldsymbol{\varepsilon}_{n+1}$ and $\boldsymbol{\varepsilon}_{n+1}^{vp}$.

On the other hand, the computational structure domain Ω is divided into n_e elements which are defined by n_p nodes. Accordingly, it is easily to transform the weak forms into the following systems of discrete equations similar with Chapter 2:

$$\begin{cases} \boldsymbol{K}_u \boldsymbol{U}_{n+1} = \boldsymbol{F}_{u,n+1}^{ext} + \boldsymbol{F}_{n+1}^{vp} \\ \boldsymbol{K}_d \boldsymbol{d}_{n+1} = \boldsymbol{F}_{d,n+1} \end{cases} \tag{4.32}$$

$\boldsymbol{K}_u$ and $\boldsymbol{K}_d$ are the global stiffness matrices, $\boldsymbol{F}_{u,n+1}^{ext}$, $\boldsymbol{F}_{d,n+1}$ the global nodal forces vectors, respectively for the displacement and damage fields, and $\boldsymbol{F}_{n+1}^{vp}$ the global nodal force vector related to viscoplastic flow:

$$\begin{cases} \boldsymbol{K}_u = \displaystyle\int_{\Omega} \left[\boldsymbol{B}_u^T \mathbb{C}(d_{n+1}) \boldsymbol{B}_u \right] \mathrm{d}V \\ \boldsymbol{F}_{u,n+1}^{ext} = \displaystyle\int_{\Omega} \left[\boldsymbol{N}_u^T \cdot \boldsymbol{b} \right] \mathrm{d}V + \int_{\partial\Omega} \left[\boldsymbol{N}_u^T \cdot \boldsymbol{t} \right] \mathrm{d}S \\ \boldsymbol{F}_{n+1}^{vp} = \displaystyle\int_{\Omega} \left[\boldsymbol{B}_u^T \mathbb{C}(d_{n+1}) : \boldsymbol{\varepsilon}_{n+1}^{vp} \right] \mathrm{d}V \end{cases} \tag{4.33}$$

and

$$\begin{cases} \boldsymbol{K}_d = \int_\Omega \left[(\frac{g_c}{l_d} + 2\mathcal{H}_{n+1} + \frac{\eta_d}{\Delta t}) \boldsymbol{N}_d^T \boldsymbol{N}_d + g_c l_d \boldsymbol{B}_d^T \boldsymbol{B}_d \right] \mathrm{d}V \\ \boldsymbol{F}_{d,n+1} = \int_\Omega (2\mathcal{H}_{n+1} + \frac{\eta_d}{\Delta t} d_n) \boldsymbol{N}_d^T \mathrm{d}V \end{cases} \tag{4.34}$$

3.2 Staged coupling algorithm

It is worth noticing that the displacement (and stress) and cracking evolution problems are strongly coupled. Indeed, the displacement (stress) evolution is affected by the damage process. For instance, the elastic stiffness tensor and viscoplastic threshold are functions of damage variable. Inversely, the damage evolution is driven by the mechanical field through the stored elastic and viscoplastic energy. Therefore, both problems should be solved in a coupled way. However, it is demonstrated that the energy history functional $\mathcal{H}(t)$ given in Equation (4.34) is non-convex with respect to the couple of unknowns ($\boldsymbol{u}$, d) (Bourdin et al., 2000, 2008). As a consequence, it is difficult to solve the systems of coupled equations Equation (4.32) by using the conventional Newton-Raphson procedure. However, the functional $\mathcal{H}(t)$ is convex with respect to one of two unknowns ($\boldsymbol{u}$ or d), if the other one is fixed. In general, the so-called alternating minimization (AM) solver proposed in (Bourdin et al., 2000, 2008) is widely used and adopted here. In the AM solver, two solution stages are successively performed at the k^{th} iteration of a specific loading step $n+1$. This is summarized as follows:

I) Solving the displacement problem with the damage field fixed at $\boldsymbol{d}_{n+1}^{k-1}$ obtained from the last iteration:

$$\boldsymbol{U}_{n+1}^{k} = [\boldsymbol{K}_u^{k-1}(\mathbb{C})]^{-1} \cdot \left[\boldsymbol{F}_{u,n+1}^{ext} + \boldsymbol{F}_{n+1}^{vp} \right] \text{, with } \mathbb{C} = \mathbb{C}(\boldsymbol{d}_{n+1}^{k-1})$$

II) Solving the phase-field problem using the updated displacement field and history energy functional:

$$\boldsymbol{d}_{n+1}^{k} = [\boldsymbol{K}_d^{k}]^{-1} \cdot \boldsymbol{F}_{d,n+1}^{k}(\mathcal{H}) \text{ , with } \mathcal{H}_{n+1}^{k} = \mathcal{H}(\boldsymbol{U}_{n+1}^{k})$$

These two stages are repeated until the convergence criterion $\|\boldsymbol{d}_{n+1}^{k} - \boldsymbol{d}_{n+1}^{k-1}\| \leq \epsilon$ is verified. According to (Ambati et al., 2015), a convergence tolerance is taken as $\epsilon = 1 \times 10^{-5}$.

4 Simulation of laboratory tests on Jinping marble

In view of assessing the efficiency of time-dependent phase-field model, representative laboratory tests are investigated in this section. It is worth noticing that the emphasis of phase-field model is to capture the progressive damage toward cracking process. For the sake of simplicity, instantaneous plastic deformation is not taken into account. Inelastic strains, failure and post-failure softening are entirely attributed to damage evolution and localization as well as viscoplastic flow. Therefore, the proposed phase-field model is mainly suitable for brittle rocks under low confining pressure. For this reason, a typical brittle rock, Jinping marble, is here selected. This rock has been widely investigated in the context of stability analysis of high slopes around the Jinping I hydraulic power plant.

Short term triaxial compression tests and long term creep tests are considered. Representative experimental data are selected from previous studies (Zhou et al., 2015a; Liu and Shao, 2017). The laboratory tests were performed on cylindrical samples of $50\ mm$ in diameter and $100\ mm$ in height. For the sake of simplicity, two-dimensional plane strain simulations are performed. The specimen geometrical domain is divided into 200×400 (80 000) elements. According to experimental observations (Zhou et al., 2015a; Liu and Shao, 2017), failure patterns of samples are mainly characterized by localized fractures even if the samples are subjected to uniform macroscopic stresses and displacements. The onset of localized fractures or non-uniform stress and strain fields is generally related to material heterogeneity. Without detailed descriptions of such heterogeneity of tested samples and in order to enhance the onset of localized fractures, a small weak region (one element) is placed at the sample center where the value of g_c is reduced by 1%. The boundary conditions are composed of a uniform normal stress on the lateral surfaces (denoted as σ_3) and a uniform vertical displacement on the upper boundary surface, which is used to calculate the average axial strain ε_1. As output results, one obtains the average lateral strain ε_3 and axial stress σ_1.

4.1 Short term triaxial tests

For modeling of short term mechanical behavior, two elastic parameters and the critical energy release rate g_c should be identified. The elastic parameters of Jinping marble are directly taken from the previous experimental studies (Zhou et al., 2015a) and the fol-

lowing values are used: Young's modulus $E = 45000\ MPa$ and Poisson's ratio $\nu = 0.15$. The critical fracture energy (or energy release rate) g_c is a key parameter in the phase-field model. Its value is generally identified form uniaxial tension or bending tests, which are not available for the studied rock. Further, it is found that the value of g_c identified from tensile test could not be suitable for cracking under compressive stresses (Yu et al., 2021b,a). However, the value of g_c can be indirectly estimated from the peak values of deviatoric stress obtained in triaxial compression tests. Moreover, it is found that for most rocks, the values of g_c can vary with confining stress. Inspired by the previous studies (Yu et al., 2021b,a), the following empirical relation is here adopted: $g_c = g_{c0}e^{\varsigma(\sigma_c/\sigma_r)}$, with σ_c being the confining stress and $\sigma_r = 1MPa$ the reference normalizing pressure. g_{c0} denotes the value of g_c for uniaxial compression with $\sigma_c = 0$ and the parameter ς controls its variation with confining stress. For the case of Jinping marble studied here, by using the peak deviatoric stresses obtained in three triaxial compression tests respectively with 0, 10 and 20 MPa confining stress, we have obtained $g_{c0} = 2.0937N/mm$ and $\varsigma = 0.0466$. Finally, the length scale parameter l_d is generally taken as 1 to 3 times of the smallest element size. It is set here to 0.25 mm.

Comparisons between experimental data and simulation results are presented in Figure 4.1 for three values of confining pressure. The main features of mechanical behavior of Jinping marble are correctly reproduced by the relatively simple phase-field model. The values of peak deviatoric stress are well predicted. For low confining pressures (0 and 10 MPa), the post-peak brittle failure process is also properly described. For the test with a high confining pressure (20 MPa), it seems that the marble exhibits a brittle-ductile transition. Quite large plastic strains, in particular in the radial direction, are observed. There is a residual strength in the post-peak regime due to the frictional effect along closed cracks. All these features are not properly captured by the simple elastic-brittle model as it is not the emphasis of the present work. However, these features can be improved by incorporating an instantaneous plastic deformation mechanism in the phase-field model or/and taking into account the friction effect along localized cracks. This will be performed in our future studies.

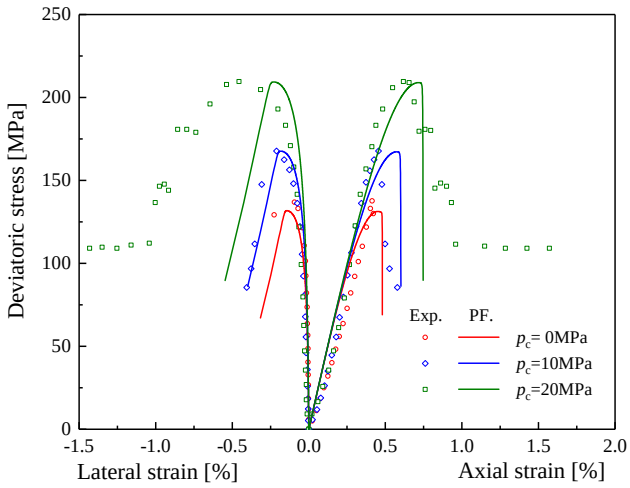

Figure 4.1: Axial and radial strains versus deviatoric stress of Jinping marble in triaxial compression tests with different pressures: comparisons between numerical results and experimental data (Zhou et al., 2015a)

4.2 Uniaxial and triaxial creep tests

At first, an uniaxial compression creep test reported in Zhou et al. (2015a) is considered. Five additional parameters involved in the viscoplastic model should be identified, say η^{vp}, σ_s, c_v, n and m. These parameters cannot be directly calculated from experimental measurements and they are generally calibrated from the optimal numerical fitting of creep tests. Basically, the parameter σ_s defines the threshold of viscoplastic flow and can be determined at the end of elastic stage in a triaxial creep test. η^{vp} mainly controls the initial creep rate during the primary creep stage while n affects the creep rate evolution. m describe the viscoplastic hardening effect on the transition from the primary to secondly creep stages. The viscoplastic potential parameter c_v controls the volumetric viscoplastic strain and can be identified from the lateral creep strain curve. For the marble samples tested in Zhou et al. (2015a), the following values of viscoplastic parameters are obtained: $\eta^{vp} = 1 \times 10^{-7} s^{-1}$, $\sigma_s = 100$ MPa, $c_v = 0.01$, $n = 3.2$ and $m = 7980$. In Figure 4.2, we show the axial and radial strains as functions of time under an axial stress of 113 MPa. The evolution of damage is also reported. It is found that the numerical predictions obtained using the elastic-viscoplastic and phase-field model are in good agreement with the experimental data. The main features of creep deformation behavior of Jinping marble are well described by the proposed model. In particular, typical three

stages of creep deformation are found in this test, namely an increasing primary creep stage, an quasi-stationary stage and an accelerating one leading to the sample failure. It is further to observe the creep deformation rate is clearly linked to the damage evolution which also exhibits three distinct stages. During the first stage, the damage increases quickly due to the applied axial stress. Then it evolves slowly with the viscoplastic strain. Finally, the maximum value in the sample increases very rapidly and reaches 1 causing the macroscopic failure of sample.

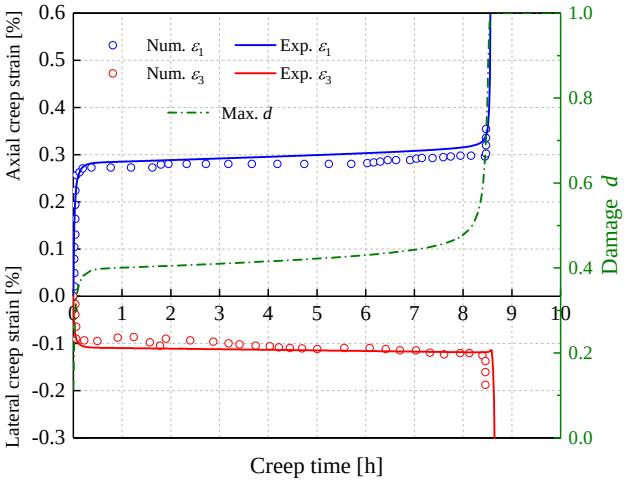

Figure 4.2: Evolution of axial and lateral strains as well as damage variable with time in an uniaxial compression creep test under an axial stress of 113 MPa: comparisons between numerical results and experimental data Zhou et al. (2015a)

In Figure 4.3, we show the damage variable distributions inside the sample obtained at different instances during the uniaxial compression creep test. Due to the presence of weak element, the damage localization starts from the center of sample. Two quasi symmetric localized damage bands are obtained. This configuration is close to fracture modes widely observed in rock samples (Zhou et al., 2015a). It is worth noticing that the use of a weak element is an artificial technique to facilitate the onset of damage localization. In future studies, this point can be addressed by considering the spatial variability of micro-structure of rocks such as porosity and mineral composition.

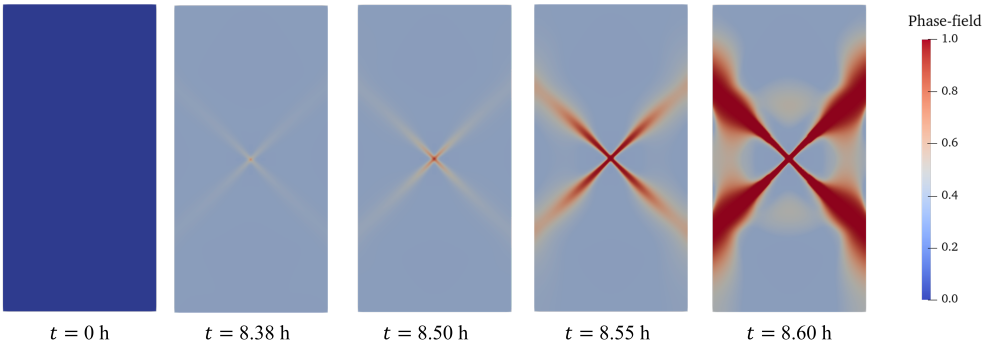

Figure 4.3: Evolution of damage distribution of uniaxial compression creep test

Moreover, two triaxial compression creep tests under a confining pressure of 30MPa, also performed on Jinping marble respectively with a single and multiple deviatoric stress steps, are investigated. The experimental data are taken from Liu and Shao (2017). The samples used in these tests and those used in Zhou et al. (2015a) were drilled at different zones. Therefore, there are some quantitative differences on mechanical parameters. For instance, the elastic properties measured in triaxial compression tests (Liu and Shao, 2017) are as follow: Young's modulus $E = 30000\ MPa$ and Poisson's ratio $\nu = 0.15$. The critical fracture energy g_c is again fitted from the peak deviatoric stress and one gets $g_c = 1.2775\ N/mm$. The parameters for viscoplastic flow are as follows: $\eta_d = 1 \times 10^{-10} Ns/mm^2$, $\eta^{vp} = 1 \times 10^{-7} s^{-1}$, $\sigma_s = 70MPa$, $c_v = 0.26$, $n = 2.4$ and $m = 1080$. However, the same finite element mesh and the same value of length scale l_d as those in the uniaxial creep test are used.

Table 4.1
Reference set of model's parameters for rock samples investigated in (Liu and Shao, 2017)

Elastic and phase-field parameters	E (MPa)	ν (-)	g_c (N/mm)	p_c (MPa)	l_d (mm)
Values	30000	0.15	1.2775	30	0.25
Viscoplastic parameters	η^{vp} (s^{-1})	σ_s (MPa)	n (-)	m (-)	c_v (-)
Values	1×10^{-7}	70	2.4	1080	0.26

The creep test with a single loading step was performed under a deviatoric stress of 143 MPa. Numerical predictions are compared with experimental data in Figure 4.4(a), together with the damage variable evolution. A good concordance is obtained. In this test, one obtains mainly a primary creep phase. Both axial and radial strains evolve towards stationary values and creep strain rates decrease with time. Another important feature is that the radial creep strain is clearly larger than the axial one. This means that the viscoplastic deformation induces an important volumetric dilatance. In the second test, four loading steps were realized with increasing values of deviatoric stress from 65 MPa to 130 MPa. Comparisons between numerical results and experimental data of axial and radial strains are shown in Figure 4.4(b). It is interesting to observe that the creep strain rate increases with the rise of deviatoric stress. When this one is high, a small increment of deviatoric stress can generate large creep strains, for instance during the last loading step with an increment of 10 MPa. The damage variable evolution trend is fully consistent with that of strains. Again, the radial creep strain is clearly larger than the axial one. There is a good agreement between numerical and experimental results for the axial strain as well as for the radial one when the deviatoric stress is low (the first two loading steps). But more and more scatters are observed when the deviatoric stress is high (the last two steps). This indicates that the volumetric dilation is enhanced during creep process by material damage. As a possible improvement of the viscoplastic model, the volumetric dilation parameter c_v should evolve with damage.

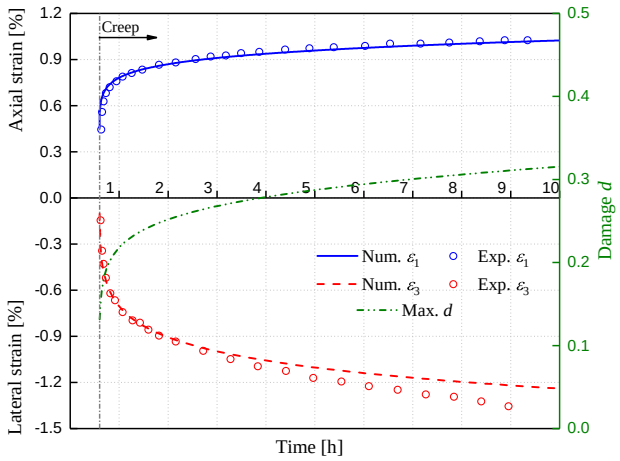

(a) creep test with a single loading step ($q = 143MPa$)

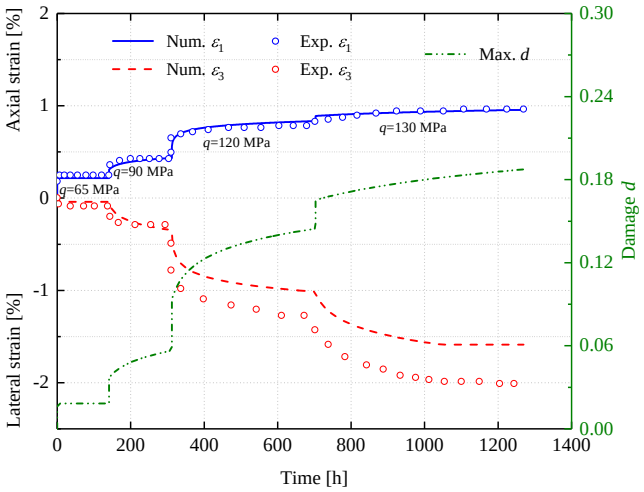

(b) creep test with multiple loading steps

Figure 4.4: Variations of axial and lateral strains in triaxial compression creep tests under a confining pressure of 30 MPa respectively with a single and multiple loading steps, together with damage variable evolution

4.3 Sensitive analysis

Some comparative calculations are presented here in order to investigate effects of some key parameters on short and long-term mechanical responses of rocks.

Firstly, the influences of geometry discretization as well as the characteristic length are studied. For this purpose, six cases with different minimum element size h and length

scale l_d are considered and detailed in Table 4.2. These case are chosen for the following strategy. In the cases 1 to 4, the characteristic length is equal to or higher than the minimum element size, $l_d \geq h$, while in the cases 5 and 6, it is smaller than the minimum element size $l_d < h$. Moreover, in order to facilitate the comparison and interpretation, the value of g_c is accordingly reset with that of the length scale l_d. The objective is to obtain a very close value of uniaxial compression strength for all the cases considered to that reported in Zhou et al. (2015a).

Table 4.2
Different sets of considered parameters for sensitivity study of uniaxial compression test reported in Zhou et al. (2015a)

Case No.	l_d (mm)	h (mm)	g_c (N/mm)	Case No.	l_d (mm)	h (mm)	g_c (N/mm)
1	1.0	1.0	2.08	4	1.0	0.5	2.08
2	0.5	0.5	1.04	5	0.5	1.0	1.04
3	0.25	0.25	0.52	6	0.25	0.5	0.52

In Figure 4.5, we first show the overall strain-stress curves of uniaxial compression test for six cases considered in Table 4.2. It is confirmed that all six cases give a quasi identical uniaxial compression strength. However, the responses are slightly different in the post-peak regime. For those cases where $l_d \geq h$ (cases 1-4), the mechanical behavior is almost the same while the curves of the cases where $l_d < h$ (cases 5, 6) are lower than the other cases. However, significant differences are observed in the uniaxial creep test as shown in the same figure. Although the similar primary creep stages are obtained, the period of quasi constant creep rate for the cases with $l_d < h$ (cases 5, 6) is clearly shorter than those with $l_d \geq h$ (cases 1-4). In other words, the accelerated creep stage occurs earlier. According these results, it is recommended to ensure the condition of $l_d \geq h$ in order to obtain the stable numerical results in both pre- and post-peak regimes.

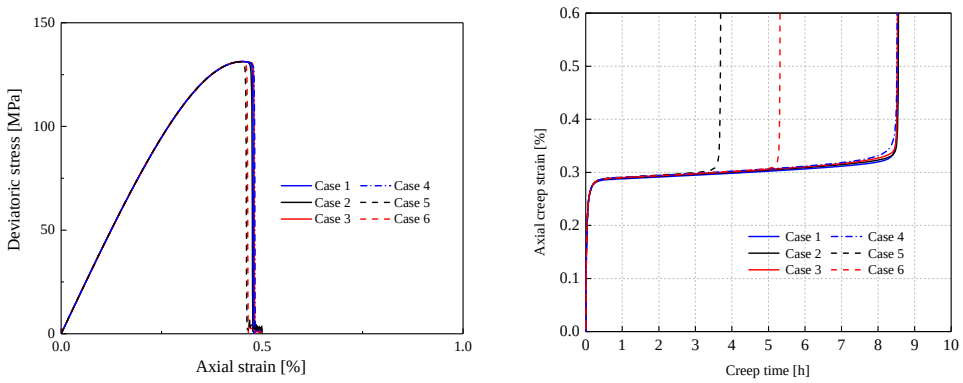

Figure 4.5: Influence of characteristic length and mesh size on overall strain-stress curve in uniaxial compression test (left) and on strain evolution in uniaxial compression creep test (right)

On the other hand, the influence of length scale parameter l_d and mesh size on cracking pattern is also investigated and presented in Figure 4.6. One can clearly see that it is the length parameter l_d that controls the width of localized cracks (damaged zones) rather than the mesh size h. For instance, both the cases 1 and 4 show a very similar distribution of damage variable though they have different element size. At the same time, with the decrease of l_d, the width of localized cracked zones becomes finer from the case 1 to 3.

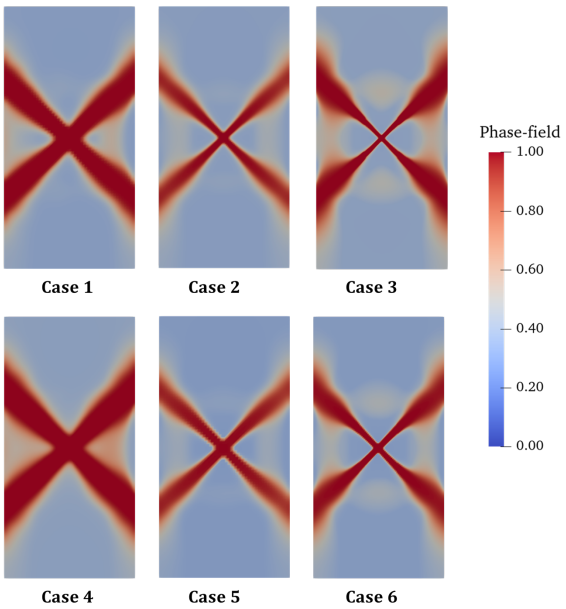

Figure 4.6: Distribution of damage in uniaxial compression creep test in different cases

The coupling effect of viscoplastic flow and damage evolution is considered. Indeed, in the proposed viscoplastic model, the viscoplastic threshold is weakened by the damage growth though the degradation function $g_{vp}(d)$ introduced in the loading function f^{vp} Equation (4.9). Two calculations are performed on the uniaxial creep test by respectively considering that the viscoplastic threshold is affected $g_{vp}(d) = (1-d)^2$ or not affected $g_{vp}(d) = 1$ by the damage evolution. Comparisons between two cases are presented in Figure 4.7. One can see that in the case without degradation, an primary creep is obtained. However, due to the degradation of viscoplastic threshold by damage, three creep stages are observed. The creep strains during the primary stage are much larger than those in the case without degradation. After a period of quasi constant creep rate, an accelerated creep stage occurs and leads to a rapid failure. These results show that the damage degradation effect can play an essential role in time-dependent deformation of rocks.

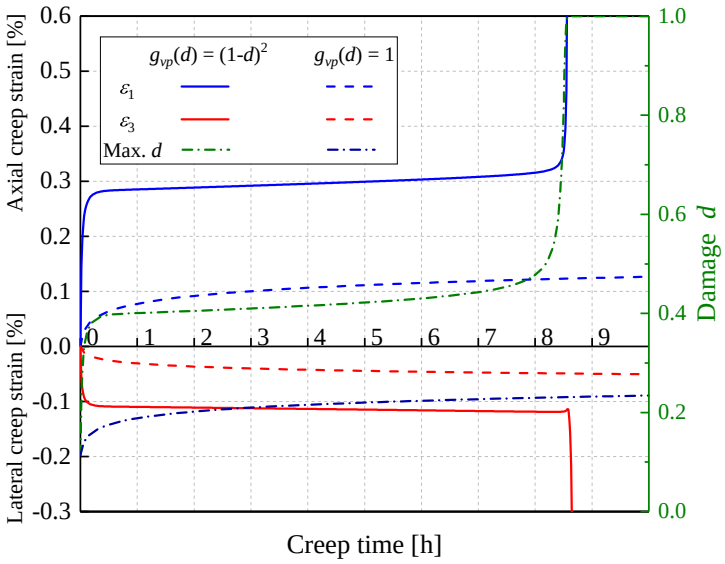

Figure 4.7: Influence of damage degradation effect on viscoplastic flow in uniaxial creep test

In the second example, the influence of critical fracture energy g_c on creep deformation is studied. For this purpose, three different values of g_c ($1.225N/mm$, $1.2375N/mm$, $1.2775N/mm$) are used in simulations of the triaxial creep test with one-step axial loading. Comparisons between three calculations are presented in Figure 4.8 in terms of variations of strains and damage variable. It is obvious that the damage evolution rate is higher when the value of g_c is lower. Accordingly, the rate of creep strains is also en-

hanced by the decrease of critical fracture energy. In the case with $g_c = 1.2375N/mm$, it seems that the damage variable evolves towards a stationary value. In the case with $g_c = 1.225N/mm$, the damage evolution rate evolves to a constant value. Finally, In the case of $g_c = 1.2775N/mm$, the damage evolution rate is accelerated after a period of time and evolves towards to unit, producing an accelerated creep phase. There is a close connection between time-dependent deformation and damage evolution.

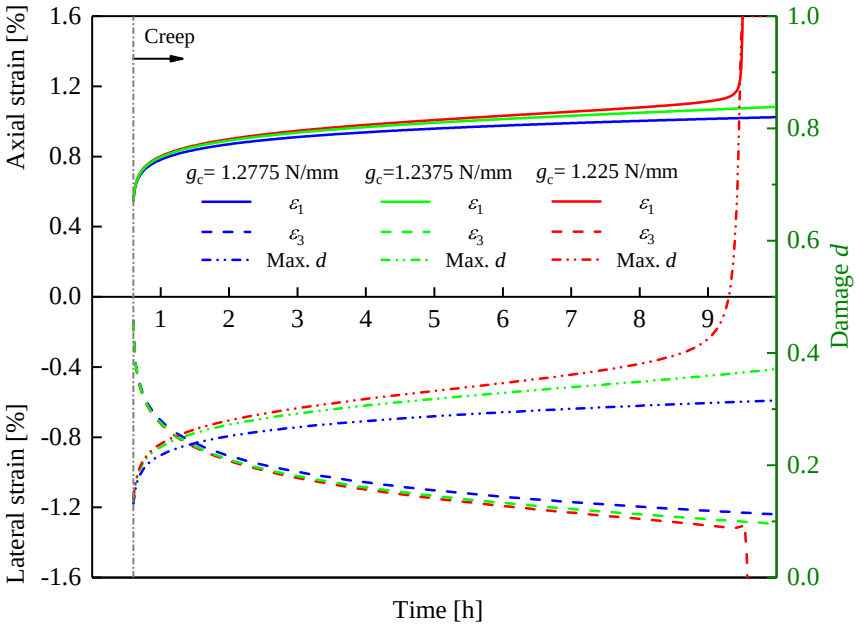

Figure 4.8: Influences of critical fracture energy g_c on time-dependent strains and damage evolution in a triaxial compression creep test with a confining pressure of 30 MPa

Moreover, as a time-dependent viscoplastic phase-field model is used in this study, the time-discretization scheme can affect the obtained numerical results. For this purpose, the sensitivity of creep deformation to the time increment size is here investigated. Four different values of Δt are chosen and compared. The obtained results are presented in Figure 4.9(a). It can be seen that the creep strain curves become almost unchanged when the time increment is less than $1.0s$. As a consequent, the this value of $\Delta t = 1.0s$ is chosen in all calculations of this section. In addition, the influences of two viscoplastic parameters η^{vp} and n on creep strain are also studied. It is shown that η^{vp} mainly controls the initial creep rate during the primary stage. As presented in Figure 4.9(b), higher the value of parameter η^{vp} is, bigger the slope of primary creep curve is. The parameter n

affects the creep rate evolution. On other word, the creep rate reduces quickly when a small value of n is used, as shown in Figure 4.9(c).

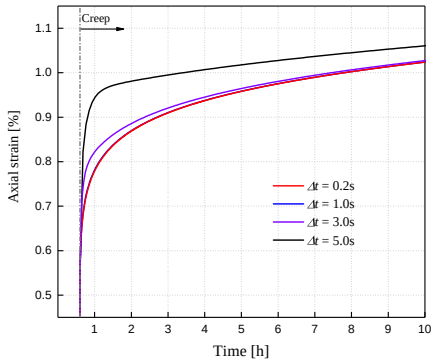

(a) Effect of Δt

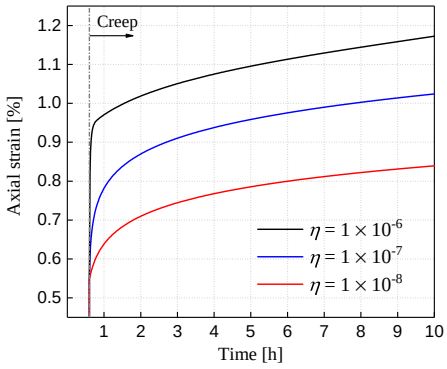

(b) Effect of η^{vp}

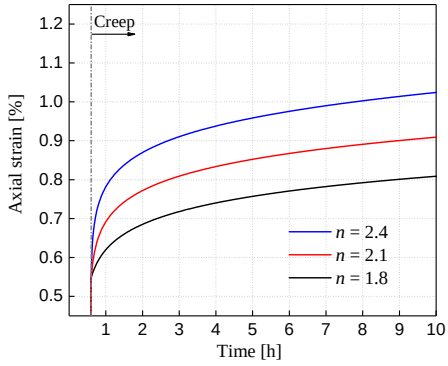

(c) Effect of n

Figure 4.9: Sensitive analysis of time increment and two viscoplastic parameters in a triaxial compression creep test with a confining pressure of 30 MPa

5 Conclusions

In this paper, we have proposed a new phase-field model for modeling the time-dependent cracking process of rocks. The viscoplastic deformation is coupled with the evolution of cracks. More precisely, the viscoplastic flow rate is enhanced by the induced damage through the weakening of creep threshold while the viscoplastic strain energy contributes to the damage evolution. The proposed model has been applied to describe the short and long term mechanical behavior of marble from the left bank of Jinping hydropower station. Numerical results were compared with experimental data from lab-

oratory tests. It was found that the main features of marble mechanical responses were correctly described by the proposed model. The phase-field based model provides an efficient tool for modeling the transition from diffuse damage to localized cracks.

From the results obtained from the present study, it can be concluded that the induced damage is one of the keys mechanisms of brittle rocks such as marble. The macroscopic failure of those rocks is mainly due to the coalescence of micro-cracks leading to macroscopic fractures. The time-dependent evolution of damage or growth of micro-cracks is a key parameter controlling the long-term stability of structures in such rocks. Moreover, there is a strong interaction between viscoplastic deformation and damage evolution.

CHAPTER 5

Phase-field modeling of cracking process in partially saturated porous media

1 Introduction

The main objective of this chapter is to describe the progressive failure of saturated and unsaturated porous media. The whole process starting from diffuse damage to localized macroscopic cracks is described. Therefore, the phase field method seems to be a good choice. As new contributions, we shall propose an improved phase-field model for modeling cracking process in both saturated and unsaturated porous media. Two independent damage variables are used to better describe tensile, shear and mixed cracks. A new evolution criterion is proposed for each damage mechanism by considering the effect of water pore pressure and saturation degree. In particular, the evolution criterion of shear crack is based on an effective stress concept which is continuously valid for both saturated and unsaturated cases. The effect of effective mean stress on rock shear strength is also taken into account. Moreover, the role of material micro-structural heterogeneity on the damage localization process is also incorporated in the new model. The new phase-field model is implemented in a finite element framework for coupled hydro-mechanical and cracking problems.

Throughout the chapter, the following assumptions and simplifications are adopted. We consider here a quasi-static and isothermal hydro-mechanical coupling problem by neglecting the acceleration terms. The fluid flow through a porous continuum is described by the linear Darcy conduction law and mass balance condition. The effect of induced

cracks on the fluid flow is taken into account through the variation of permeability only. It is not envisaged to consider the fluid flow inside individual cracks. The assumption of small strains is adopted. Only two-dimensional plane deformation problems are considered in this paper.

2 Formulation of new phase-field method for dry media

2.1 Regularized cracks surface description by two phase fields

We consider here a solid material occupying the domain Ω and damaged by a set of sharp cracks Γ. In order to conveniently describe tensile and shear cracks in geological materials, inspired by some previous studies (Fei and Choo, 2021; Yu et al., 2021a,b), two independent phase-field (damage) variables d^t and d^s are here adopted. Therefore, the approximated crack surface area for each family of cracks is given by:

$$A_{\Gamma^\alpha} = \int_{\Gamma^\alpha} \mathrm{d}A \cong \int_{\Omega} \gamma^\alpha(d^\alpha, \nabla d^\alpha)\mathrm{d}\Omega, \quad \text{with } \alpha \in \{t, s\} \tag{5.1}$$

Two scalar-valued functions $\gamma^\alpha(\alpha \in \{t, s\})$ denote the tensile and shear crack density. Among various available forms for crack density of phase-field method (Bourdin et al., 2000; Pham et al., 2011; Wu, 2017), the following commonly used one (Bourdin et al., 2000) is here adopted two crack density functions:

$$\gamma^\alpha(d^\alpha, \nabla d^\alpha) = \frac{(d^\alpha)^2}{2l_d} + \frac{l_d}{2}|\nabla d^\alpha|^2, \quad \text{with } \alpha \in \{t, s\} \tag{5.2}$$

$l_d > 0$ denotes a length scale parameter which is in relation with the width of smeared cracks (or localized damage bands). The crack density functions $\gamma^\alpha(\alpha \in \{t, s\})$ are dependent on both damage variables d^α and their gradients ∇d^α. This non-local formulation allows the regularization of damage localization problems. Numerically, it is possible to avoid the suspicious mesh dependency of numerical solutions. Moreover, the crack propagation (or damage evolution) is assumed as an irreversible process, $\dot{d}^\alpha \geq 0$. This leads to the non-negative evolution rate of crack surface density functions defined as:

$$\dot{\gamma}^\alpha = \left(\frac{d^\alpha}{l_d}\right)\dot{d}^\alpha + l_d \nabla d^\alpha \cdot \nabla \dot{d}^\alpha \geq 0, \quad \text{with } \alpha \in \{t, s\} \tag{5.3}$$

2.2 Total energy functional

The emphasis of this study is put on elastic solid materials exhibiting progressive cracking process. The assumption of small strains is throughout assumed. Consequently, one can write the total energy functional E of solid in Ω as the following general form:

$$E(\boldsymbol{\varepsilon}, d^t, d^s) = \int_{\Omega} \psi(\boldsymbol{\varepsilon}, d^t, d^s) \mathrm{d}V + D^{crack} \tag{5.4}$$

ψ is the stored elastic strain energy density per unit volume. The term D^{crack} represents the energy needed to create new crack surfaces.

The mechanical properties of materials are generally affected by the induced cracks. In the case of elasticity, suitable degradation functions are usually introduced to determine the elastic stiffness tensor and strain energy of cracked materials. At the same time, tensile and shear cracks can affect differently the elastic properties of materials. In order to conveniently describe the deterioration of elastic properties, the elastic strain energy is commonly decomposed into several additive parts (Amor et al., 2009; Choo and Sun, 2018; Zhou et al., 2020). Similarly, different decomposition methods are also proposed for stress and strain tensors (Miehe et al., 2010a). In the present work, the elastic strain energy of cracked materials $w(\boldsymbol{\varepsilon})$ is decomposed into a tensile part and a compressive part. It is also assumed that the tensile damage affects the tensile energy part and the shear damage affects the compressive energy part. Therefore, the elastic strain energy of cracked materials is written as:

$$\begin{cases} \psi(\boldsymbol{\varepsilon}, d^t, d^s) = g(d^t) w_+(\boldsymbol{\varepsilon}) + g(d^s) w_-(\boldsymbol{\varepsilon}) \\ w_+(\boldsymbol{\varepsilon}) = \dfrac{1}{2} \boldsymbol{\sigma}_+^0 : \boldsymbol{\varepsilon} \\ w_-(\boldsymbol{\varepsilon}) = \dfrac{1}{2} \boldsymbol{\sigma}_-^0 : \boldsymbol{\varepsilon} \end{cases} \tag{5.5}$$

$\boldsymbol{\sigma}_+^0$ and $\boldsymbol{\sigma}_-^0$ denote the positive and negative cones of the stress tensor $\boldsymbol{\sigma}^0$ acting on the undamaged material. They are classically calculated with the spectral decomposition operators $\mathbb{P}_\sigma^\pm$ widely used in previous researches (Zhang et al., 2020; Yu et al., 2021a):

$$\begin{cases} \boldsymbol{\sigma}_+^0 = \mathbb{P}_\sigma^+ : \boldsymbol{\sigma}^0 \\ \boldsymbol{\sigma}_-^0 = \mathbb{P}_\sigma^- : \boldsymbol{\sigma}^0 \end{cases} \tag{5.6}$$

The stress tensor $\boldsymbol{\sigma}^0$ of the corresponding undamaged material is given by $\boldsymbol{\sigma}^0 = \mathbb{C}^{b0} : \boldsymbol{\varepsilon}$, with $\mathbb{C}^{b0}$ being the elastic stiffness tensor of undamaged bulk material. It is noticed that the decomposition operators verify the condition $\mathbb{P}_\sigma^+ + \mathbb{P}_\sigma^- = \mathbb{I}$, with $\mathbb{I}$ being the fourth order unit tensor. The stress-strain relations of damaged material are then deduced from the elastic strain energy:

$$\boldsymbol{\sigma} = \frac{\partial \psi}{\partial \boldsymbol{\varepsilon}} = g(d^t)\boldsymbol{\sigma}_+^0 + g(d^s)\boldsymbol{\sigma}_-^0 = \mathbb{C}^b(d^t, d^s) : \boldsymbol{\varepsilon} \tag{5.7}$$

The fourth order tensor $\mathbb{C}^b(d^t, d^s)$ defines the elastic stiffness of damaged bulk material, which is given by:

$$\mathbb{C}^b(d^t, d^s) = \left[g(d^t)\mathbb{P}_\sigma^+ + g(d^s)\mathbb{P}_\sigma^- \right] : \mathbb{C}^{b0} \tag{5.8}$$

It is noticed that the stress decomposition method is adopted in this study instead of the strain decomposition one commonly used in previous studies (Miehe et al., 2010a). One of the advantages is that the stress decomposition is suitable to incorporate fluid pressure effect on crack propagation in porous media as shown below. Concerning the damage effects on elastic properties, the most common form of degradation function is here adopted:

$$g(d^\alpha) = \left(1 - d^\alpha\right)^2, \quad \text{with } \alpha \in \{t, s\} \tag{5.9}$$

Based on the Griffith theory (Griffith, 1921; Thomas, 1994), the energy needed for the propagation of cracks is directly related to the crack surface area created, and it is fully dissipated. Therefore, according to the crack surface density given in Equation (5.2), the dissipated energy during cracks growth reads:

$$D^{crack} = \int_\Omega \left[g_c^t \gamma^t(d^t, \nabla d^t) + g_c^s \gamma^s(d^s, \nabla d^s) \right] \mathrm{d}V \tag{5.10}$$

The parameters g_c^t and g_c^s denote the material toughness for the tensile and shear crack respectively.

2.3 Evolution of damage fields

In this work, for the sake of convenience, we assume that each damage mechanism (tensile and shear) is an independent dissipation process. Further, the description of evo-

lution of each damage process is based on the variational approach proposed by Francfort and Marigo (1998), by considering brittle fracture as an energy minimization problem. Similarly, the evolution of each damage field can be determined by minimizing the total energy functional $E(\boldsymbol{\varepsilon}, d^t, d^s)$, with respect to each damage variable. By applying the unilateral stationary condition for the total energy functional with respect to each damage variable, i.e. $\delta E = 0$ for $\delta d^\alpha > 0$ and $\delta E > 0$ for $\delta d^\alpha = 0$ ($\alpha = t, s$) and by calculating the first order variations of E, one obtains the following evolution equations for the two damage fields:

$$\begin{cases} -2(1-d^t)w_+(\boldsymbol{\varepsilon}) + \dfrac{g_c^t}{l_d}d^t - g_c^t l_d div(\nabla d^t) = 0 \\ -2(1-d^s)w_-(\boldsymbol{\varepsilon}) + \dfrac{g_c^s}{l_d}d^s - g_c^s l_d div(\nabla d^s) = 0 \end{cases} \tag{5.11}$$

It is seen that the evolution of shear damage should be controlled by the stored strain energy due to compressive stress $w_-(\boldsymbol{\varepsilon})$. However, it is well known that the shear cracking in rock-like materials is rather induced by the maximum shear stress and influenced by the mean stress (confining pressure in triaxial compression condition). In order to take into account these physical features, a stress-based driving force is here introduced for the evolution of shear damage instead of using $w_-(\boldsymbol{\varepsilon})$. To this end, the widely used Mohr–Coulomb failure criterion is adapted to define such a shear damage driving force. Inspired by previous works (Li et al., 2017; Zhou et al., 2019b; Yu et al., 2021a), the following expression is proposed:

$$w_-(\boldsymbol{\varepsilon}) \Rightarrow w_-^s = \frac{1}{2\mu}\left\langle \frac{\langle\sigma_3\rangle_- - \langle\sigma_1\rangle_-}{2cos\varphi} + \frac{\langle\sigma_3\rangle_- + \langle\sigma_1\rangle_-}{2}tan\varphi - c \right\rangle_+^2 \tag{5.12}$$

σ_1 and σ_3 represent the major and minor principal stresses respectively. c and φ are the cohesion and frictional angle of material. $\langle x\rangle_+ = x$ if $x > 0$ and $\langle x\rangle_+ = 0$ if $x \leq 0$, inversely for $\langle x\rangle_-$.

On the other hand, to ensure irreversible evolution condition of damage field $\dot{\gamma}^\alpha \geq 0$ and $\dot{d^\alpha} \geq 0$ ($\alpha \in \{t, s\}$), the historical driving energy function proposed by Miehe et al. (2010a) is here adopted:

$$\mathcal{H}^t(t) = \max_{\tau\in[0,t]}[w_+(\tau)] \quad \text{and} \quad \mathcal{H}^s(t) = \max_{\tau\in[0,t]}[w_-^s(\tau)] \tag{5.13}$$

Consequently, the governing equations of two damage fields are expressed as:

$$2(1-d^{\alpha})\mathcal{H}^{\alpha} - g_c^{\alpha}\left[\frac{d^{\alpha}}{l_d} - l_d div(\nabla d^{\alpha})\right] = 0, \quad \text{with } \alpha \in \{t, s\} \tag{5.14}$$

3 Extension to partially saturated porous media

3.1 Total energy function for damaged variably saturated porous media

In this section, the phase-field method introduced above is extended to partially saturated porous media. In general case, pores are filled with at least two fluid phases such as liquid (water) and gas (dry air). In the context of landslides, the gas phase is general in contact with the atmosphere and the consequence of gas pressure change is much less important than that of water. Therefore, it is usual to neglect the air pressure change. The water pressure can be positive in saturated condition or negative in unsaturated one. In this case, the capillary pressure becomes $p_c = -p_w$. With this assumption in hand, the poroelastic constitutive model for the undamaged material can be written as follows (Coussy, 2010):

$$\begin{cases} \mathrm{d}\boldsymbol{\sigma}^0 = \mathbb{C}^{b0} : \mathrm{d}\boldsymbol{\varepsilon} - bS_w \mathrm{d}p_w \mathbf{I} \\ \mathrm{d}p_w = M_{ww}\left[- bS_w \mathrm{d}\varepsilon_v + \left(\frac{\mathrm{d}m}{\rho}\right)_w\right] \end{cases} \tag{5.15}$$

p_w denotes water pressure. m_w and ρ_w represent the water mass change per unit volume and volumetric mass. b and M_{ww} are Biot's coefficient and modulus. $\varepsilon_v = \boldsymbol{\varepsilon} : \mathbf{I}$ denotes the volume strain. S_w is water saturation degree. From the first relation of Equation (5.15), it is possible to obtain an effective stress which is the thermodynamic force conjugate to the strain tensor. It is conventionally called the Bishop's effective stress (Bishop, 1959) and here defined in the following incremental form:

$$\mathrm{d}\boldsymbol{\sigma}^{b0} = \mathrm{d}\boldsymbol{\sigma}^0 + bS_w \mathrm{d}p_w \mathbf{I} = \mathbb{C}^{b0} : \mathrm{d}\boldsymbol{\varepsilon} \tag{5.16}$$

The accumulated value of $\boldsymbol{\sigma}^{b0}$ is calculated incrementally as the value of S_w evolve with time. Moreover, the water saturation S_w can be related to the capillary pressure p_c through the water retention curve. Among various forms available, the widely used form initially

proposed by van Genuchten (1980) is here adopted:

$$S_w = S_r + S_e(1 - S_r), \quad S_e = \left[1 + \left(\frac{p_c}{p_{cr}}\right)^n\right]^{-m}, \quad p_c \geq 0 \tag{5.17}$$

where S_r is the residual degree of saturation, p_{cr} is a critical reference pressure, n and $m(= 1 - 1/n)$ are model's parameters.

Due to the presence of fluid, the stored energy ψ can be conveniently seen as the sum of elastic strain energy of porous medium and that related to fluid mass change. Accordingly, the total energy functional E is rewritten in the following general form:

$$E(\boldsymbol{\varepsilon}, m_w, m_{nw}, d^t, d^s) = \int_\Omega \left[\psi^{pm}(\boldsymbol{\varepsilon}, d^t, d^s) + \psi^{fl}(\boldsymbol{\varepsilon}, m_w, d^t, d^s)\right] \mathrm{d}V + D^{crack} \tag{5.18}$$

The stored elastic energy of porous medium ψ^{pm} can be expressed as a function of the Bishop effective stress. As for dry medium, this part of energy is affected by the two damage variables d^t and d^s, one gets:

$$\begin{cases} \psi^{pm}(\boldsymbol{\varepsilon}, d^t, d^s) = g(d^t) w_+^{b0}(\boldsymbol{\varepsilon}) + g(d^s) w_-^{b0}(\boldsymbol{\varepsilon}) \\ w_+^{b0}(\boldsymbol{\varepsilon}) = \dfrac{1}{2} \boldsymbol{\sigma}_+^{b0} : \boldsymbol{\varepsilon} \\ w_-^{b0}(\boldsymbol{\varepsilon}) = \dfrac{1}{2} \boldsymbol{\sigma}_-^{b0} : \boldsymbol{\varepsilon} \end{cases} \tag{5.19}$$

The positive and negative cones of the Bishop's effective stress are calculated by using the same projection operators as those given in Equation (5.6), say $\boldsymbol{\sigma}_+^{b0} = \mathbb{P}_\sigma^+ : \boldsymbol{\sigma}^{b0}$ and $\boldsymbol{\sigma}_-^{b0} = \mathbb{P}_\sigma^- : \boldsymbol{\sigma}^{b0}$. The total stress tensor increment of damaged porous media is finally given by:

$$\mathrm{d}\boldsymbol{\sigma} = \mathbb{C}^b(d^t, d^s) : \mathrm{d}\boldsymbol{\varepsilon} - bS_w \mathrm{d}p_w \mathbf{I} \tag{5.20}$$

In general case, the energy due to fluid mass change $\psi^{fl}(\boldsymbol{\varepsilon}, m_w, d^t, d^s)$ is also affected by two damage processes. However, this will induce a high complexity in damage evolution equations (Heider and Markert, 2017; Heider and Sun, 2020). In many previous studies (Miehe et al., 2015b; Miehe and Mauthe, 2016; Aldakheel et al., 2021), it was found that the role of fluid free energy in the cracking process was quite limited. In the case of partially saturated media, according to preliminary results, the damage evolution processes are mainly controlled by stress (strain) state and water pressure. Therefore, the

contribution of the fluid energy to the damage evolution can be neglected. Thus, one has:

$$\psi^{fl}(\boldsymbol{\varepsilon}, m_w, d^t, d^s) \equiv \psi^{fl}(\boldsymbol{\varepsilon}, m_w) = \frac{1}{2} M_{ww} \left[bS_w \varepsilon_v - \left(\frac{m}{\rho} \right)_w \right]^2 \tag{5.21}$$

The energy dissipated during crack creation D^{crack} remains unchanged with respect to the dry medium.

On the other hand, the physically based driving energy for the shear damage evolution w_-^s given in Equation (5.12) for dry materials is also extended to partially saturated media by taking into account the effect of water pressure. Indeed, the Bishop effective stresses are now used. One obtains:

$$w_-^{bs} = \frac{1}{2\mu} \left\langle \frac{\langle \sigma_3^b \rangle_- - \langle \sigma_1^b \rangle_-}{2cos\varphi} + \frac{\langle \sigma_3^b \rangle_- + \langle \sigma_1^b \rangle_-}{2} tan\varphi - c \right\rangle_+^2 \tag{5.22}$$

σ_1^b and σ_3^b are the Bishop effective major and minor principal stresses. Accordingly, the energy history functionals for two damage mechanisms of partially saturated media become:

$$\mathcal{H}^t(t) = \max_{\tau \in [0,t]} [w_+^{bs}(\tau)] \quad \text{and} \quad \mathcal{H}^s(t) = \max_{\tau \in [0,t]} [w_-^{bs}(\tau)] \tag{5.23}$$

These new expressions of energy history functionals are used in the governing equations of two damage fields given in Equation (5.14) for partially saturated media.

3.2 Governing equations for hydro-mechanical fields

Based on the assumptions mentioned above, the mechanical problem is governed by the static balance equations:

$$\text{div}(\boldsymbol{\sigma}) + \vec{f_b} = 0 \tag{5.24}$$

$\vec{f_b}$ denotes mechanical body force.

By considering Darcy's conduction law, the fluid mass balance equation and the constitutive relations given in Equation (5.15), the fluid diffusivity equation is expressed as:

$$\frac{k_r k_p}{\mu_w} \text{div}\left(\nabla p_w - \rho_w \vec{g}\right) = \frac{1}{M_{ww}} \frac{\mathrm{d}p_w}{\mathrm{d}t} + bS_w \frac{\mathrm{d}\varepsilon_v}{\mathrm{d}t} \tag{5.25}$$

where k_p denotes the saturated permeability, μ_w represents the dynamic water viscosity,

and $\vec{g}$ the gravitational acceleration. The relative permeability of partially saturated media, k_r, is proportional to the saturation degree S_w. The specific form of such a relation should be identified form experimental data. In this study, the following widely used relation is adopted:

$$k_r = \sqrt{S_w}\left[1 - \left(1 - S_w^{1/m}\right)^m\right]^2 \tag{5.26}$$

The Biot's modulus of pore water is given by:

$$\frac{1}{M_{ww}} = \frac{S_w^2(b-\phi)}{\kappa_s} + \frac{S_w\phi}{\kappa_w} - \phi\frac{\partial S_w}{\partial p_c} \tag{5.27}$$

in which ϕ is the porosity.And κ_s and κ_w represent the bulk moduli of solid skeleton and water respectively.

3.3 Influence of cracking on fluid flow

It is known that the presence of open cracks enhances the permeability of porous media. However, in the framework of phase-field method, sharp cracks are approximated by localized damaged zones. Though some approximate methods have been suggested to estimate the opening of crack from damage field (Lee et al., 2017; Yoshioka et al., 2020), they are not easy to implement and usually dependent on mesh configuration. As an alternative approach, the permeability in damaged zones can be expressed as a function of damage variable (Heider and Markert, 2017; Yu et al., 2021a). As the permeability change is mainly controlled by open cracks, it is assumed that it depends on the tensile damage d^t only. Further, inside the fully cracked zones with $d^t \Rightarrow 1$, the porosity should also tend towards the unity $\phi \Rightarrow 1$. Then, the porosity inside the damaged zones is also a function of tensile damage. Moreover, when a tensile crack is closed, the value of d^t remains stationary. But its effect on permeability and porosity vanishes. This unilateral effect is also taken into account. A simplified opening-closure criterion is here adopted. When the volumetric strain is positive, the crack is considered as open. Otherwise, the crack is closed. Therefore, the following empirical relations are proposed to describe the

changes of permeability and porosity:

$$\begin{cases} k_p(d^t) = k_p^0 \exp\left(\left\langle \dfrac{\varepsilon_v}{|\varepsilon_v|} \right\rangle \beta d^t\right) \\ \phi(d^t) = \phi^0 + \left\langle \dfrac{\varepsilon_v}{|\varepsilon_v|} \right\rangle (1-\phi^0) d^t \end{cases} \tag{5.28}$$

where k_p^0 and ϕ^0 are the initial values of permeability and porosity. The parameter β controls the evolution of permeability. The operator $\langle x \rangle$ denotes $\langle x \rangle = x$ if $x \geq 0$, otherwise $\langle x \rangle = 0$.

4 Numerical implementation in finite element method

The numerical implementation procedure for solving the coupled hydro-mechanical and damage problem with the proposed phase field model is summarized in this section.

4.1 Weak form

In this work, the classical finite element method is employed to solve the coupled hydro-mechanical and damage problem. By using the standard Galerkin procedure with the test functions $\delta \boldsymbol{u}$, δp_w and δd^α respectively, one can transform the governing functions Equations (5.14), (5.24) and (5.25) to the weak forms for the hydro-mechanical coupling problem:

$$\begin{cases} \displaystyle\int_\Omega \left[\nabla(\delta \boldsymbol{u}) : \left[\mathbb{C}(d^t, d^s) : \nabla \boldsymbol{u} - S_w b p_w \mathbf{I}\right]\right] \mathrm{d}\Omega = \int_{\partial\Omega} \delta \boldsymbol{u} : \vec{T} \mathrm{d}S + \int_\Omega \delta \boldsymbol{u} : \vec{f}_b \mathrm{d}\Omega \\ \displaystyle\int_\Omega \left[\nabla(\delta p_w) : \frac{k_r \boldsymbol{k}_p(d^t)}{\mu_w} : \left(\nabla p_w - \rho_w \vec{g}\right)\right] \mathrm{d}\Omega + \int_\Omega \delta p_w \cdot \frac{1}{M_{ww}} \dot{p}_w \mathrm{d}\Omega \\ \displaystyle + \int_\Omega \delta p_w \cdot S_w b \mathbf{I} : \nabla \dot{\boldsymbol{u}} \mathrm{d}\Omega = \int_{s_\omega} \delta p_w \cdot -\vec{\omega} \cdot \vec{n} dS \end{cases} \tag{5.29}$$

and for two damage evolution problems:

$$\begin{cases} \displaystyle\int_\Omega \left[(g_c^t\, l_d + 2\mathcal{H}^t)\delta d^t \cdot d^t + g_c^t l_d \nabla(\delta d^t) : \nabla(d^t)\right] \mathrm{d}\Omega = \int_\Omega \delta d^t \cdot 2\mathcal{H}^t \mathrm{d}\Omega \\ \displaystyle\int_\Omega \left[(g_c^s\, l_d + 2\mathcal{H}^s)\delta d^s \cdot d^s + g_c^s l_d \nabla(\delta d^s) : \nabla(d^s)\right] \mathrm{d}\Omega = \int_\Omega \delta d^s \cdot 2\mathcal{H}^s \mathrm{d}\Omega \end{cases} \tag{5.30}$$

4.2 Geometrical discretization

The studied structure domain Ω is divided into a finite number of elements based on the standard Bubnov-Galerkin approach. The solution target is here transformed to determine the set of nodal values of displacement components (denoted by the vector $\mathbf{U}$), pore water pressure (denoted by the vector $\mathbf{P}$) and those of damage variables (denoted by the vector $\mathbf{d}^{\alpha}, \alpha = t, s$). The distributions of these unknowns inside each element are then approximated in terms of their nodal values by using suitable shape functions, namely as:

$$\begin{aligned} \boldsymbol{u}(\boldsymbol{x}) &= \mathbf{N}_u(\boldsymbol{x})\mathbf{U}^e \quad p_w(\boldsymbol{x}) = \mathbf{N}_p(\boldsymbol{x})\mathbf{P}^e \quad d(\boldsymbol{x}) = \mathbf{N}_d(\boldsymbol{x})\mathbf{d}^e \\ \boldsymbol{\varepsilon}(\boldsymbol{x}) &= \mathbf{B}_u(\boldsymbol{x})\mathbf{U}^e \quad \nabla p_w(\boldsymbol{x}) = \mathbf{B}_p(\boldsymbol{x})\mathbf{P}^e \quad \nabla d(\boldsymbol{x}) = \mathbf{B}_d(\boldsymbol{x})\mathbf{d}^e \end{aligned} \tag{5.31}$$

where $\mathbf{N}_u(\boldsymbol{x})$, $\mathbf{B}_u(\boldsymbol{x})$, $\mathbf{N}_p(\boldsymbol{x})$, $\mathbf{B}_p(\boldsymbol{x})$ and $\mathbf{N}_d(\boldsymbol{x})$, $\mathbf{B}_d(\boldsymbol{x})$ are the matrices of shape functions and their derivatives for the displacement field, water pressure and damage fields, respectively. It should be noticed that the choice of shape functions $\mathbf{N}_u(\boldsymbol{x})$ and $\mathbf{N}_p(\boldsymbol{x})$ has a significant effect on the stability of solution procedure (Cajuhi et al., 2018; Gavagnin et al., 2020). Inspired by previous studies (Zienkiewicz, 2001) and in order to satisfy the so-called Ladyzhenskaya–Babuška–Brezzi condition, quadratic shape functions for the displacement and linear shape functions for the pore pressure and two damage variables (Taylor-Hood pair P2-P1) are here adopted.

With the geometrical discretization, the integral weak forms of the hydro-mechanical coupling problem can be rewritten as:

$$\begin{bmatrix} \mathbf{R}_{uu} & \mathbf{C}_{up} \\ \mathbf{0} & \mathbf{R}_{pp} \end{bmatrix} \begin{bmatrix} \mathbf{U} \\ \mathbf{P} \end{bmatrix} + \begin{bmatrix} \mathbf{0} & \mathbf{0} \\ \mathbf{C}_{pu} & \mathbf{M}_{pp} \end{bmatrix} \begin{bmatrix} \dot{\mathbf{U}} \\ \dot{\mathbf{P}} \end{bmatrix} = \begin{bmatrix} \mathbf{F}_u \\ \mathbf{F}_{\omega} \end{bmatrix} \tag{5.32}$$

in which:

$$\begin{cases} \mathbf{R}_{uu} = \int_{\Omega}(\mathbf{B}_u^T)\mathbb{C}(d^t, d^s)\mathbf{B}_u \mathrm{d}\Omega \\ \mathbf{C}_{up} = \int_{\Omega}(\mathbf{B}_u^T)(-S_w b\mathbf{I})\mathbf{N}_p \mathrm{d}\Omega \\ \mathbf{F}_u = \int_{\partial\Omega}(\mathbf{N}_u^T)\vec{T}\mathrm{d}S + \int_{\Omega}(\mathbf{N}_u^T)\vec{f}_b \mathrm{d}\Omega \\ \mathbf{R}_{pp} = \int_{\Omega}(\mathbf{B}_p^T)(k_r \boldsymbol{k}_p(d^t)/\mu_w)\mathbf{B}_p dV \\ \mathbf{M}_{pp} = \int_{\Omega}(\mathbf{N}_p^T)(\frac{1}{M_{ww}})\mathbf{N}_p dV \\ \mathbf{C}_{pu} = \int_{\Omega}(\mathbf{N}_p)(S_w b\mathbf{I})(\mathbf{B}_u^T)\mathrm{d}\Omega \\ \mathbf{F}_{\omega} = \int_{\Omega}(\mathbf{B}_p^T)\left[\frac{k_r \boldsymbol{k}_p(d^t)}{\mu_w}\rho_w \vec{g}\right]\mathrm{d}\Omega - \int_{s_{\omega}}(\mathbf{N}_p^T)\vec{\omega}_{n+1}.\mathbf{n}dS \end{cases}$$

Similarly, one gets the linear system of equations for the tensile damage field:

$$\begin{cases} \mathbf{K}_{d^t}\mathbf{d}^t = \mathbf{F}_{d^t} \\ \mathbf{K}_{d^t} = \int_\Omega \left[(g_c^t\, l_d + 2\mathcal{H}^t)\mathbf{N}_d^T\mathbf{N}_d + g_c^t l_d \mathbf{B}_d^T\mathbf{B}_d\right] \mathrm{d}\Omega \\ \mathbf{F}_{d^t} = \int_\Omega 2\mathcal{H}^t\mathbf{N}_d^T \mathrm{d}\Omega \end{cases} \tag{5.33}$$

and for the shear damage field:

$$\begin{cases} \mathbf{K}_{d^s}\mathbf{d}^s = \mathbf{F}_{d^s} \\ \mathbf{K}_{d^s} = \int_\Omega \left[(g_c^s\, l_d + 2\mathcal{H}^s)\mathbf{N}_d^T\mathbf{N}_d + g_c^s l_d \mathbf{B}_d^T\mathbf{B}_d\right] \mathrm{d}\Omega \\ \mathbf{F}_{d^s} = \int_\Omega 2\mathcal{H}^s\mathbf{N}_d^T \mathrm{d}\Omega \end{cases} \tag{5.34}$$

4.3 Time discretization

The total loading history (designed by the total time T) is divided into a number of incremental steps such as $t = 0, t_1, ..., t_n, t_{n+1}, ..., T$. For the current loading step $n+1$, the time increment is denoted as $\Delta t = t_{n+1} - t_n$. The time discretization of unknowns is carried out by the generalized trapezoidal method (Lewis et al., 1998), which transforms the systems of Equations (5.32) to (5.34) into the following forms:

$$\begin{aligned} &\begin{bmatrix} \chi\mathbf{R}_{uu} & \chi\mathbf{C}_{up} \\ \mathbf{C}_{pu} & \Delta t\chi\mathbf{R}_{pp} + \mathbf{M}_{pp} \end{bmatrix} \begin{bmatrix} \mathbf{U} \\ \mathbf{P} \end{bmatrix}^{n+1} \\ &\quad = \begin{bmatrix} (\chi-1)\mathbf{R}_{uu} & (\chi-1)\mathbf{C}_{up} \\ \mathbf{C}_{pu} & \mathbf{M}_{pp} - (1-\chi)\Delta t\mathbf{R}_{pp} \end{bmatrix} \begin{bmatrix} \mathbf{U} \\ \mathbf{P} \end{bmatrix}^{n} + \begin{bmatrix} \mathbf{F}_u \\ \Delta t\mathbf{F}_\omega \end{bmatrix} \end{aligned} \tag{5.35}$$

and,

$$\begin{cases} \mathbf{K}_{d^t}\mathbf{d}_{n+1}^t = \mathbf{F}_{d^t} \\ \mathbf{K}_{d^s}\mathbf{d}_{n+1}^s = \mathbf{F}_{d^t} \end{cases} \tag{5.36}$$

The coefficient $0 \leq \chi \leq 1$ is used to adopt a suitable time integration scheme. In order to better describe the transition from unsaturated to saturated state due to rainfall, an implicit integration with $\chi = 1$ is here adopted.

4.4 Staged coupling algorithm

The hydro-mechanical solutions (displacement, water pressure, strains and stresses) are strongly coupled with the damage evolution. According to many previous studies, it is generally hard to solve these problems in a fully coupled way. Different types of numerical algorithms have been proposed to efficiently solve such coupled problems (Bourdin et al., 2008; Gerasimov and De Lorenzis, 2016; Wu et al., 2020a; Mandal et al., 2021). Among those, a staggered scheme (named as Alternate Minimization method) (Bourdin et al., 2000, 2008) has shown its robustness and it is widely used in phase field problems. More precisely, two solution steps are successively performed at the k^{th} iteration of a specific loading step $n+1$. This is summarized as follows:

I) Solving the coupled displacement-pressure problems $\mathbf{U}_{n+1}^{k}$ and $\mathbf{P}_{n+1}^{k}$ with the constant damage values $\boldsymbol{d}_{n+1}^{\alpha,k-1}$ obtained from the last iteration;

II) Solving the damage problems $\boldsymbol{d}_{n+1}^{\alpha,k}$ using the updated energy history functions with the displacement field $\mathbf{U}_{n+1}^{k}$ and water pressure field $\boldsymbol{P}_{n+1}^{k}$;

These two steps are repeated until the convergence criterion $\|\boldsymbol{d}_{n+1}^{\alpha,k} - \boldsymbol{d}_{n+1}^{\alpha,k-1}\| \leq \epsilon$ is verified. According to (Ambati et al., 2015), a convergence tolerance is taken as $\epsilon = 1 \times 10^{-5}$.

5 Analysis of triaxial compression test

In this section, we shall verify the ability of the proposed model to describe the basic mechanical behavior of brittle rocks under compressive stress, in particular the process of initiation and localization of cracks. For this purpose, the experimental data from conventional triaxial compression tests on sandstone reported in (Jia et al., 2020) are selected. The effect of heterogeneous distribution of porosity on the onset and propagation of cracks is also investigated. However, it is worth noticing that the simulations presented here do not constitute a real validation of the proposed model. Indeed, the numerical results are not only related to the model used but also to the set of input parameters (Babuska and Oden, 2004). In general, the set of experimental data for the identification of parameters and for the validation of the model should be different and independent. If possible, some comparisons with analytical solutions are also needed. Unfortunately, the data set is quite limited for the studied material for a full validation of the model. At the

same time, due to the progressive localization of damage fields, it appears very hard to get analytical solutions. New experimental data should be collected in our future work.

5.1 Description of numerical model

The tested sandstone was collected from the dam site of a hydropower plant in Southwest China. The mineralogical compositions were determined with the X-ray diffraction method in the previous studies (Yu et al., 2019; Jia et al., 2020). This rock is mainly composed of quartz (55%), feldspar (25%), sandy and clay detritus (20%). The solid grains constitute a quasi continuous matrix phase and the majority of pores are embedded in such a matrix phase. As a first approximation, the sandstone can be seen as a porous medium constituted of an equivalent solid matrix and embedded pores. The classical Mori-Tanaka scheme (Mori and Tanaka, 1973) seems to be suitable to estimate the effective elastic properties of such a porous medium. The macroscopic bulk κ^{hom} and shear μ^{hom} moduli are given by Equation (3.29). The values for the studied sandstone are presented in Table 5.1.

As the porosity has a direct influence on the macroscopic elastic behavior of sandstone, it is used as the micro-structural parameter to represent the material heterogeneity. For this purpose, the standard Weibull distribution Equation (3.30) is adopted to describe the random distribution of porosity ϕ.

In this study, five numerical specimens with different values of heterogeneity index ($m_i = 1.1,\ 1.5,\ 2,\ 5,\ 10$) are selected in this study. The size of samples is $50 \times 100\ mm$. The corresponding spatial distributions of porosity and related Young's modulus are presented in Figure 5.1.

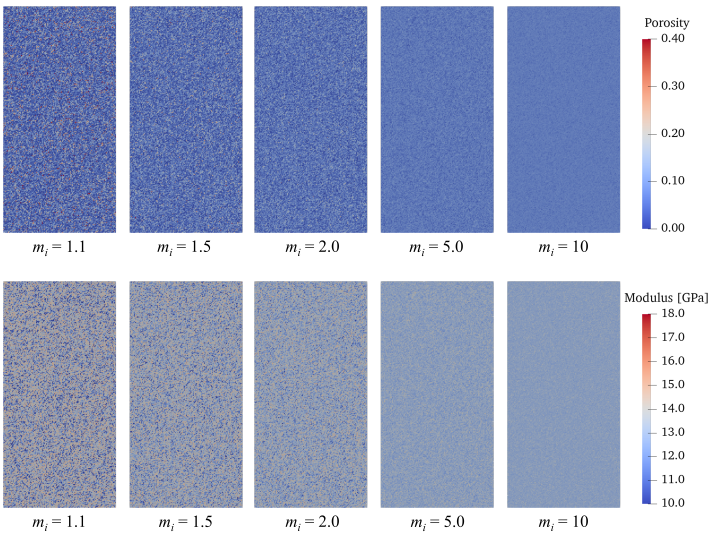

Figure 5.1: Spatial distributions of porosity and corresponding macroscopic elastic modulus for five values of m_i

In the present phase field model, four other parameters controlling two damage processes should also be determined. The values of tensile crack toughness g_c^t is generally estimated from the macroscopic uniaxial tensile strength while that of g_c^s from the uniaxial compression strength. The values of cohesion and friction parameter c and φ can be evaluated from the macroscopic compression strength envelop for different values of confining stresses. The reference values of these parameters are given in Table 5.1.

Table 5.1
Input parameters for sandstone

Parameters	Unit	Value	Parameters	Unit	Value
Matrix bulk modulus κ_s	GPa	3.125	Matrix shear modulus μ_s	GPa	6.25
Average porosity $\bar{\phi}$	$\%$	8.43	Smeared crack length l_d	mm	0.5
Tensile crack energy g_c^t/l_d	N/m^2	1.4×10^3	Shear crack energy g_c^s/l_d	N/m^2	2.4×10^3
Cohesion c	MPa	0.38	Frictional angle φ	$^\circ$	49.44

5.2 Stress-strain curves and failure pattern

A series of numerical calculations are performed on selected heterogeneous samples.It is worth noticing that conventional triaxial compression tests are performed on cylindrical samples. The geometry and applied stresses verify the axisymmetric conditions. But due to the localization of strains and damage, the obtained crack patterns are almost never axisymmetric. In the ideal situation, full three-dimensional calculations should be performed. However, for the sake of simplicity, two-dimensional plane strain calculations are widely conducted for modeling triaxial tests. Two types of comparisons are considered: a quantitative comparison of overall stress-strain curves, and a rather qualitative comparison of crack patterns. In our study, two-dimensional plane strain calculations are also performed, as for many previous studies. Each sample is divided into 40000 triangular elements. The reference value of material length scale parameter is selected as l_d = 0.5 mm.

Among five samples shown in Figure 5.1, the sample with $m_i = 10$ has the smallest heterogeneity of porosity. It is first used to present the studied sandstone. In Figure 5.2,

one shows the comparisons of global stress-strain curves between the phase-field model and the experimental data for two values of confining stress (Jia et al., 2020). The basic mechanical behavior of sandstone is well reproduced by the proposed model both in the pre- and post-peak regimes. The influence of confining stress on the mechanical strength is also well captured.

In order to follow the progressive cracking process, four representative points are selected on the stress-strain curves in Figure 5.2 (a, b, c and d). The distributions of two damage variables at these loading points for a confining stress of 5MPa are shown in Figure 5.3. At the loading step (a), although the differential stress is at the peak value, the damage values are moderate and clearly less than 1. But there is a rapid increase of damage state during the subsequent three loading steps. Moreover, localized cracks (damage concentration bands) appear more and more clearly. Finally, one obtains two major macroscopic cracks. The apparition of these cracks leads to a fast decrease of differential stress and material softening. It is worth noticing that in many previous studies on cracking modeling with phase field method, in order to facilitate the onset of damage or strain localization, an artificial weak zone was introduced (Fei and Choo, 2020b; Yu et al., 2021b). In our study, the macroscopic elastic properties are not uniform in the sample due to the spatial variability of porosity. There is no need to introduce such an artificial weak zone. The onset and propagation of localized cracks are physically affected by the material heterogeneity. It is also interesting to notice that although compressive stresses are applied, both tensile and shear cracks are observed. Indeed, due to the non-uniform distribution of porosity and strains, the stress field is also non-uniform and local tensile zones can be obtained.

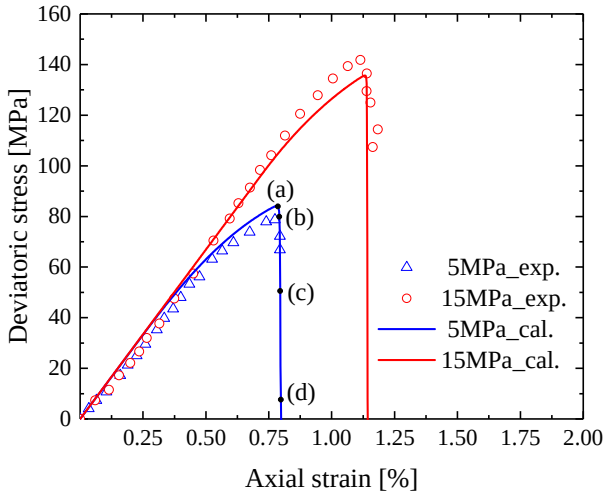

Figure 5.2: Axial strain versus differential stress curves for the specimen with $m_i = 10$ under two values of confining stress: comparisons between numerical results and experimental data (Jia et al., 2020)

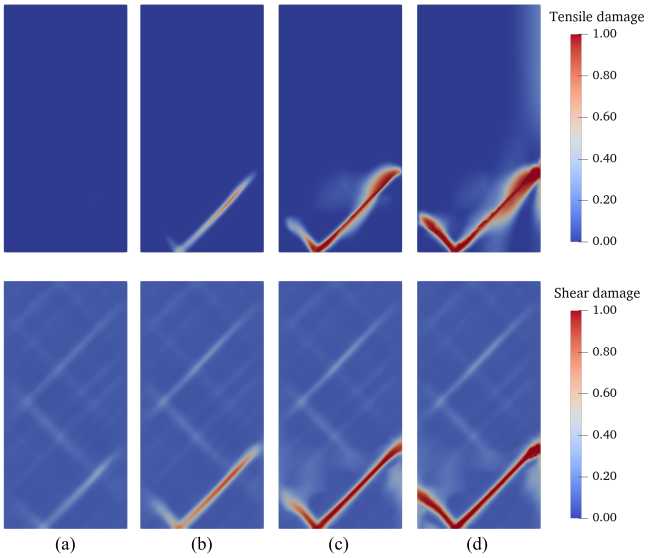

Figure 5.3: Distributions of tensile and shear damage in the specimen with $m_i = 10$ at four different loading steps (see Figure 5.2) during a triaxial compression test with 5 MPa confining stress

5.3 Sensitivity analysis

Comparative calculations are presented here in order to investigate the effects of some key parameters on the mechanical responses of rock, in particular, the heterogeneity index, mesh size and scale length parameter.

The influence of material heterogeneity m_i on the mechanical behavior of sandstone is investigated by comparing the numerical results obtained with five different samples presented in Figure 5.1. The predicted axial strain versus differential stress curves are presented in Figure 5.4 for a triaxial compression test under a confining stress of 5 MPa. It is shown that the macroscopic mechanical responses can be influenced by the material heterogeneity. The peak differential stress is lower when the material heterogeneity is stronger (lower value of m_i). This indicates that the non-uniform distribution of porosity can enhance the growth of micro-cracks. In Figure 5.5, the corresponding distributions of damage fields in five numerical specimens are presented at the state of peak differential stress. The cracking pattern is also affected by the material heterogeneity. But for all the cases, the macroscopic failure is always driven by the formation of some major localized cracks.

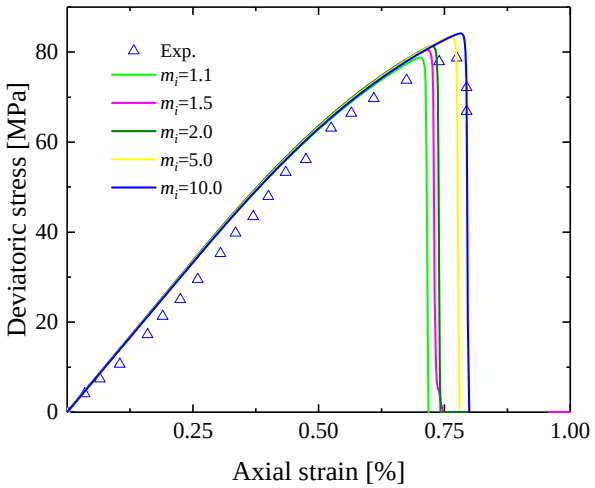

Figure 5.4: Axial strain versus differential stress curves for five samples with different values of heterogeneity index m_i in a triaxial compression test with 5 MPa confining stress

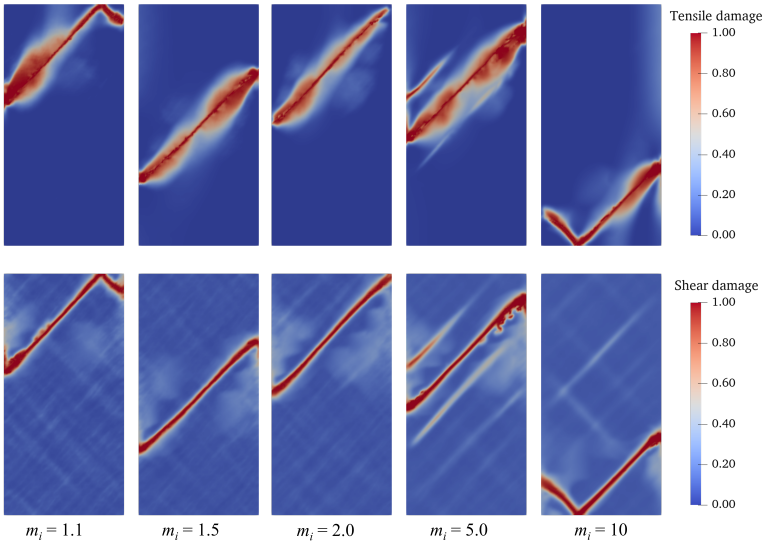

Figure 5.5: Distributions of tensile and shear damages in five heterogeneous samples in a triaxial compression test with 5MPa confining stress

The influences of mesh size and scale length are also studied. Five cases with different values of minimum element size h^e and scale length l_d are considered and presented in Table 5.2. In many previous studies (Miehe et al., 2010b; Wang et al., 2022), the ratio h^e/l_d is usually higher than 1. Therefore, by setting the ratio to $h^e/l_d = 1$, the influence of l_d is here studied in the cases 1 to 3. According to the results shown in Figure 5.6, it is found that the width of localized cracks becomes larger with the increase of l_d. In the case 4 and case 5, the characteristic length is fixed to $l_d = 0.5mm$ while two different values of minimum element size are considered. One can see that the width of localized cracks is not affected by the mesh size. The distribution of localized cracks is affected by the material heterogeneity. Comparing with the cases 1 to 3, it is clear that the width of localized cracks is controlled by l_d and quasi independent on mesh size.

Table 5.2
Different sets of parameters for sensitivity study of mesh size and scale length parameter in triaxial compression test

Case No.	l_d (mm)	h^e (mm)	Case No.	l_d (mm)	h^e (mm)
1	1.0	1.0	4	0.5	1.0
2	0.5	0.5	5	0.5	0.25
3	0.25	0.25			

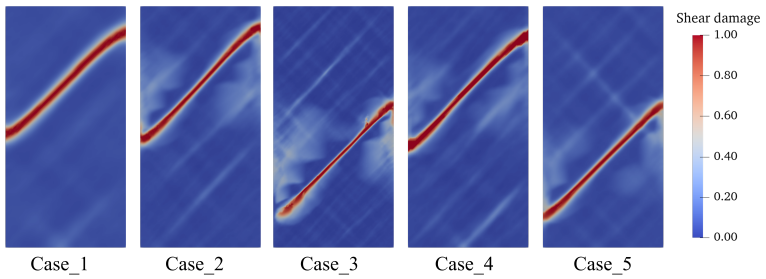

Figure 5.6: Distributions of shear damage in a triaxial compression test with 5MPa confining stress for five cases

6 Desaturation of a sand column

In this section, we aimed to validate the hydro-mechanical coupling procedure by comparing the numerical simulation of drainage test on a sand column with the experiment conducted by Liakopoulos (1964). In the preliminary phase of the original experimental test ($t < 0$), a column of perspex was filled with Del Monte sand in height of 1.0 m and constrained the lateral sides by rigid and impervious wall. This sand column was saturated by adding water from the top and allowed to drain freely at the bottom until the uniform wero water pressure was observed throughout the sand column ($t = 0$). Then, the experiment concerned outflow of water from the bottom of this sand column due to the gravity and measured the water pressures at different height along the sand column.

In order to reproduce the condition of the experiment, the geometry and mechanical boundary conditions are presented in Figure 5.7. The column is discretized in 320 structured triangular elements. To modeling the initial hydraulic experimental conditions ($t < 0$), a homogeneous water pressure field $p_w = 0$ is specified before the desaturation. The lateral sides are set to be impervious. Due to the gravity, the water outflows at the bottom. For this reason, the water pressure on pervious bottom is fixed to 0 during the whole simulation time ($t \geq 0$).

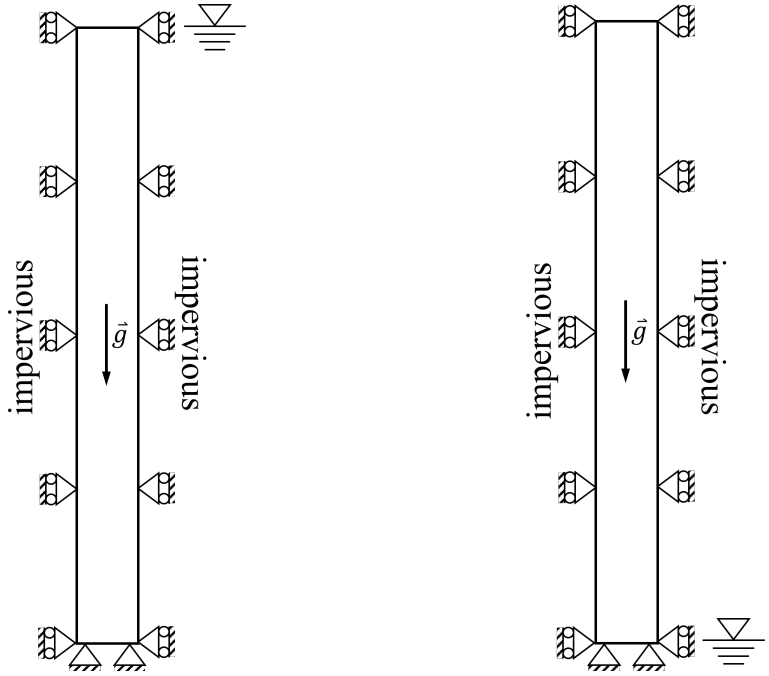

(a) $t < 0$ **(b)** $t \geq 0$

Figure 5.7: Geometry and boundary conditions for the sand column

As suggested by previous study (Callari and Abati, 2009), the following relations for water saturation degree and relative permeability are adopted here:

$$\begin{cases} S_w = 1 - 1.9722 \times 10^{-11} p_c^{2.4279} \\ k_r = 1 - 2.207(1 - S_w)^{0.9529} \end{cases}$$

The mechanical and hydraulic parameters are listed in Table 5.3. It is necessary to mention that the damage critical energy g_c^t and g_c^s have been set to be 1×10^{16} for the reason that no damage is considered in this example.

Table 5.3
Input parameters for Del Monte sand

Parameters	Unit	Value	Parameters	Unit	Value
Drained Young modulus E	MPa	1.3	Drained Poisson coefficient ν	-	0.4
Initial porosity ϕ	%	29.75	Saturated permeability k_p	m^2	4.5×10^{-13}
Biot coefficient b	-	1.0	Solid bulk modulus κ_s	GPa	1000

In Figure 5.8, the numerical prediction of pore water pressures at different times along the sand column were compared with those of the experiment in Liakopoulos (1964). Although the pore air pressure has been assumed to be zero for the simplicity, it can be seen that a good agreement with available experimental data in terms of pore water pressure distribution along the sand column.

As shown in Figure 5.8, the water loss from the bottom induces capillary pressure development along the column starting from the top. Consequently, the settlement at top of sand column induced by suction and gravity for different time steps were presented in Figure 5.9. Due to the lack of experiment data, the numerical predicted results were compared with a previous study (Callari and Abati, 2009) where this problem was studied by FEM. Again, it can find that the vertical displacement predicted by this study has a good agreement with the data from Callari and Abati (2009).

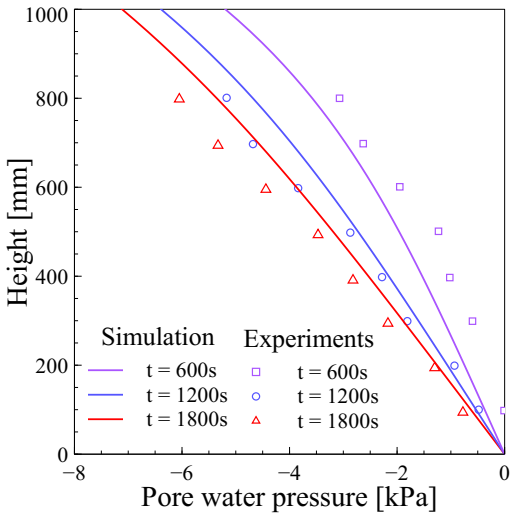

Figure 5.8: Distribution of numerical predicted pore water pressure for different times and the comparison with experimental data (Liakopoulos, 1964).

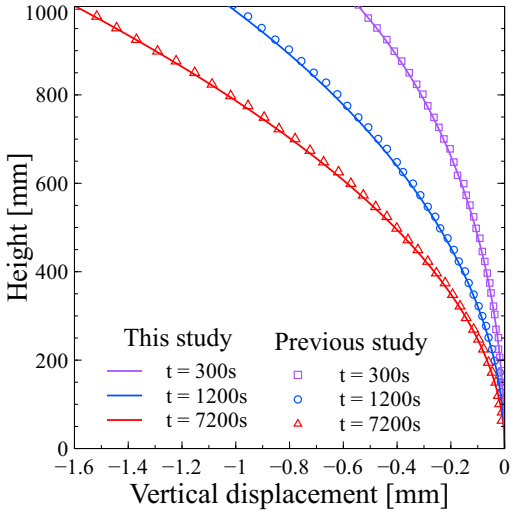

Figure 5.9: Distribution of numerical predicted vertical displacement for different times and the comparison with previous study (Callari and Abati, 2009).

7 Constrained desiccation test

In this section, a constrained desiccation test is performed in order to show the capability of the model to describe the onset and propagation of cracks for the hydro-mechanical coupling problems. For this purpose, the experimental data from Peron et al. (2009) and

Stirling et al. (2017) are employed as qualitative reference to the numerical prediction in our study.

7.1 Description of numerical model

The clayey soil were used in both Peron et al. (2009) and Stirling et al. (2017). However, Peron et al. (2009) conducted the test on a rectangular specimen which was restrained at the bottom of the mould. Differently, Stirling et al. (2017) put the specimen into a semi-cylindrical mould. In this work, we establish a 2D numerical model representing the longitudinal cross-section as shown in Figure 5.10 based on the real geometry of the two experiments and some other numerical model (Cajuhi et al., 2018; Heider and Sun, 2020). Half of the specimen is studied here which is in dimension of $285mm \times 51mm$. The symmetry boundary condition has been applied on the right boundary. According to previous study (Stirling et al., 2017; Heider and Sun, 2020), most of cracks in domain are induced by tensile stress. In order to generate sufficient tensile stressed, the bottom of numerical model has been considered to be fixed. On the other hand, several flaws are placed on the top surface of the geometry representing the imperfections (such as micro-cracks) of the surface in experiments.

The drying condition is simulated by a constant flux $\omega = 6 \times 10^{-7}$m/s applied on the discharge boundary (Stirling et al., 2017; Cajuhi et al., 2018; Heider and Sun, 2020). The mechanical and hydraulic parameters used in this numerical test are summarized in Table 5.4. It should be noticed that the Young's modulus is assumed to be influenced by the water content $w = S_w \frac{\phi \rho_w}{(1-\phi)\rho_s}$.

This test is not aiming at quantitatively reproducing the experimental results but just at verifying if a qualitative agreement can be obtained. Thus, the parameters for phase-field formulations $g_c^t = g_c^s = 1.21 \times 10^{-3}$N/mm are adopted. On the other hand, the length scale parameter l_d is chosen as 2.0mm. Accordingly, the analysis geometry has been divided into 37584 triangle elements with the size h^e around 1.0mm.

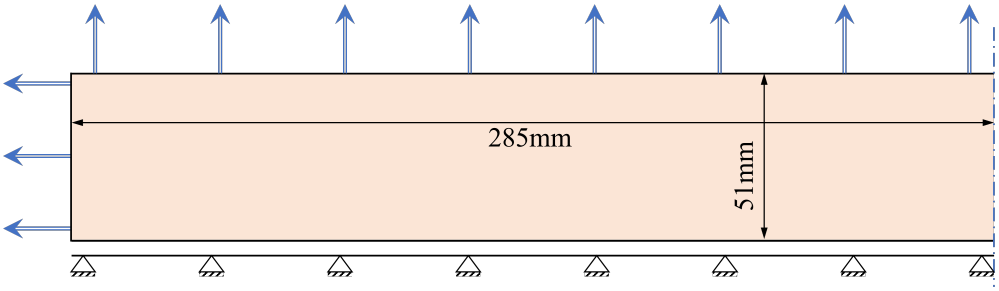

Figure 5.10: Illustration of the geometry and boundary conditions of the 2D symmetric desiccation model

Table 5.4
Reference set of mechanical and hydraulic parameters

Parameters	Symbol	Value	Unit
Young's modulus	E	$1770e^{-0.297w}$	MPa
Poisson's ratio	ν	0.3	-
Initial Porosity	ϕ	41	%
Saturated permeability	k_p	1×10^{-15}	m^2
Residual water saturation	S_r	15	%
critical reference pressure	p_r	357.14	kPa
Van Genuchten model parameter	n	1.3	-

7.2 Numerical prediction of drying-induced fracture

During constrained desiccation test, the authors (Peron et al., 2009) observed several cracks starting at the upper drying surface and propagating to the bottom of the specimen. Furthermore, cracking starting at the lower corners of the sample was observed, leading to partial detachment of the bottom surface. A schematic representation of these desiccation cracks is shown in Figure 5.11.

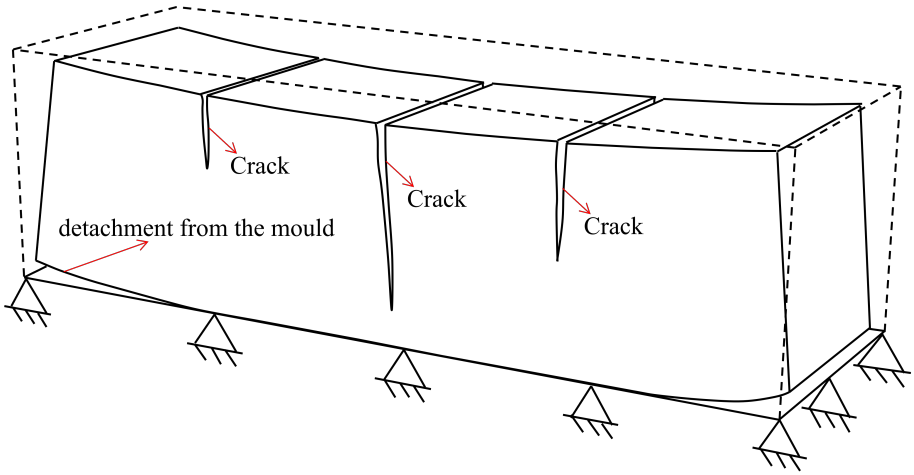

Figure 5.11: Schematic representation of desiccation cracks inspired by the experimental results in Peron et al. (2009).

The distributions of pore water pressure and displacement for early stage ($t = 300s$ which is before localization cracks occur) of desiccation are presented in Figure 5.12. As we can see that the suction develops first on the free surface of the specimen when the drying process starts. The left upper corner suffers the largest negative pore water pressure. It also induces that the vertical shrinkage larger than the lateral shrinkage. In Figure 5.12, one can find that the vertical displacement on upper and bottom of left boundary are negative and positive respectively, while the horizontal displacement is uniform along the upper drying surface of the specimen. For this reason, the tensile crack on the left bottom is observed first as shown in Figure 5.13(a). This behavior has been observed in diverse experiments related to desiccation cracks in soils and also plain cement.

With further drying, the capillary pressure increase at the upper region and drive the localization of tensile cracks on upper surface as shown in Figure 5.13, without shear cracks. Then, the tensile cracks propagates inside of the specimen due to the increase of lateral shrinkage. At the same time, the crack at the corner propagates along the bottom and induce the detachment with the mould further as observed in experiment. Then, one of the vertical cracks reaches the bottom and enhance the detachment. After the enough detachment chich would lead to the release of the constraints, no further cracking would be observed even with further desiccation occuring in free boundaries. As can be seen in Figure 5.13, no shear cracks is observed.

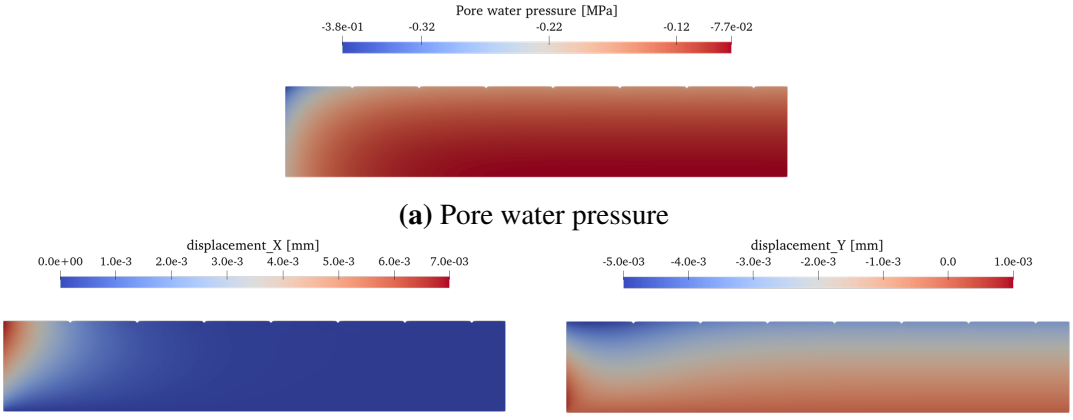

(a) Pore water pressure

(b) Lateral displacement

(c) Vertical displacement

Figure 5.12: Distribution of pore water pressure and displacement after $300s$ for desiccation

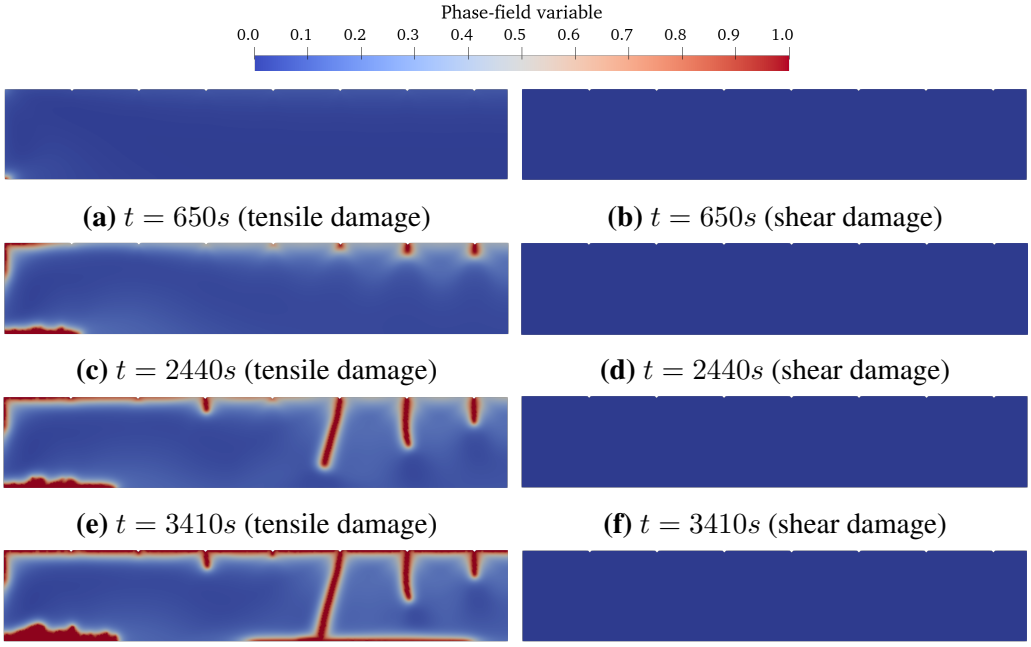

(a) $t = 650s$ (tensile damage)

(b) $t = 650s$ (shear damage)

(c) $t = 2440s$ (tensile damage)

(d) $t = 2440s$ (shear damage)

(e) $t = 3410s$ (tensile damage)

(f) $t = 3410s$ (shear damage)

(g) $t = 7200s$ (tensile damage)

(h) $t = 7200s$ (shear damage)

Figure 5.13: Distribution of phase-field variables at different time of desiccation

8 Conclusion

In this work, an extended phase-field model is proposed to describe the onset and propagation of cracks in saturated and unsaturated rock-like porous materials. Two phase-

field variables are introduced to conveniently capture the tensile, shear and mixed cracks. The effects of pore water pressure on the evolution of two damage fields are taken into account for both saturated and unsaturated conditions. In particular, the evolution of shear cracks is driven by the frictional shear force and influenced by the effective normal stress. Further, the material spatial heterogeneity is also considered for a better description of the crack initiation.

The proposed model is first applied to describe the deformation and progressive failure process of brittle rocks in the laboratory scale. The main features of mechanical behavior of sandstone are well captured by the phase field model, including the overall stress-strain curves and localized crack patterns. It is found that at this scale and under uniform macroscopic stresses, the non-uniform distribution of porosity plays a crucial role on the localization of damage and the occurrence of macroscopic cracks. Furthermore, even all applied stresses are compressive, tensile cracks can still appear due to the strong heterogeneity of local stresses and strains.

The hydro-mechanical solution has been validated by comparing the stimulation results of desaturation of a sand column with experimental data of that one. On the other hand, the simulation of a constrained desiccation test is used to verify the hydro-mechanical damage coupling procedure. The numerical results indicate that the proposed model can reproduce a qualitative agreement with the observation in experiment.

CHAPTER 6

Application of proposed phase-field models to analysis of landslides

1 Introduction

In this chapter, we shall apply the phase-field models proposed in previous chapters into the failure analysis of landslides. Firstly, the slope instability has been studied by the phase-field model considering the frictional-damage coupling in Chapter 3. Next, the hydro-mechanical coupling phase-filed model in Chapter 5 will be employed to analyze the rainfall-induced landslides both for a simplified slope and a real engineering case. In addition, the time-dependent phase-field method coupling with the viscoplastic model in Chapter 4 is applied to modeling time-dependent deformation and failure process of a high slope section in the left bank of Jinping-I hydropower station in China. Numerical predictions are compared with field measurements.

2 Application to slope failure analysis with frictional sliding

Landslide is one of the most frequent natural hazards causing heavy economical and human looses. The progressive cracking is at the origin of slope instability. The frictional sliding is the main mechanism of cracking and instability of many slopes. In this section, the proposed coupled damage-friction phase field model is employed to instability anal-

ysis of slope. Based on the previous study (Fei and Choo, 2020b), a simplified slope is considered as shown in Figure 6.1. The slope surface has an inclination angle of $45°$ to the horizontal axis and a height of 10m. The bottom boundary of slope is assumed to fixed on a rigid ground. The right boundary is free of vertical displacement but constrained of horizontal motion. A rigid foundation is located at the slope crest on the center of which a vertical displacement increment of $\Delta u = -1 \times 10^{-3}$m is prescribed at each loading step. As the proposed model takes the effect of confining stress into account, the initial stresses due to the gravity are considered herein. The basic parameters of slope are taken from the previous work (Fei and Choo, 2020b): Young's modulus $E = 10$MPa, Poisson's ratio $\mu = 0.4$ and mass density $\rho = 2040$kg/m^3. The length parameter for phase field modeling is set to $l_d = 0.05$m. The mesh in the potential sliding region is locally refined to $l_d/h = 4$, while in the other region $l_d/h = 1$. As a result, 292700 triangle elements are used. Finally, the critical energy release rate and internal frictional coefficient are chosen as $g_c = 0.25$N/mm and $\eta^{pl} = 0.1$.

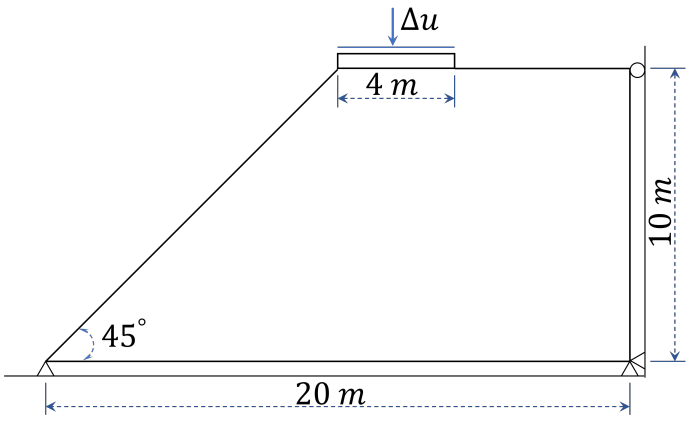

Figure 6.1: Geometry and boundary conditions of a simplified slope

The evolution of damage distribution at successive loading levels is presented in Figure 6.2. It is found that the cracking process starts from the right foot of rigid foundation and then propagates toward the left free surface until the slope is crossed by a major cracked band, whose width progressively becomes larger in the region closer to the left free surface. It should be reminded that as the mean stress increases with the depth due to the gravity, the frictional sliding threshold of material is also increasing with the depth. For this reason, the predicted slip surface has a quasi circle shape and its position is controlled by the local maximum shear stress. The distribution of displacement vector at

$\Delta u = 0.105$mm is given in Figure 6.3. It is clear that the slip motion is strongly piloted by the frictional sliding process. The maximum displacement is found along the cracked surface. This result seems to be very consistent with many field observations and to the classical instability study by using limit analysis methods.

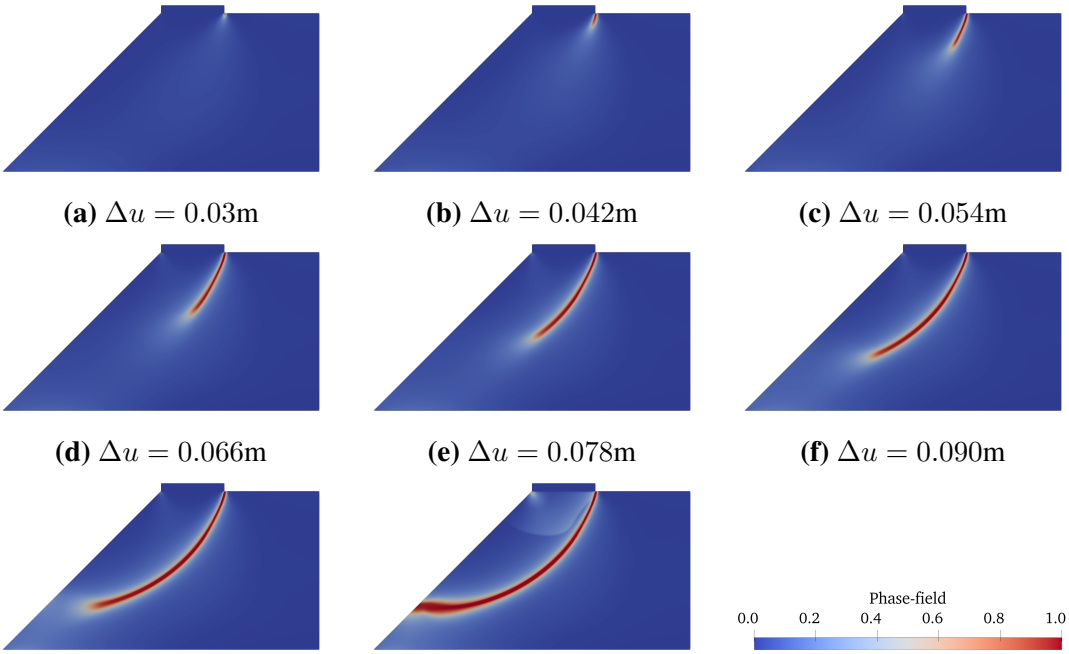

(a) $\Delta u = 0.03$m **(b)** $\Delta u = 0.042$m **(c)** $\Delta u = 0.054$m

(d) $\Delta u = 0.066$m **(e)** $\Delta u = 0.078$m **(f)** $\Delta u = 0.090$m

(g) $\Delta u = 0.099$mm **(h)** $\Delta u = 0.105$mm

Figure 6.2: Distribution of induced damage and failure pattern of slope

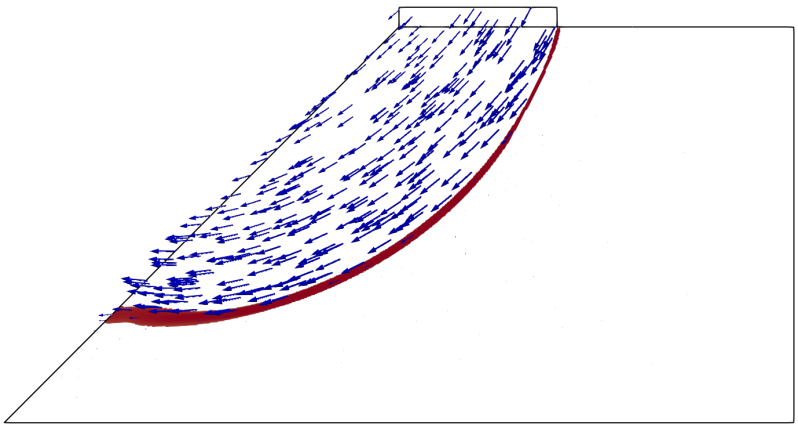

Figure 6.3: Distribution of displacement vector at $\Delta u = 0.105$mm

As mentioned above, our new model explicitly incorporates the friction-damage cou-

pling in closed cracks under compressive stresses. The frictional coefficient η^{pl} is a key parameter. Its influence on the slope failure pattern is here studied. For this purpose, two values of η^{pl} are used: $\eta^{pl} = 0.10$ and $\eta^{pl} = 0.17$. The corresponding damage distributions at the slope failure state are presented in Figure 6.4. It is shown that the parameter η^{pl} has a significant influence on the slip surface pattern. A bigger value of η^{pl} leads to a larger radius of the predicted slip surface. This is due to the fact that the maximum shear stress distribution is affected by the local frictional coefficient. This result seems to indicate that for a high value of η^{pl}, the sliding surface may not fully cross the slope and reach the left free surface. The catastrophic landslide ricks may be reduced by reinforcing the friction coefficient of rock and soil.

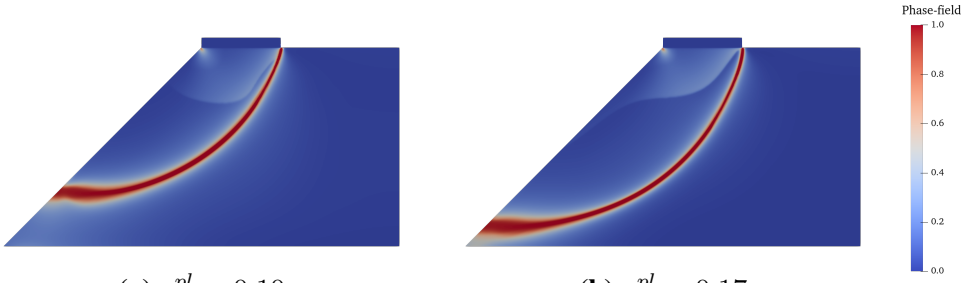

(a) $\eta^{pl} = 0.10$ **(b)** $\eta^{pl} = 0.17$

Figure 6.4: Influence of frictional coefficient η^{pl} on cracking process of slope

3 Application to analysis of rainfall induced landslide

In this section, we shall apply the extended phase-field model for variably saturated porous media to analyzing rainfall-induced deformation and cracking process of slopes. Two cases are considered, a simplified case and a real engineering case.

3.1 Study of a simplified case

In this example, a simplified slope, which has an inclination angle of $40°$ to the horizon with a height of 20m as shown in Figure 6.5(a) (Kim et al., 2012), is considered. The material constituting the slope is assumed to be a rock J_{1-2Z}. Thus, the failure mechanism of this slope due to a constant rainfall $1.8 \times 10^{-6} m/s$ (which is equal to the permeability of the material) is analyzed. The slope section is divided into 73794 triangular elements,

as shown in Figure 6.5(b). The minimum size of elements is about 0.15 m. Thus, the length scale parameter is chosen as $l_d = 0.15m$.

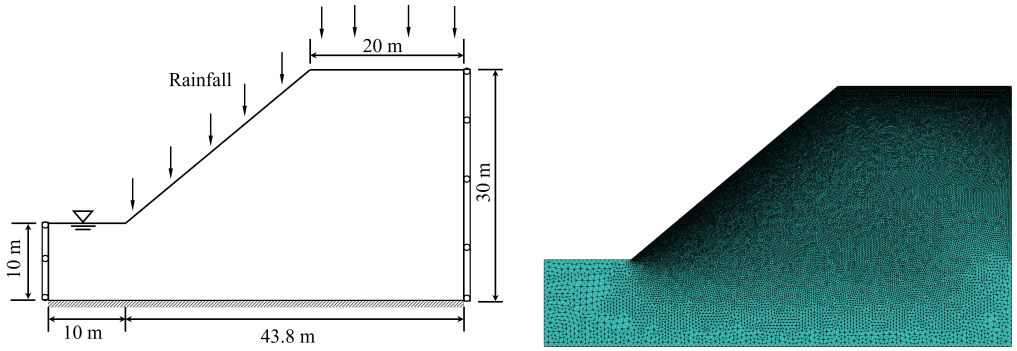

(a) Geometrical and boundary conditions **(b)** finite element mesh generation

Figure 6.5: Geometrical domain of a simplified slope section and finite element mesh

One objective here is to study the influence of material homogeneity on cracking process and failure pattern of the slope. For this purpose, the heterogeneity index $m_i = 1.1$ is adopted here. The corresponding non-uniform distribution of Young's Modulus due to heterogeneous porosity is shown in Figure 6.6 according to Weibull distribution in Equation (3.30). The set of parameters used in numerical calculation are given in Table 6.1.

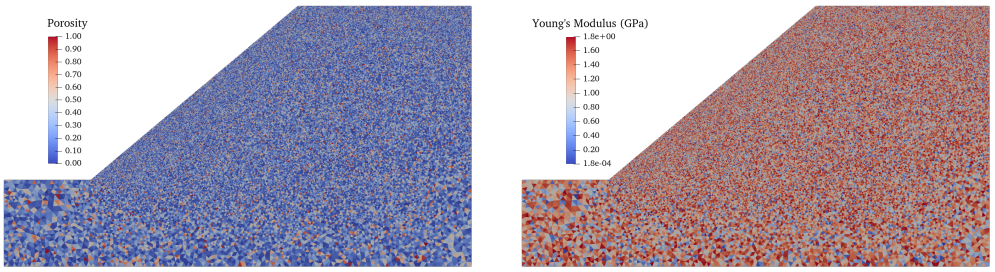

(a) Porosity **(b)** Macroscopic Young's modulus

Figure 6.6: Spatial distributions of porosity and corresponding macroscopic elastic modulus

Table 6.1
Input parameters for failure analysis of a simplified slope

Parameters	Unit	Value	Parameters	Unit	Value
Matrix bulk modulus κ_s	GPa	1.135	Matrix shear modulus μ_s	GPa	0.725
Average porosity $\bar{\phi}$	%	28.57	Heterogeneity index h	-	1.1
Residual saturation S_r	%	8	Critical pressure p_{cr}	kPa	17.5
Water retention parameter n	-	3.9	Material scale length l_d	mm	0.25
Tensile crack energy g_c^t/l_d	N/m^2	1.49×10^2	Shear crack energy g_c^s/l_d	N/m^2	2.17×10^2
Cohesion c	kPa	87.5	Frictional angle φ	$^\circ$	29.2

The distributions of both tensile and shear damage are shown in Figure 6.7 for the different levels of rainfall. It is shown that the shear damage occurs earlier and propagates faster than the tensile one. It seems that the shear damage (cracking) is the dominating mechanism in the slope failure. Despite of the spatial heterogeneity of elastic modulus, the cracking process starts from the slope toe zone and then propagates toward the top surface. The width of cracked zone becomes progressively larger in the region closer to the top surface. In Figure 6.8, the distribution of water pressure and the displacement vector at the rainfall level of 1230.5 mm are presented. One can observe that upper region of the slope still remains unsaturated (negative water pressure) while the lower one is progressively saturated by the rainfall infiltration. The displacement vector indicates that the the failure pattern is mainly piloted by the sliding along the inclined slope surface.

From the results obtained in this example, one can see that compared with the material heterogeneity and with the absence of initial macroscopic fractures, the cracking process

is mainly driven by the mechanical loading (slope weight) and water infiltration.

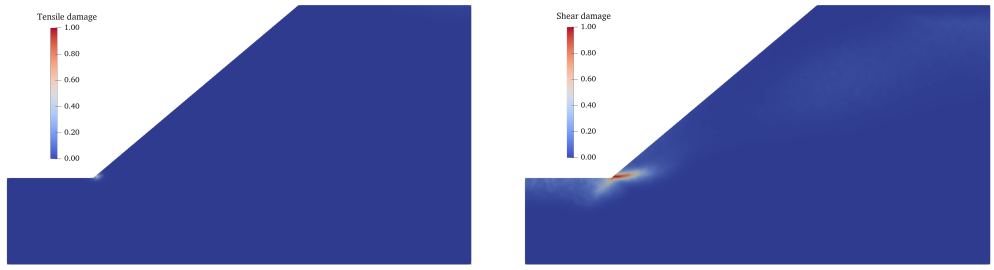

(a) Rainfall = $1166.47mm$(Tensile damage) **(b)** Rainfall = $1166.47mm$ (Shear damage)

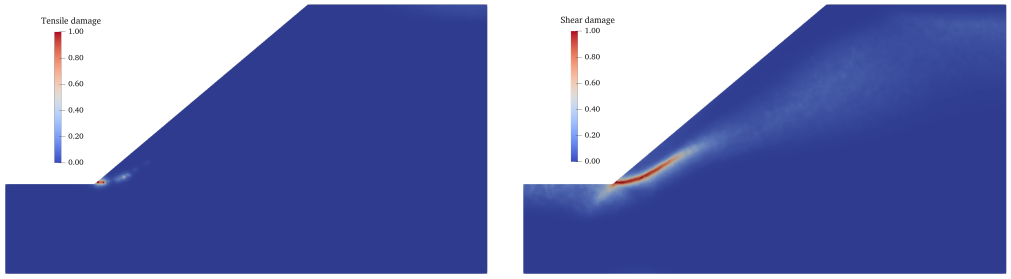

(c) Rainfall = $1185.84mm$ (Tensile damage) **(d)** Rainfall = $1185.84mm$ (Shear damage)

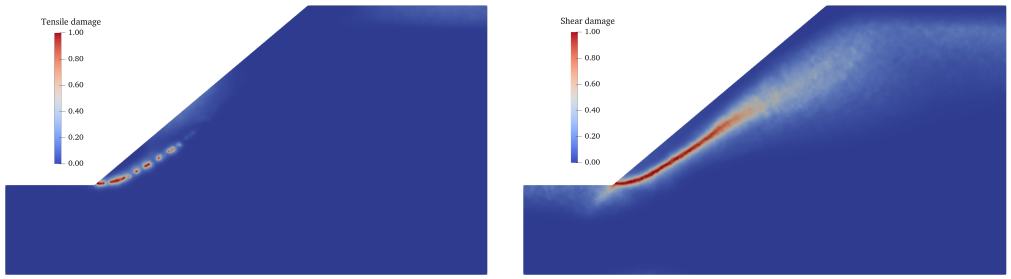

(e) Rainfall = $1205.28mm$ (Tensile damage) **(f)** Rainfall = $1205.28mm$ (Shear damage)

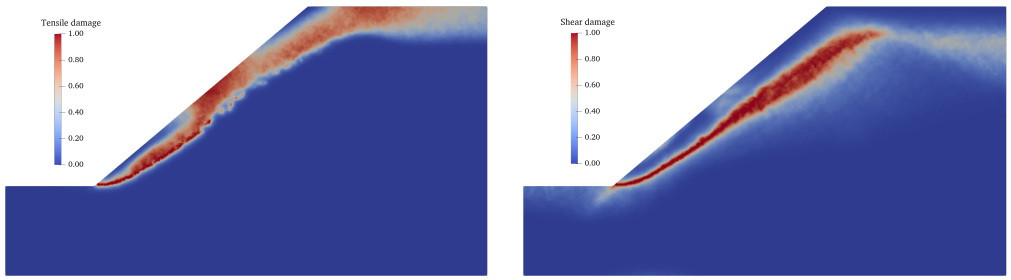

(g) Rainfall = $1230.5mm$ (Tensile damage) **(h)** Rainfall = $1230.5mm$ (Shear damage)

Figure 6.7: Distribution evolution of rainfall-induced tensile and shear cracks

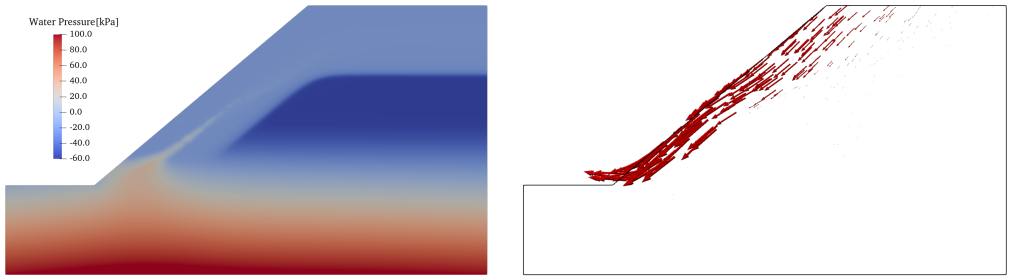

(a) Water pressure **(b)** Displacement vector

Figure 6.8: Distribution of pore water pressure and displacement vector

3.2 Study of a real case

In this sub-section, the phase-field method for partially saturated porous media is applied to a typical engineering case, the Mayanpo slope in China.

3.2.1 Engineering geological conditions

The Mayanpo slope is situated in the right bank of Xiangjiaba Hydropower station, which lies on thedownstream of the Jinsha River in Shuifu County, Yunnan Province, China (Zhang et al., 2018).

According to the morphological investigation, the elevation of Mayanpo slope ranges from $300m$ to $624m$ in the east-west axial. And a gully, named as Mayan gully, cuts through the slope from north to south with the elevation ranging between $350m$ and $500m$. Though the Manyanpo slope has an average slope gradient of $12°$ - $20°$, the slope gradient varies spatially due to the existence of the Mayan gully and Jinsha River. Specifically, the closer near the gully or the river, the steeper the slope is, vice versa. The drilling exploration gave the information of stratum in Mayanpo slope. The selected section in this work is shown in Figure 6.9. The slope can be divided into two layers. The rock in the upper layer is composed of fine-grained sandstone mixed with siltstone (recognized as J_{1-2Z}), and the bedrock is a clayey rock (recognized as T_4^3).

On the other hand, based on the field investigation, a series of thin-layered rock strata, which are considered as weak inter-layers, are found within the layer of sandstone in the upper part. According to previous studies (Tang et al., 2009; Jiang et al., 2012; Zhang et al., 2018), these weak inter-layers have a significant effect on the deformation and

stability of the slope due to their pool mechanical properties. Furthermore, the field monitoring data (Jiang et al., 2012; Zhang et al., 2018) indicated that the most sliding zone in the Mayanpo slope area was controlled by a most developed thin weak layer, named as JC-1. For this reason, the cross section after the first excavation with the weak layers is selected as a typical profile, as shown in Figure 6.9, for purpose of studying the failure process of rainfall-induced landslide.

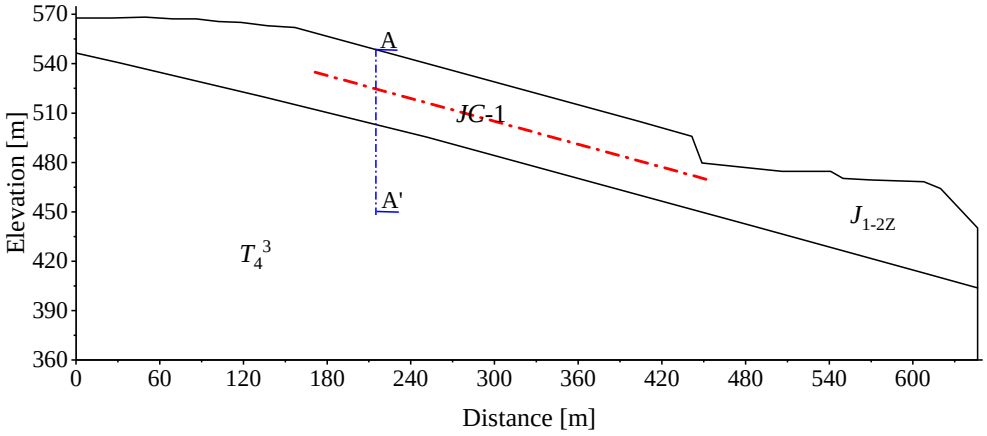

Figure 6.9: Geometrical parameters of selected slope section

3.2.2 Setting of numerical model

According to previous studies (Jiang et al., 2012; Zhang et al., 2018), the mechanical properties of the thin weak (cracked) layer $JC-1$ are significantly deteriorated with respect to those of the surrounding sandstone layer. In order to take into account this initial weak zone with the framework of phase-field method, it is convenient to set a large initial value of damage variables (approaching to 1). However, this solution with an initial damage field generally leads to some numerical issues (Borden et al., 2012; Klinsmann et al., 2015; Strobl and Seelig, 2016). An alternative method is here preferred. An initial value of energy history functional is attributed in the weak zone around the cracked layer $JC-1$ for each damage field (tensile and shear) with the following distribution function:

$$H_0^{t/s}(\boldsymbol{x}) = \begin{cases} \dfrac{g_c^{t/s}}{2l_d}\dfrac{d}{1-d}\left(1-\dfrac{2L(\boldsymbol{x})}{l_d}\right) & L(\boldsymbol{x}) \leq \dfrac{l_d}{2} \\ 0 & \text{otherwise} \end{cases} \tag{6.1}$$

in which $L(\boldsymbol{x})$ represents the shortest distance from an arbitrary point $\boldsymbol{x}$ to the initial cracked layer center $JC-1$. The critical value $d = 0.999$ is set in all following calculations.

The selected slope section is divided into 134592 triangular elements, as shown in Figure 6.10. The size of element in the first layer is smaller (about 0.5 m) than that in the bedrock as it is expected that the induced damage should be larger there.

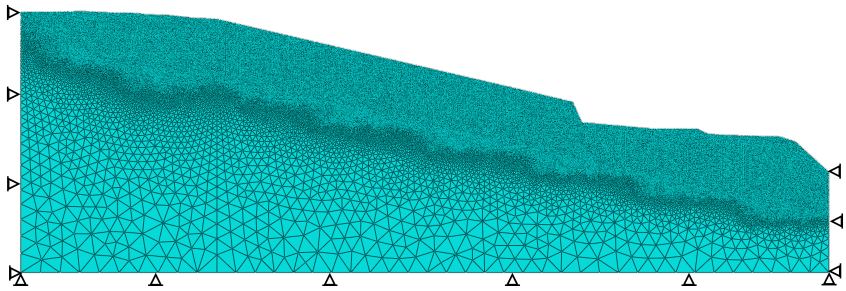

Figure 6.10: Finite element mesh used for numerical modeling of selected slope section

Most of the input parameters used here are collected from the previous studies, for instance (Tang et al., 2009; Jiang et al., 2012, 2013; Zhang et al., 2018). First of all, similarly with the simulation of triaxial compression tests, the sandstone J_{1-2Z} in the first layer is considered as a heterogeneity material with a random distribution of porosity and its macroscopic elastic properties are estimated by using the homogenization relations Equation (3.29). According to those previous studies, the porosity of sandstone considered here is quite uniform. Therefore, a weak heterogeneity index of $m_i = 10$ is adopted. The average porosity is $\bar{\phi} = 28.57\%$. The elastic properties of solid matrix are evaluated as $\kappa_s = 1.135GPa$ and $\mu_s = 0.725GPa$ respectively. However, the bedrock layer T_4^3 is considered as a homogeneous material with Young's modulus of $E = 19GPa$ and Poisson's ratio of $\nu = 0.15$ and its average porosity is about 11.36%. The values of intrinsic permeability are $1.8 \times 10^{-13}m^2$ for the layer J_{1-2Z} and $1 \times 10^{-15}m^2$ for the bedrock T_4^3. The parameters of water retention curve for the first layer are: $S_r = 0.08$, $p_{cr} = 17.5kPa$ and $n = 3.9$. In the opposite, during the whole analysis, the bedrock is fully saturated. Therefore, it is not useful to define the water retention properties for this layer. The length scale parameter for phase field analysis is chosen as $l_d = 0.5m$ for both two layers. It is estimated that the critical energy values are $g_c^t/l_d = 1.49 \times 10^2 N/m^2$ and $g_c^s/l_d = 2.17 \times 10^2 N/m^2$ for the first layer and $g_c^t/l_d = 4.06 \times 10^3 N/m^2$ and

$g_c^s/l_d = 5.36 \times 10^3 N/m^2$ for the bedrock one. The cohesion and frictional angle are $c = 87.5kPa$ and $\varphi = 29.2°$ for the sandstone in the first layer J_{1-2Z} and $c = 380kPa$ and $\varphi = 49.44°$ in the bedrock. The set of parameters involved in the simulation is summarized in Table 6.2.

Table 6.2
Input parameters for cracking analysis of Mayanpo slope

Material	Parameters	Symbol	Unit	Value
Rock J_{1-2Z}	Matrix bulk modulus	κ_s	GPa	1.135
	Matrix shear modulus	μ_s	GPa	0.725
	Average porosity	$\bar{\phi}$	%	28.57
	Heterogeneity index	m_i	-	10
	Residual saturation	S_r	%	8
	Critical pressure	p_{cr}	kPa	17.5
	Water retention parameter	n	-	3.9
	Tensile crack energy	g_c^t/l_d	N/m^2	1.49×10^2
	Shear crack energy	g_c^s/l_d	N/m^2	2.17×10^2
	Smeared crack energy	l_d	m	0.5
	Cohesion	c	kPa	87.5
	Frictional angle	φ	°	29.20
Rock T_4^3	Young's modulus	E	GPa	19
	Poisson's ration	ν	-	0.15
	Porosity	ϕ	%	11.36
	Tensile crack energy	g_c^t/l_d	N/m^2	4.06×10^3
	Shear crack energy	g_c^s/l_d	N/m^2	5.36×10^3
	Smeared crack energy	l_d	m	0.5
	Cohesion	c	kPa	380
	Frictional angle	φ	°	49.44

On the other hand, the rainfall infiltration is a complex problem. According to (Mein and Larson, 1973), there are two distinct stages during the process of infiltration. At the

first stage, the rainfall intensity is below the infiltration capacity of the ground, and all the rainfall can infiltrate into the ground. At the second stage, when the rainfall intensity is above the infiltration capacity, the surface ponding occurs and a variety of water flux disappears as runoff. In the present work, the rainfall is assumed to be a water flux applied to the surface of slope. To simplify the problem, a rainfall intensity of 6.48 mm/h, which is equivalent to the permeability of slope surface ($= 1.8 \times 10^{-6} m/s$), is chosen. Hence, it is reasonable to assume that all the rainfall infiltrates into the slope without significant surface ponding.

3.2.3 Failure mechanism analysis

According to the field investigations (Tang et al., 2009; Jiang et al., 2012, 2013; Zhang et al., 2018), many cracks and fractures were found in the slope, as shown in Figure 6.11. They can be divided into two groups. One is recognized as tensile cracks, which are intensively distributed on the top part of slope and at the south side of pool. The maximum value of the tensile crack width reaches up to $80cm$, and the depth more than $10m$. The other one contains tensile - shear mixed cracks. They are found around the toe and excavated zones of slope with the width ranging between 1 to $10cm$.

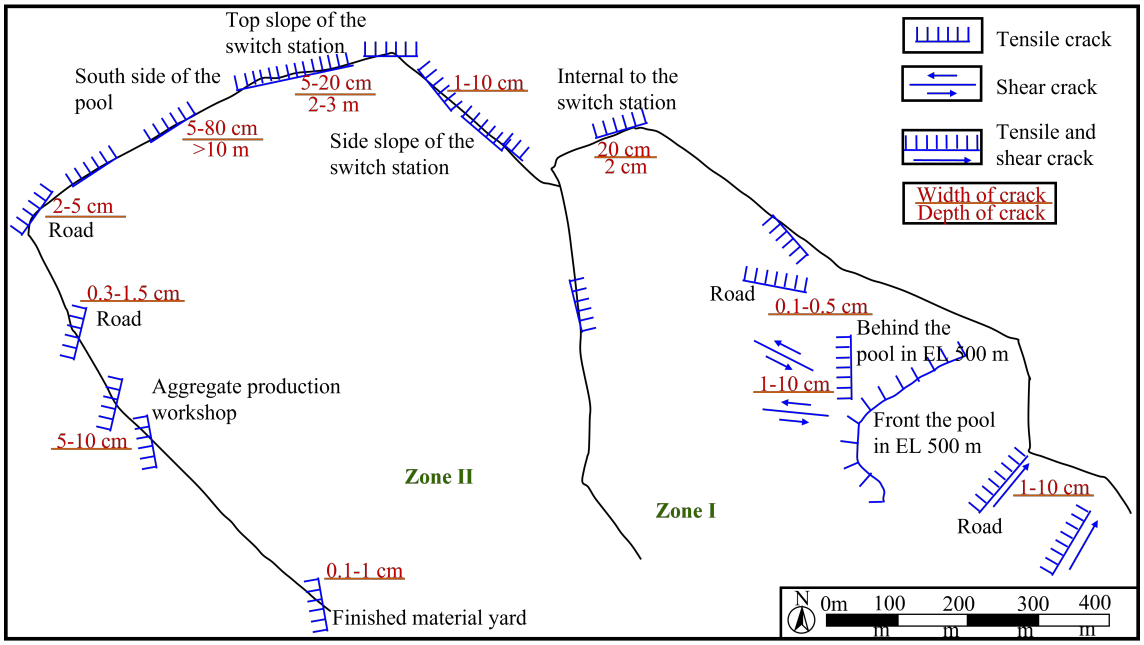

Figure 6.11: Field investigation of cracks and fractures characteristic distribution in Mayanpo slope (Zhang et al., 2018)

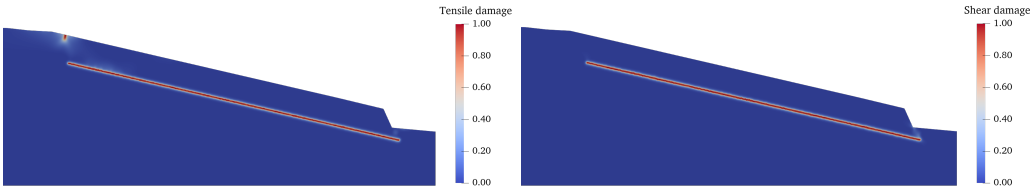

(a) Rainfall = $568.9mm$ (Tensile damage) **(b)** Rainfall = $568.9mm$ (Shear damage)

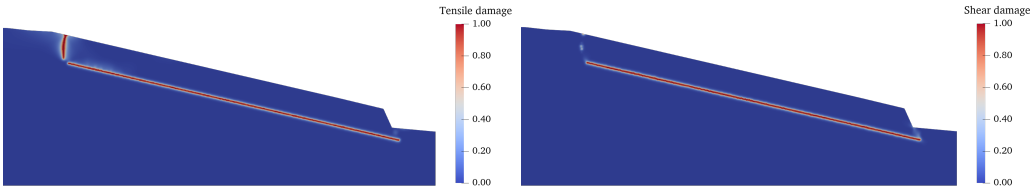

(c) Rainfall = $598.7mm$ (Tensile damage) **(d)** Rainfall = $598.7mm$ (Shear damage)

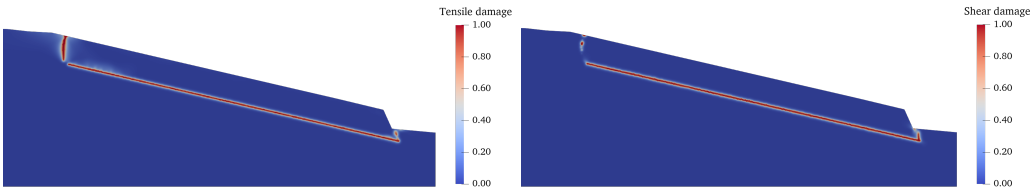

(e) Rainfall = $645.5mm$ (Tensile damage) **(f)** Rainfall = $645.5mm$ (Shear damage)

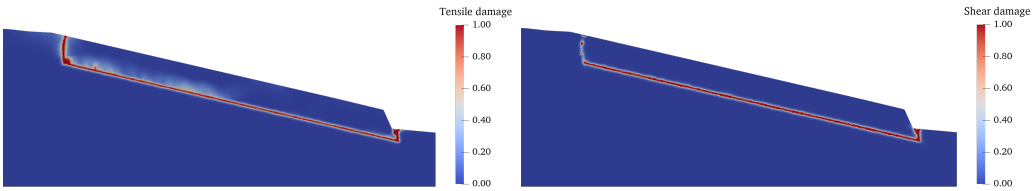

(g) Rainfall = $651.3mm$ (Tensile damage) **(h)** Rainfall = $651.3mm$ (Shear damage)

Figure 6.12: Progressive evolution of rainfall-induced tensile and shear cracks

In Figure 6.12, the evolutions of both tensile and shear cracks are presented for different rainfall infiltration levels. Qualitatively, the numerical distributions of cracks are consistent with the field observation. More precisely, the tensile cracks firstly appear on the top zone when the cumulative rainfall reaches $568.9mm$, as shown in Figure 6.12(a). The tensile cracks propagate vertically with the rainfall infiltration to reach the initial cracked layer. At the same time, the growth of shear cracks is more moderate than the tensile one. When the rainfall infiltration level reaches $645.5mm$, as shown in Figures 6.12(e) and 6.12(f), both tensile and shear cracks appear around the excavated zone of the lower part of slope. With the continuation of rainfall infiltration, the tensile cracks in the top part of slope and the tensile - shear cracks in the excavated zone are connected to the

initial cracked layer (see Figures 6.12(g) and 6.12(h)). At this stage, there is clearly an occurrence risk of landslide.

In Figure 6.13, we show the pore water pressure distributions at the initial state before rainfall and at the rainfall infiltration of $651.3mm$ when the macroscopic fractures appear. At the initial state, the upper zone of slope is unsaturated where the water pressure is less than zero. With the rainfall, this zone is progressively saturated leading to the decrease of capillary pressure and effective stress. This is the physical cause of cracks growth. It is interesting to notice that the pore water pressures inside the highly damaged zones are clearly higher than that in the surrounding ones. This is due to the high permeability in those damaged zones. Therefore, it is clear that the occurrence of cracking process is inherently correlated with the resaturation of ground and the increase of pore water pressure. Mutually, the water infiltration is enhanced by the propagation of cracks.

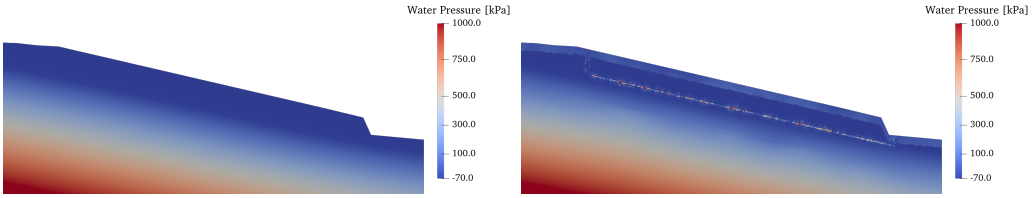

(a) Initial state **(b)** Rainfall = $651.3mm$

Figure 6.13: Distribution of pore water pressure at two selected states

The distribution of displacement vector at the rainfall state of $651.3mm$ is shown in Figure 6.14. One can see that the motion of landslide is mainly driven by the sliding along the right-down direction due to the gravity effect of ground. Further, the displacement of slope is concentrated alongside the existing weak zone and fully consistent with the evolution of cracked zones. The displacements inside the undamaged regions are very small.

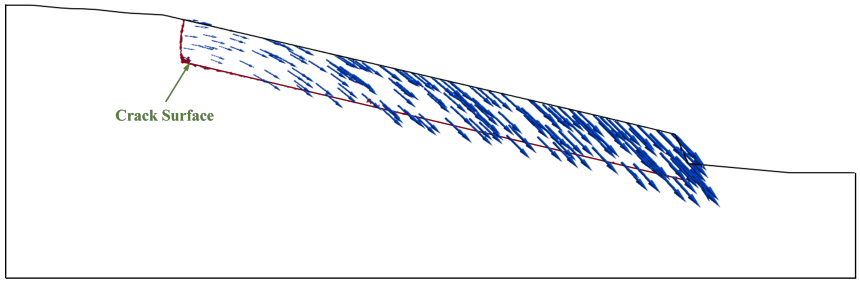

Figure 6.14: Distribution of displacement vector at rainfall = $651.3mm$

For a better understanding of the failure process in rainfall induced landslide, the displacement profiles along the selected section A-A' in Figure 6.9 are presented in Figure 6.15 for different infiltration instances. It can be seen that the displacement inside the region above the pre-cracked layer $JC-1$ is much larger than that of the zone below $JC-1$. The difference becomes more and more significant with the rise of rainfall infiltration level. There is a strong displacement discontinuity across the initial cracked layer. At the same time, the displacement inside the region below the pre-cracked layer remains very small and does not evolve significantly with the rainfall time. Therefore, it seems that the sliding along the weak layer has a key role in the failure process of slope caused by the rainfall infiltration and seepage.

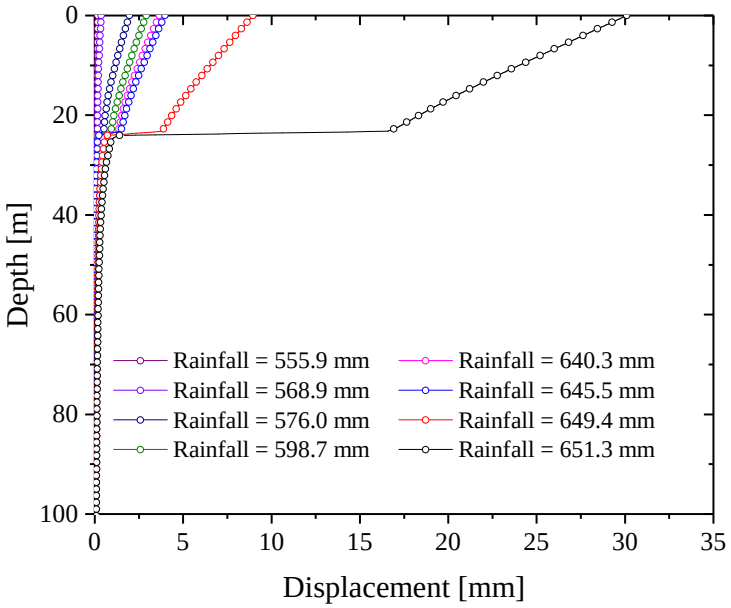

Figure 6.15: Displacement profiles along a selected section A-A' with different rainfall infiltration levels

4 Time-dependent behavior of left bank high slope of Jinping I hydropower station

As an example of engineering application, time-dependent mechanical responses of the left bank high slope of Jinping I hydropower plant are investigated by using the pro-

posed time-dependent phase-field model.

4.1 Summary of engineering geological conditions

The Jinping I hydropower station, one of the highest and largest ones all over the world, is built at the Pusiluogou in the west of Great River Bend of Yalong River which is adjacent to Muli and Yanyuan counties in Liangshan Yi Autonomous Region. It is near Xichang (27°32′-28°10′N, 101°46′-102°25′E), about 500 km southwest of Chengdu, Sichuan Province, PR China. The double-curvature arch dam, of $305\ m$ in height with a crest at $1885\ m$ above the sea level (asl), is constructed in a typical V-shaped valley (Qi et al., 2010). Due to the height of the dam, the retained reservoir level will reach $1880\ m$ asl, with a total reservoir capacity 7.76 billion m^3 and the regulated storage 4.91 billion m^3.

The valley is cut through the Triassic Zagunao Formation which consists of sandstone, slate and marble. In view of its location between the Tibetan Plateau and Sichuan Basin, the area is characterized by complex geological conditions (Huang et al., 2010), especially on the left bank of the valley. A typical geological profile (L9-L9) of the left bank was reported in Hu et al. (2020). Accordingly the slope rises at an angle between 70°-80° below $1900\ m$ asl and 40°-50° above. In addition, the bedrock of slope is composed of metamorphic rocks belonging to the Zagunao group of the middle and upper Triassic ($T_{2\text{-}3Z}$) which can be divided into three members Zhou et al. (2016): a green schist member ($T^1_{2\text{-}3Z}$), a marble member ($T^2_{2\text{-}3Z}$) and a slate and low-grade metamorphic sandstone member ($T^3_{2\text{-}3Z}$). Moreover, a large number of faults and fractures are observed in this area Zhou et al. (2016), for instance, the fault referred as f_2 is shown in Figure 6.16(a). To sum up, the geological conditions at the dam site are extremely complex and request an in-depth investigation of stability conditions of the left abutment slope. In this context, the present study shall provide a numerical analysis of time-dependent deformation and damage by using an efficient phase-field method.

4.2 Description of numerical model

Here we consider the typical two-dimensional section L9-L9 of the left bank high slope of Jinping I hydro-power station. In Figure 6.16(a), the geometrical domain and main geological layers of the section are presented. The studied domain is of $370\ m$ in

width and of $450\ m$ in height. The slope section composition is simplified to be composed of three principal rock layers respectively referred to as II, III and IV, and a major fault zone named as f_2. Based on the studies related to the laboratory tests presented above and field investigations (Huang et al., 2010; Hu et al., 2020), the basic model's parameters of each layers are given in Table 6.3. As the fault zone f_2 is mainly constituted with filled materials, it is here considered as a thin layer with a small critical fracture energy g_c. In Figure 6.16(b), one also shows the finite element mesh adopted in this study. It is composed of 12523 elements and 12729 nodes in total. The length scale parameter for the regularized crack description is taken as $l_d = 0.25\ m$, which is equal to the minimum size of element.

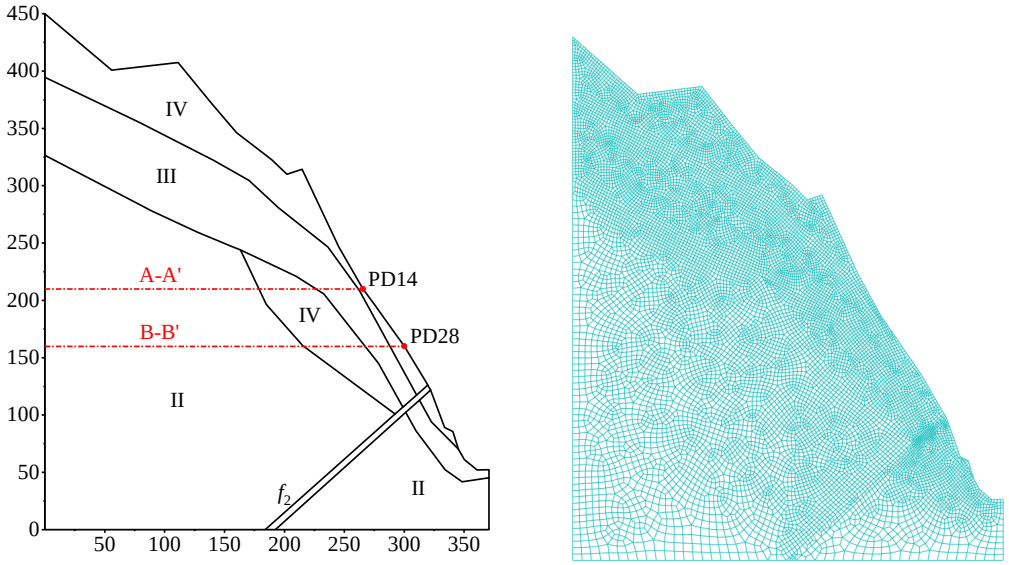

(a) composition of L9-L9 slope section **(b)** finite element mesh generation

Figure 6.16: Geometrical domain of a selected slope section and finite element mesh generation

Table 6.3
Reference set of physical, elastic and phase-field parameters of different rock layers

	Rock layers			
	Layer II	Layer III	Layer IV	Fault f_2
Density ρ (kg/m^3)	2800	2700	2700	2600
Young's modulus E (MPa)	25000	8500	2500	3000
Poisson's ratio ν	0.23	0.26	0.3	0.28
Critical energy g_c (N/mm)	900	104	28.3	1.08

Table 6.4
Reference set of viscoplastic parameters

Parameters	η^{vp}	σ_s	n	m	c_v
	(s^{-1})	(MPa)	(-)	(-)	(-)
Values	1×10^{-9}	5.8	2.8	1030	0.24

4.3 Main results of reference case

Main results obtained from a reference calculation using the parameters given in Tables 6.3 and 6.4 are first presented and discussed.

First of all, in Figure 6.17, the distributions of instantaneous displacement and damage induced by self gravity of slope are given. One can see that the maximum instantaneous displacement is obtained in the top zone of the slope. The fault layer is highly damaged. A small but not negligible damage distribution is also found inside the weak zone IV as

shown in the Figure 6.17(b).

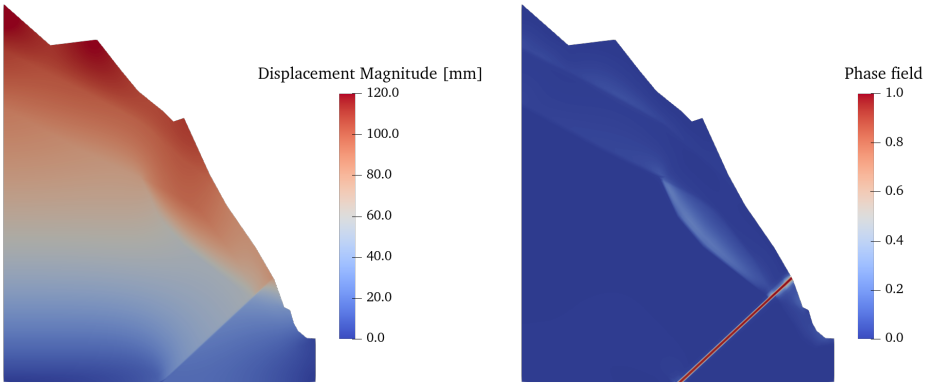

(a) Instantaneous displacement **(b)** Gravity induced damage

Figure 6.17: Instantaneous displacement and damage distributions induced by gravity effect inside the slope

The time-dependent behavior of the slope is then studied by taking the instantaneous results presented in Figure 6.17 as the initial conditions. As the gravity effect is already taken into account and there is no other applied loads, the long-term stability of the slope is entirely controlled by the time-dependent mechanical behavior of rock layers. Based on the $in-situ$ measured data reported in Hu et al. (2020), the time-dependent deformation of the slope during a forty month period (from 1^{st} January 2010 to 15^{th} April 2013)) is investigated in this work. Indeed, for the purpose of monitoring the deformation evolution of the left bank slope with the time, some monitoring points have been set, for instance the points $PD14$ and $PD28$ in the section $L9-L9$ as shown in Figure 6.16(a). The comparison between the measured displacement and numerical prediction is presented in Figure 6.18. It seems that the numerical predicted evolution of displacement at the two monitoring points is in good agreement with the measured data.

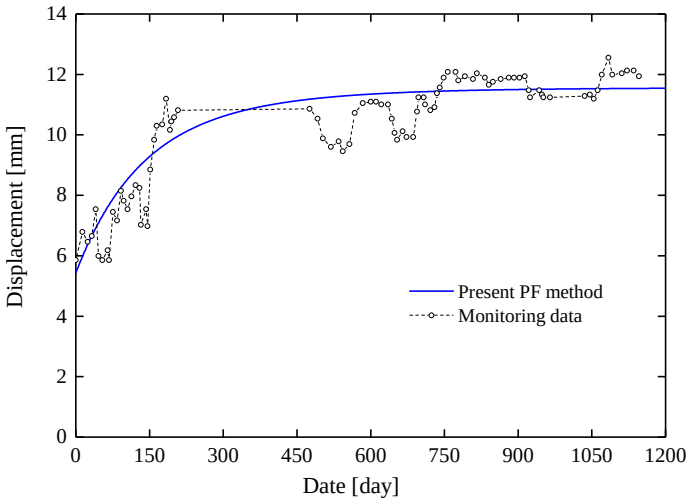

(a) monitoring point PD14

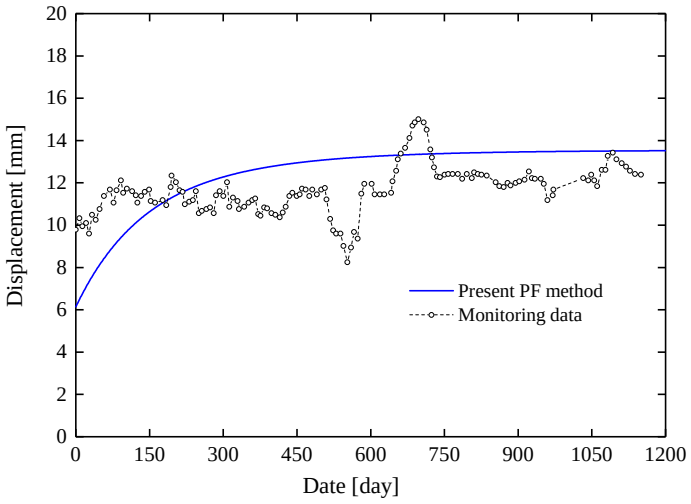

(b) monitoring point PD28

Figure 6.18: Comparisons of displacement evolution between measured and calculated values at two monitoring points (From 1^{st} January 2010 to 15^{th} April 2013)

The distribution of displacement and damage increments with respect to the instantaneous values at the end of calculation period (1200 days) are shown in Figure 6.19. Differently with the instantaneous results shown in Figure 6.17, the maximum time-dependent displacement increase is obtained inside the weak layer IV and around the fault layer

f_2. At the same time, the damage distribution inside the weak layer IV exhibits a time-dependent growth. In order to show some quantitative examples, the variations of damage variable along two selected cut lines $A-A'$ and $B-B'$ defined in Figure 6.16(a) are also presented for three representative instances. One can see that the maximum damage value increases from 0.161 to 0.307 on the line $A-A'$ and 0.156 to 0.295 on $B-B'$. This clearly shows that the time-dependent damage evolution related to micro-crack growth is the main mechanism driving the time-dependent deformation of the slope.

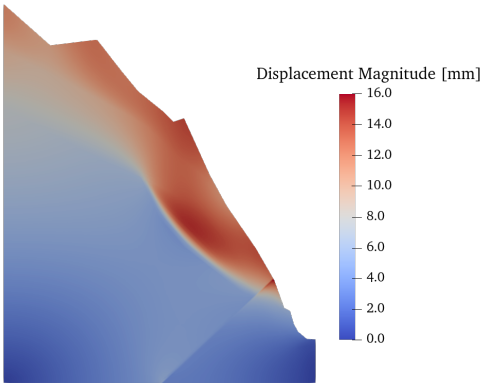

(a) Displacement increment

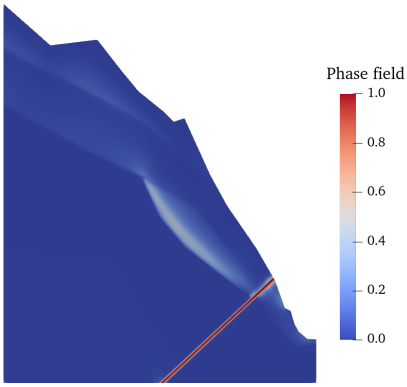

(b) Damage increment

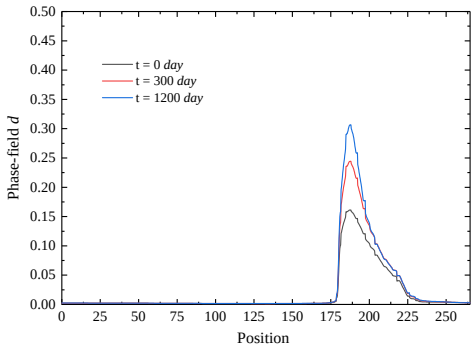

(c) Section $A-A'$

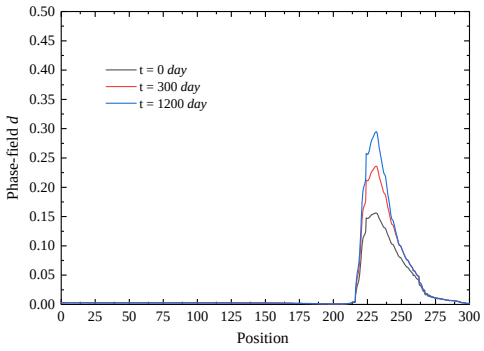

(d) Section $B-B'$

Figure 6.19: Distributions of displacement and damage increments with respect to the instantaneous values at the end of calculation period (1200 days), and variation of damage along the two cut lines defined in Figure 6.16(a) at three different instances

4.4 Sensitivity analysis of water weakening effect

Most slopes are subjected to water saturation change due to raining and reservoir level variation. It is also known that the mechanical properties of most rocks are sensitive to

water content. In particular, a number of previous studies have shown that the critical fracture energy or stress intensity factor of rocks could be significantly reduced by an increase of water saturation degree (Henry et al., 1977; Waza et al., 1980; Nara et al., 2012). In the case of the Jinping left bank slope, according to the experimental study reported in Huining et al. (2013), the failure strength of all rock layers considered here can be reduced by 10% due to water saturation. Therefore, it is crucial to investigate the consequence of such water weakening effect of the long-term deformation and stability of slopes.

However, as a first approximation, a simplified approach is adopted in this work. We shall not perform fully coupled hydromechanical calculations. The water weakening effect is taken into account simply by considering that the critical fracture energy g_c for each rock layer is reduced by different ratios. The predicted displacement evolution with time at the two monitoring points are presented in Figures 6.20 and 6.21 for two ratios of reduction. It is clear that the displacement is enhanced by the reduction of g_c. The amplification of displacement is quite small for a reduction of 5%. However, with a reduction of g_c by 10%, the displacements at two monitoring points are significantly amplified and exhibit an accelerating phase leading to sliding of slope. This seems to indicate that if the critical fracture energy parameter g_c is reduced by water saturation to some critical value, it is possible to generate the instability of slope.

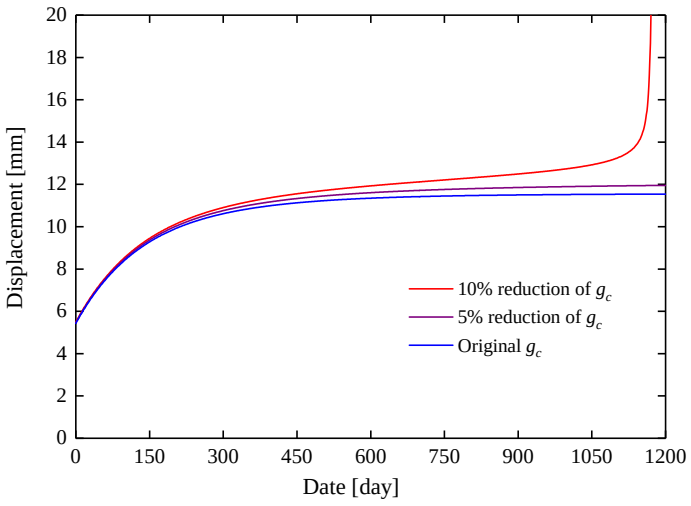

(a) Point PD14

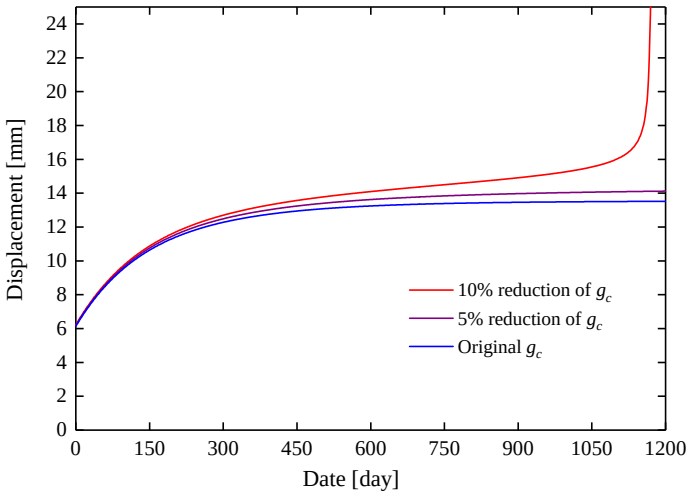

(b) Point PD28

Figure 6.20: Consequences of critical energy parameter g_c reduction on displacement evolution at two monitoring points

In order to better investigate the instability mechanism induced by the weakening of rock fracture resistance, in Figure 6.21, we show the damage variable distribution at six different time stages. One can see that at the first stage, the damage is mainly concentrated in the fault layer f_2 and the other zones are weakly affected by cracking process, as shown in Figure 6.21(a). Then, the damage zone propagates into the layer IV due to the increase of creep strains (see Figure 6.21(b)). There is further the coalescence of damage between these two layers causing macroscopic cracking (d close to 1) around the toe zone of the slope, as illustrated in Figure 6.21(c). From the stage d, the damaged zones propagate towards to the top region of the slope (see Figures 6.21(d) and 6.21(e)). Finally, in Figure 6.21(f), a large cracked band is formed and it leads to the instability of the slope.

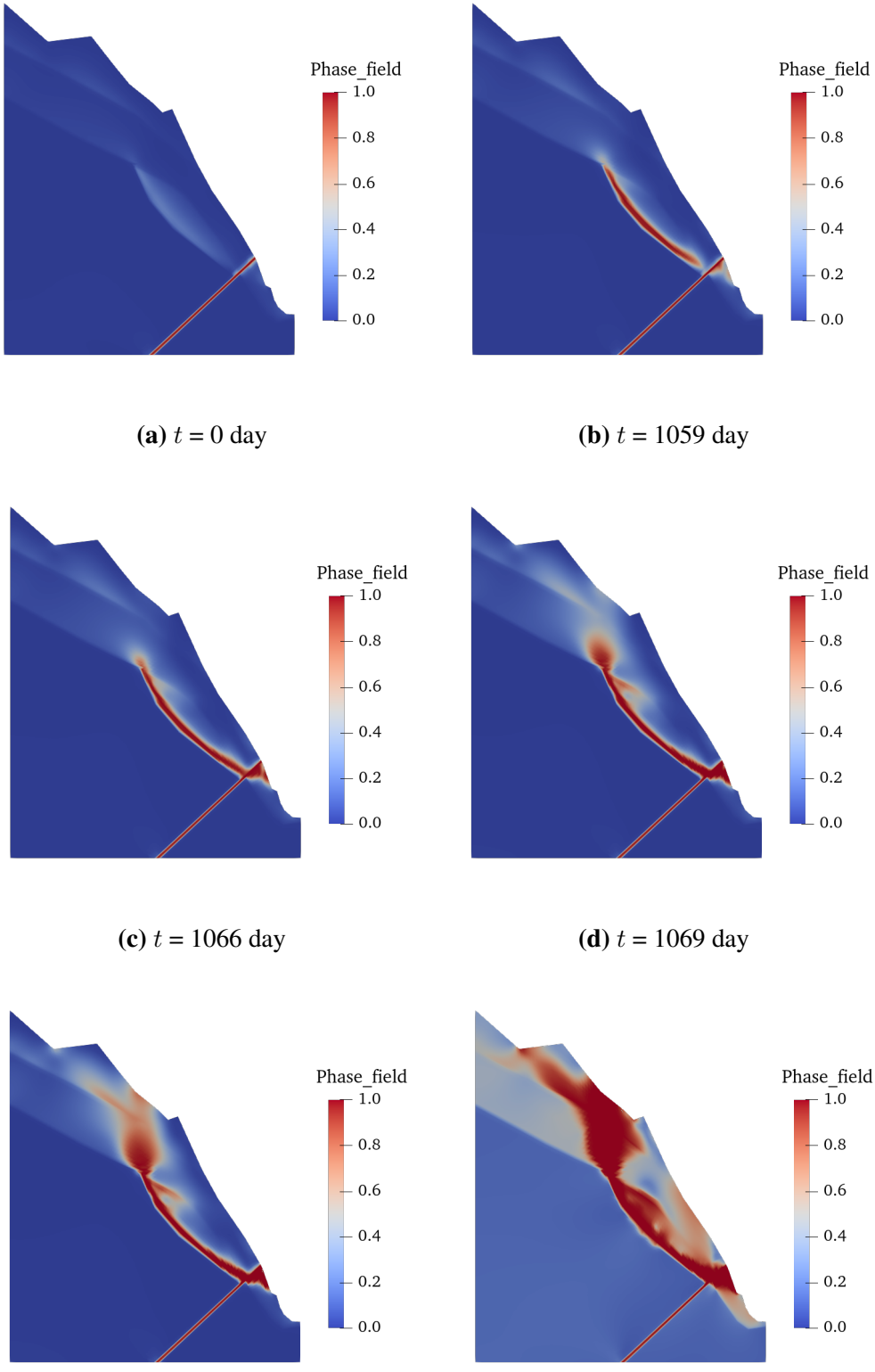

(a) t = 0 day **(b)** t = 1059 day

(c) t = 1066 day **(d)** t = 1069 day

(e) t = 1070 day **(f)** t = 1071 day

Figure 6.21: Evolution of damage distribution at six different time stages

5 Conclusion

In this chapter, the new phase-field model with damage-frictional coupling is firstly employed to predict the progressive failure of slope instability. The predicted slip surface has a quasi circle shape which seems to be very consistent with many field observation and to the classical instability study based on limit analysis methods.

Next, the proposed phase-field model for partially saturated media is applied to the analysis of rainfall induced deformation and failure of slopes. A simplified case and a real slope are investigated. The cracks patterns obtained from numerical modeling are qualitatively consistent with the field observations. The proposed model is able to capture the main physical mechanisms involved in the rainfall induced landslides. The pore water pressure rise due to rainfall modifies the distribution of effective stress in the slope and then the initial equilibrium condition. Tensile cracks can be directly induced by the pore water pressure rise. The diminution of effective normal stress facilitates the occurrence of shear cracks which are driven by the excessive shear stress. The growth of damage enhances the water infiltration kinetics in the cracked zones. At the scale of slopes, due to the existence of initial weak layers, the role of material heterogeneity becomes negligible.

Then, the short and long term deformation and cracking process of the left bank of Jinping hydropower station have been studied by applying the proposed phase-field model for modeling the time-dependent cracking process of rock-like materials. It can be found that the time-dependent evolution of damage or growth of micro-cracks is a key parameter controlling the long-term stability of structures. Moreover, there is a strong interaction between viscoplastic deformation and damage evolution. It is crucial to take into account this type of interaction in long-term stability analysis of slopes.

CONCLUSIONS AND PERSPECTIVES

1 Conclusions

This thesis has contributed to developing the phase-field method more suitable in modeling the onset and propagation of cracks in rock-like materials under different conditions. Accordingly, several novel phase-field models have been proposed in previous chapters to deal with the problems of fractures and cracks induced by different reasons. To be specifically, the contributions of new phase-field models are summarized as following.

First of all, the variational structure of a classical phase-field method with volumetric-deviatoric split of strain tensor has been presented. Besides, the implementation of this model in framework of finite element method has also been illustrated in detail. The material heterogeneity has been considered as the random distribution of inclusions in rock-like materials. According to the investigation of numerical triaxial tests with different inclusions distribution, it is found that the pattern of localized cracks is directly influenced by the spatial heterogeneity of elastic properties of the rock. The proposed method could capture the onset of crack localization automatically without artificial weak element.

Next, we proposed a new phase-field model formulated in a rigorous thermodynamics framework, which is able to describe open and closed cracks, smooth and frictional crack surfaces. The general continuity conditions at the crack opening- closure transition point are fully verified for the energy functions, the stress-strain relations, and the driving forces for crack propagation. The plastic sliding between closed fracture lips has also been considered in this model. The numerical assessments indicated that this model is able to physically take into account the influence of confining stress on the mechanical behavior of materials. Moreover, it also can describe the unloading-reloading hysteresis loop correctly. The ability to describe tensile, shear and mixed modes of cracking has been verified either. Further, the numerical predictions of failure patterns are very consistent with most experimental observations such as crack propagation deviation and crack bridging.

Then, a viscous phase-field method coupling with a viscoplastic model has been introduced to take the progressive growth of cracks and viscoelastic and/or viscoplastic

deformation into account. In this model, the progressive growth of cracks is driven by the viscoplastic deformation and the induced phase field affects the degradation of the threshold of viscoplastic flow. Its efficiency is assessed through comparisons with laboratory tests both of the short and long term mechanical behavior. The results in this thesis shows that the time-dependent evolution of damage or growth of micro-cracks is a key parameter controlling the long-term stability of those materials with viscoplastic. Moreover, there is a strong interaction between viscoplastic deformation and damage evolution.

In addition, the onset and propagation of cracks in saturated and unsaturated rock-like porous materials is numerical modeled by an extended phase-field method. The tensile, shear, and mixed cracks are represented by two independent phase-field variables in this model. The coupling between the pore pressure and evolution of fractures is also considered for both saturated and unsaturated conditions. The proposed model is then applied to describe the deformation and progressive failure process of brittle rocks in the laboratory scale. It is proved that the mechanical driving cracks and drying induced cracks are well reproduced by the proposed phase-field model.

All these new phase-field models are applied to analyze the stability of slopes with different engineering conditions. The first application is modeling the failure surface in a slope with vertical displacement loading at the slope crest. The frictional slip has been considered. It successfully reproduced a similar slip surface with one indicated by traditional limit analysis methods. Second, the rainfall-induced landslides have been studied by the phase-field model for saturated and unsaturated rock-like porous materials. The numerical results of cracking scenarios are consistent with the real field observations. Then, the model coupling with viscoplastic is applied to modeling time-dependent deformation and failure process of a high slope section. The efficiency of this model is verified by comparing the numerical results with field measurements.

In summary, this thesis provides several new phase-field methods to numerical modeling the onset and propagation of cracks in rock-like materials with complex conditions. The potential of these models are also been demonstrated.

2 Perspectives

There are still several extensions of the present works in modeling the initiation and growth of cracks in rock-like materials and geological engineering structures.

In present study, all the system has been assumed to be a static or quasi-static process. However, the geological engineering problems usually involve significant dynamic effects. For instance, the flow of fluids in porous materials has been treated as a dynamic problem in our works. Therefore, establishing the dynamic formulations for both displacement field and phase field is a valuable research topic for more accurate simulation of landslides.

In practice, the models proposed in this thesis are valid in three-dimensional conditions. While all the examples in our works are in two-dimensions. Thus, the numerical example in three-dimensional should be carried out in a near future.

Alternatively, most geomechanical and geological engineering problems contain a high degree of uncertainty on input data. It is crucial and desirable to perform a comprehensive uncertainty analysis in order to identify the key parameters controlling the rainfall-induced or time-dependent landslides. Furthermore, the weakening effect of water saturation on the fracture toughness of rocks is another key factor to be taken into account. This constitutes an interesting challenge in our future work.

On the other hand, it is very important for analysis of landslides to know the situation after broken. However, the present phase-field models are implemented in framework of finite element method (FEM) which could cause the difficulties in calculation with large deformation. Consequently, implementing the phase-field model in other numerical method such as material point method (MPM) (de Vaucorbeil et al., 2020) which could address the issues of large deformation for FEM.

REFERENCES

Agathos, K., Bordas, S.P.A., Chatzi, E., 2019. Improving the conditioning of xfem/gfem for fracture mechanics problems through enrichment quasi-orthogonalization. Computer Methods in Applied Mechanics and Engineering 346, 1051–1073. doi:10.1016/j.cma.2018.08.007.

Aldakheel, F., Noii, N., Wick, T., Wriggers, P., 2021. A global–local approach for hydraulic phase-field fracture in poroelastic media. Computers & Mathematics with Applications 91, 99–121. doi:10.1016/j.camwa.2020.07.013.

Alessi, R., Marigo, J.J., Vidoli, S., 2015. Gradient damage models coupled with plasticity: Variational formulation and main properties. Mechanics of Materials 80, 351–367. doi:10.1016/j.mechmat.2013.12.005.

Alliche, A., 2016. A continuum anisotropic damage model with unilateral effect. Mechanical Sciences 7, 61–68. doi:10.5194/ms-7-61-2016.

Ambati, M., Gerasimov, T., De Lorenzis, L., 2015. A review on phase-field models of brittle fracture and a new fast hybrid formulation. Computational Mechanics 55, 383–405. doi:10.1007/s00466-014-1109-y.

Ambrosio, L., Tortorelli, V.M., 1990. Approximation of functional depending on jumps by elliptic functional via t-convergence. Communications on Pure and Applied Mathematics 43, 999–1036. doi:10.1002/cpa.3160430805.

Amor, H., Marigo, J.J., Maurini, C., 2009. Regularized formulation of the variational brittle fracture with unilateral contact: Numerical experiments. Journal of the Mechanics and Physics of Solids 57, 1209–1229. doi:10.1016/j.jmps.2009.04.011.

Armero, F., Garikipati, K., 1996. An analysis of strong discontinuities in multiplicative finite strain plasticity and their relation with the numerical simulation of strain localization in solids. International Journal of Solids and Structures 33, 2863–2885. doi:10.1016/0020-7683(95)00257-X.

Armero, F., Linder, C., 2009. Numerical simulation of dynamic fracture using finite elements with embedded discontinuities. International Journal of Fracture 160, 119–141. doi:10.1007/s10704-009-9413-9.

Atkinson, B.K., 1982. Subcritical crack propagation in rocks: Theory, experimental results and applications. Journal of Structural Geology 4, 41–56. doi:10.1016/0191-8141(82)90005-0.

Atkinson, B.K., 1984. Subcritical crack growth in geological materials. Journal of Geophysical Research: Solid Earth 89, 4077–4114. doi:10.1029/JB089iB06p04077.

Babuska, I., Oden, J., 2004. Verification and validation in computational engineering and science: Basic concepts. Computer Methods in Applied Mechanics and Engineering 193, 4057–4066. doi:10.1016/j.cma.2004.03.002.

Belytschko, T., Black, T., 1999. Elastic crack growth in finite elements with minimal remeshing. International Journal for Numerical Methods in Engineering 45, 601–620. doi:10.1002/(SICI)1097-0207(19990620)45:5<601::AID-NME598>3.0.CO;2-S.

Belytschko, T., Fish, J., Engelmann, B.E., 1988. A finite element with embedded localization zones. Computer Methods in Applied Mechanics and Engineering 70, 59–89. doi:10.1016/0045-7825(88)90180-6.

Bishop, A.W., 1959. The principle of effective stress. Teknisk ukeblad 39, 859–863.

Bobaru, F., Duangpanya, M., 2012. A peridynamic formulation for transient heat conduction in bodies with evolving discontinuities. Journal of Computational Physics 231, 2764–2785. doi:10.1016/j.jcp.2011.12.017.

Bonini, M., Debernardi, D., Barla, M., Barla, G., 2007. The mechanical behaviour of clay shales and implications on the design of tunnels. Rock Mechanics and Rock Engineering 42, 361. doi:10.1007/s00603-007-0147-6.

Borden, M.J., Hughes, T.J.R., Landis, C.M., Anvari, A., Lee, I.J., 2016. A phase-field formulation for fracture in ductile materials: Finite deformation balance law derivation, plastic degradation, and stress triaxiality effects. Computer Methods in Applied Mechanics and Engineering 312, 130–166. doi:10.1016/j.cma.2016.09.005.

Borden, M.J., Verhoosel, C.V., Scott, M.A., Hughes, T.J.R., Landis, C.M., 2012. A phase-field description of dynamic brittle fracture. Computer Methods in Applied Mechanics and Engineering 217–220, 77–95. doi:10.1016/j.cma.2012.01.008.

Borja, R.I., 2000. A finite element model for strain localization analysis of strongly discontinuous fields based on standard galerkin approximation. Computer Methods in Applied Mechanics and Engineering 190, 1529–1549. doi:10.1016/S0045-7825(00)00176-6.

Borja, R.I., 2008. Assumed enhanced strain and the extended finite element methods: A unification of concepts. Computer Methods in Applied Mechanics and Engineering 197, 2789–2803. doi:10.1016/j.cma.2008.01.019.

Bourdin, B., Chukwudozie, C., Yoshioka, K., 2012. A variational approach to the numerical simulation of hydraulic fracturing, in: All Days, SPE, San Antonio, Texas, USA. pp. SPE–159154–MS. doi:10.2118/159154-MS.

Bourdin, B., Francfort, G.A., Marigo, J.J., 2000. Numerical experiments in revisited brittle fracture. Journal of the Mechanics and Physics of Solids 48, 797–826. doi:10.1016/S0022-5096(99)00028-9.

Bourdin, B., Francfort, G.A., Marigo, J.J., 2008. The variational approach to fracture. Journal of Elasticity 91, 5–148. doi:10.1007/s10659-007-9107-3.

Bryant, E.C., Sun, W., 2018. A mixed-mode phase field fracture model in anisotropic rocks with consistent kinematics. Computer Methods in Applied Mechanics and Engineering 342, 561–584. doi:10.1016/j.cma.2018.08.008.

Budiansky, B., O'connell, R.J., 1976. Elastic moduli of a cracked solid. International Journal of Solids and Structures 12, 81–97. doi:10.1016/0020-7683(76)90044-5.

Burt, N.J., Dougill, J.W., 1977. Progressive failure in a model heterogeneous medium. Journal of the Engineering Mechanics Division 103, 365–376. doi:10.1061/JMCEA3.0002234.

Cai, M., Horii, H., 1993. A constitutive model and fem analysis of jointed rock masses. International Journal of Rock Mechanics and Mining Sciences & Geomechanics Abstracts 30, 351–359. doi:10.1016/0148-9062(93)91719-Y.

Cajuhi, T., Sanavia, L., De Lorenzis, L., 2018. Phase-field modeling of fracture in variably saturated porous media. Computational Mechanics 61, 299–318. doi:10.1007/s00466-017-1459-3.

Callari, C., Abati, A., 2009. Finite element methods for unsaturated porous solids and their application to dam engineering problems. Computers & Structures 87, 485–501. doi:10.1016/j.compstruc.2008.12.012.

Cao, R.h., Cao, P., Lin, H., Fan, X., Zhang, C., Liu, T., 2019. Crack initiation, propagation, and failure characteristics of jointed rock or rock-like specimens: A review. Advances in Civil Engineering 2019, 1–31. doi:10.1155/2019/6975751.

Chaboche, J.L., 1988. Continuum damage mechanics: Part i—general concepts. Journal of Applied Mechanics 55, 59–64. doi:10.1115/1.3173661.

Chambon, R., Caillerie, D., Matsuchima, T., 2001. Plastic continuum with microstructure, local second gradient theories for geomaterials: Localization studies. International Journal of Solids and Structures 38, 8503–8527. doi:10.1016/S0020-7683(01)00057-9.

Chang, W.J., Chou, S.H., Huang, H.P., Chao, C.Y., 2021. Development and verification of coupled hydro-mechanical analysis for rainfall-induced shallow landslides. Engineering Geology 293, 106337. doi:10.1016/j.enggeo.2021.106337.

Chen, H., Qin, S., Xue, L., Xu, C., 2021. Why the xintan landslide was not triggered by the heaviest historical rainfall: Mechanism and review. Engineering Geology 294, 106379. doi:10.1016/j.enggeo.2021.106379.

Chen, L., Wang, C.P., Liu, J.F., Liu, J., Wang, J., Jia, Y., Shao, J.F., 2015. Damage and plastic deformation modeling of beishan granite under compressive stress conditions. Rock Mechanics and Rock Engineering 48, 1623–1633. doi:10.1007/s00603-014-0650-5.

Cheng, D., Cui, Y., Su, F., Jia, Y., Choi, C.E., 2018. The characteristics of the mocoa compound disaster event, colombia. Landslides 15, 1223–1232. doi:10.1007/s10346-018-0969-1.

Cho, S.E., 2020. Failure distribution analysis of shallow landslides under rainfall infiltration based on fragility curves. Landslides 17, 79–91. doi:10.1007/s10346-019-01257-w.

Choo, J., Sun, W., 2018. Coupled phase-field and plasticity modeling of geological materials: From brittle fracture to ductile flow. Computer Methods in Applied Mechanics and Engineering 330, 1–32. doi:10.1016/j.cma.2017.10.009.

Chow, C.L., Wang, J., 1987. An anisotropic theory of elasticity for continuum damage mechanics. International Journal of Fracture 33, 3–16. doi:10.1007/BF00034895.

Cormery, F., Welemane, H., 2002. A critical review of some damage models with unilateral effect. Mechanics Research Communications 29, 391–395. doi:10.1016/S0093-6413(02)00262-8.

Costin, L.S., 1985. Time-Dependent Damage and Creep of Brittle Rock. Technical Report SAND-84-2244C; CONF-851039-1. Sandia National Labs., Albuquerque, NM (USA).

Coussy, O., 2010. Mechanics and Physics of Porous Solids. John Wiley & Sons, Ltd, Chichester, UK. doi:10.1002/9780470710388.

Cristescu, N., Gioda, G., et al., 1994. Visco-Plastic Behaviour of Geomaterials. Springer.

Cuomo, S., Di Perna, A., Martinelli, M., 2021. Modelling the spatio-temporal evolution of a rainfall-induced retrogressive landslide in an unsaturated slope. Engineering Geology 294, 106371. doi:10.1016/j.enggeo.2021.106371.

De Borst, R., Mühlhaus, H.B., 1992. Gradient-dependent plasticity: Formulation and algorithmic aspects. International Journal for Numerical Methods in Engineering 35, 521–539. doi:10.1002/nme.1620350307.

de Vaucorbeil, A., Nguyen, V.P., Sinaie, S., Wu, J.Y., 2020. Material point method after 25 years: Theory, implementation, and applications, in: Advances in Applied Mechanics. Elsevier. volume 53, pp. 185–398. doi:10.1016/bs.aams.2019.11.001.

Debernardi, D., Barla, G., 2009. New viscoplastic model for design analysis of tunnels in squeezing conditions. Rock Mechanics and Rock Engineering 42, 259. doi:10.1007/s00603-009-0174-6.

Desmorat, R., 2016. Anisotropic damage modeling of concrete materials. International Journal of Damage Mechanics 25, 818–852. doi:10.1177/1056789515606509.

Dias-da-Costa, D., Alfaiate, J., Sluys, L.J., Júlio, E., 2010. A comparative study on the modelling of discontinuous fracture by means of enriched nodal and element techniques and interface elements. International Journal of Fracture 161, 97–119. doi:10.1007/s10704-009-9432-6.

Diehl, P., Lipton, R., Wick, T., Tyagi, M., 2022. A comparative review of peridynamics and phase-field models for engineering fracture mechanics. Computational Mechanics 69. doi:10.1007/s00466-022-02147-0.

Dragon, A., Halm, D., Désoyer, T., 2000. Anisotropic damage in quasi-brittle solids: Modelling, computational issues and applications. Computer Methods in Applied Mechanics and Engineering 183, 331–352. doi:10.1016/S0045-7825(99)00225-X.

Dragon, A., Mróz, Z., 1979. A continuum model for plastic-brittle behaviour of rock and concrete. International Journal of Engineering Science 17, 121–137. doi:10.1016/0020-7225(79)90058-2.

Dramis, F., Farabollini, P., Gentili, B., Pambianchi, G., 2002. Neotectonics and large-scale gravitational phenomena in the umbria–marche apennines, italy, in: Seismically Induced Ground Ruptures and Large Scale Mass Movements. Field Excursion and Meeting 21–27 September 2001, Citeseer. pp. 17–30.

Dvorkin, E.N., Cuitiño, A.M., Gioia, G., 1990. Finite elements with displacement interpolated embedded localization lines insensitive to mesh size and distortions. International Journal for Numerical Methods in Engineering 30, 541–564. doi:10.1002/nme.1620300311.

Eker, R., Aydın, A., 2021. Long-term retrospective investigation of a large, deep-seated, and slow-moving landslide using insar time series, historical aerial photographs, and uav data: The case of devrek landslide (nw turkey). CATENA 196, 104895. doi:10.1016/j.catena.2020.104895.

Evans, B., Fredrich, J.T., Wong, T.F., 1990. The brittle-ductile transition in rocks: Recent experimental and theoretical progress, in: The Brittle-Ductile Transition in Rocks. American Geophysical Union (AGU), pp. 1–20. doi:10.1029/GM056p0001.

Fabre, G., Pellet, F., 2006. Creep and time-dependent damage in argillaceous rocks. International Journal of Rock Mechanics and Mining Sciences 43, 950–960. doi:10.1016/j.ijrmms.2006.02.004.

Fan, X., Xu, Q., Scaringi, G., Dai, L., Li, W., Dong, X., Zhu, X., Pei, X., Dai, K., Havenith, H.B., 2017. Failure mechanism and kinematics of the deadly june 24th 2017 xinmo landslide, maoxian, sichuan, china. Landslides 14, 2129–2146. doi:10.1007/s10346-017-0907-7.

Fei, F., Choo, J., 2020a. A phase-field method for modeling cracks with frictional contact. International Journal for Numerical Methods in Engineering 121, 740–762. doi:10.1002/nme.6242.

Fei, F., Choo, J., 2020b. A phase-field model of frictional shear fracture in geologic materials. Computer Methods in Applied Mechanics and Engineering 369, 113265. doi:10.1016/j.cma.2020.113265.

Fei, F., Choo, J., 2021. Double-phase-field formulation for mixed-mode fracture in rocks. Computer Methods in Applied Mechanics and Engineering 376, 113655. doi:10.1016/j.cma.2020.113655.

Fourie, A.B., 1996. Predicting rainfall-induced slope instability. Proceedings of the Institution of Civil Engineers - Geotechnical Engineering 119, 211–218. doi:10.1680/igeng.1996.28757.

Fourie, A.B., Rowe, D., Blight, G.E., 1999. The effect of inæltration on the stability of the slopes of a dry ash dump. Géotechnique 49, 1–13. doi:10.1680/geot.1999.49.1.1.

Francfort, G.A., Marigo, J.J., 1998. Revisiting brittle fracture as an energy minimization problem. Journal of the Mechanics and Physics of Solids 46, 1319–1342. doi:10.1016/S0022-5096(98)00034-9.

Frantziskonis, G., Desai, C.S., 1987. Elastoplastic model with damage for strain softening geomaterials. Acta Mechanica 68, 151–170. doi:10.1007/BF01190880.

Frattini, P., Crosta, G., Sosio, R., 2009. Approaches for defining thresholds and return periods for rainfall-triggered shallow landslides. Hydrological Processes 23, 1444–1460. doi:10.1002/hyp.7269.

Fredlund, D.G., Rahardjo, H., 1993. Soil Mechanics for Unsaturated Soils. John Wiley & Sons.

Gambarotta, L., 2004. Friction-damage coupled model for brittle materials. Engineering Fracture Mechanics 71, 829–836. doi:10.1016/S0013-7944(03)00020-1.

Gao, Y., Yin, Y., Li, B., Feng, Z., Wang, W., Zhang, N., Xing, A., 2017. Characteristics and numerical runout modeling of the heavy rainfall-induced catastrophic landslide–debris flow at sanxicun, dujiangyan, china, following the wenchuan ms 8.0 earthquake. Landslides 14, 1361–1374. doi:10.1007/s10346-016-0793-4.

Gavagnin, C., Sanavia, L., De Lorenzis, L., 2020. Stabilized mixed formulation for phase-field computation of deviatoric fracture in elastic and poroelastic materials. Computational Mechanics 65, 1447–1465. doi:10.1007/s00466-020-01829-x.

Gerasimov, T., De Lorenzis, L., 2016. A line search assisted monolithic approach for phase-field computing of brittle fracture. Computer Methods in Applied Mechanics and Engineering 312, 276–303. doi:10.1016/j.cma.2015.12.017.

Gerstle, W., Sau, N., Silling, S., 2007. Peridynamic modeling of concrete structures. Nuclear Engineering and Design 237, 1250–1258. doi:10.1016/j.nucengdes.2006.10.002.

Goswami, S., Anitescu, C., Chakraborty, S., Rabczuk, T., 2020. Transfer learning enhanced physics informed neural network for phase-field modeling of fracture. Theoretical and Applied Fracture Mechanics 106, 102447. doi:10.1016/j.tafmec.2019.102447.

Gravouil, A., Moës, N., Belytschko, T., 2002. Non-planar 3d crack growth by the extended finite element and level sets—part ii: Level set update. International Journal for Numerical Methods in Engineering 53, 2569–2586. doi:10.1002/nme.430.

Griffith, A.A., 1921. The phenomena of rupture and flow in solids. Philosophical Transactions of the Royal Society of London. Series A, Containing Papers of a Mathematical or Physical Character 221, 163–198. doi:10.1098/rsta.1921.0006.

Gurson, A.L., 1977. Continuum theory of ductile rupture by void nucleation and growth: Part i—yield criteria and flow rules for porous ductile media. Journal of Engineering Materials and Technology 99, 2–15. doi:10.1115/1.3443401.

Halm, D., Dragon, A., 1996. A model of anisotropic damage by mesocrack growth; unilateral effect. International Journal of Damage Mechanics 5, 384–402. doi:10.1177/105678959600500403.

Halm, D., Dragon, A., 1998. An anisotropic model of damage and frictional sliding for brittle materials. European Journal of Mechanics - A/Solids 17, 439–460. doi:10.1016/S0997-7538(98)80054-5.

Haque, U., da Silva, P.F., Devoli, G., Pilz, J., Zhao, B., Khaloua, A., Wilopo, W., Andersen, P., Lu, P., Lee, J., Yamamoto, T., Keellings, D., Wu, J.H., Glass, G.E., 2019. The human cost of global warming: Deadly landslides and their triggers (1995–2014). Science of The Total Environment 682, 673–684. doi:10.1016/j.scitotenv.2019.03.415.

Hashin, Z., 1988. The differential scheme and its application to cracked materials. Journal of the Mechanics and Physics of Solids 36, 719–734. doi:10.1016/0022-5096(88)90005-1.

Hayhurst, D.R., 1972. Creep rupture under multi-axial states of stress. Journal of the Mechanics and Physics of Solids 20, 381–382. doi:10.1016/0022-5096(72)90015-4.

He, W., Wu, Y.F., Xu, Y., Fu, T.T., 2015. A thermodynamically consistent nonlocal damage model for concrete materials with unilateral effects. Computer Methods in Applied Mechanics and Engineering 297, 371–391. doi:10.1016/j.cma.2015.09.010.

Heider, Y., 2021. A review on phase-field modeling of hydraulic fracturing. Engineering Fracture Mechanics 253, 107881. doi:10.1016/j.engfracmech.2021.107881.

Heider, Y., Markert, B., 2017. A phase-field modeling approach of hydraulic fracture in saturated porous media. Mechanics Research Communications 80, 38–46. doi:10.1016/j.mechrescom.2016.07.002.

Heider, Y., Sun, W., 2020. A phase field framework for capillary-induced fracture in unsaturated porous media: Drying-induced vs. hydraulic cracking. Computer Methods in Applied Mechanics and Engineering 359, 112647. doi:10.1016/j.cma.2019.112647.

Henry, J.P., Paquet, J., Tancrez, J.P., 1977. Experimental study of crack propagation in calcite rocks. International Journal of Rock Mechanics and Mining Sciences & Geomechanics Abstracts 14, 85–91. doi:10.1016/0148-9062(77)90200-5.

Hofacker, M., Miehe, C., 2013. A phase field model of dynamic fracture: Robust field updates for the analysis of complex crack patterns. International Journal for Numerical Methods in Engineering 93, 276–301. doi:10.1002/nme.4387.

Homand-Etienne, F., Hoxha, D., Shao, J.F., 1998. A continuum damage constitutive law for brittle rocks. Computers and Geotechnics 22, 135–151. doi:10.1016/S0266-352X(98)00003-2.

Horii, H., Nemat-Nasser, S., 1983. Overall moduli of solids with microcracks: Load-induced anisotropy. Journal of the Mechanics and Physics of Solids 31, 155–171. doi:10.1016/0022-5096(83)90048-0.

Hu, K., Shao, J.F., Zhu, Q.Z., Zhao, L.y., Wang, W., Wang, R.B., 2020. A micromechanics-based elastoplastic friction-damage model for brittle rocks and its application in deformation analysis of the left bank slope of jinping i hydropower station. Acta Geotechnica 15, 3443–3460. doi:10.1007/s11440-020-00977-x.

Hu, K., Zhu, Q.z., Chen, L., Shao, J.f., Liu, J., 2018. A micromechanics-based elastoplastic damage model for rocks with a brittle–ductile transition in mechanical response. Rock Mechanics and Rock Engineering 51, 1729–1737. doi:10.1007/s00603-018-1427-z.

Huang, R., Lin, F., Yan, M., 2010. Deformation mechanism and stability evaluation for the left abutment slope of jinping i hydropower station. Bulletin of Engineering Geology and the Environment 69, 365–372. doi:10.1007/s10064-010-0283-1.

Huespe, A.E., Oliver, J., Sanchez, P.J., Blanco, S., Sonzogni, V., 2006. Strong discontinuity approach in dynamic fracture simulations. Mecánica Computacional , 1997–2018.

Huining, X., Zhong, Z., Jin, X., Haonan, R., Ming, N., Lu, W., Hanhuai, Z., Jingxi, Y., 2013. Experimental study of weakening effect of high water head on weak rock masses from jinping i hydropower station. Chinese Journal of Rock Mechanics and Engineering 32, 4207–4214.

Hult, J., 1974. Creep in continua and structures, in: Zeman, J.L., Ziegler, F. (Eds.), Topics in Applied Continuum Mechanics, Springer, Vienna. pp. 137–155. doi:10.1007/978-3-7091-4188-5_7.

Hun, D.A., 2020. Fracture Modeling in Clay Materials under Hydric shrinkageModélisation de Fissure Dans Les Matériaux Argileux Sous Retrait Hydrique : Numerical Models, Comparisons with Experiments and Stochastic Aspects. Ph.D. thesis. Université Paris-Est.

Hun, D.A., Guilleminot, J., Yvonnet, J., Bornert, M., 2019. Stochastic multiscale modeling of crack propagation in random heterogeneous media. International Journal for Numerical Methods in Engineering 119, 1325–1344. doi:10.1002/nme.6093.

Intrieri, E., Carlà, T., Gigli, G., 2019. Forecasting the time of failure of landslides at slope-scale: A literature review. Earth-Science Reviews 193, 333–349. doi:10.1016/j.earscirev.2019.03.019.

Irfan, M., Uchimura, T., Chen, Y., 2017. Effects of soil deformation and saturation on elastic wave velocities in relation to prediction of rain-induced landslides. Engineering Geology 230, 84–94. doi:10.1016/j.enggeo.2017.09.024.

Jefferson, A.D., Mihai, I.C., 2015. The simulation of crack opening–closing and aggregate interlock behaviour in finite element concrete models. International Journal for Numerical Methods in Engineering 104, 48–78. doi:10.1002/nme.4934.

Jia, C., Zhang, Q., Wang, S., 2020. Experimental investigation and micromechanical modeling of elastoplastic damage behavior of sandstone. Materials 13, 3414. doi:10.3390/ma13153414.

Jiang, L., Sun, J.H., Wang, W.S., 2012. Study on deformation and stability of high slope with weak intercalated layers. Applied Mechanics and Materials 204–208, 3142–3145. doi:10.4028/www.scientific.net/AMM.204-208.3142.

Jiang, L., Yu, H., Sun, J., Wang, W., Zhu, Z., 2013. Study on stability and field test of mayanpo slope at xiangjiaba hydropower station. Water Resources and Hydropower Engineering , 01doi:10.13928/j.cnki.wrahe.2013.01.030.

Jirásek, M., 2000. Comparative study on finite elements with embedded discontinuities. Computer Methods in Applied Mechanics and Engineering 188, 307–330. doi:10.1016/S0045-7825(99)00154-1.

Jirásek, M., Belytschko, T., 2002. Computational Resolution of Strong Discontinuities.

Jirásek, M., Patzák, B., 2002. Consistent tangent stiffness for nonlocal damage models. Computers & Structures 80, 1279–1293. doi:10.1016/S0045-7949(02)00078-0.

Ju, J.W., 1990. Isotropic and anisotropic damage variables in continuum damage mechanics. Journal of Engineering Mechanics 116, 2764–2770. doi:10.1061/(ASCE)0733-9399(1990)116:12(2764).

Ju, J.W., Chen, T.M., 1994. Effective elastic moduli of two-dimensional brittle solids with interacting microcracks, part i: Basic formulations. Journal of Applied Mechanics 61, 349–357. doi:10.1115/1.2901451.

Kachanov, L.M., 1958. Time of the rupture process under creep conditions, izy akad. Nank S. S. R. Otd Tech Nauk 8, 26–31.

Karma, A., Kessler, D.A., Levine, H., 2001. Phase-field model of mode iii dynamic fracture. Physical Review Letters 87, 045501. doi:10.1103/PhysRevLett.87.045501.

Khalil, Z., Elghazouli, A., Martínez Pañeda, E., 2022. A generalised phase field model for fatigue crack growth in elastic-plastic solids with an efficient monolithic solver. Computer Methods in Applied Mechanics and Engineering 388, 114286. doi:10.1016/j.cma.2021.114286.

Kilic, B., Agwai, A., Madenci, E., 2009. Peridynamic theory for progressive damage prediction in center-cracked composite laminates. Composite Structures 90, 141–151. doi:10.1016/j.compstruct.2009.02.015.

Kim, J., Jeong, S., Regueiro, R.A., 2012. Instability of partially saturated soil slopes due to alteration of rainfall pattern. Engineering Geology 147–148, 28–36. doi:10.1016/j.enggeo.2012.07.005.

Kinoshita, N., Mura, T., 1971. Elastic fields of inclusions in anisotropic media. physica status solidi (a) 5, 759–768. doi:10.1002/pssa.2210050332.

Klinsmann, M., Rosato, D., Kamlah, M., McMeeking, R.M., 2015. An assessment of the phase field formulation for crack growth. Computer Methods in Applied Mechanics and Engineering 294, 313–330. doi:10.1016/j.cma.2015.06.009.

Knighton, D., 1998. Fluvial Forms and Processes: A New Perspective. Second ed., Routledge, London. doi:10.4324/9780203784662.

Krajcinovic, D., Fonseka, G.U., 1981. The continuous damage theory of brittle materials, part 1: General theory. Journal of Applied Mechanics 48, 809–815. doi:10.1115/1.3157739.

Krajcinovic, D., Silva, M.A.G., 1982. Statistical aspects of the continuous damage theory. International Journal of Solids and Structures 18, 551–562. doi:10.1016/0020-7683(82)90039-7.

Kuhn, C., Müller, R., 2008. A phase field model for fracture. PAMM 8, 10223–10224. doi:10.1002/pamm.200810223.

Kuhn, C., Müller, R., 2010. A continuum phase field model for fracture. Engineering Fracture Mechanics 77, 3625–3634. doi:10.1016/j.engfracmech.2010.08.009.

Kuhn, C., Schluter, A., Muller, R., 2015. On degradation functions in phase field fracture models. Computational Materials Science 108, 374–384.

Kukemilks, K., Wagner, J.F., Saks, T., Brunner, P., 2018. Physically based hydrogeological and slope stability modeling of the turaida castle mound. Landslides 15, 2267–2278. doi:10.1007/s10346-018-1038-5.

Lancioni, G., Royer-Carfagni, G., 2009. The variational approach to fracture mechanics. a practical application to the french panthéon in paris. Journal of Elasticity 95, 1–30. doi:10.1007/s10659-009-9189-1.

Lanoye, E., Cormery, F., Kondo, D., Shao, J., 2013. An isotropic unilateral damage model coupled with frictional sliding for quasi-brittle materials. Mechanics Research Communications 53, 31–35. doi:10.1016/j.mechrescom.2013.07.009.

Lee, S., Wheeler, M.F., Wick, T., 2017. Iterative coupling of flow, geomechanics and adaptive phase-field fracture including level-set crack width approaches. Journal of Computational and Applied Mathematics 314, 40–60. doi:10.1016/j.cam.2016.10.022.

Lemaitre, J., 1985. A continuous damage mechanics model for ductile fracture. Journal of Engineering Materials and Technology 107, 83–89. doi:10.1115/1.3225775.

Lemaitre, J., 1986. Local approach of fracture. Engineering Fracture Mechanics 25, 523–537. doi:10.1016/0013-7944(86)90021-4.

Lewis, R.W., Schrefler, B.A., Lewis, R.W., 1998. The Finite Element Method in the Static and Dynamic Deformation and Consolidation of Porous Media. 2nd ed ed., John Wiley, Chichester ; New York.

Li, C., Wang, M., Liu, K., 2018. A decadal evolution of landslides and debris flows after the wenchuan earthquake. Geomorphology 323, 1–12. doi:10.1016/j.geomorph.2018.09.010.

Li, L., Jin, Y., Jia, Y., Rougelot, T., Burlion, N., Shao, J., 2020a. Influence of inclusion rigidity on shrinkage induced micro-cracking of cementitious materials. Cement and Concrete Composites 114, 103773. doi:10.1016/j.cemconcomp.2020.103773.

Li, P., Yvonnet, J., Combescure, C., 2020b. An extension of the phase field method to model interactions between interfacial damage and brittle fracture in elastoplastic composites. International Journal of Mechanical Sciences 179, 105633. doi:10.1016/j.ijmecsci.2020.105633.

Li, Z., Zhu, Q.h., Tian, B.l., Sun, T.f., Yang, D.w., 2017. A damage model for hard rock under stress-induced failure mode, in: Advanced Engineering and Technology III: Proceedings of the 3rd Annual Congress on Advanced Engineering and Technology (CAET 2016), Hong Kong, 22-23 October 2016, CRC Press. p. 87.

Liakopoulos, A.C., 1964. Transient Flow through Unsaturated Porous Media. Ph.D. thesis. University of California. Berkeley.

Lin, F., Wu, L.Z., Huang, R.Q., Zhang, H., 2018. Formation and characteristics of the xiaoba landslide in fuquan, guizhou, china. Landslides 15, 669–681. doi:10.1007/s10346-017-0897-5.

Ling, H.I., Wu, M.H., Leshchinsky, D., Leshchinsky, B., 2009. Centrifuge modeling of slope instability. Journal of Geotechnical and Geoenvironmental Engineering 135, 758–767. doi:10.1061/(ASCE)GT.1943-5606.0000024.

Liu, X.Y., Xiao, Q.Z., Karihaloo, B.L., 2004. Xfem for direct evaluation of mixed mode sifs in homogeneous and bi-materials. International Journal for Numerical Methods in Engineering 59, 1103–1118. doi:10.1002/nme.906.

Liu, Z., Shao, J., 2017. Strength behavior, creep failure and permeability change of a tight marble under triaxial compression. Rock Mechanics and Rock Engineering 50, 529–541. doi:10.1007/s00603-016-1134-6.

Loew, P.J., Peters, B., Beex, L.A., 2019. Rate-dependent phase-field damage modeling of rubber and its experimental parameter identification. Journal of the Mechanics and Physics of Solids 127, 266–294. doi:10.1016/j.jmps.2019.03.022.

Løland, K.E., 1980. Continuous damage model for load-response estimation of concrete. Cement and Concrete Research 10, 395–402. doi:10.1016/0008-8846(80)90115-5.

Lorentz, E., 2017. A nonlocal damage model for plain concrete consistent with cohesive fracture. International Journal of Fracture 207, 123–159. doi:10.1007/s10704-017-0225-z.

Lu, Y., Shao, J., 2002. Modelling of anisotropic damage in brittle rocks under compression dominated stresses. International Journal for Numerical and Analytical Methods in Geomechanics 26, 945–961. doi:10.1002/nag.230.

Luo, Z., Zhu, Z., Ruan, H., Shi, C., 2015. Extraction of microcracks in rock images based on heuristic graph searching and application. Computers & Geosciences 85, 22–35. doi:10.1016/j.cageo.2015.08.013.

Mandal, T.K., 2021. Phase Field Fracture Modelling of Solids: Dynamics, Anisotropy, and Multi-Physics. Thesis. Monash University. doi:10.26180/16834729.v1.

Mandal, T.K., Nguyen, V.P., Wu, J.Y., Nguyen-Thanh, C., de Vaucorbeil, A., 2021. Fracture of thermo-elastic solids: Phase-field modeling and new results with an efficient monolithic solver. Computer Methods in Applied Mechanics and Engineering 376, 113648. doi:10.1016/j.cma.2020.113648.

Mánica, M., Gens, A., Vaunat, J., Ruiz, D.F., 2017. A time-dependent anisotropic model for argillaceous rocks. application to an underground excavation in callovo-oxfordian claystone. Computers and Geotechnics 85, 341–350. doi:10.1016/j.compgeo.2016.11.004.

Mazars, J., 1986. A description of micro- and macroscale damage of concrete structures. Engineering Fracture Mechanics 25, 729–737. doi:10.1016/0013-7944(86)90036-6.

McDonnell, J.J., 1990. The influence of macropores on debris flow initiation. Quarterly Journal of Engineering Geology and Hydrogeology 23, 325–331. doi:10.1144/GSL.QJEG.1990.023.04.06.

Mein, R.G., Larson, C.L., 1973. Modeling infiltration during a steady rain. Water Resources Research 9, 384–394. doi:10.1029/WR009i002p00384.

Meredith, P.G., Atkinson, B.K., 1985. Fracture toughness and subcritical crack growth during high-temperature tensile deformation of westerly granite and black gabbro. Physics of the Earth and Planetary Interiors 39, 33–51. doi:10.1016/0031-9201(85)90113-X.

Miehe, C., Hofacker, M., Schänzel, L.M., Aldakheel, F., 2015a. Phase field modeling of fracture in multi-physics problems. part ii. coupled brittle-to-ductile failure criteria and crack propagation in thermo-elastic–plastic solids. Computer Methods in Applied Mechanics and Engineering 294, 486–522. doi:10.1016/j.cma.2014.11.017.

Miehe, C., Hofacker, M., Welschinger, F., 2010a. A phase field model for rate-independent crack propagation: Robust algorithmic implementation based on operator splits. Computer Methods in Applied Mechanics and Engineering 199, 2765–2778. doi:10.1016/j.cma.2010.04.011.

Miehe, C., Mauthe, S., 2016. Phase field modeling of fracture in multi-physics problems. part iii. crack driving forces in hydro-poro-elasticity and hydraulic fracturing of fluid-saturated porous media. Computer Methods in Applied Mechanics and Engineering 304, 619–655. doi:10.1016/j.cma.2015.09.021.

Miehe, C., Mauthe, S., Teichtmeister, S., 2015b. Minimization principles for the coupled problem of darcy–biot-type fluid transport in porous media linked to phase field modeling of fracture. Journal of the Mechanics and Physics of Solids 82, 186–217. doi:10.1016/j.jmps.2015.04.006.

Miehe, C., Welschinger, F., Hofacker, M., 2010b. Thermodynamically consistent phase-field models of fracture: Variational principles and multi-field fe implementations. International Journal for Numerical Methods in Engineering 83, 1273–1311. doi:10.1002/nme.2861.

Moës, N., Dolbow, J., Belytschko, T., 1999. A finite element method for crack growth without remeshing. International Journal for Numerical Methods in Engineering 46, 131–150. doi:10.1002/(SICI)1097-0207(19990910)46:1<131::AID-NME726>3.0.CO;2-J.

Moës, N., Gravouil, A., Belytschko, T., 2002. Non-planar 3d crack growth by the extended finite element and level sets—part i: Mechanical model. International Journal for Numerical Methods in Engineering 53, 2549–2568. doi:10.1002/nme.429.

Morelli, S., Pazzi, V., Frodella, W., Fanti, R., 2018. Kinematic reconstruction of a deep-seated gravitational slope deformation by geomorphic analyses. Geosciences 8, 26. doi:10.3390/geosciences8010026.

Mori, T., Tanaka, K., 1973. Average stress in matrix and average elastic energy of materials with misfitting inclusions. Acta metallurgica 21, 571–574. doi:10.1016/0001-6160(73)90064-3.

Mumford, D., Shah, J., 1989. Optimal approximations by piecewise smooth functions and associated variational problems. Communications on Pure and Applied Mathematics 42, 577–685. doi:10.1002/cpa.3160420503.

Murakami, S., 1988. Mechanical modeling of material damage. Journal of Applied Mechanics 55, 280–286. doi:10.1115/1.3173673.

Murakami, S., Kamiya, K., 1997. Constitutive and damage evolution equations of elastic-brittle materials based on irreversible thermodynamics. International Journal of Mechanical Sciences 39, 473–486. doi:10.1016/S0020-7403(97)87627-8.

Nara, Y., Kaneko, K., 2005. Study of subcritical crack growth in andesite using the double torsion test. International Journal of Rock Mechanics and Mining Sciences 42, 521–530. doi:10.1016/j.ijrmms.2005.02.001.

Nara, Y., Kaneko, K., 2006. Sub-critical crack growth in anisotropic rock. International Journal of Rock Mechanics and Mining Sciences 43, 437–453. doi:10.1016/j.ijrmms.2005.07.008.

Nara, Y., Morimoto, K., Hiroyoshi, N., Yoneda, T., Kaneko, K., Benson, P.M., 2012. Influence of relative humidity on fracture toughness of rock: Implications for subcritical crack growth. International Journal of Solids and Structures 49, 2471–2481. doi:10.1016/j.ijsolstr.2012.05.009.

Nguyen, T.T., Yvonnet, J., Bornert, M., Chateau, C., Sab, K., Romani, R., Le Roy, R., 2016. On the choice of parameters in the phase field method for simulating crack initiation with experimental validation. International Journal of Fracture 197, 213–226. doi:10.1007/s10704-016-0082-1.

Nguyen, T.T., Yvonnet, J., Zhu, Q.Z., Bornert, M., Chateau, C., 2015. A phase field method to simulate crack nucleation and propagation in strongly heterogeneous materials from direct imaging of their microstructure. Engineering Fracture Mechanics 139, 18–39. doi:10.1016/j.engfracmech.2015.03.045.

Oliver, J., 1996. Modelling strong discontinuities in solid mechanics via strain softening constitutive equations. part 1: Fundamentals. International Journal for Numerical Methods in Engineering 39, 3575–3600. doi:10.1002/(SICI)1097-0207(19961115)39:21<3575::AID-NME65>3.0.CO;2-E.

Oliver, J., Huespe, A.E., Pulido, M.D.G., Chaves, E., 2002. From continuum mechanics to fracture mechanics: The strong discontinuity approach. Engineering Fracture Mechanics 69, 113–136. doi:10.1016/S0013-7944(01)00060-1.

Oliver, J., Huespe, A.E., Sánchez, P.J., 2006. A comparative study on finite elements for capturing strong discontinuities: E-fem vs x-fem. Computer Methods in Applied Mechanics and Engineering 195, 4732–4752. doi:10.1016/j.cma.2005.09.020.

Ortiz, M., 1985. A constitutive theory for the inelastic behavior of concrete. Mechanics of Materials 4, 67–93. doi:10.1016/0167-6636(85)90007-9.

Paliwal, B., Ramesh, K.T., 2008. An interacting micro-crack damage model for failure of brittle materials under compression. Journal of the Mechanics and Physics of Solids 56, 896–923. doi:10.1016/j.jmps.2007.06.012.

Palmer, A.C., Rice, J.R., Hill, R., 1973. The growth of slip surfaces in the progressive failure of over-consolidated clay. Proceedings of the Royal Society of London. A. Mathematical and Physical Sciences 332, 527–548. doi:10.1098/rspa.1973.0040.

Peng, S., Johnson, A.M., 1972. Crack growth and faulting in cylindrical specimens of chelmsford granite. International Journal of Rock Mechanics and Mining Sciences & Geomechanics Abstracts 9, 37–86. doi:10.1016/0148-9062(72)90050-2.

Peron, H., Laloui, L., Hueckel, T., Hu, L.B., 2009. Desiccation cracking of soils. European Journal of Environmental and Civil Engineering 13, 869–888. doi:10.1080/19648189.2009.9693159.

Perzyna, P., 1966. Fundamental problems in viscoplasticity, in: Advances in Applied Mechanics. Elsevier. volume 9, pp. 243–377.

Pham, K., Amor, H., Marigo, J.J., Maurini, C., 2011. Gradient damage models and their use to approximate brittle fracture. International Journal of Damage Mechanics 20, 618–652. doi:10.1177/1056789510386852.

Pijaudier-Cabot, G., Bažant, Z.P., 1987. Nonlocal damage theory. Journal of Engineering Mechanics 113, 1512–1533. doi:10.1061/(ASCE)0733-9399(1987)113:10(1512).

Qi, S., Wu, F., Zhou, Y., Song, Y., Gong, M., 2010. Influence of deep seated discontinuities on the left slope of jinping i hydropower station and its stability analysis. Bulletin of Engineering Geology and the Environment 69, 333–342. doi:10.1007/s10064-010-0268-0.

Rabczuk, T., Belytschko, T., 2004. Cracking particles: A simplified meshfree method for arbitrary evolving cracks. International Journal for Numerical Methods in Engineering 61, 2316–2343. doi:10.1002/nme.1151.

Rabczuk, T., Gracie, R., Song, J.H., Belytschko, T., 2010. Immersed particle method for fluid–structure interaction. International Journal for Numerical Methods in Engineering 81, 48–71. doi:10.1002/nme.2670.

Rabczuk, T., Ren, H., 2017. A peridynamics formulation for quasi-static fracture and contact in rock. Engineering Geology 225, 42–48. doi:10.1016/j.enggeo.2017.05.001.

Rabotnov, Y.N., Leckie, F.A., Prager, W., 1970. Creep problems in structural members. Journal of Applied Mechanics 37, 249. doi:10.1115/1.3408479.

Rahardjo, H., Lim, T., Chang, M., Fredlund, D., 1995. Shear-strength characteristics of a residual soil. Canadian Geotechnical Journal 32, 60–77. doi:10.1139/t95-005.

Rahimi, A., Rahardjo, H., Leong, E.C., 2011. Effect of antecedent rainfall patterns on rainfall-induced slope failure. Journal of Geotechnical and Geoenvironmental Engineering 137, 483–491. doi:10.1061/(ASCE)GT.1943-5606.0000451.

Ren, F., Ma, G., Wang, Y., Fan, L., 2016a. Pipe network model for unconfined seepage analysis in fractured rock masses. International Journal of Rock Mechanics and Mining Sciences 88, 183–196. doi:10.1016/j.ijrmms.2016.07.023.

Ren, H., Zhuang, X., Anitescu, C., Rabczuk, T., 2019. An explicit phase field method for brittle dynamic fracture. Computers & Structures 217, 45–56. doi:10.1016/j.compstruc.2019.03.005.

Ren, H., Zhuang, X., Cai, Y., Rabczuk, T., 2016b. Dual-horizon peridynamics. International Journal for Numerical Methods in Engineering 108, 1451–1476. doi:10.1002/nme.5257.

Richard, B., Ragueneau, F., 2013. Continuum damage mechanics based model for quasi brittle materials subjected to cyclic loadings: Formulation, numerical implementation and applications. Engineering Fracture Mechanics 98, 383–406. doi:10.1016/j.engfracmech.2012.11.013.

Rokkam, S., Gunzburger, M., Brothers, M., Phan, N., Goel, K., 2019. A nonlocal peridynamics modeling approach for corrosion damage and crack propagation. Theoretical and Applied Fracture Mechanics 101, 373–387. doi:10.1016/j.tafmec.2019.03.010.

Rokkam, S., Phan, N., Gunzburger, M., Shanbhag, S., Goel, K., 2018. Meshless peridynamics method for modeling corrosion crack propagation, in: 6th International Conference on Crack Paths (CP 2018)(Verona, Italy). http://www. Cp2018. Unipr. It.

Rudnicki, J.W., Rice, J.R., 1975. Conditions for the localization of deformation in pressure-sensitive dilatant materials. Journal of the Mechanics and Physics of Solids 23, 371–394. doi:10.1016/0022-5096(75)90001-0.

Rumble, J., 2017. CRC Handbook of Chemistry and Physics. Eighty-sixth ed., CRC press.

Saksala, T., Brancherie, D., Harari, I., Ibrahimbegovic, A., 2015. Combined continuum damage-embedded discontinuity model for explicit dynamic fracture analyses of quasi-brittle materials. International Journal for Numerical Methods in Engineering 101, 230–250. doi:10.1002/nme.4814.

Samaniego, C., Ulloa, J., Rodríguez, P., Houzeaux, G., Vázquez, M., Samaniego, E., 2021. A phase-field model for ductile fracture with shear bands: A parallel implementation. International Journal of Mechanical Sciences 200, 106424. doi:10.1016/j.ijmecsci.2021.106424.

Shen, R., Waisman, H., Guo, L., 2019. Fracture of viscoelastic solids modeled with a modified phase field method. Computer Methods in Applied Mechanics and Engineering 346, 862–890.

Shen, W.Q., Shao, J.F., 2017. A micro-mechanics-based elastic–plastic model for porous rocks: Applications to sandstone and chalk. Acta Geotechnica doi:10.1007/s11440-017-0536-2.

Shen, W.Q., Shao, J.F., Kondo, D., De Saxcé, G., 2015. A new macroscopic criterion of porous materials with a mises-schleicher compressible matrix. European Journal of Mechanics - A/Solids 49, 531–538. doi:10.1016/j.euromechsol.2014.09.010.

Shi, G., Yang, X., Yu, H., Zhu, C., 2019. Acoustic emission characteristics of creep fracture evolution in double-fracture fine sandstone under uniaxial compression. Engineering Fracture Mechanics 210, 13–28. doi:10.1016/j.engfracmech.2018.09.004.

Shou, K.J., Chen, J., 2021. On the rainfall induced deep-seated and shallow landslide hazard in taiwan. Engineering Geology 288, 106156. doi:10.1016/j.enggeo.2021.106156.

Silling, S.A., 2000. Reformulation of elasticity theory for discontinuities and long-range forces. Journal of the Mechanics and Physics of Solids 48, 175–209. doi:10.1016/S0022-5096(99)00029-0.

Silling, S.A., Askari, E., 2005. A meshfree method based on the peridynamic model of solid mechanics. Computers & Structures 83, 1526–1535. doi:10.1016/j.compstruc.2004.11.026.

Simo, J.C., Oliver, J., Armero, F., 1993. An analysis of strong discontinuities induced by strain-softening in rate-independent inelastic solids. Computational Mechanics 12, 277–296. doi:10.1007/BF00372173.

Simo, J.C., Rifai, M.S., 1990. A class of mixed assumed strain methods and the method of incompatible modes. International Journal for Numerical Methods in Engineering 29, 1595–1638. doi:10.1002/nme.1620290802.

Song, J.H., Areias, P.M.A., Belytschko, T., 2006. A method for dynamic crack and shear band propagation with phantom nodes. International Journal for Numerical Methods in Engineering 67, 868–893. doi:10.1002/nme.1652.

Sterpi, D., Gioda, G., 2009. Visco-plastic behaviour around advancing tunnels in squeezing rock. Rock Mechanics and Rock Engineering 42, 319–339. doi:10.1007/s00603-007-0137-8.

Stirling, R.A., Glendinning, S., Davie, C.T., 2017. Modelling the deterioration of the near surface caused by drying induced cracking. Applied Clay Science 146, 176–185. doi:10.1016/j.clay.2017.06.003.

Strobl, M., Seelig, T., 2016. On constitutive assumptions in phase field approaches to brittle fracture. Procedia Structural Integrity 2, 3705–3712. doi:10.1016/j.prostr.2016.06.460.

Su, K., 2003. Constitutive models for the meuse/haute-marne argillites–modex-rep, european commission–nuclear science and technology. Contract n FIKW-CT2000-00029, Deliverable , 2–3.

Sukumar, N., Chopp, D.L., Moran, B., 2003. Extended finite element method and fast marching method for three-dimensional fatigue crack propagation. Engineering Fracture Mechanics 70, 29–48. doi:10.1016/S0013-7944(02)00032-2.

Sun, P., Wang, H., Wang, G., Li, R., Zhang, Z., Huo, X., 2021. Field model experiments and numerical analysis of rainfall-induced shallow loess landslides. Engineering Geology 295, 106411. doi:10.1016/j.enggeo.2021.106411.

Sun, S., Sundararaghavan, V., 2014. A peridynamic implementation of crystal plasticity. International Journal of Solids and Structures 51, 3350–3360. doi:10.1016/j.ijsolstr.2014.05.027.

Sysala, S., Cermak, M., Koudelka, T., Kruis, J., Zeman, J., Blaheta, R., 2016. Subdifferential-based implicit return-mapping operators in computational plasticity. ZAMM - Journal of Applied Mathematics and Mechanics / Zeitschrift für Angewandte Mathematik und Mechanik 96, 1318–1338. doi:10.1002/zamm.201500305.

Tan, P., Jin, Y., Pang, H., 2021. Hydraulic fracture vertical propagation behavior in transversely isotropic layered shale formation with transition zone using xfem-based czm method. Engineering Fracture Mechanics 248, 107707. doi:10.1016/j.engfracmech.2021.107707.

Tang, C.A., Liu, H., Lee, P.K.K., Tsui, Y., Tham, L.G., 2000. Numerical studies of the influence of microstructure on rock failure in uniaxial compression — part i: Effect of heterogeneity. International Journal of Rock Mechanics and Mining Sciences 37, 555–569. doi:10.1016/S1365-1609(99)00121-5.

Tang, J., Wang, Y., Tang, X., 2009. Research on deformation mechanics of mayampo slope creep deformation rock mass, in: ISRM International Symposium on Rock Mechanics - SINOROCK 2009, OnePetro.

Tavenas, F., Leroueil, S., 1981. Creep and failure of slopes in clays. Canadian Geotechnical Journal 18, 106–120. doi:10.1139/t81-010.

Thirard, G., Thiery, Y., Gourdier, S., Grandjean, G., Maquaire, O., François, B., Bitri, A., Coulibaly, S., Lissak, C., Costa, S., 2022. Hydromechanical assessment of a complex landslide through geophysics and numerical modeling: Toward an upgrade for the villerville landslide (normandy, france). Engineering Geology 297, 106516. doi:10.1016/j.enggeo.2022.106516.

Thomas, A.G., 1994. The development of fracture mechanics for elastomers. Rubber Chemistry and Technology 67, 50–67. doi:10.5254/1.3538688.

Tohari, A., Nishigaki, M., Komatsu, M., 2007. Laboratory rainfall-induced slope failure with moisture content measurement. Journal of Geotechnical and Geoenvironmental Engineering 133.

Tsai, T.L., Chen, H.E., Yang, J.C., 2008. Numerical modeling of rainstorm-induced shallow landslides in saturated and unsaturated soils. Environmental Geology 55, 1269–1277. doi:10.1007/s00254-007-1075-1.

van Genuchten, M.T., 1980. A closed-form equation for predicting the hydraulic conductivity of unsaturated soils. Soil Science Society of America Journal 44, 892–898. doi:10.2136/sssaj1980.03615995004400050002x.

Vassaux, M., Richard, B., Ragueneau, F., Millard, A., 2015. Regularised crack behaviour effects on continuum modelling of quasi-brittle materials under cyclic loading. Engineering Fracture Mechanics 149, 18–36. doi:10.1016/j.engfracmech.2015.09.040.

Voyiadjis, G.Z., Taqieddin, Z.N., Kattan, P.I., 2008. Anisotropic damage–plasticity model for concrete. International Journal of Plasticity 24, 1946–1965. doi:10.1016/j.ijplas.2008.04.002.

Wang, C., Xiong, W.P., Chang, X., Ye, L.Y., Li, X., 2018. Analysis of variable working conditions for propeller-ice interaction. Ocean Engineering 156, 277–293. doi:10.1016/j.oceaneng.2018.02.026.

Wang, H., 2015. Numerical modeling of non-planar hydraulic fracture propagation in brittle and ductile rocks using xfem with cohesive zone method. Journal of Petroleum Science and Engineering 135, 127–140. doi:10.1016/j.petrol.2015.08.010.

Wang, L., Yin, Y., Zhang, Z., Huang, B., Wei, Y., Zhao, P., Hu, M., 2019a. Stability analysis of the xinlu village landslide (chongqing, china) and the influence of rainfall. Landslides 16, 1993–2004. doi:10.1007/s10346-019-01240-5.

Wang, M., Yu, Z., Jin, Y., Shao, J., 2021. Modeling of damage and cracking in heterogeneous rock-like materials by phase-field method. Mechanics Research Communications 114, 103612. doi:10.1016/j.mechrescom.2020.103612.

Wang, M., Yu, Z., Shen, W., Shao, J., 2022. Numerical study of time-dependent deformation and cracking in brittle rocks with phase-field method and application to slope instability analysis. International Journal of Rock Mechanics and Mining Sciences 155, 105144. doi:10.1016/j.ijrmms.2022.105144.

Wang, Y., Zhou, X., Kou, M., 2019b. An improved coupled thermo-mechanic bond-based peridynamic model for cracking behaviors in brittle solids subjected to thermal shocks. European Journal of Mechanics - A/Solids 73, 282–305. doi:10.1016/j.euromechsol.2018.09.007.

Waza, T., Kurita, K., Mizutani, H., 1980. The effect of water on the subcritical crack growth in silicate rocks. Tectonophysics 67, 25–34. doi:10.1016/0040-1951(80)90162-6.

Wells, G.N., Sluys, L.J., 2000. Application of embedded discontinuities for softening solids. Engineering Fracture Mechanics 65, 263–281. doi:10.1016/S0013-7944(99)00120-4.

Wheeler, M.F., Wick, T., Wollner, W., 2014. An augmented-lagrangian method for the phase-field approach for pressurized fractures. Computer Methods in Applied Mechanics and Engineering 271, 69–85. doi:10.1016/j.cma.2013.12.005.

Wilson, E.L., 1974. The static condensation algorithm. International Journal for Numerical Methods in Engineering 8, 198–203. doi:10.1002/nme.1620080115.

Wong, H., Zobel, M., Buenfeld, N., Zimmerman, R., 2009. Influence of the interfacial transition zone and microcracking on the diffusivity, permeability and sorptivity of cement-based materials after drying. Magazine of Concrete Research 61, 571–589. doi:10.1680/macr.2008.61.8.571.

Wong, T.f., Baud, P., 2012. The brittle-ductile transition in porous rock: A review. Journal of Structural Geology 44, 25–53. doi:10.1016/j.jsg.2012.07.010.

Wu, J.Y., 2017. A unified phase-field theory for the mechanics of damage and quasi-brittle failure. Journal of the Mechanics and Physics of Solids 103, 72–99. doi:10.1016/j.jmps.2017.03.015.

Wu, J.Y., Cervera, M., 2018. A novel positive/negative projection in energy norm for the damage modeling of quasi-brittle solids. International Journal of Solids and Structures 139–140, 250–269. doi:10.1016/j.ijsolstr.2018.02.004.

Wu, J.Y., Huang, Y., Nguyen, V.P., 2020a. On the bfgs monolithic algorithm for the unified phase field damage theory. Computer Methods in Applied Mechanics and Engineering 360, 112704. doi:10.1016/j.cma.2019.112704.

Wu, J.Y., Huang, Y., Zhou, H., Nguyen, V.P., 2021. Three-dimensional phase-field modeling of mode i + ii/iii failure in solids. Computer Methods in Applied Mechanics and Engineering 373, 113537. doi:10.1016/j.cma.2020.113537.

Wu, J.Y., Li, F.B., Xu, S.L., 2015. Extended embedded finite elements with continuous displacement jumps for the modeling of localized failure in solids. Computer Methods

in Applied Mechanics and Engineering 285, 346–378. doi:10.1016/j.cma.2014.11.013.

Wu, J.Y., Nguyen, V.P., Nguyen, C.T., Sutula, D., Sinaie, S., Bordas, S.P., 2020b. Phase-field modeling of fracture, in: Advances in Applied Mechanics. Elsevier. volume 53, pp. 1–183. doi:10.1016/bs.aams.2019.08.001.

Wu, W., 2015. Recent Advances in Modeling Landslides and Debris Flows. Springer.

Xie, N., Zhu, Q.Z., Xu, L.H., Shao, J.F., 2011. A micromechanics-based elastoplastic damage model for quasi-brittle rocks. Computers and Geotechnics 38, 970–977. doi:10.1016/j.compgeo.2011.07.014.

Xu, X.P., Needleman, A., 1994. Numerical simulations of fast crack growth in brittle solids. Journal of the Mechanics and Physics of Solids 42, 1397–1434. doi:10.1016/0022-5096(94)90003-5.

Yang, S., Jiang, Y., Xu, W., Chen, X., 2008. Experimental investigation on strength and failure behavior of pre-cracked marble under conventional triaxial compression. International Journal of Solids and Structures 45, 4796–4819. doi:10.1016/j.ijsolstr.2008.04.023.

Yang, S.Q., Jing, H.W., Wang, S.Y., 2012. Experimental investigation on the strength, deformability, failure behavior and acoustic emission locations of red sandstone under triaxial compression. Rock Mechanics and Rock Engineering 45, 583–606. doi:10.1007/s00603-011-0208-8.

Yang, W., Zhang, Q., Li, S., Wang, S., 2014. Time-dependent behavior of diabase and a nonlinear creep model. Rock Mechanics and Rock Engineering 47, 1211–1224. doi:10.1007/s00603-013-0478-4.

Yashima, A., 2001. Slope failure at tunnel entrance due to excavation and its countermeasure, modern tunneling science and technology. IS-KYOTO2001 , 557–562.

Yoshioka, K., Naumov, D., Kolditz, O., 2020. On crack opening computation in variational phase-field models for fracture. Computer Methods in Applied Mechanics and Engineering 369, 113210. doi:10.1016/j.cma.2020.113210.

Yu, J., Xu, W., Jia, C., Wang, R., Wang, H., 2019. Experimental measurement of permeability evolution in sandstone during hydrostatic compaction and triaxial deformation. Bulletin of Engineering Geology and the Environment 78, 5269–5280. doi:10.1007/s10064-018-1425-0.

Yu, Z., Shao, J., Duveau, G., Vu, M.N., Armand, G., 2021a. Numerical modeling of deformation and damage around underground excavation by phase-field method with hydromechanical coupling. Computers and Geotechnics 138, 104369. doi:10.1016/j.compgeo.2021.104369.

Yu, Z., Shao, J.F., Vu, M.N., Armand, G., 2021b. Numerical study of thermo-hydro-mechanical responses of in situ heating test with phase-field model. International Journal of Rock Mechanics and Mining Sciences 138, 104542. doi:10.1016/j.ijrmms.2020.104542.

Zafati, E., Richard, B., 2019. Anisotropic continuum damage constitutive model to describe the cyclic response of quasi-brittle materials: The regularized unilateral effect. International Journal of Solids and Structures 162, 164–180. doi:10.1016/j.ijsolstr.2018.12.009.

Zeng, Q., Yao, J., Shao, J., 2020. An extended finite element solution for hydraulic fracturing with thermo-hydro-elastic–plastic coupling. Computer Methods in Applied Mechanics and Engineering 364, 112967. doi:10.1016/j.cma.2020.112967.

Zhang, F., Yashima, A., Nakai, T., Ye, G.L., Aung, H., 2005a. An elasto-viscoplastic model for soft sedimentary rock based on tij concept and subloading yield surface. Soils and foundations 45, 65–73. doi:10.3208/sandf.45.1_65.

Zhang, L.L., Zhang, L.M., Tang, W.H., 2005b. Rainfall-induced slope failure considering variability of soil properties. Géotechnique 55, 183–188. doi:10.1680/geot.2005.55.2.183.

Zhang, M., Yin, Y., Huang, B., 2015. Mechanisms of rainfall-induced landslides in gently inclined red beds in the eastern sichuan basin, sw china. Landslides 12, 973–983. doi:10.1007/s10346-015-0611-4.

Zhang, S., Jiang, W., Tonks, M.R., 2020. A new phase field fracture model for brittle materials that accounts for elastic anisotropy. Computer Methods in Applied Mechanics and Engineering 358, 112643. doi:10.1016/j.cma.2019.112643.

Zhang, S.l., Zhu, Z.h., Qi, S.c., Hu, Y.x., Du, Q., Zhou, J.w., 2018. Deformation process and mechanism analyses for a planar sliding in the mayanpo massive bedding rock slope at the xiangjiaba hydropower station. Landslides 15, 2061–2073. doi:10.1007/s10346-018-1041-x.

Zhang, W., Cai, Y., 2010. Continuum Damage Mechanics and Numerical Applications. Springer Science & Business Media.

Zhang, X., Sloan, S.W., Vignes, C., Sheng, D., 2017. A modification of the phase-field model for mixed mode crack propagation in rock-like materials. Computer Methods in Applied Mechanics and Engineering 322, 123–136. doi:10.1016/j.cma.2017.04.028.

Zhao, L., Zhu, Q., Xu, W., Dai, F., Shao, J., 2016. A unified micromechanics-based damage model for instantaneous and time-dependent behaviors of brittle rocks. International Journal of Rock Mechanics and Mining Sciences 84, 187–196. doi:10.1016/j.ijrmms.2016.01.015.

Zhao, L.Y., Shao, J.F., Zhu, Q.Z., 2018a. Analysis of localized cracking in quasi-brittle materials with a micro-mechanics based friction-damage approach. Journal of the Mechanics and Physics of Solids 119, 163–187. doi:10.1016/j.jmps.2018.06.017.

Zhao, L.Y., Zhu, Q.Z., Shao, J.F., 2018b. A micro-mechanics based plastic damage model for quasi-brittle materials under a large range of compressive stress. International Journal of Plasticity 100, 156–176. doi:10.1016/j.ijplas.2017.10.004.

Zhao, X.G., Cai, M., Wang, J., Ma, L.K., 2013. Damage stress and acoustic emission characteristics of the beishan granite. International Journal of Rock Mechanics and Mining Sciences 64, 258–269. doi:10.1016/j.ijrmms.2013.09.003.

Zhao, X.G., Wang, J., Cai, M., Cheng, C., Ma, L.K., Su, R., Zhao, F., Li, D.J., 2014. Influence of unloading rate on the strainburst characteristics of beishan granite under true-triaxial unloading conditions. Rock Mechanics and Rock Engineering 47, 467–483. doi:10.1007/s00603-013-0443-2.

Zhao, Y., Wang, Y., Wang, W., Wan, W., Tang, J., 2017. Modeling of non-linear rheological behavior of hard rock using triaxial rheological experiment. International Journal of Rock Mechanics and Mining Sciences 93, 66–75. doi:10.1016/j.ijrmms.2017.01.004.

Zhou, C., Jiang, Q., Wei, W., Chen, Y., Rong, G., 2016. Safety monitoring and stability analysis of left bank high slope at jinping-i hydropower station. Quarterly Journal of Engineering Geology and Hydrogeology 49, 308–321. doi:10.1144/qjegh2015-037.

Zhou, H., Yang, Y., Gao, H., Zhang, C., Hu, D., 2015a. Experimental investigations on the short- and long-term behaviour of jinping marble in deep tunnels. European Journal of Environmental and Civil Engineering 19, s83–s96. doi:10.1080/19648189.2015.1064622.

Zhou, H.W., Wang, Z.H., Ren, W.G., Liu, Z.L., Liu, J.F., 2019a. Acoustic emission based mechanical behaviors of beishan granite under conventional triaxial compression and hydro-mechanical coupling tests. International Journal of Rock Mechanics and Mining Sciences 123, 104125. doi:10.1016/j.ijrmms.2019.104125.

Zhou, J.W., Xu, W.Y., Yang, X.G., 2010. A microcrack damage model for brittle rocks under uniaxial compression. Mechanics Research Communications 37, 399–405. doi:10.1016/j.mechrescom.2010.05.001.

Zhou, S., Zhuang, X., Rabczuk, T., 2019b. Phase field modeling of brittle compressive-shear fractures in rock-like materials: A new driving force and a hybrid formulation. Computer Methods in Applied Mechanics and Engineering 355, 729–752. doi:10.1016/j.cma.2019.06.021.

Zhou, S., Zhuang, X., Rabczuk, T., 2020. Phase field method for quasi-static hydro-fracture in porous media under stress boundary condition considering the effect of initial stress field. Theoretical and Applied Fracture Mechanics 107, 102523. doi:10.1016/j.tafmec.2020.102523.

Zhou, X.P., Gu, X.B., Wang, Y.T., 2015b. Numerical simulations of propagation, bifurcation and coalescence of cracks in rocks. International Journal of Rock Mechanics and Mining Sciences 80, 241–254. doi:10.1016/j.ijrmms.2015.09.006.

Zhu, Q., Shao, J., 2017. Micromechanics of rock damage: Advances in the quasi-brittle field. Journal of Rock Mechanics and Geotechnical Engineering 9, 29–40. doi:10.1016/j.jrmge.2016.11.003.

Zhu, Q.Z., Kondo, D., Shao, J.F., 2008. Micromechanical analysis of coupling between anisotropic damage and friction in quasi brittle materials: Role of the homogenization scheme. International Journal of Solids and Structures 45, 1385–1405. doi:10.1016/j.ijsolstr.2007.09.026.

Zhu, Q.Z., Shao, J.F., 2015. A refined micromechanical damage–friction model with strength prediction for rock-like materials under compression. International Journal of Solids and Structures 60–61, 75–83. doi:10.1016/j.ijsolstr.2015.02.005.

Zhu, Q.Z., Shao, J.F., Kondo, D., 2011. A micromechanics-based thermodynamic formulation of isotropic damage with unilateral and friction effects. European Journal of Mechanics - A/Solids 30, 316–325. doi:10.1016/j.euromechsol.2010.12.005.

Zhu, Q.Z., Zhao, L.Y., Shao, J.F., 2016. Analytical and numerical analysis of frictional damage in quasi brittle materials. Journal of the Mechanics and Physics of Solids 92, 137–163. doi:10.1016/j.jmps.2016.04.002.

Zhuang, X., Zhou, S., Huynh, G., Areias, P., Rabczuk, T., 2022. Phase field modeling and computer implementation: A review. Engineering Fracture Mechanics 262, 108234. doi:10.1016/j.engfracmech.2022.108234.

Zhuang, X., Zhou, S., Sheng, M., Li, G., 2020. On the hydraulic fracturing in naturally-layered porous media using the phase field method. Engineering Geology 266, 105306. doi:10.1016/j.enggeo.2019.105306.

Zi, G., Rabczuk, T., Wall, W., 2007. Extended meshfree methods without branch enrichment for cohesive cracks. Computational Mechanics 40, 367–382. doi:10.1007/s00466-006-0115-0.

Zienkiewicz, O.C. (Ed.), 2001. Computational Geomechanics: With Special Reference to Earthquake Engineering. reprint ed., Wiley, Chichester.

Zimmerman, R.W., 1991. Elastic moduli of a solid containing spherical inclusions. Mechanics of Materials 12, 17–24. doi:10.1016/0167-6636(91)90049-6.